Eruptive History and Magmatic Evolution of Corbetti Caldera in the Main Ethiopian Rift



David J. Colby

Pembroke College

University of Oxford

A thesis submitted for the degree of

Doctor of Philosophy

Trinity 2023

This thesis is dedicated to my family, who inspired and nurtured a love of the natural world.

Funding

I am grateful that this research has received funding from multiple agencies and funding bodies. The Natural Environment Research Council has funded this research via grant NE/L013932/1 (RiftVolc) and an Oxford DTP studentship (NE/L002612/1) to David Colby. Additional funding for analysis has been kindly provided by Fonds National de la Recherche Scientifique (F.R.S.-FNRS) MIS grant F.4515.20 to Karen Fontijn and the Wiener Anspach Foundation grant "The Magmatic Evolution of Geothermally Active Calderas in Ethiopia" to Karen Fontijn, David Pyle and Tamsin Mather.

Statement of Originality

I confirm the work submitted here is my own and has not been submitted to any other degree awarding institution. Whilst this thesis is my own work, parts were written in collaboration with others, the specifics of which are outlined below.

Chapter 2 was written in collaboration with my supervisors David Pyle, Karen Fontijn and Tamsin Mather and collaborators from the University of Addis Ababa, Abate Melaku, Million Mengesha and Gezahegn Yirgu. I undertook the main body of work, leading the fieldwork, collecting data, analysing samples and writing the manuscript. My co-authors helped to facilitate and support the fieldwork, interpreting the volcanic successions and editing the manuscript in preparation for submission.

Chapter 3 was also written in collaboration with my supervisors and collaborators from Addis Ababa University. I undertook the samples preparation, analysis and interpretation of the data as well as writing the manuscript. My co-authors provided edits to the manuscript and alongside the discussion of ideas and helping to develop the themes of the paper

Chapter 4 was written in collaboration with my supervisors. I conducted the data collection and analysis, wrote the chapter and my supervisors provided discussion of ideas, and comments and feedback on the chapter.

Acknowledgements

Firstly, I would like to thank my supervisors, Professor David Pyle, Professor Tamisn Mather and Dr Karen Fontijn. Thank you for supervising me over the last 5 years. By sharing your knowledge and insight, you have continually inspired me to persevere and question. Thank you for spending time with me in the field as part of my fieldwork and on field trips and sharing your experience with me. Thank you for the opportunity to work with you and to study such an interesting area. Thank you, as well, for your understanding and support during the challenges of the last few years.

I am indebted to Professor Gezahegn Yirgu, without whom, I would not have been able to conduct the fieldwork this thesis is based on. I am grateful for this support in setting up the fieldwork and for his contributions and feedback to the papers in this thesis. During my time in the field, I was privileged to work with Abate and Million, who were amazing. Their expertise in conducting field campaigns in Ethiopia ensured that everything ran smoothly in the field, and their support in discussing ideas and contributing to the manuscripts is greatly appreciated. I want to thank Seid Abubaker of Ethioder for this excellent driving and his "No coffee, no work" motto. I am grateful to Hamiyou Bekera, our guide while in the field, ensuring a safe and productive field campaign. Fieldwork and sample export were kindly permitted by the authorities of the Oromia region and the Ministry of Mines and Petroleum of Ethiopia, respectively.

I would also like to thank Owen Green, Matthew Beverley Smith and Jon Wells for their help and guidance with sample preparation for geochemical analysis and preparing thin sections. I want to thank Anderew Matzden for his time and support in setting me up on the EMPA and helping with the analysis, and Activation Laboratories for conducting the ICP-OES and ICP-MS analysis. I would also like to thank Wendy Debouge and Jeroen de Jong for conducting the Sr isotope analysis. Thank you to the NERC DTP for providing me with this studentship and to Victoria and all the staff at the DTP for making the experience so enjoyable. I would also like to thank the members of the Oxford

Volcanology group for the interesting discussions and for always being happy to lend a helping hand. Many more people have helped and guided me along the way, and I want to thank them all for their influence in getting me to this point.

A huge thank you goes out to all my friends, old and new. Thank you for all the pub trips, whiskeys, board game sessions, walks in the Cotswolds, weekend trips away, and late-night chats. In particular, I would like to thank my housemates, Ben, Ian, Matthew and Nacho. You have been a joy to live with, I have had an amazing time, and you have made the experience of the past 4 years thoroughly enjoyable despite unprecedented challenges.

I am also hugely grateful for the support of my partner, Kirsty. Thank you for putting up with my ramblings about volcanoes, comforting me when things get tough, and always remembering what's important; fun food!

Finally, I would like to thank my Mum and Dad, brother, Sam, my Grandparents and wider family for their unwavering support, encouragement and guidance, despite not understanding anything I have done! I am fortunate that my family have always encouraged me to explore and be curious about the natural world. I would not have taken the path I have, were it not for them. Thank you.

Abstract

The East African Rift (EAR) is dominated by peralkaline volcanism, making it an ideal location to study such typically rift-related volcanism and the processes behind the evolution of these enigmatic magmas. Over 120 million people live within a 100 km radius of a volcano within the EAR, and with the ongoing development of geothermal projects associated with large silicic centres, investigating the nature of past volcanism becomes vital for understanding these systems and informing future hazard assessments. The Main Ethiopian Rift (MER) forms part of the EAR and hosts 59 Holocene volcanoes exhibiting diverse eruptive products. This thesis focuses on one of these centres, a restless caldera in the southern section of the MER: Corbetti caldera.

Through fieldwork, and geochemical and petrological investigations of peralkaline eruptive products, this thesis sheds light on Corbetti's eruptive history, magmatic processes, and, by comparison with literature data, the variation in peralkaline magmas originating across the MER. This thesis shows that Corbetti has followed a similar evolutionary pattern to other calderas in the MER. It provides a comprehensive account of Corbetti's eruptive history, presents a relative chronology of activity, constrains the age of the Biftu Tuff cone to < 7375 ± 54 cal BP and delimits several new distinct lava flows from Chabbi. This work shows that over the last 2.3 ka Corbetti has experienced at least one eruption every 300-400 years. These eruptions have almost exclusively been peralkaline rhyolites, with only a single basaltic eruption found (reported and documented here for the first time). Detailed geochemical investigation reveals the monotony of erupted compositions and elucidates how peralkaline magmas are derived from alkali basalts through progressive fractional crystallisation. Water content in the alkali basalts (~0.5-1.2 wt.%) and peralkaline magmas (~ 7 wt.%) are estimated, and storage depths constrained using barometry (50-190 MPa) and RhyoliteMELTS modelling (150-250 MPa). The distinct lack of geochemical and petrological diversity of peralkaline magmas at Corbetti is in stark contrast to the rest of the rift. This thesis reviews the geochemical variation in peralkaline products across the MER and investigates the mineralogical controls on observed liquid lines of descent, with a focus on the Qz-Or-Ab-Ns-Ac residua system. Distinct trends at the alkali-feldspar quartz cotectic are identified, influenced by the proportion and composition of the fractionating feldspar phase and the presence or absence of Na-rich clinopyroxene. This thesis also presents

evidence from some MER centres showing a shift in the location of the quartz-feldspar cotectic, which may be in response to variations in storage depth or concentration of halogens, particularly F, in the melt.

This work presents new insights into Corbetti's past eruptions, underlining potential hazards associated within this actively uplifting caldera. It also enhances our understanding of the generation and storage of peralkaline magmas and highlights the homogeneity of Corbetti's magmas compared to the diverse range of peralkaline compositions observed across the rift. These findings contribute to hazard assessments and further our knowledge of rift-related volcanism.

Contents

1 Introduction **1**

1.1 Motivation and scope of research 1

1.2 Research objectives 7

1.3 Thesis Outline 8

1.3.1 Stratigraphy and Eruptive History 9

1.3.2 Magma Storage Conditions 9

1.3.3 Diversity in Peralkaline Magmas across the Main Ethiopian Rift . . 10

1.3.4 Conclusions and further work 10

2 Stratigraphy and Eruptive History of Corbetti Caldera in the Main Ethiopian Rift **11**

2.1 Introduction 14

2.1.1 Regional Setting 14

2.1.2 Corbetti Caldera 16

2.2 Samples and Methods 18

2.2.1 Field Campaign 18

2.2.2 Stratigraphic Framework 18

2.2.3 Geochemistry and ^{14}C dating 19

2.3 Results:Stratigraphy 20

2.3.1 Northern Caldera Wall (NCW) 20

2.3.2 Southern Caldera Wall (SCW) 27

2.3.3 Central Caldera Section (CC) 37

2.3.4 Central Gully (CG) 43

2.3.5 Urji Slopes (US) 48

2.3.6 Chabbi and the Biftu Tuff Cone 53

2.4 Geochemistry 62

2.4.1 Major Element Geochemistry 62

2.4.2 Trace Element Geochemistry 62

2.5 Discussion: Eruptive History of Corbetti Caldera 64
2.5.1 Early Phases of Activity 67
2.5.2 Post-caldera activity 70
2.5.2.1 Biftu Tuff Cone 73
2.5.3 Recurrence rate and Hazard Implications 74
2.6 Conclusions 75
2.7 Acknowledgements 76

3 Magma storage conditions beneath a peralkaline caldera in the Main Ethiopian Rift 77
3.1 Introduction 80
3.1.1 Geological Setting of Corbetti Caldera 81
3.1.2 Overview of studied units 82
3.2 Methods 84
3.2.1 Whole Rock, Glass and Mineral Geochemistry 84
3.2.2 $^{87}Sr/^{86}Sr$ Isotope Analysis 85
3.2.3 RhyoliteMELTS 86
3.2.4 Thermobarometry and Hygrometry 87
3.2.4.1 Basaltic Tuff (NCW_H) 87
3.2.4.2 Peralkaline Rhyolite Ignimbrite (NCW_F) 87
3.3 Results 88
3.3.1 Geochemistry and $^{87}Sr/^{86}Sr$ Ratios 88
3.3.2 Mineralogy 93
3.3.2.1 Olivine 93
3.3.2.2 Feldspars 98
3.3.2.3 Clinopyroxene 98
3.3.2.4 Other Phases 98
3.3.3 Thermobarometry and Hygrometry 99
3.3.4 Pressure Estimates 102
3.3.5 RhyoliteMelts 104
3.4 Discussion 107
3.4.1 Basaltic Eruption 107
3.4.2 Peralkaline Magmas 110
3.4.3 Depth of Magma Storage 112
3.5 Conclusion 115
3.6 Acknowledgements 116

4 Diversity in Peralkaline Magmas across the Main Ethiopian Rift **117**
4.1 Introduction . . . 120
4.1.1 Peralkaline Magmas . . . 124
4.2 Methodology . . . 125
4.3 Results . . . 128
4.3.1 Mineral Assemblages . . . 135
4.4 Discussion . . . 137
4.4.1 Geochemical Diversity . . . 137
4.4.2 The Qz-Or-Ab-Ac-Ns residua system . . . 147
4.4.3 Carmichael and MacKenzie Cotectic . . . 147
4.4.4 Di Carlo and Romano Cotectic . . . 153
4.4.5 Location of the quartz-feldspar cotectic in peralkaline systems . . . 155
4.5 Conclusion . . . 155

5 Conclusions **159**
5.1 Physical Volcanology . . . 159
5.2 Magma Storage Conditions . . . 160
5.3 Diversity in Peralkaline Magmas . . . 166
5.4 Future Work . . . 167
5.4.1 Palaeomagnetism . . . 167
5.4.2 Volcanic Risk . . . 168
5.4.3 Peralkaline Magmas . . . 170
5.5 Concluding Remarks . . . 171

References **197**

A Appendices for Chapter 2 **199**

B Appendices for Chapter 3 **221**

C Appendices for Chapter 4 **243**

List of Figures

1.1 A) Overview map of the East African Rift, highlighting the location of the Main Ethiopian Rift (Black Box). B) Detailed view of the Main Ethiopian Rift (MER) showing the location of major volcanic centres and Corbetti caldera highlighted by the black rectangle. C) Close-up view of Corbetti Caldera (ramparts indicated by black triangles after Hunt et al. 2019) and the Wonji fault belt (WFB; Agostini et al. 2011. 2

1.2 Geological Map of Corbetti caldera showing the major fault structures that have been previously identified and the location of the post-caldera edifices. Legend highlight previously identified lithofacies and units. CO3-CO6 are previously identified obsidian lavas from Chabbi. After Rapprich et al. 2016, Hunt et al.2019 and Clarke 2020. 5

1.3 The Qz-Or-Ab-Ns-Ac residua system's ternary plot shows the quartz-feldspar cotectic. The isotherms are projected at PH2O=100 MPa Carmichael and MacKenzie (1963). B) shows a cartesian form of this diagram (Wilke et al., 2017) highlighting the intersection of the thermal valley with the quart-feldspar cotectic. The Whole Rock Minimum (WR-Min) composition is the most evolved whole rock composition for peralkaline magmas, and the Effective Minimum composition (EMC) is the most differentiated, high FeOt, peralkaline composition reported (Macdonald et al., 2021; White et al., 2023). Two cotectics are projected, one after Carmichael and MacKenzie (1963) and the other after Di Carlo et al. (2010) & Romano et al. (2020). . 6

2.1 A) Overview map of the East African Rift (EAR) showing major fault structures and location of silicic volcanoes. B) Overview map of the Main Ethiopian Rift (MER) showing the location of central silicic volcanoes and major settlements. Corbetti, the focus of this study, is in the southern part of the MER. C) Map showing location of Corbetti Caldera and a section of the Wonji Fault Belt (WFB). Faults after Agostini et al. 2011 15

2.2 A) Geological setting of Corbetti Caldera, highlighting the major features, geological facies within the caldera and the sampling locations for this study [after Rapprich et al. (2016); Hunt et al. (2019); Clarke (2020)] B) Detail of sample locations in the Northern Caldera wall. C) Detail of sample locations in Southern caldera wall. D) Detail of Central Caldera sample locations E) Detail of Central Gully section sample locations. F) Detail of sample locations around the slopes of Urji. G) Detail of sample locations around the Biftu Tuff Cone and older pre-caldera deposits. H) Detail of sample locations of drainage gullies. 22

2.3 Field photos highlight outcrops in the Northern Caldera wall. Symbols denote location of collected samples and site localities are marked in Figure 2.2. A) Site 25 showing a jointed rhyolite lava (NCW_A) and the contact between an overlying pyroclastic succession, inferred to be NCW_D. B) Site 24 showing the pyroclastic succession (NCW_B) capped with a thin lava (NCW_C) and further pyroclastic succession (NCW_D). C) Welded ignimbrite at Site 3, showing the contact between the underlying red ignimbrite. D) Detail of the welded ignimbrite (NCW_F). E) Laminated ash-rich horizons (NCW_H) at Site 4. Horizons vary between loose unconsolidated ash and sintered ash. F) Ash aggregate (Accretionary Lapilli) bearing horizon at Site 23 (NCW_H). 23

2.4 A) Stratigraphic log of units exposed in the northern caldera wall (Figure. 2.2B) and described in Table 2.2. B) Stratigraphic logs of exposures in the Southern Caldera wall (Fig. 2.2C) highlighting lateral correlations between outcrops. Units described in Table 2.2. Symbols denote the location of samples which underwent geochemical analysis (See Section 2.4). 26

2.5 A) Shows overview of outcrop at Site 7 (Figure 2.2C) and location of panels B and C. B and C show details of the outcrop with C highlighting the major lithofacies observed (see Table 2.3). D) Outcrop at Site 29 (Figure 2.2C) showing presence of Bedded Pumice and WKYP units capping the succession. Symbols denote units sampled for geochemical analysis and presented in Figures 2.14 and 2.15 28

2.6 A) Panoramic image of quarry in the southern caldera wall (Site 6, Figure 2.2C) highlighting the identified units outline in Table 2.3 and Figure 2.4. C) Detail of the upper portion of the exposure which outcrops to the west of the panorama in A. Symbols denote location of samples. 29

2.7 Selected outcrops in the Central Caldera (Figure 2.2D) highlighting the presence of key units outlined in Figure 2.10 & Table 2.4. A-B) Site 15 (MER001 of Fontijn et al. (2018)) overview and detail of major units. C) Site 17 showing the Bedded Pumice horizon and the consistent staining of the upper portion of the unit. Symbols denote the location of samples analysed in later sections. 38

2.8 A) Selected stratigraphic logs for outcrops in the Central Caldera (Figure 2.2D) highlighting the major correlations (Table 2.4). B) Stratigraphic logs of outcrops in the north-eastern gully (Figure 2.2E) with highlighted correlations based upon lateral tracing of units (Table 2.5). Symbols denote location of analysed samples. 42

2.9 Field photos from Sites in the central gully section of the caldera highlighted in Figure 2.2E. A) Site 40, Bedded Pumice unit overlying an ash rich deposit. B) & C) outcrops at Site 41 of the WKYP and Bedded Pumice unit overlying ash-rich horizon. Slumping features observed. Flow packages refer to the alternation between ash rich horizons and thin pumice fall horizons which suggest the passage of a dilute PDC followed by a small period of pumice fallout before another PDC inundates the area. D) Large outcrop of Bedded Pumice and WKYP units capped with an ash rich PDC at Site 43. E) Outcrop opposite Site 43 showing contact between WKYP and CO5. Absence of CG_E suggests it was deposited after CO5. F) Shows characteristic features of the Bedded Pumice unit and WKYP overlain by CO5. G) Shows deposit of CG_E overlying CO5. H) Dilute ash rich PDC deposit (CG_E) comprises of multiple flow packages 48

2.10 Stratigraphic logs from locations on and around the flanks of the Wendo Koshe Cone of Urji. Sample locations are highlighted in Figure 2.2F and units are described in Table 2.6. A) Outcrop on the flanks of the Wendo Koshe Cone (Site 21) showing the Bedded Pumice unit with the characteristic reverse grading and staining by overlying paleosol. This is overlain by the coarse-grained, obsidian bearing pumice fall deposit seen at numerous locations in the central caldera (CC_B; Figure 2.8) B) Outcrop on the flanks of the Wendo Koshe Cone showing proximal deposits characteristic of a pumice cone eruption. C & D) Outcrops at Site 38 showing similar characteristics described in Rapprich et al. (2016). E) Rhyolite flow on the flanks of Urji which grades to glassy obsidian. 50

2.11 Overview of our proposed development of Chabbi. A) Caldera forming eruption followed by the development of Artu, Urji and Chabbi. Box highlights Chabbi and region of subsequent maps. B-D) The most heavily eroded areas of Chabbi are associated with pumice cone eruptions forming multiple vents some of which overlap; however the relative timing of these eruptions is difficult to constrain. E) Eruption of CO3 from a now eroded vent. CO3 has multiple lobes which over-ride earlier portions of the deposit. The timing of the deposits on the south-eastern flank are thought to occur around this time however no dates for these eruptions are currently available. F) Lava flow from a now buried vent, ogives can still be seen on the surface of the flow although it has been subsequently buried. G) Further pumice cone eruptions forming the Hot Cone (central) and the Eastern Cone (right) of Mohr (1966). H) Eruption of CO4 which is inferred to have overridden part of the eastern cone. I) Eruption of CO4a from a vent near the eastern cone. This flow erupted through CO4. J) Eruption of the Biftu Tuff cone. Two vents are seen on the western flank of Chabbi however the timing of their formation is uncertain After (Clarke, 2020). K) Eruption of CO5 from a now buried vent. Following this eruption two other vents formed erupting small lava flows which are identified here for the first time and termed CO5a and CO5b. L) Eruption of CO6 from a central vent. This is the most recent flow on Chabbi and has multiple lobes which override earlier portions of the flow. 56

2.12 A) Detail of the CO4 and CO4a (Figure 2.11) showing the surface morphology of the two flows and surrounding features. Ogives visible in CO4a suggest the vent of the eruption is slightly offset from the eastern cone vent suggesting it is sourced from a different vent. In addition, the ogives on the upper portions of CO4 are clearly not altered by the presence of CO4a suggesting CO4a was emplaced later on top of CO4. B) Change in elevation along profile highlighted in A. The abrupt change in height highlights the presence of CO4a and provides further evidence for it being a separate flow. 58

2.13 Stratigraphic log and field photos of outcrops in a drainage gully near the shores of Lake Hawassa. Field sites are marked in Figure2.2H) Outcrop at Site 12 showing the upper portion of a dilute PDC with a shell-bearing horizon and lapilli tuff B) Outcrop at Site 31 (Figure 2.2H) showing the complex and varied structures within the dilute PDC associated with the Biftu Tuff Cone C) Wave ripples and stratification observed at Site 10. Shells incorporated into deposit. D) Overview of Site 9 showing PDC succession caped with the WKYP. E) Complex cross stratification and ripples at Site 10. F) overview of Site 11 showing chute and pool structures and incorporation of shells into PDC. 61

2.14 A) Total alkali silica diagram highlighting the limited variation in erupted compositions from Corbetti. Samples were grouped based upon correlations outlined in previous sections. Error bar is calculated from the 2*RSD% of standard. Samples from Rapprich et al. (2016) and glass compositions from Fontijn et al. (2018) are shown for comparison. B) Peralkaline classification distinguishing between comendite and pantellerite composition using the divide proposed by Macdonald (1974). Errors smaller than symbols. 63

2.15 Trace element plots for samples analysed in this study. Legend is the same as Figure 2.14. Incompatible-incompatible (Y, Nb, La, Rb vs Zr) plots show a clear fractional crystallisation trend. Error bars smaller than symbols. . . 65

3.1 A) Regional map of the East African Rift, highlighting the area in B. B) Central and Southern section of the Main Ethiopian Rift, showing the location of Corbetti Caldera, and other major silicic centres. C) Overview map of Corbetti Caldera highlighting regional faults and the Wonji Fault Belt (WFB). Faults after Agostini et al. (2011) 81

3.2 Geological map of Corbetti Caldera highlighting the sample locations (after Hunt et al. 2019 & Colby et al. 2022). B) Detail of the northern caldera walls showing sample sites of samples analysed in this study. 84

3.3 Field photos of deposits in north caldera walls (Site 3 & 4; Figure 3.2B) highlighting outcrops of the welded ignimbrite (NCW_F) and basaltic tuff (NCW_H). Adapted from Colby et al. 2022 84

3.4 A) Total Alkali-Silica plot comparing the glass compositions reported here with glass (G) and whole-rock (WR) basaltic compositions reported at other calderas within the MER. Aluto; Teklemariam et al. (1996) (WR); Hutchison et al. (2016c) (WR); Fontijn et al. (2018) (G), Boku: Tadesse et al. (2019) (WR), Boset: Brotzu et al. (1980) (WR); Furman et al. (2006) (WR); Fontijn et al. (2018) (WR), Fantale: Furman et al. (2006) (WR); Rooney et al. (2007) (WR); Giordano et al. (2014) (WR), Gedemsa: Chernet and Hart (1999) (WR); Peccerillo et al. (2003) (WR); Rooney et al. (2007) (WR); Giordano et al. (2014) (WR), Kone: Rooney et al. (2007)(WR); Fontijn et al. (2018)(G), Tullu Moye: Fontijn et al. (2018) (G), BBTM: Tadesse et al. (2023) (WR). B) TAS plot (Axis the same as A) showing the composition of the obsidian lithics compared with WR peralkaline rhyolite samples from Corbetti. 89

3.5 Harker diagrams showing the variation of basaltic glass compositions recorded within the basaltic tuff (NCW_H). Samples above 50 wt.% SiO_2 show increased scatter in MnO, FeOt, TiO_2 and Na_2O. High P_2O_5 values are unusual, however, similar P_2O_5 values in alkali basalts are also reported at Aluto and may be due to the late fractionation of apatite (Hutchison et al., 2016c). Although not observed in Corbettis erupted products, apatite is likely to be present through the crystallisation sequence (Field et al., 2012). 90

3.6 Selected incompatible whole rock trace element data plots which show fractional crystallisation trends. Black lines highlight the trends of different ratios of Zr to respective elements. 92

3.7 Spider diagrams showing the mean whole rock trace element variation for selected units at Corbetti normalised to the primitive mantle (McDonough and Sun, 1995)-symbols as in Figure 3.6. The least fractionated sample is the basaltic tuff (NCW_H) 93

3.8 Variation in $^{87}Sr/^{86}Sr$ ratio values reported across the MER in comparison to the values in this study. One of Corbetti's eruptive units (NCW_E) records an elevated $^{87}Sr/^{86}Sr$ ratio indicating a degree of crustal contamination that may result from the incorporation of country rock during eruption or through assimilation of country rock due to a higher magma flux in the lead up to the development of this magma body. Other samples from Corbetti show similar values with some slight elevations observed with may indicate a minor degree of crustal contamination but are in line with other samples from the MER. Data downloaded from the the GeoRoc database (Downloaded on 1st Dec 2023 https://georoc.eu/). Fantale:Furman et al. (2006); Giordano et al. (2014); Ayalew et al. (2016); Kone: Furman et al. (2006); Peccerillo et al. (2007); Ayalew et al. (2016); Boset: Furman et al. (2006); Ronga et al. (2009); Ayalew et al. (2016); Boku: Boccaletti et al. (1995); Gedemsa: Boccaletti et al. (1995); Barberio et al. (1999); Peccerillo et al. (2003); Giordano et al. (2014); Ayalew et al. (2016); Castillo et al. (2020); Aluto: Deniel (2009); Corbetti: Rapprich et al. (2016) 94

3.9 A) and B) are thin section images of NCW_H in plain and cross-polarised light. Olivine and plagioclase can be seen hosted in glass. C) shows the area highlighted in A1 in BSE (View of area is rotated ~45° clockwise): presence of plagioclase and olivine hosted in a basaltic glass with visible vesicles. The olivine phenocryst contains Fe-Ti Oxide inclusions. D) Olivine phenocrysts hosted in glass. E) Cross-polarised image of crystalline enclave found within NCW_F showing dense concentration of feldspars, clinopyroxenes, and Fe-Ti Oxides. F) BSE image of area highlighted in E (View rotated ~90° clockwise). G and H) plain polarised images of NCW_F glass and mineral phases. 97

3.10 Range in Fo contents for the core and rims of analysed olivine phenocrysts and range in An content of plagioclase phenocrysts from the basaltic tuff (NCW_H) 97

3.11 Tri-plot showing the range of feldspar compositions recorded in the basaltic tuff (Purple), peralkaline ignimbrite (Blue) and enclave (Orange). Shows some alkali-feldspars are present within the basaltic tuff and are likely antecrystic. 99

3.12 Equilibrium plot showing Fo contents of the rims and cores of olivines plotted against the Mg# of the host glass. Olivines in equilibrium with their host glass will fall within the equilibrium field $Kd_{(Fe-Mg}{}^{ol-liq}$ 0.3 ± 0.3 defined after (Roeder and Emslie, 1970). Rim and core compositions from the same olivivne phenocrysts are compared to the glass composition they are hosted in. Where there is an offset between the rim and core Fo values it indicates a degree of zonation. 100
3.13 Temperatures calculated using glass-only thermometry, olivine-liquid pairs, and plagioclase-liquid pairs. Glass-only thermometry was calculated at 3 different H_2O contents, from anhydrous to 1 wt.% H_2O. Olivine and Plagioclase temperatures were determined at a range of pressures (250 MPa to 50 MPa at 50 MPa steps). 101
3.14 Calculated temperatures and water contents of plagioclase-liquid pairs and alkali feldspar liquid pairs. Data overlain with RhyoliteMELTS output which best match the natural composition of the welded ignimbrite. Grey region shows the range in H_2O contents found in quartz-hosted melt inclusions from Corbetti (Iddon and Edmonds, 2020). The gap between the melt inclusion data and the petrological hygrometry likely suggests melt inclusion volatile contents may have been reset prior to eruption. Solid lines reflect H_2O solubility in a rhyolitic melt calculated using the method of Allabar et al. (2022). 103
3.15 Comparing the output of the RhyoliteMELTS runs which most closely match the natural compositions found at Corbetti. RhyoliteMELTS provides a good fit for certain oxdies; however consistently under-predicts the concentration of Na_2O and over estimates K_2O compared with natural samples. This may suggest that this basaltic composition is not reflective of the parental basalts from which the peralklaine products are differentiated. . . . 106
3.16 Schematic overview of estimated magma storage depths at Corbetti combining petrological and geophysical techniques. Details can be found in Table B.2. CPX-only barometry has a high associated error or 320 MPa; however, results are in good agreement with geophysical observations. The magnetotelluric survey places the top of the conductive hot zone at around 5 km (Gíslason et al., 2015). Seismic surveys also suggest the presence of geothermal fluids at < 5km depth in the crust (Lavayssière et al., 2019). Figure adapted from Lloyd et al. (2018a) with data from this study and recent geophysical studies overlain. 114

4.1 (A) Map showing the location of the MER, which forms part of the wider East African Rift system, and (B) the location of peralkaline complexes, which form the focus of this study.(WFB after Agostini et al. 2011 121

4.2 Total alkali-silica diagram showing the range in evolved peralkaline compositions across the MER. Fentale: Gibson (1972); Webster et al. (1993); Giordano et al. (2014), Kone: Peccerillo et al. (2007); Fontijn et al. (2018); Iddon and Edmonds (2020), Boset: Brotzu et al. (1980); Ronga et al. (2009); Macdonald et al. (2012); Fontijn et al. (2018), Boku: Boccaletti et al. (1995); Tadesse et al. (2023), Gedemsa: Boccaletti et al. (1995); Barberio et al. (1999); Yirgu et al. (1999); Peccerillo et al. (2007); Giordano et al. (2014); Fontijn et al. (2018), Bora Baricha Fontijn et al. (2018), Tullu Moye: Di Paola (1972); Trua et al. (1999); Fontijn et al. (2018), Aluto Teklemariam et al. (1996); Trua et al. (1999); Hutchison et al. (2016c); Gleeson et al. (2017); Fontijn et al. (2018), Corbetti: Macdonald and Gibson (1969); Di Paola (1972); Rapprich et al. (2016); Fontijn et al. (2018); Colby et al. (2022) 122

4.3 Classification plot after Macdonald (1974) of whole rock, glass, and melt inclusion data showing the range in peralkaline compositions reported across the MER and within individual volcanic centres. Plots (top left to bottom right) are ordered from north to south along the rift. PT: Trachytic pantellerite, CT: Trachytic comendite, P: Pantellerite, C: Comendite. The symbols are coloured by their peralkalinity index (molar $(Na_2O+K_2O)/Al_2O_3$). . . . 123

4.4 A) Sketch of the Qz-Ab-Or-Ac-Ns residua system at PH2O = 1000 bar; after Carmichael and MacKenzie (1963). The solid line shows the location of the Quartz-Feldspar cotectic in the acmite (Ac) 8.3% + Ns 8.3% system. The dotted line shows the location of the thermal valley based on experiments by Carmichael and MacKenzie (1963). Dashed lines show isotherms in °C. B) Sketch of the isobaric projection of the Qz-Ab-Or system in a cartesian form showing the change in the proportion of Or with increasing Qz*. Cotectic of Carmichael and MacKenzie (1963) (CM63) and Di Carlo et al. (2010) & Romano et al. (2020) (D10+R20) are shown for comparison (White et al., 2023). The location of the whole rock minimum (WR-Min; lowest Al_2O_3 and highest FeOt compositions of whole rock data) and effective minimum composition (EMC; Macdonald et al. 2012, Macdonald et al. 2021, White et al. 2023) is also shown. 126

4.5 Qz* vs Fe/Al* (=1.33×FeOt/[Al_2O_3-4.4]). Arrows indicate trends of magma lineages which are potentially sourced from different parental magmas. Arrows denote the trends modelled trends in Section 4.4 (Tables 4.4.1, 4.4.3, 4.4.4). Where these trends can be clearly observed in other figures they are denoted. Data with Fe/Al* < 1 is classified as comendite and Fe/Al* > 1 is classified as pantellerite (White et al., 2023). 131
4.6 Variation in peralkalinity index (PI = molar(Na_2O+K_2O)/Al_2O_3) with Qz* across the MER. The red star indicates the 'thermal valley' projected location with the feldspar-quartz cotectic calculated from data on the Green Tuff, Pantelleria (Carmichael and MacKenzie, 1963; White et al., 2023). . . 132
4.7 Variation in SiO_2 with increasing Qz* across the MER. Arrows denote the modelled trends investigated in Section 4.4 (Results in tables 4.4.1, 4.4.3, 4.4.4). Boset and Gedmesa show the greatest variation in SiO_2 contents with Qz* of the studided systems. We observe a decrease in SiO_2 concentration with Qz* values > 40 which may reflec the onset of the cyrstalisation of quartz. 133
4.8 Variation in TiO_2 content across the rift with Qz*. Demonstrates a decrease in TiO_2 with increasing Qz* and a sharp decrease in TiO_2 at constant Qz* within geochemically distinct units. Arrows highlight the direction of the modelled trends (letters) investigated in Section 4.4 (Results in tables 4.4.1, 4.4.3, 4.4.4) 134
4.9 Subset of Ab-Or-An ternary plot showing the variation in reported feldspar compositions found in rhyolite/trachyte rocks at different silicic centres across the MER. Data from: Brotzu et al. (1980); Boccaletti et al. (1995); Peccerillo et al. (2003); Ronga et al. (2009); Macdonald et al. (2012). Plotted using MinPlot after Walters (2022). 136
4.10 Variation in the composition of pyroxenes across the MER. Colours as in Figure 4.2. Quad = quadrilateral, Jd = Jadite, Aeg = Aegirine, En = Enstatie, Fs = Ferrosilite, Wo = Wollastonite (Morimoto, 1989). Data from Brotzu et al. (1974); Boccaletti et al. (1995); Peccerillo et al. (2003); Ronga et al. (2009); Macdonald et al. (2012). Plotted using MinPlot after Walters (2022) 137
4.11 Mineral assemblages found in trachyte and peralkaline rocks within the MER. The colours are as in Figure 4.2. Grey data shows the compositional range of peralkaline products used in this study. CPX = clinopyroxene, Aeg = aegirine augite, Aen = aenigmatite, Kspar = alkali-feldspar, Fa = fayalite, Amph = amphibole, Bi = biotite, Fe-Ti = Fe-Ti oxide 138

4.12 Tri-plot of normative Qz*-Or-Ab CIPW components projected onto the Qz-Or-Ab-Ns-Ac residua system at PH_2O = 100 MPa. Cotectic after Carmichael and MacKenzie (1963) (Solid line) and the cotectic of Di Carlo et al. (2010) and Romano et al. (2020) (Dashed line). The red star indicates where the thermal valley intersects with the feldspar-quartz cotectic. Colours as in Figure 4.2. 148

4.13 Cartesian, isobaric projection of Figure 4.12. The red star indicates the 'thermal valley' location intersecting with the feldspar-quartz cotectic. A key feature of Boset, Gedemsa and Aluto are the units which show a sharp increase in the proportion of Or with a relatively constant Qz* value. Arrows indicate direction of the trends modelled and are presented in Tables 4.4.3 and 4.4.4. The multiple data clusters showing a vertical trend at Gedemsa relate to the geochemically distinct units identified by Fontijn et al. (2018) . 150

5.1 Composite stratigraphy of Corbetti caldera (From Chapter 2), highlighting the major stratigraphic units outlined in Chapter 2 and areas of uncertainty in the placement of certain stratigraphic units. 161

5.2 Relative chronology of lava flows from Chabbi as presented in Chapter 2, including the 3 new flows identified in this study (CO4a, CO5a and CO5b). For full explanation see Figure 2.11 162

5.3 Temperature and H_2O content of the basaltic tuff and peralkaline rhyolite estimated from plagioclase-liquid and alkali-feldspar-liquid thermometry and hygrometry as presented in Chapter 3 164

5.4 Overview of geophysical and petrological data available for Corbetti. Figure adapted from Lloyd et al. (2018a) incorporating data from this study and recent geophysical studies. Demonstrates that magma is likely stored in a conductive hot zone ~7 km beneath Corbetti with lenses of shallower melt or geothermal fluids nearer the surface. We see good agreement between the estimates of storage depths from this study and geophysical surveys. . . 165

A.1 Laminated ash horizons observed at Site 23 and correlated with NCW_H. . 200

A.2 Overview of Site 27 (Figure 2.2C) B) shows detail of the Jointed rhyolite lava (SCW_A1). C) Shows outcrop of lithic rich PDC deposit above the rhyolitic flow which is likely a different lithofacies of SCW_K however this is unclear. 200

A.3 Outcrop at Site 8 (Figure 2.2C) showing the presence of multiple pumice and ash-rich horizons capped by obsidian. Symbols show location of analysed samples. 201
A.4 A) Outcrop of CO5 at Site 58 (Figure 2.2C) showing the presence of several welded lenses within the obsidian flow. B) shows detail of folds within the flow front. C) Detail of welded material intermingled with obsidian flow. D) Outcrop of CO6 showing a welded lens similar to CO5. 202
A.5 Variation in selected trace elements with stratigraphic position. Stratigraphic position and uncertainty outlined in Figure 2.5. Different trends can be seen between the pre-and post-caldera deposits, however distinguishing between individual units based solely on the geochemistry is challenging. . 203
A.6 Conceptual model of pumice cone formation after Clarke (2020) showing the features of the Bedded Pumice observed within the field. 204

C.1 Variation in Zr content with Qz*. Only data for Zr concentrations for whole rock data are available, therefore there is minimal data beyond the whole-rock minimum composition (Qz* = 40.5; White et al. 2023). 244
C.2 Change in calculated Qz* value with Al_2O_3 concentration in glass, whole rock and melt inclusions. Samples coloured by their peralkalinity index. Demonstrates a strong negative correlation between Al_2O_3 and Qz* in peralkaline products (Qz*> 0 & PI > 1) across the MER. Trendline is defined by White et al. (2023) for Pantelleria, Italy. Whilst some of the scatter in these figures can be attributed to glass and whole rock compositions, there is generally good agreement whith centres such as Corbetti showing no difference between whole-rock and glass data. Distinctive trends in glass compositions can be observed at Kone and Gedemsa which relate to geochemically distinct stratigraphic units. 245
C.3 Variation in CaO across the MER with Qz*. Arrows at Gedemsa and Boset highlight the two main trends observed within the rift. At Boset there is a clear increase in the concentration of CaO at Qz* > 40 however this is not observed at Gedemsa. 246

List of Tables

2.1 Definitions of lithofacies (LF) notations used in this study (Branney and Kokelaar, 2002) 19

2.2 Descriptions and interpretations of units exposed in sections of the northern caldera walls (Figures 2.2B for samples locations, Figures 2.3 for field photos and 2.4 for stratigraphic log. Units presented youngest to oldest. Table 2.1 outlines the descriptions of lithofacies. LF = lithofacies. 24

2.3 Description and interpretation of units exposed in the Southern caldera wall (Figure 2.2C). Stratigraphic log outlined in Figure2.4B. Field photos of outcrops are found in figures 2.5 and 2.6 30

2.4 Description and interpretation of units exposed within the Central Caldera section as shown in Figure 2.8. (See Figure 2.2C for sample locations and Figure 2.7 for field photos). 39

2.5 Description and interpretation of observed units in the north-eastern gully (Figure 2.2E) Stratigraphic log is presented in Figure 2.8B and field photos in Figure 2.9. 44

2.6 Descriptions and interpretation of units observed on the slopes of Urji (Figure 2.2F; logs and field photos presented in Figure 2.10). 51

2.7 Radiocarbon dating and stable isotope results for shells sampled from the Biftu Tuff Cone PDC (Site30A) and overlying pumice deposit (Site 12C). Field sites are marked in Figure 2.2. Samples were analysed at Beta Analytic and calibrated using BetaCal4.20: HPD method: INTCAL20 (Reimer et al., 2020). 59

3.1 $^{87}Sr/^{86}Sr$ ratios and Sr concentrations for selected samples. Sample locations are highlighted in Colby et al. (2022). 91

3.2 Overview of minerals present in crystalline samples from Corbetti Caldera. Mineral abbreviations after Whitney and Evans (2010). Ol: Olivine, Pl: Plagioclase, Aeg: Aegirine Augite, Afs: Alkali-feldspar, Fa: Fayalite, Qz: Quartz, CPX: Clinopyroxene. 95

3.3 Results of RhyoliteMELTS simulations showing the likely conditions under which magmas at Corbetti evolved and their associated residual. The residual is calculated using the method of Gleeson et al. (2017) $\sum_X^m(\sum_i^n(X_i - \hat{X})^2/X_{SD})_X$, where n is the number of natural samples that represent the target composition, m is the number of oxides considered, X_i is the concentration of oxide X of sample i, $\hat{X}$ is the concentration of oxide X predicted by RhyoliteMELTS at a particular temperature, X_{SD} is the standard deviation of oxide X of all empirically determined compositions of natural samples representing the target composition. 105

4.1 Overview of the input parameters used for the mass balance modelling and the mineral phases used. 128

4.2 Mass balance model results investigating the mineralogical control on highlighted trends in major element data. Mass fractions equal 1. Kspar: alkalifeldspar, Q: auartz, CPX: clinopyroxene, Aen: aenigmatite, Fa: fayalite, Mg, magnetite, Il: ilmenite, Ap: apatite, Amph: amphibole, f/c%: percentage of fractional crystallisation predicted by the model, r: model residual (squared sum of the squared residuals between the known and modelled daughter compositions). The reference figure shows the direction of the trend modelled. Mineral proportions represent the percentage within the fractionating assemblage. 144

4.3 Mass balance model results investigating the mineralogical control on trends observed in the Qz-Or-Ab-Ac-Ns residua system focusing on samples following the cotectic of Carmichael and MacKenzie (1963). Kspar: Alkalifeldspar, Q: Quartz, CPX: Clinopyroxene, Aen: Aenigmatite, Fa: Fayalite, Mg, Magnetite, Il: Ilmenite, Ap: Apatite, Amph: Amphibole, f/c%: percentage of fractional crystallisation predicted by the model, r: model residual (squared sum of the squared residuals between the known and modelled daughter compositions) Mineral proportions represent the percentage within the fractionating assemblage. Figure 4.13 shows the direction of the modelled trends. 152

4.4 Mass balance model results investigating the mineralogical control on trends observed in the Qz-Or-Ab-Ac-Ns residua system (Figure 4.13) following the cotectic of Di Carlo et al. (2010) & Romano et al. (2020). Kspar: alkali-feldspar, Q: quartz, CPX: clinopyroxene, Aen: aenigmatite, Fa: fayalite, Mg: magnetite, Il: ilmenite, Ap: apatite, Amph: amphibole, f/c%: percentage of fractional crystallisation predicted by the model, r: model residual (squared sum of the squared residuals between the known and modelled daughter compositions). Mineral proportions represent the percentage within the fractionating assemblage. 154

A.1 Whole rock major element data. Details on sample locations found in electronic file or Colby et al. (2022). All values given in wt.% 205
A.2 Whole rock trace element data for collected samples in Chapter 2 in ppm . . 208
A.3 Continued whole rock trace element data from Chapter 2 in ppm 212
A.4 Continued whole rock trace element data from Chapter 2 216

B.1 Estimated magma storage depths using a range of geophysical and petrological methods. Depths were calculated using a crustal dnsity of 2800 gm^{-3} (Wilks et al., 2017). Depsite the large uncertainty, data collected in this study agree well with independent estimates from geophysical observations. 222
B.3 Glass compositions for the basaltic tuff (NCW_H) normalised to 100 wt.%. These glass compositions were used for the glass-only thermometry. 223
B.4 Analysis of olivine phenocrysts found within NCW_H normalised to 100 wt.%. Where these phenocrysts were hosted in a glass shard, the name of this is given and it's composition can be found in Table B.3 227
B.5 Compositions of plagioclase phenocrysts found within the basaltic tuff (NCW_H). The glass composition within whihc these phenocrysts were hosted is also given. These glass compositions were used for the plagioclase-liquid thermometry and hygrometry and can be found in Table B.3 228
B.6 Composition of the rare clinopyroxenes found within the basaltic tuff (NCW_H) normalised to 100 wt.% 230
B.7 Compositions of the rare alkali-feldspar phenocrysts found within the basaltic tuff (NCW_H). These are likely scavenged from an older melt. Data are normalised to 100 wt.% 230
B.8 Composition of Obsidian lithics found within NCW_H normalised to 100 wt.% 231

B.9 Glass analysis for NCW_F normalised to an anhydrous composition of 100 wt.%. All data in wt.%. For the KSpar-Liquid thermometry and hygrometry, each glass compositions was matched with every KSpar composition. Only those which passed the equilibirum test of Mollo et al. 2015 (when $^{Ksp-melt}Kd_{Or-Ab}$ 'measured' versus' 'Predicted' plot on a 1:1 line ± 0.05) are presented in Chapter 3 231
B.10 Compositions of alkali-feldspars found within NCW_F. Data are in wt.% and normalised to 100 wt.%. Were transects have been conducted the rim and the core position have been noted. 233
B.11 Clinopyroxene compositions recorded in NCW_F. All elements reported in wt.% and normalised to 100 wt.%. Core and Rim compositions noted. . . . 237
B.12 Composition of single fayalite phenocrysts found within NCW_F. Oxides reported in wt.% and normalised to 100 wt.% 239
B.13 Clinopyroxene compositions within the enclave found within NCW_F. Compositions reported in wt.% and normalized to 100 wt.% 239
B.14 Feldspar compositions found within the crystalline enclave in NCW_F. All data reported in wt.% and normalized to 100 wt.%. For the two feldspar thermometry presented in Chapter 3 each alkali feldspar composition was matched with each plagioclase composition. 240

C.1 Overview of mineral assemblages reported in trachyte and rhyolite magmas across the MER. 247
C.2 Details of the composition of each of the mineral phases used for the mass balance modelling. Where available, mineral data from the volcano of interest was used. 250
C.3 Details of each of the mass balance model results which information on the different mineral phases predicted to crystallise with their composition. Table covers model runs A - W 253
C.4 Details of mass balance model runs AA-NN exploring the controls on the trends observed in the Qz-Or-Ab-Ac-Ns residua system. 266

Chapter 1

Introduction

1.1 Motivation and scope of research

The Main Ethiopian Rift (MER) forms part of the wider East African Rift (EAR), connecting the Afar depression in the North to the Turkana and the Kenyan Rift to the South (Figure 1.1). Rifting in the MER started ~30 Ma and developed asynchronously across the northern, central and southern sections and is the classic example of an active continental rift system (Mohr et al., 1980; WoldeGabriel et al., 1990; Ebinger and Casey, 2001; Ebinger, 2005; Kendall et al., 2005; Casey et al., 2006; Pizzi et al., 2006; Kurz et al., 2007; Corti, 2009; Purcell, 2018; Boone et al., 2019). The development of the Wonji Fault Belt (WFB) ~2 Ma, a region within the northern section of the rift containing short, right-stepping echelon faults, resulted in the migration of strain away from the boundary faults and towards the centre of the rift (Casey et al., 2006). This fault belt and the development of magmatic segments marked a transition towards magma-assisted rifting (Kendall et al., 2005). The Wonji fault belt and cross-rift structures have significant control over the style and distribution of volcanism across the rift (Mohr et al., 1980; Robertson et al., 2016; Corti et al., 2022; Maestrelli et al., 2022). Over the period of rift development to the present day, the Ethiopian Rift has experienced a diverse range of eruptive styles, from the eruption of flood basalt during the early stages of rift development (Corti, 2009) to large-scale caldera-forming eruptions, the most recent of which occurred during the Pleistocene ~76-320 ka (Hutchison et al., 2016b; Vidal et al., 2022a).

The Main Ethiopian Rift (MER) provides a unique environment to study the various stages of continental rifting and associated volcanism. Ethiopia is home to 59 Holocene-

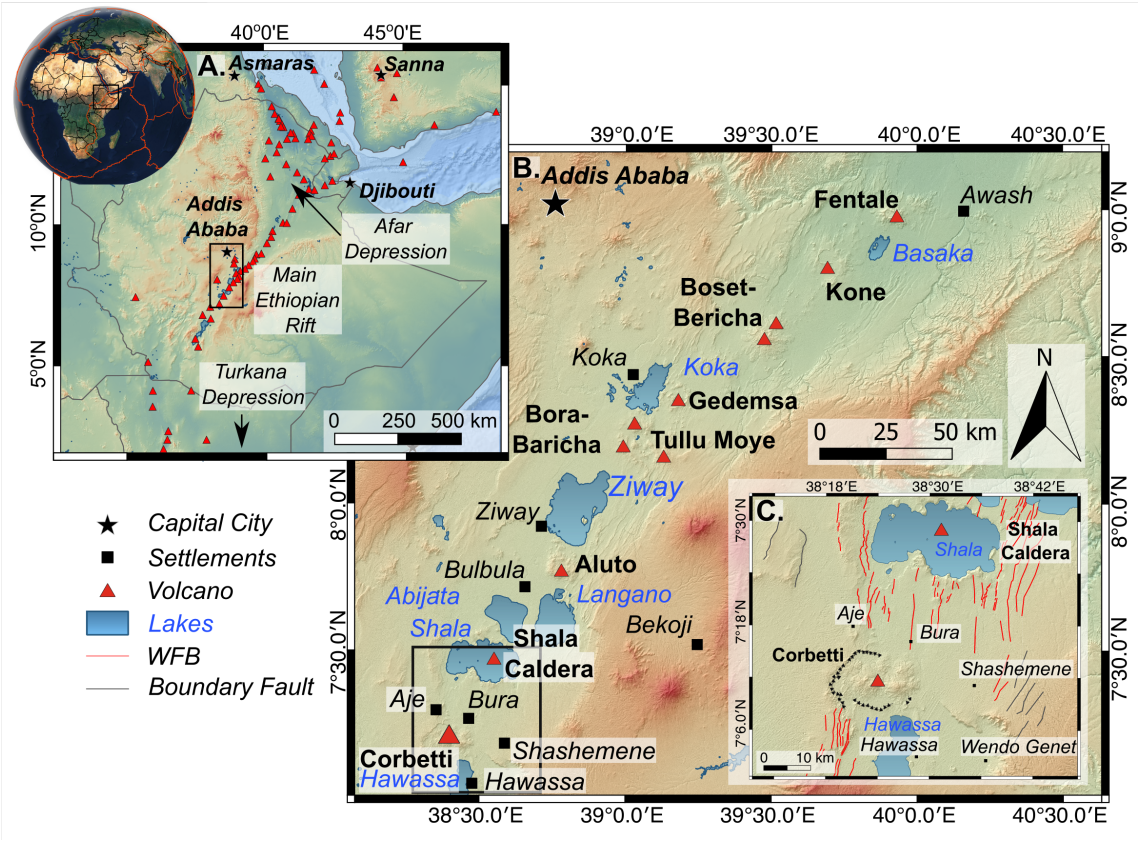

Figure 1.1: A) Overview map of the East African Rift, highlighting the location of the Main Ethiopian Rift (Black Box). B) Detailed view of the Main Ethiopian Rift (MER) showing the location of major volcanic centres and Corbetti caldera highlighted by the black rectangle. C) Close-up view of Corbetti Caldera (ramparts indicated by black triangles after Hunt et al. 2019) and the Wonji fault belt (WFB; Agostini et al. 2011.

active volcanoes and has the 5th highest risk to human life from a volcanic source of any country in the world (Aspinall et al., 2011; Loughlin et al., 2015; Biggs et al., 2021). This is primarily due to two factors, firstly, the exposure of the population and lack of direct monitoring, and secondly, due to our limited understanding of the nature of volcanism within the rift. In recent years, several large-scale research projects have sought to address gaps in our understanding of the volcanic systems in the MER and have explored the physical volcanology and geophysical observations, including seismic surveys at several centres in the MER (e.g. EAGLE; Maguire et al. 2003, Maguire et al. 2006, Bastow et al. 2011, RiftVolc 2014-2021; Hutchison et al. 2016a, Siegburg et al. 2017, Fontijn et al. 2018, Hunt et al. 2019,Tadesse et al. 2019, Biggs et al. 2021, Albino and Biggs 2021, Tadesse et al. 2023). This thesis seeks to build upon that work by investigating the eruptive history and magmatic evolution of one of these large caldera systems: Corbetti Caldera.

Corbetti is a large silicic caldera in the southern part of the MER (Figure 1.1). It has undergone at least one caldera-forming eruption, dated to ~182 ka (Hutchison et al., 2016b; Vidal et al., 2022b). This eruption was one of several large-scale caldera-forming eruptions that appear to form part of a wider flare-up of high-magnitude volcanic eruptions in the MER during the Pleistocene (Hutchison et al., 2016b). The caldera is around ~20 km from the towns of Hawassa (population 422,000) and 25 km from Shashemene (population: 208,000) (Figure 1.2; Ethiopian Statistics Agency 2022). The caldera rim has an irregular elliptical shape, approximately 15.6 × 10.9 km along the long (E-W) and short (N-S) axes, respectively (Hunt et al., 2019). Within the caldera, three post-caldera edifices have developed (Figure 1.2). Artu, to the north, is the oldest and most heavily eroded, with little known about its eruptive history. Urji is found to the west and is dominated by pumice cones and has been the source of some of the largest eruptions within the caldera. Chabbi lies to the east and is dominated by the eruption of obsidian lava flows (Mohr, 1966; Macdonald and Gibson, 1969; Rapprich et al., 2016; Fontijn et al., 2018). The contrasting styles of volcanism between Urji and Chabbi present very different hazards to the surrounding populations. Similarly, the mechanisms that control these two very differing styles of volcanism are currently poorly understood. Before this work, our understanding of the physical volcanology of Corbetti was limited, with the focus being on the most recent Plinian eruptions (VEI 4-5) known to have occurred at the centre (Rapprich et al., 2016; Martin-Jones et al., 2017; Fontijn et al., 2018). Two major Plinian/sub-Plinian eruptions, thought to have originated from Urji, have previously been identified: (i) the Bedded Pumice eruption and (ii) the Wendo Koshe Younger Pumice (WKYP). These two eruptions have

produced extensive pumice fall-out deposits, with the WKYP depositing up to 0.5 m of material in the town of Shashemene (Rapprich et al., 2016; Fontijn et al., 2018).

As with many of the large caldera systems in the MER, Corbetti predominantly erupts peralkaline rhyolite magmas (Rapprich et al., 2016; Fontijn et al., 2018). Peralkaline magmas have a molar excess of sodium and potassium oxide with respect to aluminium oxide (molar $Na_2O+K_2O/Al_2O_3 > 1$; Shand 1927) and generally have a lower viscosity compared to their calc-alkaline counterparts (Di Genova et al., 2013; Hughes et al., 2017). Peralkaline products can broadly fit into one of three different types (1) SiO_2 undersaturated, where evolution tends towards phonolites and foidites, (2) SiO_2 saturated, trending towards trachytic compositions and (3) SiO_2 oversaturated, which evolves towards comendite and pantellerite compositions (Frost and Frost, 2008; Jeffery and Gertisser, 2018). Classification into comendite or pantellerite compositions is based upon the respective concentration of Al_2O_3 and FeOt; however, the boundary, as defined by Macdonald (1974), is arbitrary. Extreme peralkaline compositions with FeOt > 15 wt.% and Al_2O_3 < 4 wt.% have been reported at Boset in the MER (Macdonald et al., 2012) and Pantelleria, Sicily (White et al., 2023). These reflect the effective 'endpoint' composition of peralkaline products (Macdonald et al., 2012, 2021; White et al., 2023). Whilst more extreme compositions can evolve, they are likely to be rheologically locked and therefore do not erupt (Macdonald et al., 2021; White et al., 2023). In generating these extreme compositions, the fractionation of alkali-feldspar is key. Alkali-feldspar fractionation can be traced by projecting data onto the Qz-Or-Ab-Ac-Ns residua system using CIPW normative components (Figure 1.3; Carmichael and MacKenzie 1963, Bailey and Schairer 1964,White et al. 2023). As a peralkaline magma cools and fractionates feldspar, it will track along the 'thermal valley' towards the feldspar-quartz cotectic. This progressive fractionation of alkali feldspars causes the residual melt to become enriched in Na and increases its peralkalinity.

The processes governing the petrogenesis of peralkaline magmas is a point of debate, with two main theories proposed: extreme fractional crystallisation (Scaillet and Macdonald, 2006; Di Carlo et al., 2010; Gleeson et al., 2017) or partial melting of the crust (Davies and Macdonald, 1987; Mahood and Stimac, 1990). A hybrid hypothesis has also been proposed, which suggests a two-stage process where fractional crystallisation dominates, followed by some degree of crustal assimilation (Peccerillo et al., 2003, 2007; Hutchison et al., 2018). Available evidence from various volcanic settings supports these hypotheses to differing degrees, indicating the complexity of these processes and that peralkaline compositions are a common but not inevitable result of magma evolution under certain conditions.

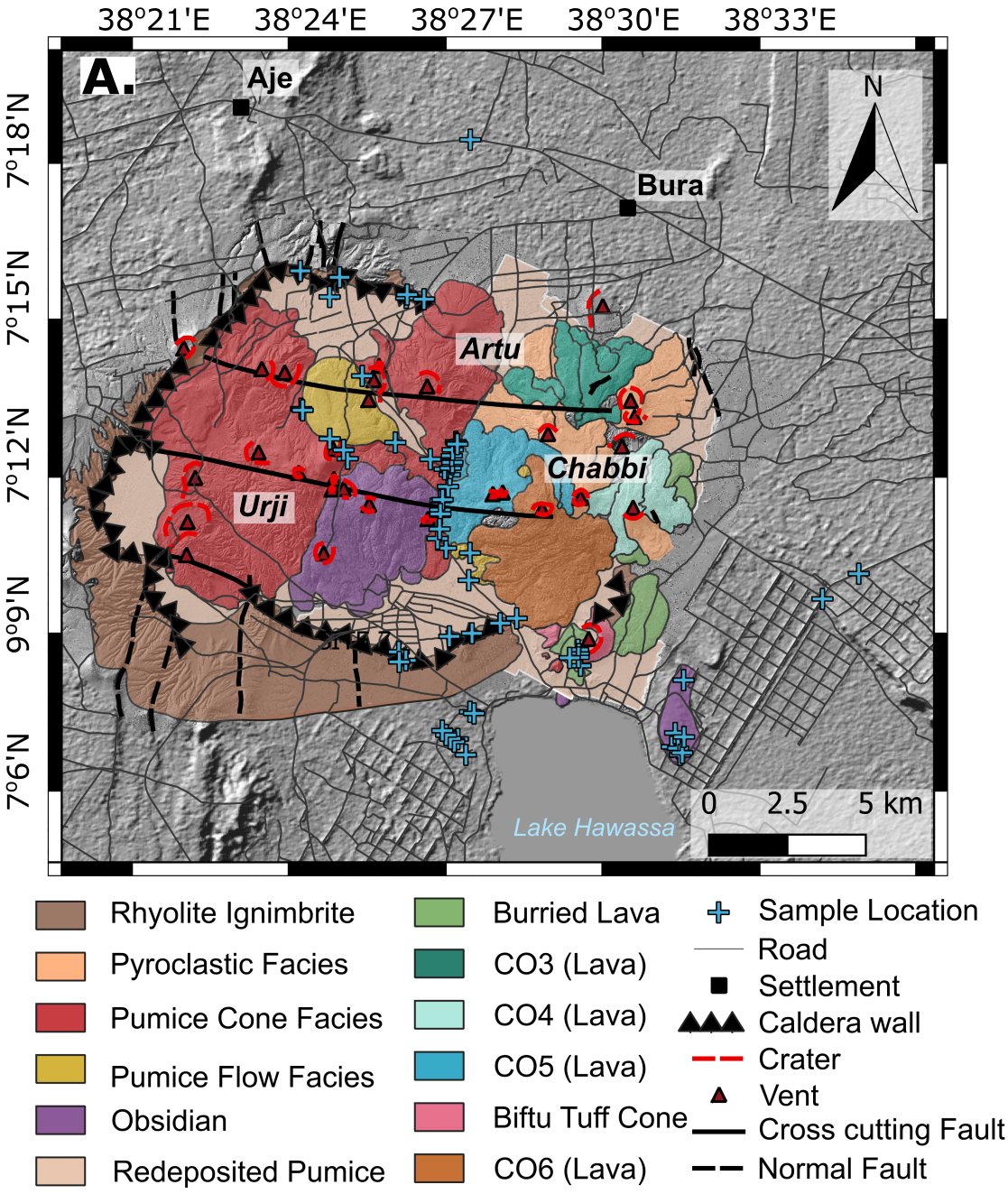

Figure 1.2: Geological Map of Corbetti caldera showing the major fault structures that have been previously identified and the location of the post-caldera edifices. Legend highlight previously identified lithofacies and units. CO3-CO6 are previously identified obsidian lavas from Chabbi. After Rapprich et al. 2016, Hunt et al.2019 and Clarke 2020.

)

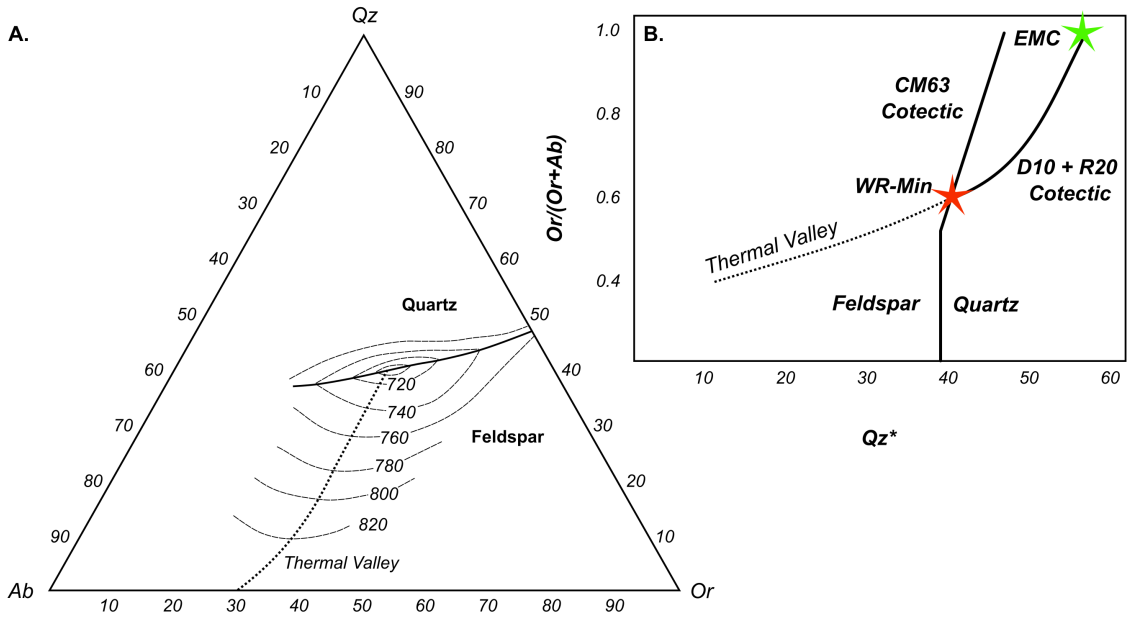

Figure 1.3: The Qz-Or-Ab-Ns-Ac residua system's ternary plot shows the quartz-feldspar cotectic. The isotherms are projected at PH2O=100 MPa Carmichael and MacKenzie (1963). B) shows a cartesian form of this diagram (Wilke et al., 2017) highlighting the intersection of the thermal valley with the quart-feldspar cotectic. The Whole Rock Minimum (WR-Min) composition is the most evolved whole rock composition for peralkaline magmas, and the Effective Minimum composition (EMC) is the most differentiated, high FeOt, peralkaline composition reported (Macdonald et al., 2021; White et al., 2023). Two cotectics are projected, one after Carmichael and MacKenzie (1963) and the other after Di Carlo et al. (2010) & Romano et al. (2020).

For several reasons, it is important to understand past activity at Corbetti and the nature of its magmatic system. Recent geophysical observations have shown Corbetti is restless and uplifting at a rate of around 4 cm/yr between 2007-2020 (Biggs et al., 2011; Lloyd et al., 2018a; Biggs et al., 2021; Albino and Biggs, 2021), having previously been thought not to be active. In addition, investigation of some of the most recent deposits has demonstrated that Corbetti has produced Plinian eruptions during the Holocene that have deposited widespread tephra fallout units across areas that are currently densely populated. This demonstrates the risk posed to the over 400,000 people who live within 30 km of Corbetti from future eruptions (Lloyd et al., 2018b). Corbetti is currently a target for geothermal exploration, with potential identified initially for generating 10 MW of electricity but potentially up to 1000 MW by 2030 with sufficient investment (InfraCo Africa, 2023). The development of geothermal projects is a fantastic opportunity for the local economy providing jobs and investment, but it provides a pull factor for people to live within the already densely populated caldera. Therefore, consideration of the volcanic risk that Corbetti poses is particularly timely.

1.2 Research objectives

This study aims to provide a greater understanding of peralkaline volcanism within the MER by focusing on Corbetti and a better understanding of Corbetti's past activity. This will be achieved through several objectives:

1. Undertake a comprehensive field study of Corbetti's eruptive deposits providing detailed descriptions of major eruptive units and, where possible, correlating them across multiple localities.

2. Develop a detailed composite stratigraphy encompassing the exposed units at Corbetti and incorporating previous observations.

3. Offer interpretations for the eruptive processes, which resulted in the emplacement of units observed at Corbetti.

4. Provide absolute or relative constraints on the timing of eruptions across the calderas.

5. Outline the geochemical characteristics of eruptive products at Corbetti caldera, investigating variation in major and trace element geochemistry.

6. Investigate the magma storage conditions at Corbetti caldera through a combination of thermodynamic modelling and petrological techniques.

7. Undertake analysis of crystal phases and glass for thermometry, barometry and hygrometry.

8. Compare the results of RhyoliteMELTS modelling with independent thermometry and hygrometry.

9. Investigate a rare basaltic eruption recorded within the caldera to constrain its composition and variation in composition through the deposit.

10. Provide an overview of the compositional variation in peralkaline magmas that erupted across the MER.

11. Present a review of the mineralogy of peralkaline products found within the MER.

12. Identify trends in major element data of peralkaline products from Corbetti and compare these to other systems in the MER. Investigate the mineralogical control on the observed trends using mass balance modelling and compare with observed mineral assemblages.

13. Track the fractionation of alkali-feldspar through the Quartz-Orthoclase-Albite-Acmite-Na silicate residua system, identify differences in the location of the quartz-alkali-feldspar cotectic and investigate the mineralogical controls on these features.

1.3 Thesis Outline

This thesis comprises 5 chapters, including this introduction (Chapter 1) and a conclusions chapter (Chapter 5). Chapter 2 has been published in the Journal of Volcanology and Geothermal Research (Colby et al., 2022) and is identical to the published versions except for minor spelling corrections and changes to the figure referencing to keep it consistent with the formatting of this thesis. Chapter 3 has been submitted for publication to the Journal of Volcanology and Geothermal Research and is currently in review. Chapter 4 will be submitted to a journal at a later stage. Below is an outline of each chapter.

1.3.1 Stratigraphy and Eruptive History

Chapter 2 explores the physical volcanology of Corbetti Caldera. In this chapter, I present the outcomes from a 3-week field campaign undertaken from Jan-Feb 2020, give detailed descriptions of the observed units, and correlate these units across multiple localities. I present evidence for these correlations and interpretations of the emplacement mechanism of the units. I also provide an overview of the geochemical variation at Corbetti caldera and compile a comprehensive composite stratigraphy incorporating observations from this study and previous work.

This work has been published in the Journal of Volcanology: David J. Colby, David M. Pyle, Karen Fontijn, Tamsin A. Mather, Abate A. Melaku, Million A. Mengesha, Gezahegn Yirgu, Stratigraphy and eruptive history of Corbetti Caldera in the Main Ethiopian Rift, Journal of Volcanology and Geothermal Research, Volume 428, 2022, `https://doi.org/10.1016/j.jvolgeores.2022.107580`.

1.3.2 Magma Storage Conditions

Chapter 3 investigates the magma storage conditions at Corbetti caldera. Here I present geochemical and petrological data on the only basaltic eruption known from Corbetti, and use RhyoliteMELTS modelling to determine the likely pressure and fO_2 conditions under which the magmas at Corbetti evolved and the initial H_2O content of the parental alkali basalt. I compare these results with a petrological investigation of two end-member compositions, using a range of mineral-liquid thermometers and hygrometers to constrain storage temperatures, pressures and water contents. These findings are then compared with geophysical observations at Corbetti and data from across the MER.

This work has been submitted to the Journal of Volcanology and Geothermal Research and is currently in review: David J. Colby, David M. Pyle, Karen Fontijn, Tamsin A. Mather, Abate A. Melaku, Million A. Mengesha and Gezahegn Yirgu, (in review), Magma storage conditions beneath a peralkaline caldera in the Main Ethiopian Rift.

1.3.3 Diversity in Peralkaline Magmas across the Main Ethiopian Rift

Chapter 4 explores the geochemical variation in peralkaline magmas across several silicic centres within the Main Ethiopian Rift. In this chapter, I explore the similarities and differences observed across the MER and highlight the lack of diversity observed at Corbetti. I outline the varying mineralogical controls on the development of peralkaline magmas and explore the data through the lens of the Qz-Or-Ab-Ac-Ns residua system. I identify evidence for multiple liquid lines of descent and mineralogical controls for generating observed peralkaline compositions within the MER.

1.3.4 Conclusions and further work

In the conclusions (Chapter 5), I highlight the key findings from this work, provide an overview of areas that require further research, and highlight the unresolved questions that can offer the basis for future studies.

Chapter 2

Stratigraphy and Eruptive History of Corbetti Caldera in the Main Ethiopian Rift

David J Colby[a], David M Pyle[a], Karen Fontijn[b], Tamsin A Mather[a], Abate A Melaku[c], Million A Mengesha[d], Gezahegn Yirgu[d]

[a] *Department of Earth Science, University of Oxford, United Kingdom*

[b] *Laboratoire G-Time, Department of Geosciences, Environment, and Society, Université libre de Bruxelles, Belgium*

[c] *School of Earth and Environmental Sciences, University of St. Andrews, United Kingdom*

[d] *School of Earth Sciences, Addis Ababa University, Ethiopia*

As published in Journal of Volcanology and Geothermal Research

(DOI:10.1016/j.jvolgeores.2022.107580)

Abstract

The East African Rift (EAR) hosts the highest density of peralkaline volcanoes of any region globally, making it an ideal location to study the subaerial and magmatic processes of peralkaline volcanism. Corbetti caldera is one such peralkaline centre found within the southern part of the Main Ethiopian Rift (MER), a segment of the EAR. Corbetti is actively deforming and has previously undergone large-scale Plinian eruptions. However, our broader understanding of Corbetti's evolution is limited. Here we present a detailed study of the pre-, syn-and post-caldera eruptive deposits and compile them into a composite stratigraphy of the volcanic sequence. We find evidence for multiple previously undocumented large-scale eruptions, including the deposition of two pre-caldera lithic lag breccias, and we identify three additional post-caldera obsidian lavas. We constrain the age of a young Tuff Cone, Biftu, which sits outside the caldera walls, to $< 7375 \pm 54$ cal BP through ^{14}C dating of shells within an associated PDC deposit. The Wendo Koshe Cone, the most recent cone within the complex, is interpreted as the remains of two cones that opened in close proximity to each other and formed the vents for two pyroclastic eruptions: Bedded Pumice and Wendo Koshe Younger Pumice (WKYP). There is abundant evidence for the occurrence of pyroclastic density currents (PDC) within the caldera, usually associated with pumice cone-forming eruptions. These flow deposits rarely extend beyond the caldera walls. From our compiled stratigraphy, we estimate a recurrence rate of one eruption per 300-400 years over the last 2.3 ky.

These findings are especially significant as Corbetti is earmarked for potential geothermal exploration, and an understanding of eruptive frequency and style provides vital context to assess the potential hazards associated with this future infrastructure.

2.1 Introduction

Quaternary volcanism within the Main Ethiopian Rift (MER) has been characterised by a diverse range of volcanic activity (Fontijn et al., 2018), from large scale caldera-forming eruptions (Hutchison et al., 2016b,c; Rampey et al., 2010; Tadesse et al., 2022) to pumice cone eruptions (Clarke et al., 2019, 2020) and the eruption of basaltic scoria cones (Hunt et al., 2019; Mazzarini et al., 2004). There have been no confirmed eruptions within the MER since the 19th century, therefore, our understanding of the past dynamics of volcanism and potential future activity can only be gained through investigations of the geological record. The products of peralkaline volcanism dominate within the rift (Peccerillo et al., 2003); however, this type of eruption has not been observed directly, making the MER a vital place to study the properties of peralkaline magmas and their deposits (Gleeson et al., 2017; Iddon et al., 2019; Iddon and Edmonds, 2020; Macdonald and Gibson, 1969; Rooney et al., 2012; Tadesse et al., 2019, and references therein). Many of the large silicic calderas of the rift lie close to large population centres and densely populated rural communities. Over 10 million people live within 30 km of one of Ethiopia's 59 Holocene volcanoes, and Ethiopia is ranked as having the 5th highest risk to human life from volcanic hazards of any country in the world (Aspinall et al., 2011; Loughlin et al., 2015; Vye-Brown et al., 2015).

Ethiopia is increasingly looking to exploit the geothermal potential of several of the large silicic centres within the rift. Aluto has hosted a geothermal plant since 1998, and plans are in place to develop sites at Tullu Moye and Corbetti (Altaye, 1984; Biggs et al., 2011; Gíslason et al., 2015; Hutchison et al., 2015). These projects could be hugely beneficial to Ethiopia's economic and energy security; however, we know little about the volcanic history or the volcanic hazards for many of the planned sites.

2.1.1 Regional Setting

The MER forms the northernmost segment of the East African Rift (EAR), a 4000 long km zone of extensional deformation caused by the divergence of the Arabian and Somalian plates from the Nubian Plate (Ebinger, 2005). The MER developed asynchronously across three main sectors: the northern (< 30 Ma), southern (18 Ma), and Central rift (6-11 Ma) (Boone et al., 2019; Purcell, 2018; WoldeGabriel et al., 1992) and is the classic example of an oblique continental rift, connecting the Afar Depression to the north, and the Turkana depression and Kenyan Rift to the south (Figure 2.1); (Ebinger, 2005). At $\sim$ 2 Ma the

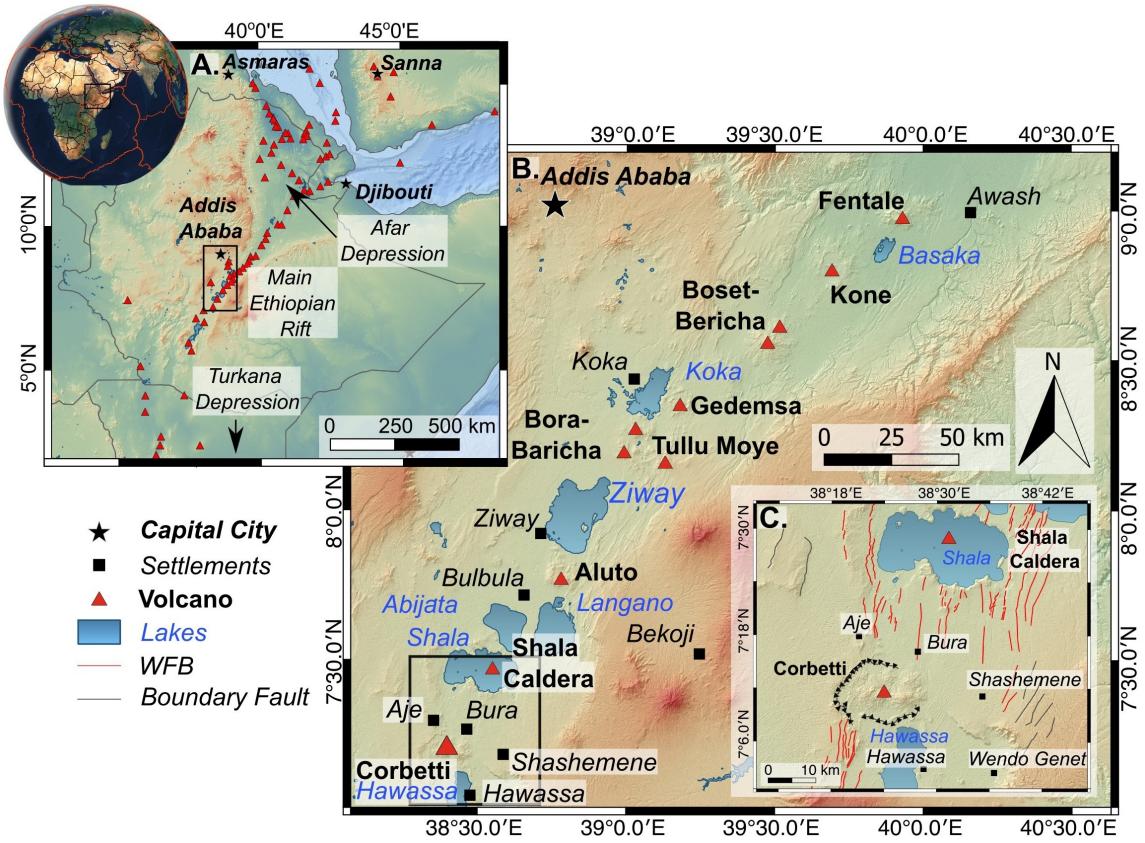

Figure 2.1: A) Overview map of the East African Rift (EAR) showing major fault structures and location of silicic volcanoes. B) Overview map of the Main Ethiopian Rift (MER) showing the location of central silicic volcanoes and major settlements. Corbetti, the focus of this study, is in the southern part of the MER. C) Map showing location of Corbetti Caldera and a section of the Wonji Fault Belt (WFB). Faults after Agostini et al. 2011

development of the Wonji Fault Belt (WFB), a region within the NMER (and incipient in the C-MER) containing numerous short, right-stepping echelon faults, resulted in the migration of strain away from the boundary faults and towards the centre of the rift (Mohr et al., 1980; Ebinger and Casey, 2001; Casey et al., 2006; Pizzi et al., 2006; Kurz et al., 2007; Corti, 2009; Corti et al., 2022). This fault belt, and the subsequent development of magmatic segments, marked a transition toward magma-dominated deformation/ rifting (Kendall et al., 2005). This transition to magma-assisted deformation and rifting is key for enabling the style and distribution of volcanism seen across the rift today. The cross rift faults within the MER and those linked to early stages of rift development play a critical role in determining the location, shape, and orientation of calderas, as well as controlling the position of post-caldera vents (Mohr et al., 1980; Robertson et al., 2016; Maestrelli et al., 2022; Corti et al., 2022).

2.1.2 Corbetti Caldera

Corbetti is located within the southernmost part of the rift (Figure 2.1) and is one of the largest calderas within the MER. It has followed an evolutionary pattern similar to other caldera volcanoes within the MER, beginning with a shield-building phase of peralkaline rhyolite lava flows, followed by at least one caldera-forming eruption, the inferred deposits of which are dated to ca. 182 ± 28 ka (Hutchison et al., 2016b). Subsequent volcanism focused around three post-caldera edifices (Artu, Urji, and Chabbi) and a rhyolitic cone (Biftu Tuff Cone), situated outside the south-eastern caldera wall (Figure 2.2)(Clarke, 2020; Fontijn et al., 2018; Hunt et al., 2019; Rapprich et al., 2016). The caldera rim has an irregular elliptical shape, approximately 15.6 × 10.9 km along the long and short axis respectively (Hunt et al., 2019), with steep cliffs on the northern and southern rim and broader, heavily incised slopes on the western side. The eroded remains of Artu cone partly cover the north-eastern section of the caldera (Figure 2.2), and younger products from Chabbi shield entirely cover the eastern portion of the caldera wall.

Previous studies have highlighted the variety of deposits associated with the post-caldera edifices. Both Urji and Chabbi have experienced explosive and effusive eruptions from numerous vents (Di Paola, 1972; Fontijn et al., 2018; Hunt et al., 2019; Rapprich et al., 2016) however, the youngest eruptions from Urji were predominantly explosive (Fontijn et al., 2018; Rapprich et al., 2016) whilst the eruption of obsidian lava flows occurred most frequently on Chabbi (Di Paola, 1972; Fontijn et al., 2018; Macdonald and Gibson, 1969; Rapprich et al., 2016). Across both edifices the erupted products are typically geochemically homogenous, crystal-poor peralkaline rhyolites (Fontijn et al., 2018; Rapprich et al., 2016).

Previous studies have identified two major explosive eruptions, the Bedded Pumice eruption and Wendo Koshe Younger Pumice (WKYP) (Fontijn et al., 2018; Rapprich et al., 2016). Deposits of these two eruptions have been correlated across multiple intra-caldera localities and at locations outside the caldera walls (Fontijn et al., 2018), including lake sediment cores (Martin-Jones et al., 2017). The Bedded Pumice unit is a rhythmically bedded pumice fall deposit containing thin cm-thick ash-rich flow packages and obsidian lithics. It is attributed to the products of a pulsating eruption that gradually built a conical deposit and is best preserved and exposed within the caldera (Fontijn et al., 2018). The Bedded Pumice is inferred to have had an approximate eruption magnitude of 4 (Fontijn et al., 2018) and is capped by a paleosol that stains the upper 30 cm of the unit. At distal locations, the Bedded Pumice unit is overlain by the geochemically-similar deposits of the WKYP eruption, a massive pumice fall deposit that lacks obsidian clasts (Fontijn et al., 2018;

Rapprich et al., 2016). Mapping the spatial distribution of this unit yielded an estimated minimum deposit volume of 1.3 km^3 and an approximate magnitude of 5 (Fontijn et al., 2018; Rapprich et al., 2016). Based on this mapping and observed field deposits, the source of this eruption is inferred to be the Wendo Koshe Cone (Figure 2.2F), the most recent cone on the flanks of Urji. Soil-carbon from the paleosol beneath WKYP is radiocarbon dated to < 2301 ± 120 cal a BP (Rapprich et al., 2016). Based on the observations of volcanic deposits from Corbetti, Fontijn et al. (2018) and Martin-Jones et al. (2017) estimated the recurrence interval of explosive eruptions to be around one eruption per 700-1000 years. However, as noted by McNamara et al. (2018), this is likely an underestimate, as deposits from smaller pumice cone forming eruptions, may be quickly eroded and therefore not recorded in the wider rock record.

Remote-sensing studies demonstrate the presence of an active geothermal system at Corbetti and provide evidence for a shallow magma plumbing system influenced by pre-existing E-W trending faults (Gíslason et al., 2015; Lavayssière et al., 2019; Lloyd et al., 2018b). Complementary InSAR studies show Corbetti has been actively deforming since at least 2009, uplifting at 6.6 ± 1.2 cm yr^{-1} (Biggs et al., 2011; Gottsmann et al., 2020; Lloyd et al., 2018a,b). This is attributed to the intrusion of ~ 10^{11} kg yr^{-1} mafic magma at ~ 7 km depth (Gottsmann et al., 2020). This demonstrates that Corbetti still has an active magma system and, therefore, still has eruptive potential. Despite this, considerable uncertainty surrounds the details of the eruptive history of Corbetti, its pre-caldera activity, and the controls on eruptive style.

The purpose of this study is to present a revised interpretation of the pre-and post-caldera eruptive activity of Corbetti, based on a new investigation of the eruptive deposits and their processes of emplacement and to document their compositions (whole rock and glass, major and trace element analysis), building on the work of previous studies (Fontijn et al., 2018; Martin-Jones et al., 2017; Rapprich et al., 2016). These data are compiled into a composite stratigraphy identifying discrete phases of activity and presented as a relative chronology for activity at Corbetti.

2.2 Samples and Methods

2.2.1 Field Campaign

A 3.5-week field campaign was undertaken in January 2020, focusing on five main regions within the caldera (Figure 2.2). These regions are a portion of the northern caldera wall (Figure 2.2B), the southern caldera wall (Figure 2.2C), road cuts through the central caldera (Figure 2.2D), exposures in a central gully Figure 2.2E), and exposures on the slopes of Urji (Figure 2.2F). These regions were selected as they were relatively accessible and encompassed the main periods of pre-and post-caldera activity, enabling the lateral tracing of units across multiple localities. This allowed for the establishment of correlations within the field. Several locations, such as portions of the western caldera and flanks of Chabbi, could not be visited due to challenges surrounding access and time constraints. However, investigation at several locations outside of the caldera (around the Biftu Tuff Cone (Figure 2.2G) and in drainage gullies near Lake Hawassa [Figure 2.2H]) were studied and yielded information on the explosive eruptions at Corbetti and the eruption of the extra-caldera, Biftu Tuff Cone (Figure 2.2G).

At each location units were systematically logged and sampled to capture any changes in texture and compositions. Figure 2.2 highlights the sample locations, and field photos show the stratigraphic location of the collected samples.

2.2.2 Stratigraphic Framework

Previous studies of Corbetti have highlighted the challenge of clearly distinguishing between eruptive units due to laterally discontinuous, highly variable lithofacies and geochemical similarities (Fontijn et al., 2018). Here we present stratigraphies from multiple sections of the caldera, highlighting correlations based upon the lateral continuity of marker horizons (e.g., paleosols, fall deposits, etc.), and outcrops of similar lithofacies, before compiling them into a wider composite stratigraphy. Not all units within a given region could be correlated accurately due to high spatial variability and low confidence in their stratigraphic position. These units are excluded from the composite stratigraphy; however, we highlight them in the relevant sections. Once compiled, the complete composite stratigraphy was separated into pre-, syn-, and post-caldera phases of activity and incorporated with a relative chronology established for Chabbi and the Biftu Tuff Cone (Clarke, 2020; Hunt

Table 2.1: Definitions of lithofacies (LF) notations used in this study (Branney and Kokelaar, 2002)

Notation	Definition	Description
mT	Massive tuff	An ash-rich tuff where the structure is massive
mL	Massive lapilli	A unit dominated by lapilli size (2-64 mm) clasts with a massive structure
mLT	Massive lapilli tuff	A tuff with lapilli sized clasts and a massive structure
dsT	Diffusely stratified tuff	An ash-rich tuff with poorly defined stratification
dsLT	Diffusely stratified lapilli tuff	A tuff with poorly defined stratification containing lapilli sized clasts. Clasts occasionally follow stratification
sT	Stratified tuff	An ash-rich tuff which shows clear stratification caused by slight changes in grain size and/or colour of ash
maccT	Massive ash aggregate bearing tuff	A massive ash-rich tuff containing ash aggregates
xsLT	Cross stratified lapilli tuff	A lapilli-bearing tuff which displays a cross-stratified fabric. These may be cross beds (> 10 mm) or cross laminations (< 10 mm)
dslBr	Diffusely stratified lithic rich breccia	Clast supported, lithic-rich unit containing compositional diverse blocks <64 mm. Shows poorly defined stratification

et al., 2019; Rapprich et al., 2016). Units are referred to in terms of their lithofacies to highlight distinguishing features using the approach of Branney and Kokelaar (2002) (for abbreviations and definitions, see Table 2.1).

2.2.3 Geochemistry and ^{14}C dating

Tephra and lava samples were selected to provide broad coverage of pre-and post-caldera activity at Corbetti and aimed to complement existing sample sets (Fontijn et al., 2018; Rapprich et al., 2016). Samples were cleaned, oven-dried, crushed, and powdered in an agate ball mill before being sent to Activation Labs (Ontario, Canada) in two batches for

major and trace element analysis. Samples were fused into beads and digested in a 5% nitric acid solution until dissolved (around 45 minutes). Major elements were determined through ICP-OES and trace elements through ICP-MS. Measured in house standard values for major and trace elements are within 10 % of reference values with the exception of Be and U which are within 15%. Values for duplicate analysis of samples were within 2 standard deviations. Detection limits are better than 0.01% for major elements and better than 30 ppm for trace elements (see supplementary information for details).

Several outcrops in drainage gullies close to the shore of Lake Hawassa (Figure 2.2H) contained abundant reworked shells of multiple gastropod species. Two shells of Melanoides tuberculata from two horizons underwent ^{14}C dating at Beta Analytic to provide a maximum age for the deposits. Samples were pre-treated using an acid etch. They were washed in deionised water to remove debris and then crushed and repeatedly subjected to HCl etches to eliminate secondary carbonate components. Samples were analysed by accelerator mass spectrometry (AMS), and the data were corrected for isotopic fractionation and calibrated using INTCAL20 (Reimer et al., 2020). Samples were also analysed for $\delta^{18}O$ and $\delta^{13}C$ to provide some information on the climatic conditions and compare with lake records from Hawassa (Lamb et al., 2002). δ13C was measured on pre-treated samples acidified in a gas bench to produce CO_2 and then analysed in an isotope ratio mass spectrometer.

2.3 Results:Stratigraphy

2.3.1 Northern Caldera Wall (NCW)

The northern caldera wall (NCW; See Figure 2.2B for sample locations) records some of the oldest activity at Corbetti, however, exposures are limited due to heavy erosion, burial by younger deposits and inaccessible outcrops. At the base of the North Caldera wall, a $>$ 15 m thick rhyolite lava (NCW_A; Figure 2.3A, Figure 2.4A, Table 2.2) is overlain at Sites 24 and 25 (Figure 2.2B) by a large bedded tephra succession (NCW_B; Figure 2.3A) dipping 17° to the east. The sequence at Site 24 is covered by a 3.8 m thick rhyolite lava (NCW_C) and capped by a second sequence of bedded tephra horizons (NCW_D; Figure 2.3B). To the east, at Sites 3 and 4 (Figure 2.2B), this lava and tephra succession is absent. Instead, a poorly consolidated red ignimbrite (NCW_E; Figure 2.3C) outcrops at the base of the sequence (this unit is also observed outside the caldera walls at Site 2 Figure 2.2A). This red ignimbrite is overlain by a eutaxitic welded ignimbrite (NCW_F; Figure 2.3C &

D) and a poorly consolidated reworked pumice horizon (NCW_G; Figure 2.3C). Slightly north of this exposure, moving up the caldera wall to Site 4, a sequence of ash aggregate bearing tuff horizons is observed (NCW_H; Figure 2.3E). A similar sequence of sintered and loosely consolidated ash horizons is also seen at Site 23 (Figure 2.2B, Figure 2.3F and A.1). Based upon the similarities in lithofacies and stratigraphic positions, units at Site 4 and Site 23 are correlated as the same unit (NCW_H).

In our compiled stratigraphy for this section (Figure 2.4A) of the caldera, we propose that units NCW_A - NCW_D were deposited before the caldera-forming eruption. The abrupt change in lithofacies between Sites 24 and 23 makes it difficult to draw clear correlations between these two sections of the caldera wall. A fault, seen as a marked drop in the height of the caldera wall, divides these two sections (Figure 2.2B;[(Hunt et al., 2017)]). This may explain the abrupt change in lithofacies observed between these locations.

Hutchison et al. (2016b) describe the ignimbrite associated with the caldera-forming eruption as a red, welded ignimbrite containing obsidian fiamme. Whilst NCW_E is not welded, we infer it to be an unwelded facies of the deposit. However, a detailed description of the dated ignimbrite is unavailable, and a lack of location and stratigraphic information makes this correlation tentative. The unconformity between NCW_E and F indicates the green welded ignimbrite is from a separate eruption. It is inferred that the emplacement of NCW_E - G occurred after the deposition of NCW_A - D due to the absence of units observed in the western portion of the caldera wall outcropping above the green welded ignimbrite. We proposed the ignimbrite was deposited in a paleovalley thus explaining its absence at the top of the succession at Site 25 (Figure 2.2B).

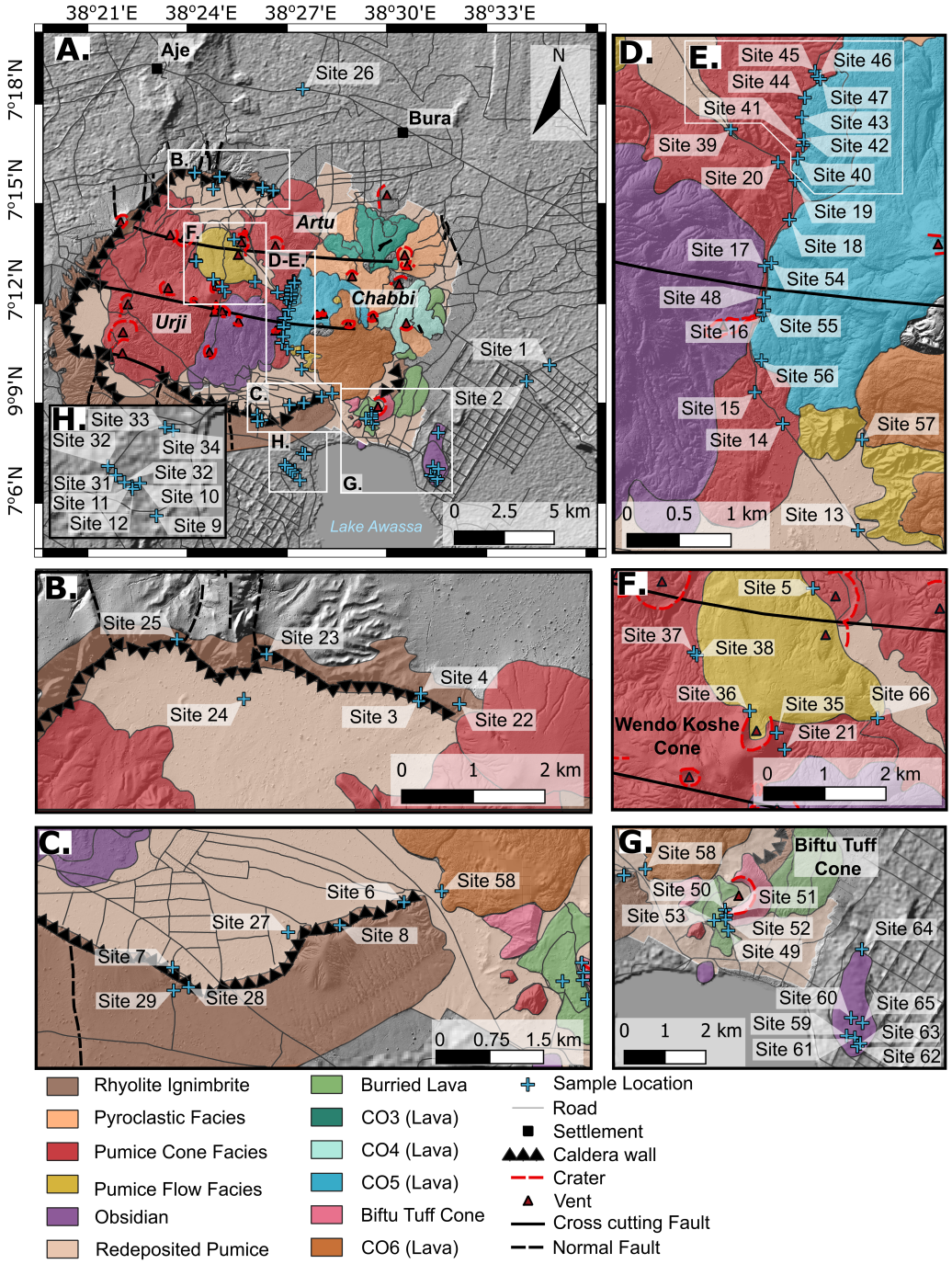

Figure 2.2: A) Geological setting of Corbetti Caldera, highlighting the major features, geological facies within the caldera and the sampling locations for this study [after Rapprich et al. (2016); Hunt et al. (2019); Clarke (2020)] B) Detail of sample locations in the Northern Caldera wall. C) Detail of sample locations in Southern caldera wall. D) Detail of Central Caldera sample locations E) Detail of Central Gully section sample locations. F) Detail of sample locations around the slopes of Urji. G) Detail of sample locations around the Biftu Tuff Cone and older pre-caldera deposits. H) Detail of sample locations of drainage gullies.

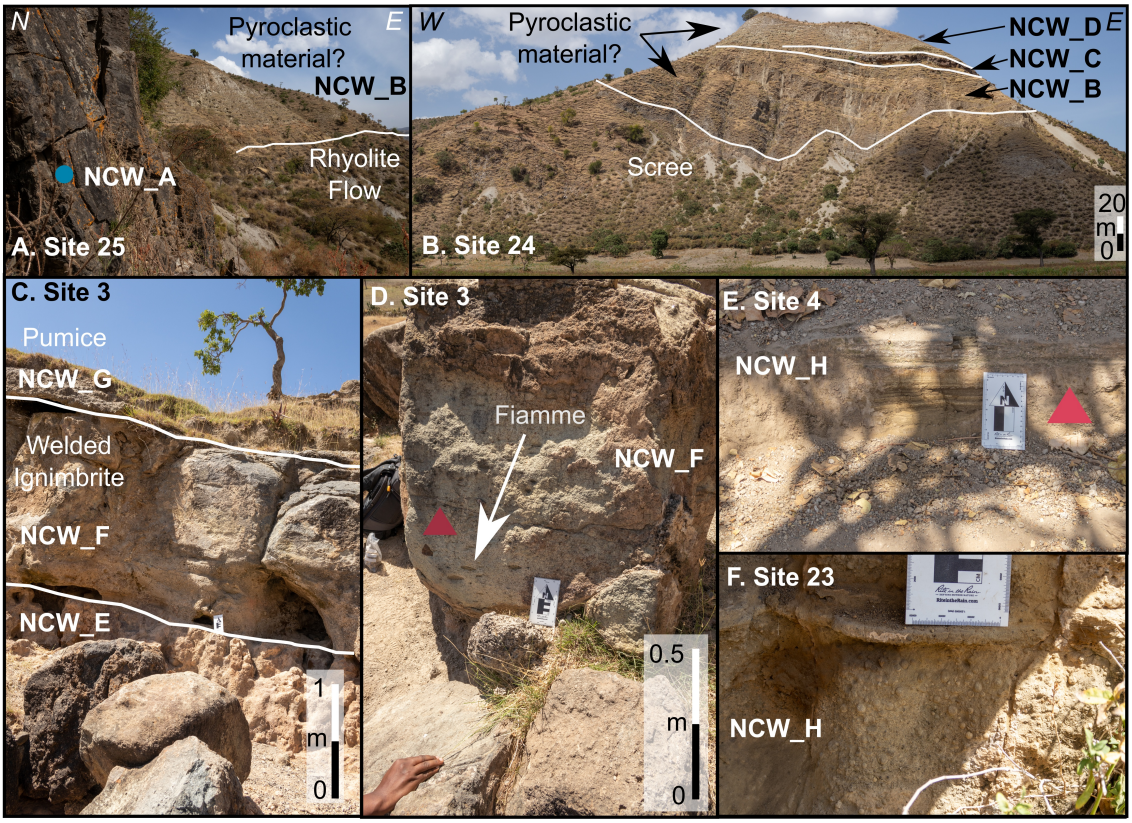

Figure 2.3: Field photos highlight outcrops in the Northern Caldera wall. Symbols denote location of collected samples and site localities are marked in Figure 2.2. A) Site 25 showing a jointed rhyolite lava (NCW_A) and the contact between an overlying pyroclastic succession, inferred to be NCW_D. B) Site 24 showing the pyroclastic succession (NCW_B) capped with a thin lava (NCW_C) and further pyroclastic succession (NCW_D). C) Welded ignimbrite at Site 3, showing the contact between the underlying red ignimbrite. D) Detail of the welded ignimbrite (NCW_F). E) Laminated ash-rich horizons (NCW_H) at Site 4. Horizons vary between loose unconsolidated ash and sintered ash. F) Ash aggregate (Accretionary Lapilli) bearing horizon at Site 23 (NCW_H).

Table 2.2: Descriptions and interpretations of units exposed in sections of the northern caldera walls (Figures 2.2B for samples locations, Figures 2.3 for field photos and 2.4 for stratigraphic log. Units presented youngest to oldest. Table 2.1 outlines the descriptions of lithofacies. LF = lithofacies.

Unit	Type Locality	LF	Thickness (m)	Description	Interpretation
NCW_H ***(Top of succession)***	Site 4/ Site 23	maccT	0.3	0.3 A stratified ash-rich unit containing sparse 5-10 mm ash aggregates, most likely accretionary lapilli. Ashy horizons varied between cemented and poorly consolidated and are 50-100 mm thick (Figure 2.3E-G).	Multiple dilute, ash-rich PDC deposits. Ash aggregates (likely accretionary lapilli) may suggest some interaction with water during the eruption (Brown et al., 2012, 2010), potentially phreatomagmatic. Stratification suggests pulsating nature of eruption with numerous waves of PDCs being generated.
NCW_G	Site 3	mL	0.37	Poorly sorted pumice deposit comprises of clast-supported, angular pumice ranging in size between 5-50 mm (Figure 2.3C).	Locally eroded pumice deposit that is incorporated with paleosol
NCW_F	Site 3	eumLT	1.7	Green, massive, eutaxitic lapilli-tuff with fiamme ~50 mm long. Sparse lithics. Unconformably overlies NCW_E (Figure 2.3C & D)	Welded ignimbrite may be related to underlying ignimbrite.

Continued on next page

Table 2.2 – continued from previous page

Unit	Type Locality	LF	Thickness (m)	Description	Interpretation
NCW_E	Site 3	mLT	2.5	Reddish, ash-rich, matrix-supported deposit with sparse pumice clasts and lithics (5-20 mm). Unit is poorly consolidated (Figure 2.3C).	Dilute PDC deposit likely associated with the 182 ± 28 ka ignimbrite identified by (Hutchison et al., 2016b; Vidal et al., 2022b).
NCW_D	Site 24	s/mLT	15.4	A succession of matrix-supported ash-rich horizons. Evidence of sparse pumice and lithics (Figure 2.3B)	Dilute PDC deposits. Multiple horizons indicate the passage of several flows, may indicate sustained eruption.
NCW_C	Site 24	Lava	3.8	Blocky lava deposit, some jointing observed (Figure 2.3B).	Small lava deposit, lack of access prevented further investigation.
NCW_B	Site 24	s/mLT	~70	Large pyroclastic succession containing multiple horizons of matrix-supported, ash-rich horizons. Horizon's dipping ~17°E. Some m scale stratification was observed (Figure 2.3B).	Deposition of multiple PDCs. Variation in bedding structures indicates varying conditions at the vent and in the flow during deposition.
NCW_A (Base of succession)	Site 25	Lava	> 15 (base not seen)	Jointed rhyolitic lava with some localised flow banding (Figure 2.3A).	Deposit of rhyolite lava emplaced during Corbetti's shield building phase. Jointing indicates slow cooling

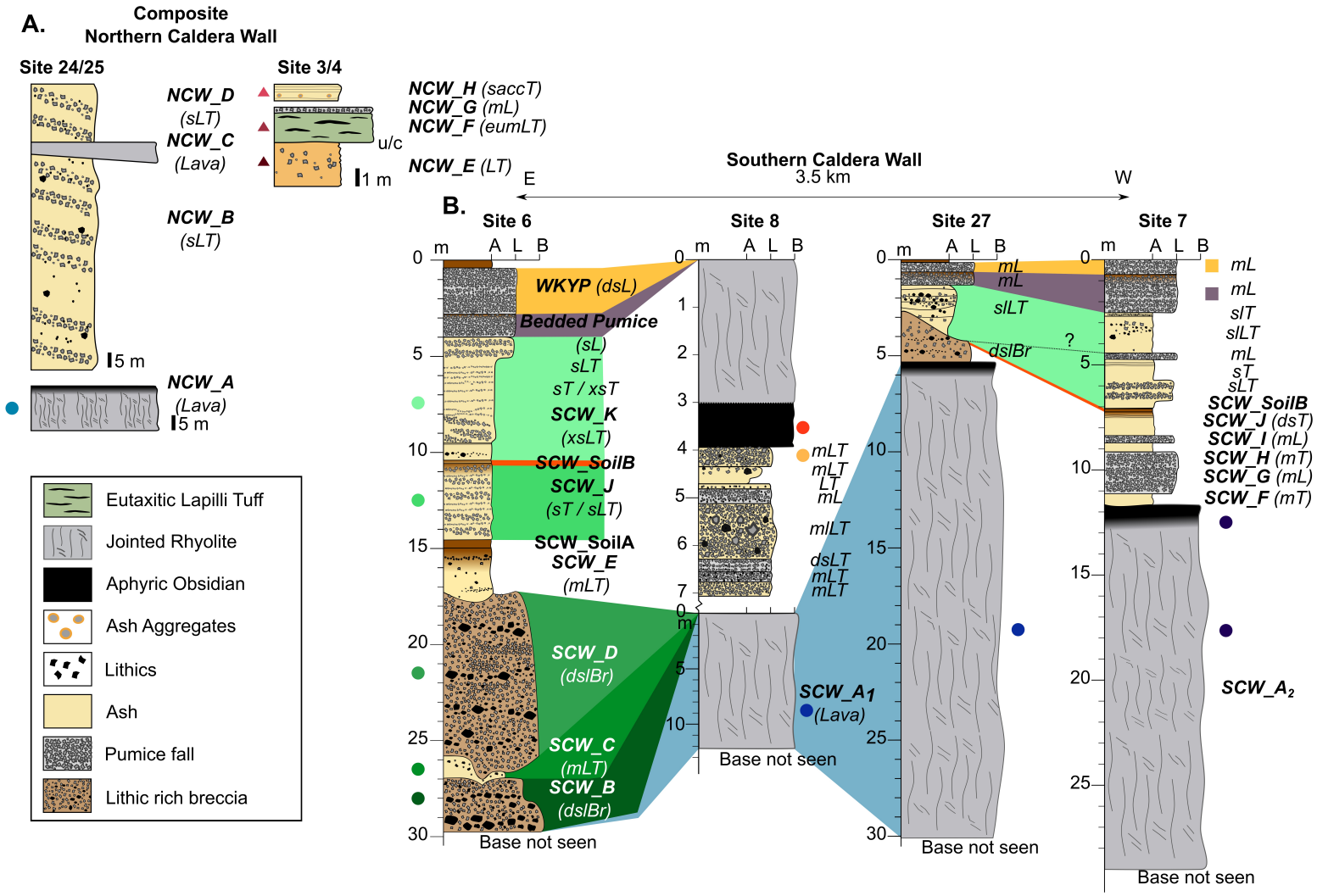

Figure 2.4: A) Stratigraphic log of units exposed in the northern caldera wall (Figure. 2.2B) and described in Table 2.2. B) Stratigraphic logs of exposures in the Southern Caldera wall (Fig. 2.2C) highlighting lateral correlations between outcrops. Units described in Table 2.2. Symbols denote the location of samples which underwent geochemical analysis (See Section 2.4).

2.3.2 Southern Caldera Wall (SCW)

Four localities in the southern portion of the caldera wall, which encompass the pre-and post-caldera activity, were studied in detail (Sites 6, 7, 8 and 27; Figure 2.2C), and observations of the stratigraphy are presented in Table 3 and Figure 2.4B. The base of the Southern Caldera wall is comprises of thick (>10 m) lavas (Figure 2.5 & Supplementary information (SI) A.1), similar to those observed in the Northern Caldera Wall. Two distinct lava units have been identified by lateral tracing of the units in the field, the distance between the two outcrops and a lack of exposures between the two localities. SCW_A1 outcrops at Site 8 and 27 (SI A.2), and SCW_A2 outcrops at Site 7 (Figure 2.5). The relative ages of these two deposits could not be constrained due to an absence of clear contact between them.

Correlating units overlying these two rhyolitic lavas (SCW_A1 & SCW_A2) is challenging due to a wide variation in lithofacies and spatial variability of outcropping units. At Site 6, lava deposits (SCW_A1) are absent and the base of the exposure comprises of two large lithic-rich breccias (SCW_B & SCW_D) inter-bedded with massive, ash-rich horizons (SCW_C & SCW_E). This sequence is capped by a paleosol (SCW_SoilA; Figure 2.4 & 2.6). Units SCW_B-E are not observed at other localities and are inferred to be deposited in a paleovalley created, in part, by the deposition of SCW_A1, which is seen to dip away to the east. A lithic breccia is also seen above SCW_A1 at Site 27 (SI A.2), however it is unclear if this is the same unit as the lithic breccias outcropping at Site 6.

Further to the west at Site 7, a succession of pumice-fall and ash-fall deposits (SCW_F - I; Table 2.3; SI A.2) is observed overlying the jointed lava (SCW_A2). These units are only observed at this location and therefore the relative timing of their eruption is difficult to establish. The sequence is capped by a diffusely stratified tuff stained by an overlying paleosol. The paleosol (Figure 2.4B, 2.5) is tentatively correlated to SCW_SoilB and the underlying tuff with SCW_J, based upon the overlying succession sharing similarities to the lithofacies observed at Site 6 (Figure 2.6).

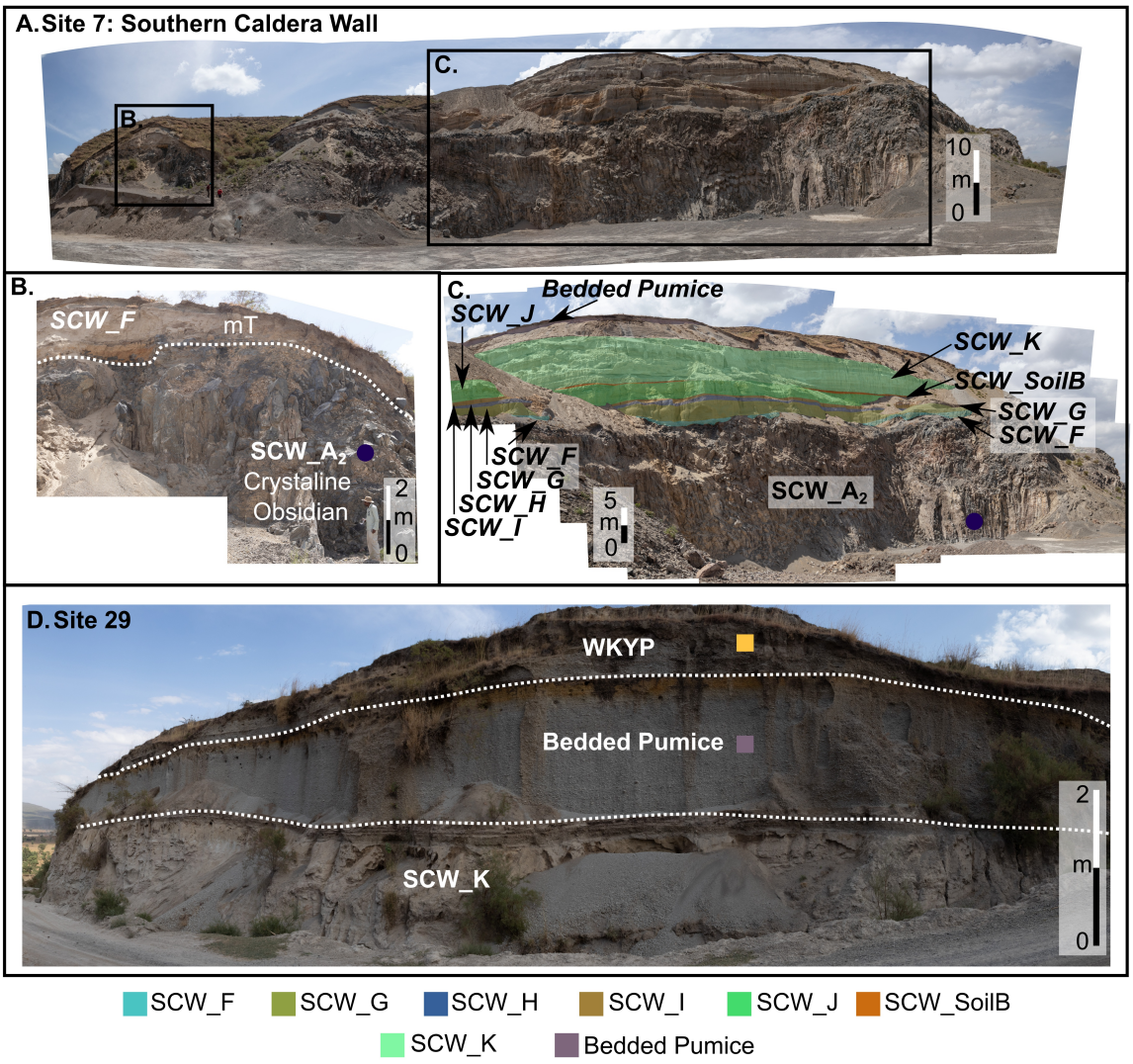

Figure 2.5: A) Shows overview of outcrop at Site 7 (Figure 2.2C) and location of panels B and C. B and C show details of the outcrop with C highlighting the major lithofacies observed (see Table 2.3). D) Outcrop at Site 29 (Figure 2.2C) showing presence of Bedded Pumice and WKYP units capping the succession. Symbols denote units sampled for geochemical analysis and presented in Figures 2.14 and 2.15

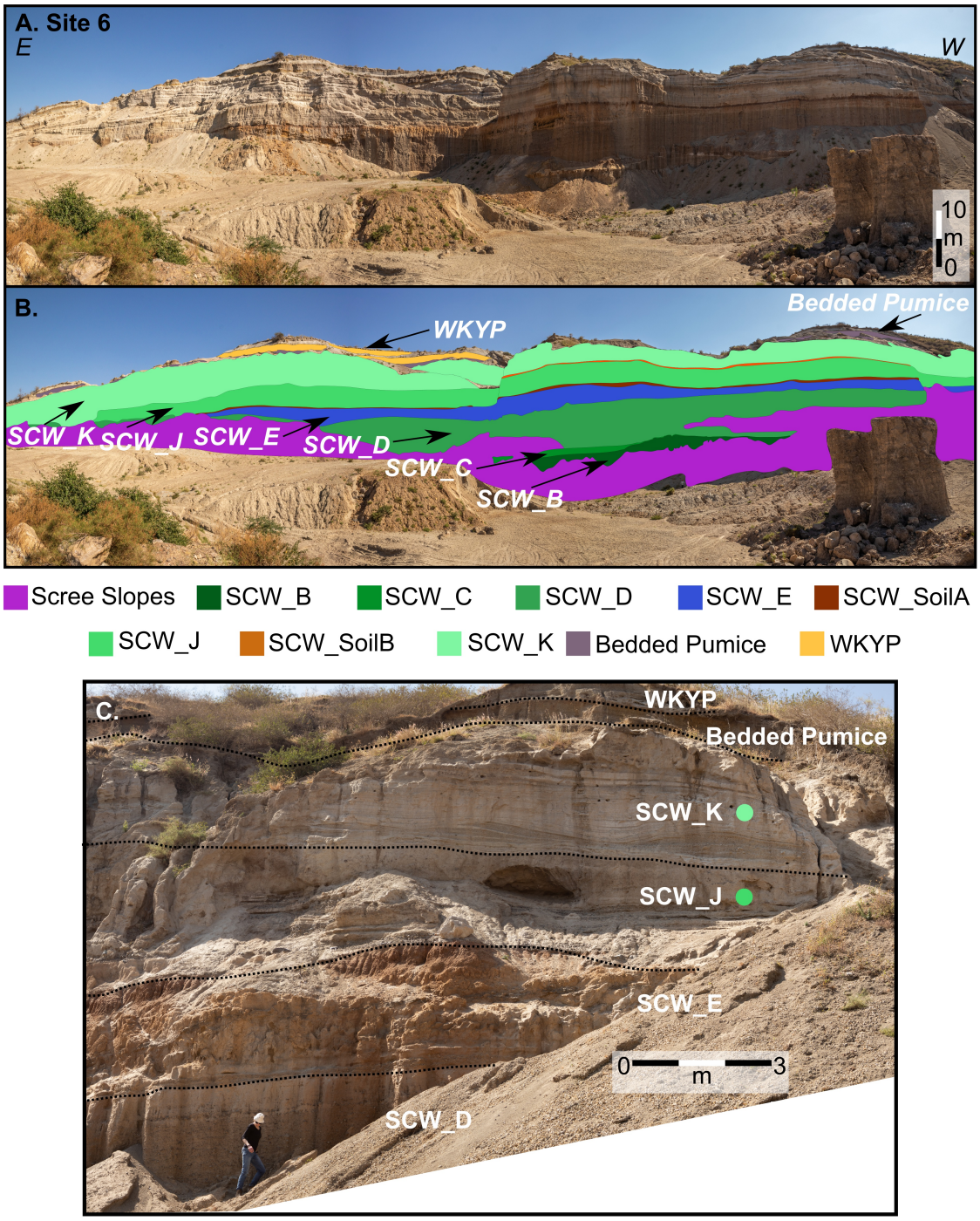

Figure 2.6: A) Panoramic image of quarry in the southern caldera wall (Site 6, Figure 2.2C) highlighting the identified units outline in Table 2.3 and Figure 2.4. C) Detail of the upper portion of the exposure which outcrops to the west of the panorama in A. Symbols denote location of samples.

Table 2.3: Description and interpretation of units exposed in the Southern caldera wall (Figure 2.2C). Stratigraphic log outlined in Figure2.4B. Field photos of outcrops are found in figures 2.5 and 2.6

Unit	Type Locality	LF	Thickness (m)	Description	Interpretation
SCW_SoilC	-	Soil	0.43	Organic layer with reworked pumice (Figure 2.5).	Topsoil
WKYP	Site 6	dsL	2.43	Massive to diffusely stratified, clast supported pumice deposit. Pumice ranges in size between 10-50 mm. Well sorted with sparse larger clasts (Figure 2.5, 2.6).	Distal pumice fall deposit of the WKYP deposit identified in Fontijn et al. (2018) and Rapprich et al. (2016). Slight bedding suggests minor changes in conditions at the eruptive vent.
Bedded Pumice	Site 6	dsL	1.18	Diffusely stratified, on the order of ~ 10-200 mm, lapilli horizon. Clast supported, angular pumice ranges in size between 5-30 mm. Top ~ 0.4 m are stained by an overlying paleosol. However, paleosol is not visible as a distinct horizon	Distal pumice fall deposit interpreted as the Bedded Pumice of Rapprich et al. (2016) and Fontijn et al. (2018). Bedding patterns suggest varying conditions at the eruptive vent.

Continued on next page

Table 2.3 – continued from previous page

Unit	Type Locality	LF	Thickness (m)	Description	Interpretation
SCW_K	Site 6	xsLT/ sT	6.51	Cross-stratified to stratified ash-rich tuff with lenses of pumice on the lee side of dune structures. Pumice ranges in size from 10-60 mm (Figure 2.6).	Dilute, ash-rich PDC, likely phreatomagmatic in origin, with lenses of coarse pumice. Sedimentary structures indicate changes in conditions at the lower flow boundary (LFB) (Branney and Kokelaar, 2002) and varying depositional regimes through space and time. The thickness of the deposit indicates a significant, sustained event
SCW_SoilB	Site 6	Soil	0.1	Dark organic layer (Figure 2.6)	Paleosol
SCW_J	Site 6	sT/sLT	4.25	Deposit varies between stratified tuff and stratified lapilli tuff. Lenses of coarse-grained pumice (~30-60 mm) and finer-grained pumice (~5-10 mm) occur throughout the deposit (Figure 2.6).	Records passage of a PDC that transitioned between dilute and granular flow, possibly phreatomagmatic. Varying conditions at the lower flow boundary resulted in the deposition of coarser and finer-grained material at different intervals.
SCW_I	Site 7	mL	0.37	Similar to SCW_G. Massive lapilli horizons comprises of well sorted angular pumice which do not exhibit any bedding features or contain lithics. Pumice ranges in size from 5-10 mm	Pumice fall deposit

Continued on next page

Table 2.3 – continued from previous page

Unit	Type Locality	LF	Thickness (m)	Description	Interpretation
SCW_H	Site 7	mT	0.44	Similar to SCW_F. Massive tuff horizon comprising fine-grained ash appears to be lithic-free. No clear signs of changes in grain size; bedding features are absent (Figure 2.5).	Ash fall deposit
SCW_G	Site 7	mL	2.07	Massive lapilli horizon comprises of well-sorted angular pumice. Pumice ranges in size from 5-40 mm; no lithic fragments were observed (Figure 2.5)	Pumice fall deposit
SCW_F	Site 7	mT	0.54	Massive tuff horizon comprises of fine-grained well-sorted ash. Unit inaccessible but appears to be lithic-free. No clear signs of changes in grain size or presence of pumice lapilli. Bedding features are absent. Unit is laterally extensive across exposure and does not display any erosive contacts (Figure 2.5)	Ash fall deposit.
SCW_SoilA	Site 6	Soil	0.43	Dark organic rich layer (Figure 2.6)	Paleosol

Continued on next page

Table 2.3 – continued from previous page

Unit	Type Locality	LF	Thickness (m)	Description	Interpretation
SCW_E	Site 6	mLT	2.4	Fine-grained ash horizon containing sparse lithic clasts. Contact with underlying breccia varies between gradational and erosional. Some lenses of pumice and lithics present. Pumice clasts range between 10-30 mm and lithics between 10-40 mm. A paleosol horizon has developed above this layer (Figure 2.6)	Records deposition of a dilute ash-rich PDC. The gradational to erosional boundary between the underlying deposit could suggest this unit records the wanning phase of the PDC. The massive nature of the deposit indicates a fluid escape regime at the LFB (Branney and Kokelaar, 2002) with the deposition of coarser-grained lenses indicative of a spatially and temporally limited transition to a traction dominated flow regime (Branney and Kokelaar, 2002). The presence of soil indicates a sustained period of quiescence after this eruptive event.

Continued on next page

Table 2.3 – continued from previous page

Unit	Type Locality	LF	Thickness (m)	Description	Interpretation
SCW_D	Site 6	dslBr	8.66	Diffusively stratified, clast supported, lithic-rich breccia which displays a moderate degree of sorting and containing angular to sub rounded lithic clasts. Comprised of fragments of red ignimbrite, flow-banded rhyolites, and sparse obsidian fragments. Some meter-sized blocks are present in the deposits. The upper portion of the unit grades up into matrix-supported fine ash (Figure 2.6).	Lithic lag breccia recording the deposition of a large granular PDC. The high concentration of lithics and remobilised ignimbrite suggest considerable remobilisation of previously erupted material. The eruption could be linked with a phase of pre-caldera edifice collapse as is observed at other MER volcanoes (Tadesse et al., 2022) and large scale caldera systems (Druitt, 1985). The large scale of this deposit suggests a sustained event.
SCW_C	Site 6	mlT	1.2	Unconsolidated ash with lenses of angular 20 - 100 mm lithics. Unit pinches and swells. Pumice is present in thicker sections and the concentration of pumice increases towards the top of the horizon. Unconformably overlies SCW_C (Figure 2.6).	Pinch and swell structures suggest deposition via a current with a spatially variable depositional regime. Ash rich, massive nature suggests a dilute PDC dominated by tractional forces. The presence of angular lithics suggests limited transport time in the current reducing the degree of clast interaction.

Continued on next page

Table 2.3 – continued from previous page

Unit	Type Locality	LF	Thickness (m)	Description	Interpretation
SCW_B	Site 6	dslBr	~ 2.86 (base not seen)	Diffusively stratified lithic-rich breccia displaying poor to moderate sorting. Unit predominantly clast-supported but grades to matrix-supported at the top of the unit, the upper ~0.3 m of which is cemented. The unit contains a diverse population of lithic clasts that making up >50% of the deposit. Lithics are primarily obsidian chips, banded rhyolite, and fragments of a red ignimbrite. Lithics are angular to sub-rounded. Lenses of coarser-grained lithic material are also seen. Pumice lapilli are present throughout, although it increases in abundance towards the top of the unit. Clasts range in size from 10 - 400 mm. A portion of the deposit displays diffuse stratification whilst the central part of the exposure displays signs of reworking (Figure 2.6).	Records depositional regime of a granular PDC. The presence of ignimbrite fragments suggests remobilisation and reworking of previously deposited material indicating the eruption from which the ignimbrite fragments are sourced must have occurred before the deposition of this unit. The lithic-rich nature of the deposit could suggest a large-scale eruption. The depositing current was likely a granular flow which was strongly controlled by paleotopography created in part by the emplacement of SCW_A1. The event could be linked to a phase of edifice collapse. A portion of the deposit shows signs of reworking

Continued on next page

Table 2.3 – continued from previous page

Unit	Type Locality	LF	Thickness (m)	Description	Interpretation
SCW_A	Site 27	Lava	~25	Jointed rhyolite lava outcrops at multiple localities in the Southern Caldera Wall. The top of the flow transitions towards glassy obsidian in places (SI A.2). SCW_A1 dips away to the east, under outcrop at Site 6 creating a paleo valley.	Pre-caldera lavas associated with the shield-building phase of Corbetti's evolution. Two flows have been identified in the southern caldera wall. SCW_A1 at Site 8 and 27 and SCW_A2 at Site 7.

The upper portion of the South Caldera Wall is dominated by a large ash-rich succession which at Site 6 comprises multiple units of ash-rich, matrix-supported tuffs containing sparse lithics and lenses of pumice (SWC_J & K Figure 2.6C) separated by a paleosol (SCW_SoilB). Two pumice horizons cap the succession and are seen to outcrop at several locations across the SCW (Figure 2.6C). The lower pumice horizon shows diffuse to massive bedding and sparse obsidian lithics are observed at the Site 7 outcrops (Figure 2.5C, D). The upper 0.3 m of the horizon are reverse graded and stained by an overlying paleosol. This unit shares features with and is correlated to the Bedded Pumice unit identified by Fontijn et al. (2018). The upper pumice horizon is massive and obsidian lithics are absent. This has been correlated to the WKYP deposits, as described in Fontijn et al. (2018) and Rapprich et al. (2016). These units are significant as they are the most widely dispersed and easily recognisable within the caldera making them an important stratigraphic marker horizon. The deposits of the Bedded Pumice unit and WKYP are seen in the upper parts of the succession at Site 7, as is the underlying matrix-supported PDC deposit (SCW_K; Figure 2.5C). This ash-rich PDC deposit is also seen in the upper section of the outcrop at Site 27 (Figure 2.2C and SI A.2). Here the unit is matrix-supported and stratified and contains abundant lithic clasts.

Units that outcrop at Site 8 have different lithofacies to other observed units in the Southern Caldera Wall (Figure 2.2C & SI A.3). The exposure occurs above SCW_A1 and comprise of a sequence of matrix-supported lithic-bearing pumice horizons and tuffs, capped with glassy obsidian which transitions into a jointed rhyolite flow (Figure 2.4B). The obsidian and rhyolite show some flow banding and spatter textures (Figure SI A.3). The relative timing of this sequence and its relationship with the other units in the Southern Caldera Wall is difficult to delimit due to the absence of other recognised units. An interpretation of this sequence is outlined in Section 2.5.1.

2.3.3 Central Caldera Section (CC)

Systematic study of exposed sections (Site 15, 17, 18, 20 and 21) along the central caldera road (Figure 2.2D) reveal multiple, laterally persistent units (Table 2.4 & Figure 2.7 & 2.8). Outcrops are commonly characterised by the presence of a large, diffusely bedded pumice deposit which occasionally grades into fine-grained ash (Figure 2.7A, B). This unit is correlated to the Bedded Pumice unit outlined in (Fontijn et al., 2018). A key feature of this unit is the reverse grading and staining from an overlying paleosol seen in the upper 0.3 m of the deposits. The consistency with which this lithofacies is observed made it a key

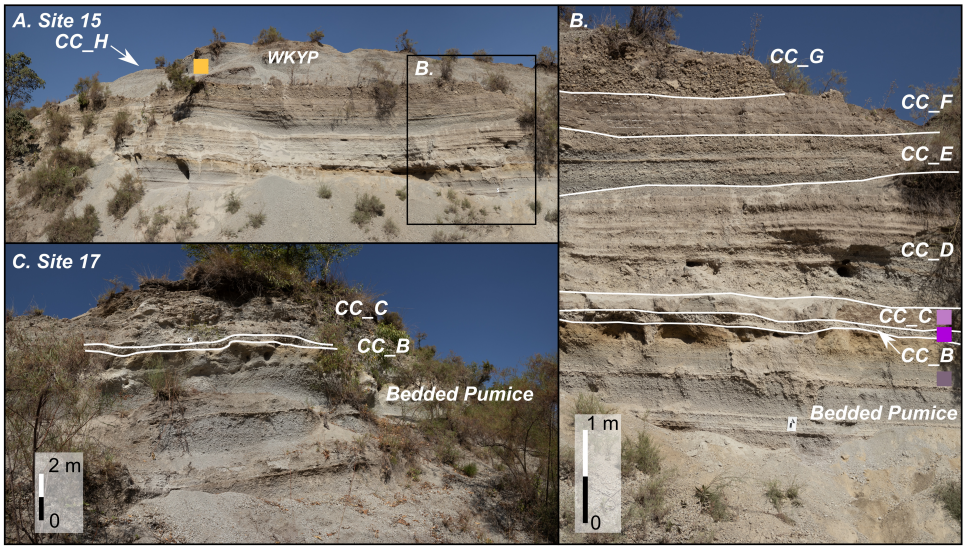

Figure 2.7: Selected outcrops in the Central Caldera (Figure 2.2D) highlighting the presence of key units outlined in Figure 2.10 & Table 2.4. A-B) Site 15 (MER001 of Fontijn et al. (2018)) overview and detail of major units. C) Site 17 showing the Bedded Pumice horizon and the consistent staining of the upper portion of the unit. Symbols denote the location of samples analysed in later sections.

marker for further correlations throughout the central caldera (Figure 2.8A). The correlation of the Bedded Pumice Unit made here agrees well with previous authors (Fontijn et al., 2018; Rapprich et al., 2016), although Site 15 (MER001 of Fontijn et al. 2018) has been updated after reassessment of the outcrop and its similarities with others in the stratigraphy. Overlying the Bedded Pumice Unit at multiple locations throughout the central caldera is a thin, obsidian-bearing, coarse-grained pumice horizon (CC_B). This latter unit and the Bedded Pumice provided the main stratigraphic makers for correlating units through the different sections within the central caldera and further correlation of deposits on the slopes of Urji.

Overlying CC_B is an ash-rich, lithic bearing PDC deposit containing a wide variety of clasts, including crystalline and flow banded rhyolite, obsidian, and pumice. At some localities, sparse ash aggregates are seen at the base of the outcrop. Units CC_D to CC (Figure2.7B & 2.8) are tentatively correlated with this deposit; however, they are described separately due to the difference in lithofacies. This sequence is subsequently overlain by a massive, well-sorted, obsidian-free pumice fall deposit attributed to the WKYP eruption (Fontijn et al., 2018). The succession is capped by massive, obsidian bearing pumice fall deposits (CC_H).

Table 2.4: Description and interpretation of units exposed within the Central Caldera section as shown in Figure 2.8. (See Figure 2.2C for sample locations and Figure 2.7 for field photos).

Unit	Type Locality	LF	Thickness (m)	Description	Interpretation
CC_Soil_A	-	Soil	0.55	Topsoil containing some reworked pumice	Topsoil
CC_H	Site 15	mL	0.46	Massive clast-supported pumice deposit containing obsidian lithics (Figure 2.7).	Pumice fall deposit only found at a single location, may be related to later eruptions of Chabbi and eroded from rest of caldera. Distinct from WKYP as unit is obsidian bearing
CO5	Site 17	Obsidian	8.43	Aphyric glassy obsidian	Lava flow from Chabbi
WKYP	Site 15	mL	1.87	Massive clast-supported pumice deposit (Figure 2.7). Well sorted with some rare diffuse stratification observed at some localities. Lithics absent	Pumice fall deposit, bedding observed at some localities reflects proximal location to vent and slight variations in eruptive intensity.
CC_G	Site 15	dsLT	0.4	Coarse grained, poorly sorted, obsidian bearing, ashy matrix. Diffusely-stratified lapilli tuff (Figure 2.7B)	Granular PDC
CC_F	Site 15	dsL/mT	0.7	Diffusely stratified tuff with horizons of stratified lapilli (Figure 2.7B).	Fall deposit recording variation in eruptive activity at the vent allowing the generation of both pumice and ash.

Continued on next page

Table 2.4 – continued from previous page

Unit	Type Locality	LF	Thickness (m)	Description	Interpretation
CC_E	Site 15	sL/mT	1.1	Unit varies between stratified lapilli and massive tuff. Stratified lapilli are clast-supported which grades into finer-grained tuff. Pumice varied between 10-40 mm (Figure 2.7B).	Either fall deposit with variation between pumice and ash reflective of changes in eruptive conditions at the vent, or records the deposition of several dilute PDC interbedded with pumice fall deposits.
CC_C	Site 17/18	maccB / mlBr	2.75	Matrix-supported containing large pumice and lithic clasts. Lithic composition is highly varied, with banded and crystalline rhyolite present ranging in size between 10-400 mm. The base of the unit is ash-rich and contains sparse ash aggregates, most likely accretionary lapilli (Figure 2.7C).	Dilute PDC. Eruption entrained material from the conduit. Accretionary lapilli suggest some degree of water interaction during the eruption. Uncertain if pumice is juvenile or remobilised.
CC_B	Site 21	mL	0.88	Coarse-grained pumice lapilli, clast supported containing obsidian lithics. Sparse highly vesicular pumice clasts were found, however they do not appear to have any clear stratigraphic placement. Pumice clasts range in size between 10 -50 mm. Relatively poorly sorted (Figure 2.7C).	Thin pumice fall deposit commonly observed above the Bedded Pumice deposit throughout the central caldera.

Continued on next page

Table 2.4 – continued from previous page

Unit	Type Locality	LF	Thickness (m)	Description	Interpretation
Bedded Pumice	Site 15/17/18/20	dsL	6.6	Diffusely stratified (on the order of ~ 0.1 m) pumice deposit. Clast-supported angular pumice ranges between 5-20 mm. The deposit contains sparse obsidian lithics dispersed throughout. The top ~0.3 m shows reverse grading and is stained by an overlying paleosol. Some outcrops have ash-rich horizons before transitioning to fine-grained reversely graded pumice (Figure 2.7B & C).	Pumice fall deposit correlated with the Bedded Pumice units of Fontijn et al. (2018). Diffuse bedding reflects variation in eruptive conditions at the vent. Reverse grading in-upper 0.3 m reflects changing eruptive conditions at the vent (Duffield et al., 1979). Displays features of pumice cone eruption (Clarke et al., 2020).

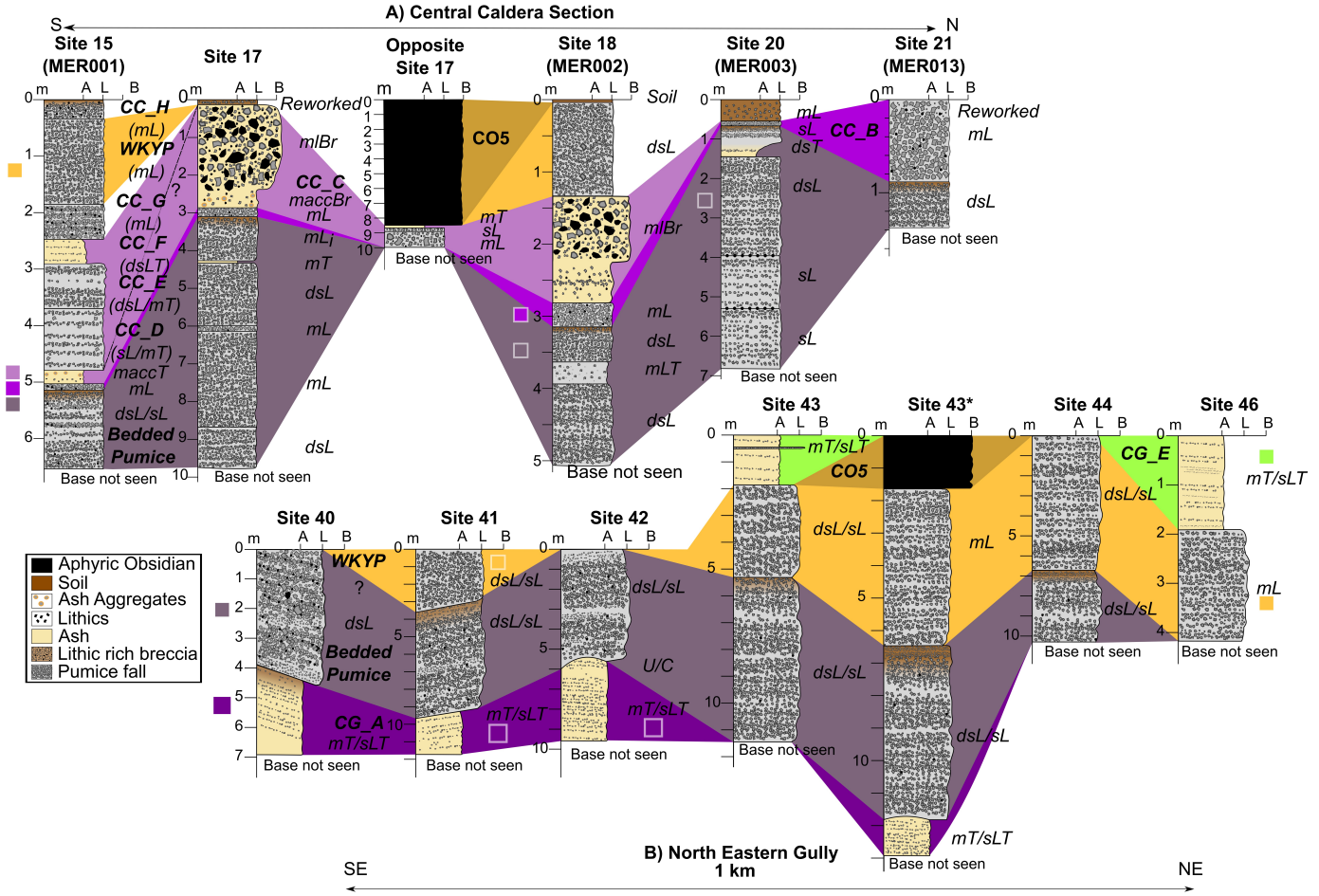

Figure 2.8: A) Selected stratigraphic logs for outcrops in the Central Caldera (Figure 2.2D) highlighting the major correlations (Table 2.4). B) Stratigraphic logs of outcrops in the north-eastern gully (Figure 2.2E) with highlighted correlations based upon lateral tracing of units (Table 2.5). Symbols denote location of analysed samples.

2.3.4 Central Gully (CG)

Outcrops in a gully off the main road through the caldera (Sites 40-44, 46; Figure 2.2D) provide clear exposures of a succession of some of Corbetti's recent activity (Table 2.5, Figure 2.8 & 2.9). At the base is an ash-rich tuff containing stratified pumice horizons (CG_A; Figure 2.9A& C). Overlying this are two large pumice fall deposits (Figure 2.9B-F). The lower pumice fall deposit displays diffuse stratification and clear flow packages of dilute PDCs (Figure 2.9C). The top of this unit is stained by an overlying paleosol. We correlated this unit to the Bedded Pumice deposit due to its similarity in lithofacies and characteristic staining by overlying soil. Above this is a massive to diffusely stratified deposit attributed to the WKYP (Figure 2.9B, D-F). Overlying the WKYP is a large obsidian lava deposit (CO5 (Rapprich et al., 2016); Figure 2.9E & F). This succession provides one of the few clear stratigraphic links between eruptive deposits of Urji and Chabbi, establishing the eruption of CO5 after the deposition of the WKYP unit. This has been key in incorporating Chabbi's relative chronology into the wider composite stratigraphy. At the top of the succession is an ash-rich tuff showing some stratified lapilli (CG_E). Although there is no contact between CG_E and CO5, its absence underlying the lava suggests it overrode CO5 and has subsequently been eroded (Figure 2.9G & H).

Table 2.5: Description and interpretation of observed units in the north-eastern gully (Figure 2.2E) Stratigraphic log is presented in Figure 2.8B and field photos in Figure 2.9.

Unit	Type Locality	LF	Thickness (m)	Description	Interpretation
CG_E	Site 46	sT/sLT	1.97	Stratified tuff to stratified lapilli tuff with lenses of coarse-grained pumice. Very fine-grained ash with pumice ranging in size between 5-20 mm (Figure 2.9D, G & H)	Dilute PDC
CG_D	Site 43	Lava	>1.68	Aphyric obsidian lava flow, unit likely thicker however only flow front observed (Figure 2.9E & G)	CO5 Obsidian Lava flow from Chabbi
WKYP	Site 43	dsL/mL	4.95	Well-sorted, clast-supported pumice deposit. Minor diffuse stratification in places but mostly massive. No lithics (Figure 2.9A-F)	Proximal pumice fall deposit. Some diffuse stratification suggests periods of slight variation in eruptive activity
Bedded Pumice	Site 43	dsL	5.51	Well-sorted, clast-supported pumice deposit. Diffuse bedding was observed throughout. Staining at the top from overlying paleosol that is no longer present. Some localities show reverse grading in the upper 0.3 m of deposit (Figure 2.9A-F)	Pumice fall deposit interbedded with ash-rich packages indicating the passage of dilute PDCs reflecting a highly unsteady eruption. Bedding reflects changes in eruptive condition at the vent. Some bedding features could also result from reworking of the deposit as it was deposited over paleo topography

Continued on next page

Table 2.5 – continued from previous page

Unit	Type Locality	LF	Thickness (m)	Description	Interpretation
CG_A	Site 42	sT/sLT	6	Ash-rich tuff with clear stratification and horizons of stratified lapilli. Sparse lithics. Pumice ranges in size between 5-10 mm (Figure 2.9A)	Dilute PDC with coarser lenses of pumice clasts.

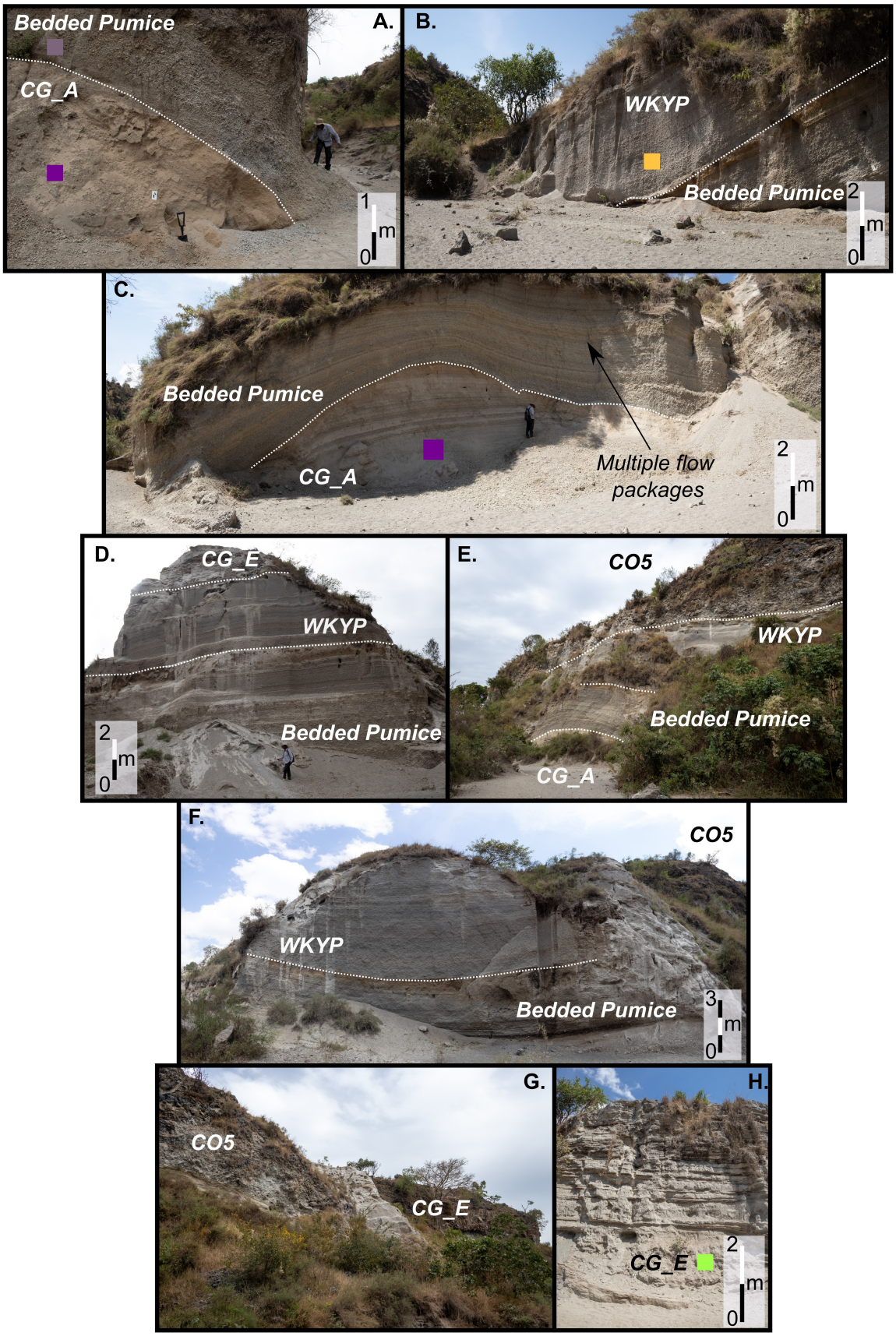

(Caption on next page.)

Figure 2.9: Field photos from Sites in the central gully section of the caldera highlighted in Figure 2.2E. A) Site 40, Bedded Pumice unit overlying an ash rich deposit. B) & C) outcrops at Site 41 of the WKYP and Bedded Pumice unit overlying ash-rich horizon. Slumping features observed. Flow packages refer to the alternation between ash rich horizons and thin pumice fall horizons which suggest the passage of a dilute PDC followed by a small period of pumice fallout before another PDC inundates the area. D) Large outcrop of Bedded Pumice and WKYP units capped with an ash rich PDC at Site 43. E) Outcrop opposite Site 43 showing contact between WKYP and CO5. Absence of CG_E suggests it was deposited after CO5. F) Shows characteristic features of the Bedded Pumice unit and WKYP overlain by CO5. G) Shows deposit of CG_E overlying CO5. H) Dilute ash rich PDC deposit (CG_E) comprises of multiple flow packages

2.3.5 Urji Slopes (US)

Multiple vents have been identified on the slopes of Urji (Hunt et al., 2019) however exposures are limited, therefore, we focus on the most recent activity associated with the Wendo Koshe Cone (Figure 2.2F). Near the edge of the Urji edifice (Site 21 Figure 2.2F), the base of the succession is large, jointed rhyolite lava (US_A; Figure 2.10E), which grades to glassy obsidian at the top. Numerous other lavas are recorded on the flanks of Urji, which are associated with older vents on the edifice (Figure 2.2A) and buried by younger deposits.

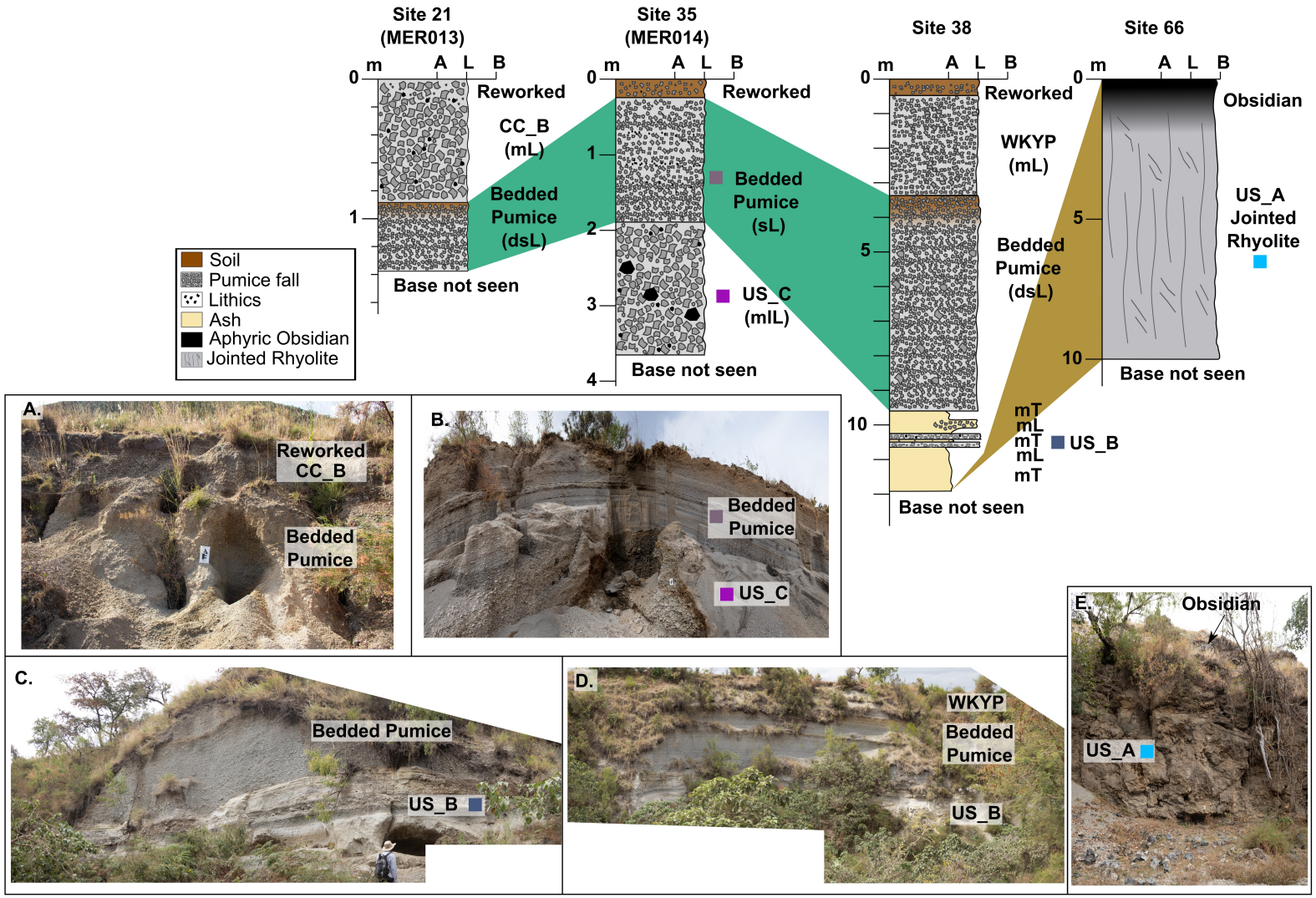

(Caption on next page.)

Figure 2.10: Stratigraphic logs from locations on and around the flanks of the Wendo Koshe Cone of Urji. Sample locations are highlighted in Figure 2.2F and units are described in Table 2.6. A) Outcrop on the flanks of the Wendo Koshe Cone (Site 21) showing the Bedded Pumice unit with the characteristic reverse grading and staining by overlying paleosol. This is overlain by the coarse-grained, obsidian bearing pumice fall deposit seen at numerous locations in the central caldera (CC_B; Figure 2.8) B) Outcrop on the flanks of the Wendo Koshe Cone showing proximal deposits characteristic of a pumice cone eruption. C & D) Outcrops at Site 38 showing similar characteristics described in Rapprich et al. (2016). E) Rhyolite flow on the flanks of Urji which grades to glassy obsidian.

Table 2.6: Descriptions and interpretation of units observed on the slopes of Urji (Figure 2.2F; logs and field photos presented in Figure 2.10).

Unit	Type Locality	LF	Thickness (m)	Description	Interpretation
WKYP	Site 38	mL	3	Massive to diffusely stratified, clast supported pumice deposit. Pumice ranged in size between 10-50 mm. Well sorted with sparse larger clasts (Figure 2.10D)	Pumice fall deposit associated with the eruption of the Wendo Koshe Cone. Eruption likely culminated with the collapse of the cone and emplacement of the outflow sheet identified by Rapprich et al. (2016)
Bedded Pumice	Site 38	dsL	6.44	Diffusely stratified, on the order of ~10-200 mm, lapilli horizon. Clast supported, angular pumice lapilli ranges in size between 5-30 mm. Top ~ 0.4 m are stained by an overlying paleosol. However, paleosol is not visible as a distinct horizon (Figure 2.10A-D)	Proximal pumice fall deposit associated with the formation of the Wendo Koshe Cone. Stratification and localised flow packages suggest highly unsteady eruption. Facies similar to those described by Clarke (2020)
US_C	Site 35	mlL	1.85	Coarse-grained pumice and lithic rich horizon. Some pumice and lithics show signs of hydrothermal alteration. Lithics blocks up to 0.5 m seen. Very poorly sorted (Figure 2.10C)	Proximal pumice fall deposit which has undergone post-deposition hydrothermal alteration. Records the highly energetic initial phases of the eruption which formed the Wendo Koshe Cone

Continued on next page

Table 2.6 – continued from previous page

Unit	Type Locality	LF	Thickness (m)	Description	Interpretation
US_B	Site 38	mT/mL	2.53	Ash-rich unit with pumice rich horizons. Pumice clasts range from 10 mm to 0.2 m. Poor sorting (Figure 2.10B)	Dilute, ash-rich PDC interbedded with pumice fall horizons. Coarse pumice-rich horizons indicate changes in the flow conditions within the current. Rapprich et al. (2016) inferred a phreatomagmatic origin.
US_A	Site 66	Lava	10	Aphyric jointed rhyolite which transitions towards glassy obsidian towards the top of the outcrop (Figure 2.10E)	Rhyolitic lava from Urji. One of several which record the initial phases of activity at Urji.

At proximal locations on the flanks of the Wendo Koshe Cone (Sites 21 and 35 Figure 2.2F), outcrops provide an insight into the cone's formation. The characteristic succession of the Bedded Pumice Unit overlain by a coarse-grained pumice horizon (CC_B) is repeated on the flanks of Urji at Site 21 (Figure 2.10A, B). A second outcrop at Site 35 (Figure 2.2F) reveals a coarse-grained, lithic-rich horizon (US_C) overlain by the Bedded Pumice unit (Figure 2.10B). The WKYP deposit is absent on the flanks of the Wendo Koshe Cone.

To the north of the Wendo Koshe Cone, the distal deposits of the Bedded Pumice and WKYP are observed in a small gully. At the base of the succession, multiple ash-rich, pumice bearing horizons are identified (US_B). This unit has previously been identified by Rapprich et al. (2016) and attributed to phreatomagmatic activity. It is overlain by a diffusely stratified pumice fall deposit which is stained by a paleosol. It was previously termed the WKPO deposit by Rapprich et al. (2016) however, it shares the characteristic reverse grading and staining in the upper 0.3 m of the deposit seen in the Bedded Pumice unit and has therefore been correlated with it. It is likely covered by an outflow sheet linked with the collapse of the Wendo Koshe Cone and an associated obsidian lava flow, which outcrops on top of this flow. Clear outcrops of this succession could not be found.

2.3.6 Chabbi and the Biftu Tuff Cone

Chabbi is a large shield volcano that sits in the eastern portion of Corbetti Caldera (Figure 2.2A). It consists of obsidian lavas erupted from numerous vents across the edifice and multiple pumice/tuff cones. Figure 2.11 presents a relative chronology of the formation of different vents, pumice cones and the emplacement of the obsidian lavas. It incorporates findings of previous studies (Hunt et al., 2019; Rapprich et al., 2016) and observations from this study using a high-resolution DEM (Hunt et al., 2019). This chronology is based upon exposures seen at the surface today, and it is anticipated multiple other eruptions occurred across this edifice, the deposits of which are now buried.

Following the caldera-forming eruption (Figure 2.11A) and the initial development of the edifice, activity at Chabbi was dominated by the formation of pumice cones on the northern flank (Figures 2.11B-D). The pumice cone highlighted in Figure 2.11B is the most heavily eroded and inferred to be the oldest exposed cone, with many of its deposits buried by subsequent activity. The cones highlighted in Figures 2.11C and 2.11D have more extensive deposits and are inferred to be slightly younger, although no absolute chronology can be established. Following the development of these pumice cones, the first (CO3) of the

four major obsidian lavas was emplaced. This deposit covers most of the northern flanks, with multiple lobes observed. One area of uncertainty surrounds the relative timing of the multiple buried lava flows and pyroclastic fans seen on the eastern flank and outside the caldera wall (Figures 2.11E and F). These may be associated with other vents which have been covered by later deposits.

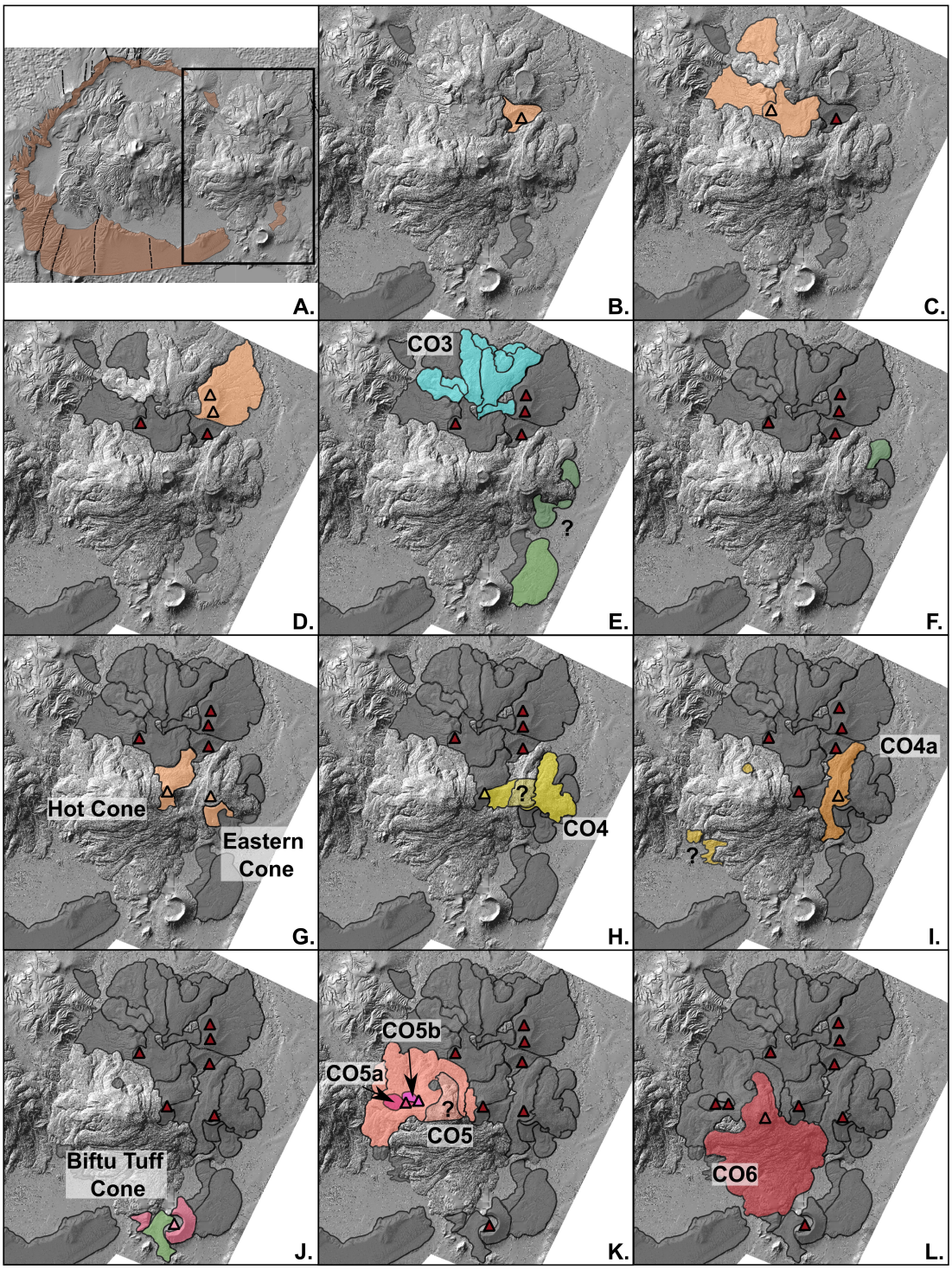

(Caption on next page.)

Figure 2.11: Overview of our proposed development of Chabbi. A) Caldera forming eruption followed by the development of Artu, Urji and Chabbi. Box highlights Chabbi and region of subsequent maps. B-D) The most heavily eroded areas of Chabbi are associated with pumice cone eruptions forming multiple vents some of which overlap; however the relative timing of these eruptions is difficult to constrain. E) Eruption of CO3 from a now eroded vent. CO3 has multiple lobes which over-ride earlier portions of the deposit. The timing of the deposits on the south-eastern flank are thought to occur around this time however no dates for these eruptions are currently available. F) Lava flow from a now buried vent, ogives can still be seen on the surface of the flow although it has been subsequently buried. G) Further pumice cone eruptions forming the Hot Cone (central) and the Eastern Cone (right) of Mohr (1966). H) Eruption of CO4 which is inferred to have overridden part of the eastern cone. I) Eruption of CO4a from a vent near the eastern cone. This flow erupted through CO4. J) Eruption of the Biftu Tuff cone. Two vents are seen on the western flank of Chabbi however the timing of their formation is uncertain After (Clarke, 2020). K) Eruption of CO5 from a now buried vent. Following this eruption two other vents formed erupting small lava flows which are identified here for the first time and termed CO5a and CO5b. L) Eruption of CO6 from a central vent. This is the most recent flow on Chabbi and has multiple lobes which override earlier portions of the flow.

Following the emplacement of CO3 (and the likely eruption of other lava flows on the southern and eastern flanks), two pumice cones formed, named the Hot Cone and Eastern Cone by Mohr (1966) (Figure 2.11G). The Hot Cone is the source of the next large obsidian deposit (CO4) recognised on Chabbi, CO4. Previously, the obsidian lavas on the eastern flank of Chabbi (Figure 2.12) have been attributed to multiple eruptions from two vents (The Hot Cone and Eastern Cone of Mohr 1966) and, more recently, to a single flow (CO4; Rapprich et al. 2016; Hunt et al. 2019). However, further investigation of the surface morphology and elevation changes away from the Hot Cone vent suggests this unit comprises two different lavas from two vents. Figure 2.12B shows elevation change along a profile of the CO4 lava. The elevation change is consistent with a flow moving away from the Hot Cone which is supported by the presence and direction of ogives on the surface of the flow. However, an abrupt change in elevation is seen ~900 m from the vent (Figure 2.12B), where a ~25 m thick obsidian lava bisects and overlies CO4 (Figure 2.12A) and is here termed CO4a. The drop in elevation seen around ~1750 m along the profile indicates the eastern extent of CO4a and the lava deposit past this point is likely the lower sections of CO4. This portion of the flow covers the flanks of the Eastern Cone, suggesting CO4 post-dates the formation of the cone. The surface morphology of CO4a indicates it flowed to the north and south, and ogives on the surface of the flow radiate out from a central point above the eastern cone, suggesting this is the source of the eruption, and it erupted through CO4. Pumice underlying CO4a has been $^{40}Ar/^{39}Ar$ dated to 19 ± 15 ka (Hutchison et al.,

2016b).

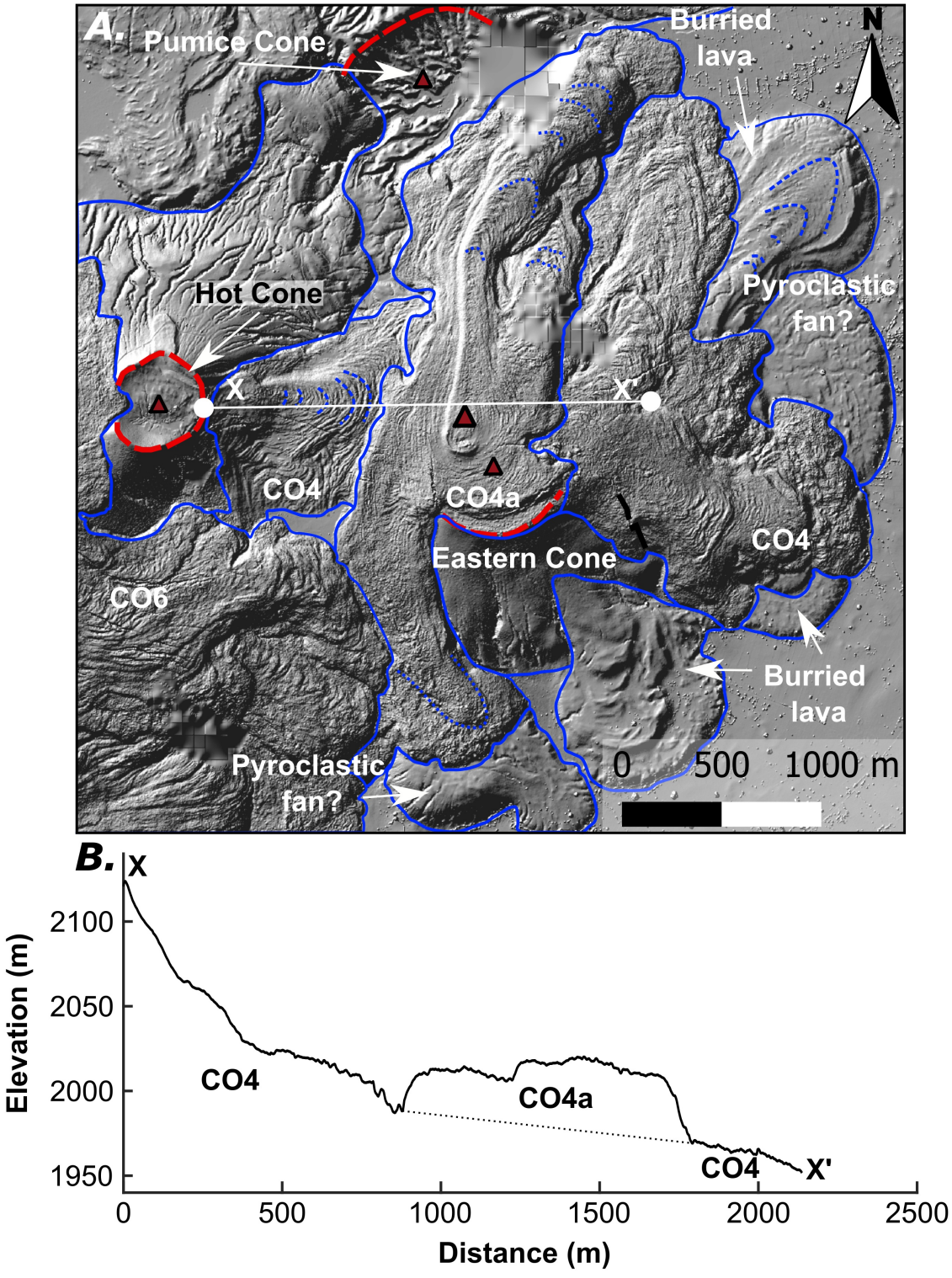

(Caption on next page.)

Figure 2.12: A) Detail of the CO4 and CO4a (Figure 2.11) showing the surface morphology of the two flows and surrounding features. Ogives visible in CO4a suggest the vent of the eruption is slightly offset from the eastern cone vent suggesting it is sourced from a different vent. In addition, the ogives on the upper portions of CO4 are clearly not altered by the presence of CO4a suggesting CO4a was emplaced later on top of CO4. B) Change in elevation along profile highlighted in A. The abrupt change in height highlights the presence of CO4a and provides further evidence for it being a separate flow.

It is inferred that the Biftu Tuff Cone, a rhyolitic tuff cone outside the caldera walls, formed after the emplacement of CO4a (Figure 2.2). The formation and collapse of this cone resulted in the emplacement of a large, ash-rich pyroclastic density current (Clarke, 2020). Outcrops of these currents have been recorded on the eastern shore of Lake Hawassa by Clarke (2020) and in drainage gullies on the north-western shore in this study (Figure 2.2H). The outcrops are dominated by a dilute, ash-rich PDC (Figures 2.3.6A-F), which displays highly variable lithofacies along the length of the drainage gully with complex mm-scale sedimentary structures (Figures 2.3.6B, C & E) to large meter scale bedforms (Figure 2.3.6F). The deposit is dominated by ash, however, some coarse pumice-rich lenses are seen in large chute and pool bedforms. These pumice clasts typically range from ~1 mm to 25 mm and are highly rounded. Clasts of fine-grain ash are also incorporated into the deposit. The base of the PDC contains reworked/remobilised shells of Melanoides tuberculata as well as other gastropods and bivalves, indicating a degree of interaction with lake sediment during eruption and deposition. ^{14}C Dating of two M. tuberculata shells collected from within the PDC deposit yielded ages of 7375 ± 54 cal BP (Site30A1) and 7131.5 ± 121.5 cal BP (Site30A2; Table 2.8). These dates and the negative δ^{13}C values and positive δ^{18}O values correspond well with measurements of organic matter from Lake Hawassa of similar ages (Lamb et al., 2002). M. tuberculata have been shown to be in equilibrium with lake water from Hawassa (Leng et al., 1999) and therefore a good proxy for climate. The elevated δ^{18}O values and low δ^{13}C values indicate the shells were deposited during the wetter period in the rift and when the height of the lake was elevated, before the transition to a more arid environment occurred around ~5130 cal BP (Lamb et al., 2002).

Table 2.7: Radiocarbon dating and stable isotope results for shells sampled from the Biftu Tuff Cone PDC (Site30A) and overlying pumice deposit (Site 12C). Field sites are marked in Figure 2.2. Samples were analysed at Beta Analytic and calibrated using BetaCal4.20: HPD method: INTCAL20 (Reimer et al., 2020).

Sample	**Material**	**Conventional Age**	**Calendar Calibration (cal BP)**		**Probability %**	**Stable Isotope**	
		±30 BP	**Max**	**Min**		δ^{13}C (± 0.3 ‰ relative to VPDB)	δ^{18}O (± 0.3 ‰ relative to VSMOW)
Site12C1	Shell	6910	7794 7829	7673 7813	91.4 4	-1.4	3.15
Site12C2	Shell	6810	7685	7585	95.4	-2.7	3.12
Site30A1	Shell	6470	7429	7321	95.4	-3.1	3.97
Site30A2	Shell	6230	7130 7253 7176	7010 7193 7151	52.5 30.1 12.8	-3.5	3.61

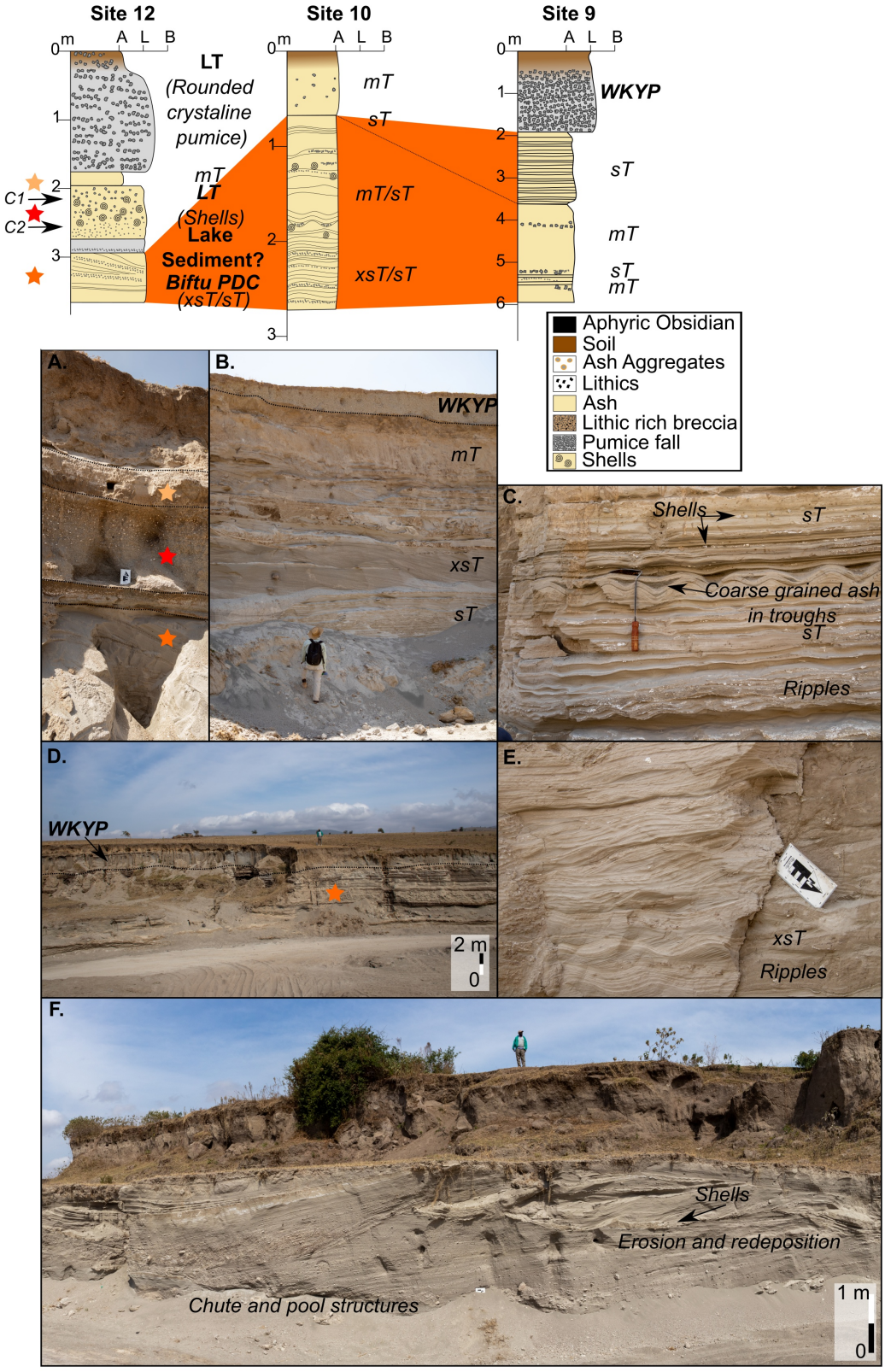

(Caption on next page.)

Figure 2.13: Stratigraphic log and field photos of outcrops in a drainage gully near the shores of Lake Hawassa. Field sites are marked in Figure2.2H) Outcrop at Site 12 showing the upper portion of a dilute PDC with a shell-bearing horizon and lapilli tuff B) Outcrop at Site 31 (Figure 2.2H) showing the complex and varied structures within the dilute PDC associated with the Biftu Tuff Cone C) Wave ripples and stratification observed at Site 10. Shells incorporated into deposit. D) Overview of Site 9 showing PDC succession caped with the WKYP. E) Complex cross stratification and ripples at Site 10. F) overview of Site 11 showing chute and pool structures and incorporation of shells into PDC.

The succession above the PDC deposit is highly variable throughout the gully due to the partial collapse of the walls obscuring outcrops. At Site 12 (Figure 2.2, the PDC is overlain by thin horizons of ashy sediment, likely lake sediment, which is subsequently overlain by a coarse-grained pumice horizon containing abundant shells and rounded pumice clasts (Figure 2.3.6A). Two shells from this unit were ^{14}C dated and yielded ages of 7751 ± 78 cal BP (Site 12C1) and 7779 ± 50 cal BP (Site 12C2; Table 2.8). These ages are significantly older than those determined for shells from the underlying PDC deposit. The stratigraphic sequence observed within the gullies (Figure 2.3.6A) clearly shows the shells from Site12C overlying the Biftu Tuff PDC. The 'upside down' age sequence is likely the result of reworking and is discussed further in Section 2.5.2.1. The sequence is capped by a pumice fall deposit (Figure 2.3.6B & D) however it is not visible at all locations along the gully. It has been correlated with the WKYP unit based on its stratigraphic position, lithofacies (mL) and the absence of obsidian lithics, a key characteristic of the deposit (Fontijn et al., 2018).

Following the emplacement of the WKYP, activity on Chabbi centred on the western flanks. One area of uncertainty is the timing and origin of the pyroclastic deposits on the western flanks of Chabbi (Figure 2.3.6I). These deposits are partially buried by CO5, which makes up the majority of the western flanks. CO5 overlies the WKYP deposit indicating it erupted < 2301 ± 120 cal BP (Rapprich et al., 2016). At the flow front of CO5, examples of ~1-2 m thick ~9 m long lenses of welded material are seen (SI A.4). This pale, fine-grained material is seen to be intermingled with the obsidian glass at the edge of the lens (SI A.4C). Some of the internal structure of the flow is also exposed in portions of the flow front, showing folding of the obsidian glass SI A.4B). Investigation of the surface morphology of CO5 has revealed the presence of distinct units which have previously been attributed to CO5. Two lavas overlie CO5 and are associated with two vents identified by Hunt et al. (2019), which we call CO5a and CO5b (Figure 2.11K). The most recent flow on Chabbi, CO6, covers the southern flank. It is sourced from a single vent with multiple

lobes overriding earlier portions of the flows. Observed outcrops of the CO6 lava show it to be glassy, crystal-free obsidian. An outcrop at Site 58 (Figure 2.2C) shows a pale lens of welded material similar to that observed in CO5 (SI A.4D).

2.4 Geochemistry

2.4.1 Major Element Geochemistry

Figure 2.14A summarises the compositions of rock samples on a total alkali-silica diagram. The legend in the geochemical plots remains consistent throughout unless otherwise stated, and the sample locations are highlighted in field photos and stratigraphic logs. The major element data shows very little variation in composition between erupted magmas, supporting previous observations (Fontijn et al., 2018; Martin-Jones et al., 2017). Most samples are rhyolitic with sparse trachyte samples.

All but two samples have a peralkalinity index (Shand, 1927, Pl = molar Na_2O + K_2O/Al_2O_3;) between 1 and 1.5. These samples can be further divided into pantellerites and comendites based upon the relative concentration of Total Iron and Al_2O_3 (Macdonald, 1974, Figure 2.14B;). Peralkaline samples from Corbetti span the comendite-pantellerite boundary with samples from pre- and post-caldera activity recording both compositions. Whole rock and glass compositions of Corbetti samples from Rapprich et al. (2016) and Fontijn et al. (2018), respectively, are also presented for comparison in these figures.

2.4.2 Trace Element Geochemistry

Figure 2.15 shows selected incompatible trace elements plotted against Zr, which is used as a proxy for fractional crystallisation because it behaves incompatibly across our sample set (Hutchison et al., 2018). The lack of mafic and intermediate compositions means the majority of the sample set reflects late-stage crystallisation characterised by depletion in Sr and Ba due to the crystallisation of alkali feldspars. Incompatible-incompatible element diagrams (Y, La, and Rb against Zr) show a clear positive trend, consistent with fractional crystallisation. The trends seen within these data are consistent with previous studies that found peralkaline magmas undergo >90% fractional crystallisation to reach these compositions (Gleeson et al., 2017; Macdonald et al., 2012; Peccerillo et al., 2007;

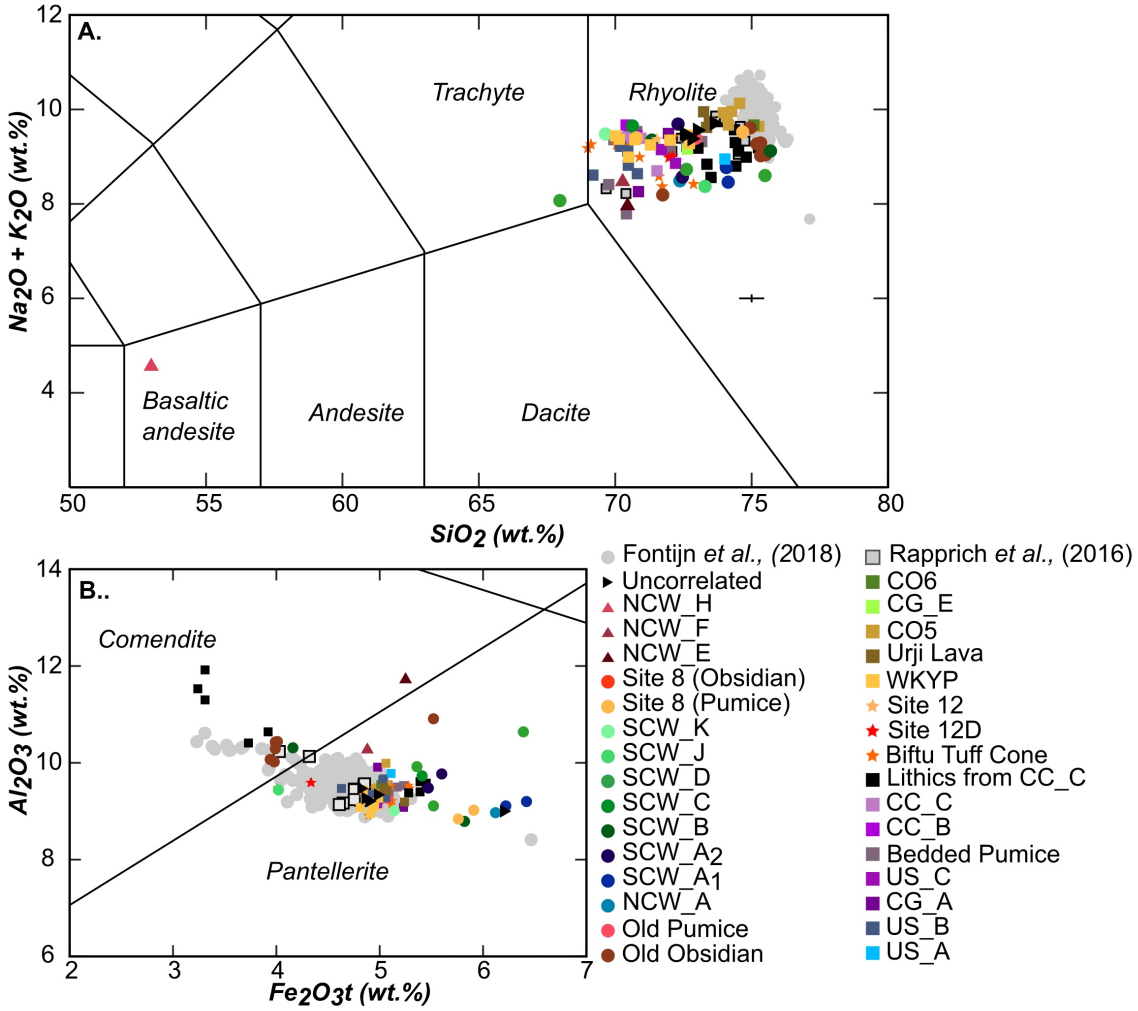

Figure 2.14: A) Total alkali silica diagram highlighting the limited variation in erupted compositions from Corbetti. Samples were grouped based upon correlations outlined in previous sections. Error bar is calculated from the 2*RSD% of standard. Samples from Rapprich et al. (2016) and glass compositions from Fontijn et al. (2018) are shown for comparison. B) Peralkaline classification distinguishing between comendite and pantellerite composition using the divide proposed by Macdonald (1974). Errors smaller than symbols.

White et al., 2009). Lithics from a PDC within the central caldera (CC_C) record higher Ba concentrations reflecting a limited amount of alkali-feldspar has been crystallised within the melt or a higher proportion of Alkali-feldspar within the sample. The lower Zr concentrations indicate that these samples likely record a point near, or just after, the onset of alkali-feldspar fractionation. The decrease in Ba is associated with the fractionation and removal of alkali-feldspar. This is mirrored in the Sr concentrations of the samples which show the characteristic signature of alkali-feldspar fractionation which is observed at other MER silicic centres (Hutchison et al., 2018). In addition there is some scatter in the whole rock Sr concentrations reported for Corbetti's samples (Figure 2.15). Decreasing Sr with Zr is associated with the fractionation of alkali-feldspar. Figure Appendix A.5 shows some variation in Zr, La, Y and Rb, concentrations between pre-and post-caldera eruptions. Incompatible element concentration in pre-caldera deposits appear to decrease with stratigraphic height potentially suggesting eruptions are tapping a less evolved magma source. This is not recorded within major element data which could suggest some degree of mixing and homogenisation has occurred. Post-caldera eruptions show a very similar range of incompatible trace element concentrations which may indicate a similar source composition and limited mixing with less evolved melts. These data also demonstrate that distinguishing between units based upon their geochemical composition is challenging (Appendix A.5).

2.5 Discussion: Eruptive History of Corbetti Caldera

By integrating our new field observations with previous authors' findings, we develop a composite stratigraphy of Corbetti caldera. Figure 2.5 outlines this compiled composite stratigraphy and includes units of uncertain stratigraphic placement. Our findings support previous observations that activity at Corbetti has ranged from eruptions generating extensive rhyolitic and obsidian lavas to the generation of multiple ash-rich pyroclastic density currents and Plinian-style fall deposits. We also find evidence for previously undocumented eruptions which suggest Corbetti has undergone multiple phases of large-scale explosive activity which may have resulted in the partial or full collapse of edifices within the complex. Whole-rock geochemical analysis (Figures 2.14 & 2.15) shows Corbetti consistently erupts peralkaline rhyolites. Whilst some variation in geochemistry is observed, it occurs over a narrow compositional range (Appendix A.5) and lacks the chemical diversity seen at other MER calderas (Rooney et al., 2012; Ronga et al., 2009; Fontijn et al., 2018; Iddon et al., 2019; Tadesse et al., 2019).

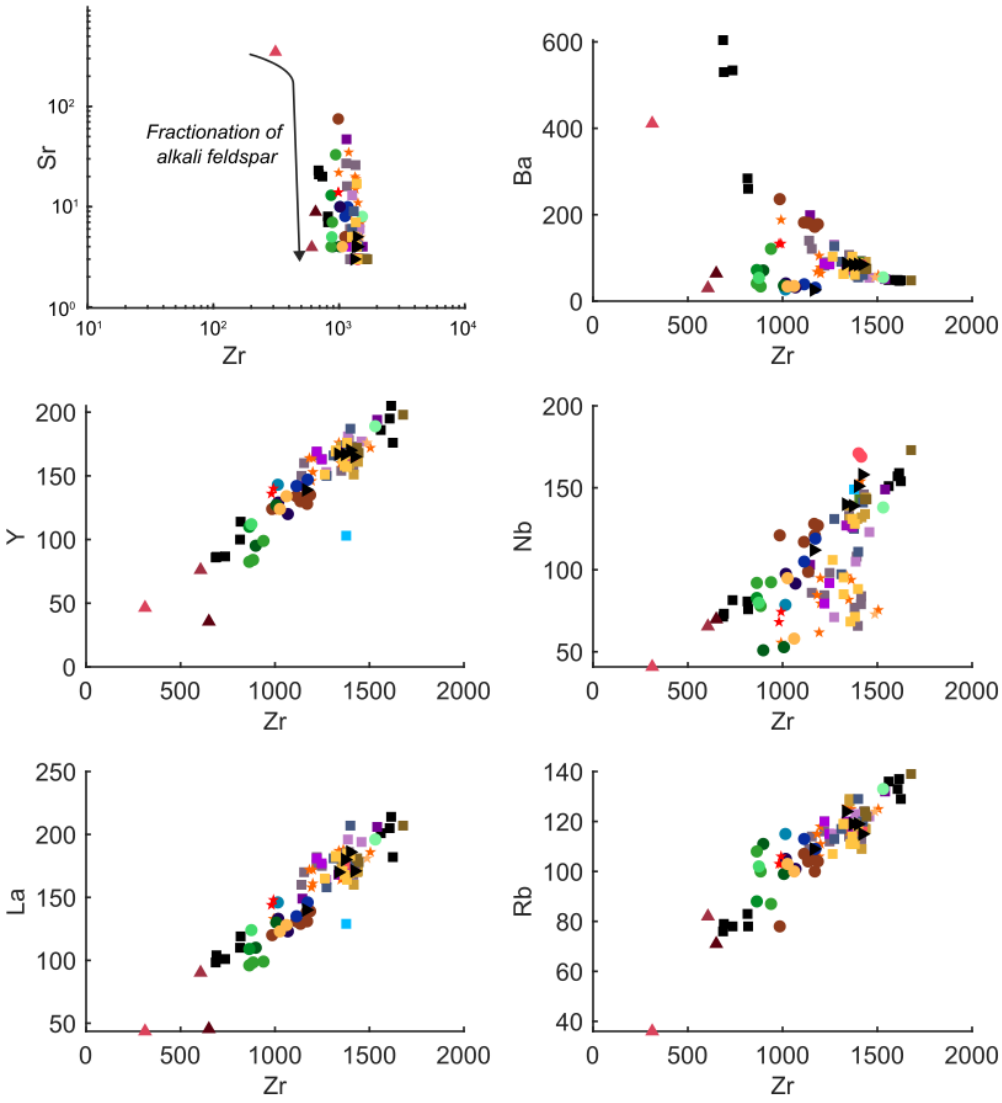

Figure 2.15: Trace element plots for samples analysed in this study. Legend is the same as Figure 2.14. Incompatible-incompatible (Y, Nb, La, Rb vs Zr) plots show a clear fractional crystallisation trend. Error bars smaller than symbols.

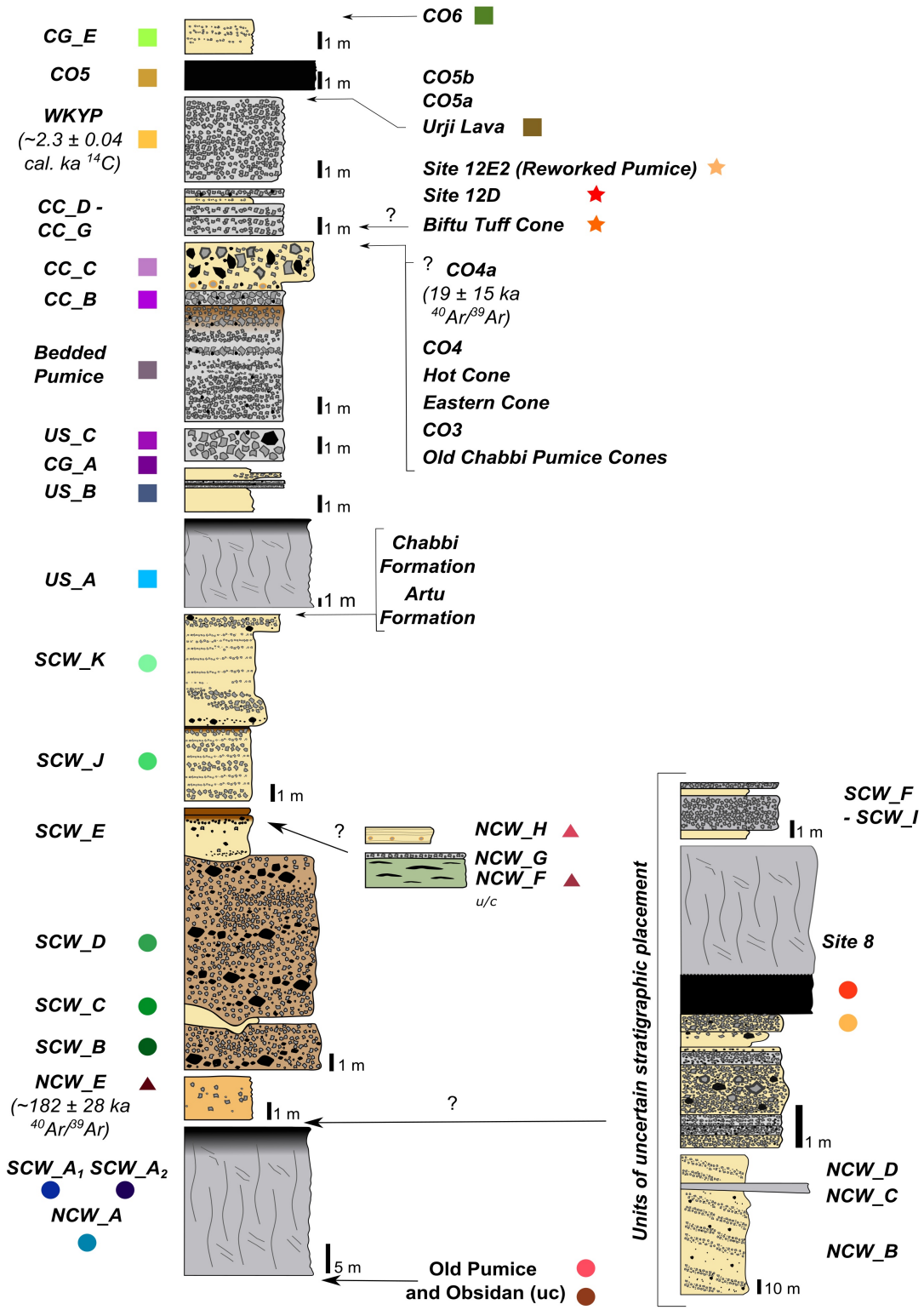

(Caption on next page.)

Figure 2.16: Composite stratigraphy of Corbetti Caldera Ethiopia showing the inferred relative chronology and incorporating the dates and relative chronologies from Rapprich et al. (2016); Hutchison et al. (2016b); Fontijn et al. (2018); Clarke (2020). Units of uncertain correlation are shown with an approximation of their relative position. Symbols denote the samples in Figure 2.14.

2.5.1 Early Phases of Activity

Early activity at Corbetti was characterised by the eruption of multiple rhyolite lavas, which are found both in the southern caldera wall (SCW_A1 & SCW_A2; Figure 2.5 & 2.6) and the northern caldera wall (NCW_A; Figure 2.3A). The eruption of these lavas resulted in the development of a low relief shield, which is typical of early evolution at other MER calderas (Hutchison et al., 2016c). The initial lavas likely erupted from distinct vents across several edifices instead of erupting from a single central edifice. We find evidence of spatially unique outcrops within the caldera wall, which have different lithofacies to surrounding areas. For instance, we infer that the outcrop at Site 8 (Figure 2.2C & SI A.3) records the deposits from a now eroded vent. The pyroclastic succession records the main phase of activity which generated PDCs and ejected obsidian ballistics before a transition to a spatter-like eruption of obsidian and rhyolite. The highly localised nature of this outcrop suggests it may originate from a proximal vent. It is common for large shield volcanoes to be polygenetic, especially in highly evolved systems (i.e., Pantelleria, Socorro), and frequently erupt pyroclastic cones (Grosse and Kervyn, 2018; Webb and Weaver, 1975). We suggest that whilst a central vent may have been present at Corbetti, eruptions occurred at multiple smaller vents across the pre-caldera shield, resulting in the highly localised deposits seen within the caldera wall today (i.e., Site 8). These vents' locations were likely influenced by pre-existing faults related to the initial stages of rifting (Lloyd et al., 2018a).

Following an early shield building phase, many silicic centres within the MER underwent caldera-forming eruptions (Hutchison et al., 2016b,c; Rampey et al., 2010). Recent work has highlighted the short timescales (decades to centuries) necessary to accumulate large magma bodies capable of feeding caldera-forming eruptions (Costa et al., 2020; Jackson et al., 2018). Within the MER, four caldera-forming eruptions (Aluto, Gedemsa, Shala Caldera and Corbetti) occurred in close temporal succession during the late Pleistocene. Hutchison et al. (2016b) linked these eruptions to an increased melt flux from a mantle-derived plume. This increased melt flux may have resulted in the remobilisation of parts of mid-crustal, highly evolved crystalline mush allowing a sizeable magma body to accumulate

at shallow depths. The proposed small timescales over which this accumulation is possible would explain why four volcanoes underwent caldera-forming eruptions over a geologically short time. However, it is a common feature of the large silicic complexes within the MER to undergo this cycle of shield building followed by caldera collapse, and there are several examples of caldera-forming eruptions that have not been directly linked to an increase in mantle activity (i.e. Tullu Moye, Kone and Melkassa; Fontijn et al. 2018).

Corbetti is a fault-controlled caldera whereby the shape of the caldera links to the reactivation of pre-existing structures within the crust (Hunt et al., 2019; Maestrelli et al., 2022; Robertson et al., 2016). Whilst Corbetti has the morphology of a caldera, the eruption associated with caldera collapse is enigmatic. Previous studies have highlighted the presence of a welded ignimbrite outcropping above the jointed rhyolite lavas (Altaye, 1984) in the western caldera walls. This unit is interpreted as the deposits from a caldera-forming eruption and dates to ~182 ± 28 ka (Hutchison et al., 2016b; Vidal et al., 2022b). Peralkaline complexes commonly produce welded PDC deposits, also from both smaller and larger eruptions, therefore, the presence of welded ignimbrites alone is not indicative of a caldera-forming eruption (Jordan et al., 2018; Mahood, 1984).

Here we find evidence of several deposits recording the deposition of welded (NCW_F) and non-welded (NCW_E) ignimbrites as well as lithic lag breccias (SCW_B & SCW_D) (Figure 2.5). Determining the relative timing of these units in relation to the caldera-forming eruption is critical, as it may demonstrate a more complex caldera formation process than previously thought. However, due to a lack of suitable crystal phases, dating these units was not possible.

As outlined in Section 2.3.1, a red ignimbrite (NCW_E) outcrops within the North caldera wall and extends some 15 km to the east. It is the most widespread ignimbrite sheet observed at Corbetti and is likely associated with a large-scale eruption. This unit is overlain by a green welded ignimbrite containing obsidian fiamme (Figure 2.3C-D). In addition, within the southern caldera wall, two lithic lag breccias are interbedded with thin dilute PDCs (Section 2.3.2; Figure 2.6). These breccias are of particular interest as they are previously undocumented and exclusively outcrop at a single location (Site 6; Figure 2.2C). Lithic lag breccias are often associated with large-scale collapse events and are commonly found within large caldera complexes (e.g., Druitt 1985; Simmons et al. 2016; Jordan et al. 2018). They are often proximal to vents, contain compositionally diverse clasts and exhibit limited structures. The breccias observed at Corbetti match these criteria (Table 2.3). The

key questions are whether any/all of the ignimbrite and lithic breccia deposits are linked to a/the caldera-forming eruption or record separate events/ phases of activity.

These units are either seen to, or inferred to, outcrop above the rhyolitic lavas. The lithic lag breccias in the southern caldera (SCW_B & SCW_D; Figure 2.6) wall contain an abundance of red ignimbrite fragments, similar to the red ignimbrite (NCW_E) seen in the northern caldera wall. No clasts of the green welded ignimbrite (NCW_F) are found within the deposit. This suggests two possible scenarios: (1) the breccias were emplaced before the red ignimbrite in the North Caldera Wall, remobilising a distinct ignimbrite horizon along with other lavas. (2) Breccias were emplaced during /after the eruption of the red ignimbrite sheet (NCW_E) but before the green welded ignimbrite (NCW_F) was emplaced. The absence of clear evidence indicating a second red ignimbrite within the caldera suggests the second scenario is more likely. Similarly, the absence of ignimbrites in the rest of the southern caldera and portions of the northern caldera wall may reflect a highly directional eruption, with most of the eruptive products travelling towards the east and subsequently being buried by Chabbi or eroded by later PDCs.

Based upon this evidence, we propose that the red ignimbrite (NCW_E) was emplaced by a large scale PDC which preferentially deposited to the north and northeast based upon observed exposures (see Section 2.3.1). This was followed by activity relating to the collapse of the edifice, which generated a large, granular PDC and remobilised significant portions of the previously deposited red ignimbrite. This PDC was strongly topographically controlled, depositing locally in a paleovalley in the modern-day southern caldera wall. Subsequently, a dilute PDC (SCW_C; Figure 2.4B) was generated scouring out portions of the lithic breccia before a second, large-scale, granular PDC (SCW_D) was emplaced in the same paleovalley. This second current may be linked to the collapse of the edifice. The emplacement of the green welded ignimbrite (NCW_F; Figure 2.3C & 2.4A) occurred after the deposition of the lithic lag breccias however it is uncertain if this occurred during the same phase of activity or was a distinct event. This may indicate that Corbetti has experienced a number of caldera-forming or ignimbrite forming eruptions or underwent a piecemeal collapse with numerous eruptions resulting in the present day caldera. It is difficult to fully evaluate this hypothesis in the absence of date-able material and further exposure of these units within the caldera.

We find numerous examples of fine-grained, ash-rich PDC deposits (e.g., SCW_J, SCW_K, NCW_H; Figures 2.3E-G, 2.6). Due to limited exposures of these deposits, there is some uncertainty surrounding their relative timing (highlighted in Figure 2.5). However,

these deposits highlight the propensity for eruptions at Corbetti to continually produce large-scale, dilute PDCs which has significant implications for understanding the future hazard posed by its eruptions.

2.5.2 Post-caldera activity

Post-caldera activity at Corbetti has centred around three main edifices, Artu, Urji and Chabbi. Artu is the oldest observable post-caldera edifice and is situated close to the northern caldera wall (Figure 2.2A). Little is known about its eruptive history as deposits have either been heavily eroded or buried by subsequent volcanism; however it is likely to have experienced pumice cone forming eruptions and associated eruption of lavas as is typical within the MER (Clarke, 2020; Clarke et al., 2019; Hutchison et al., 2016c). Activity then focused around the two major edifices seen within the caldera today, Urji and Chabbi (Figure 2.2A). These edifices formed through eruptions from numerous vents, which are strongly controlled by the W-E trending faults (Hunt et al., 2019; Lloyd et al., 2018b). The formation of multiple new vents within a caldera is commonly observed at other MER volcanoes (Hunt et al., 2019; Hutchison et al., 2016c, e.g., Aluto;), however, they tend to form on the edges of the caldera scarp likely controlled by the presence of ring faults and structural weaknesses caused by caldera collapse (Hunt et al., 2019). The fact that Urji has formed centrally within the caldera, and the vents on both Urji and Chabbi strongly align to the W-E trending faults highlights the first-order control these pre-existing structures have on the locus of volcanism at Corbetti. This observation is especially significant when considering the location of any future volcanism at Corbetti.

The relative timing of the formation of Urji and Chabbi remains unclear, however evidence from the flanks of Urji demonstrates activity likely started with a shield-building phase with the eruption of multiple rhyolite lava flows (e.g., US_A; Figure 2.10) before a transition to pumice cone eruptions, which have dominated Urji's recent eruptive history. The early activity at Chabbi is unclear; however, the oldest observed are heavily eroded pumice cones on the north and northeast flanks (Figure 2.11B-D). Buried lava and pyroclastic fans are also seen on the south-eastern flanks (Figure 2.11E, 2.12). This activity style contrasts with recent eruptions, in which the emplacement of large obsidian lavas has dominated. The reasons for this transition from pumice cone eruptions to the eruption of extensive obsidian lavas require further investigation. Previous work has identified four major obsidian lavas (CO3, CO4, CO5, CO6) however, as presented in Section 2.3.6, we have delimited a further three lavas on the flanks of Chabbi (CO4a, CO5a and CO5b; Figure

2.12). It is challenging to constrain whether these additional lavas are related to the eruptions that deposited the previously identified lavas or from different events. Evidence from the rest of the caldera suggests it is uncommon for a post-caldera eruption to form multiple vents, such as during basaltic fissure eruptions. Identification of these lavas indicates that Chabbi has been more active than previously thought.

As outlined in Section 2.3.6, we demonstrate that the obsidian deposit CO4 comprises two distinct lavas (CO4 and CO4a Figure 2.12) which erupted from different vents. Here we infer a pumice cone eruption formed the Eastern Cone, followed by the eruption of the Hot Cone and emplacement of CO4. The vent from which CO4a erupted (Figure 2.12 is offset from the central point of the eastern cone. We suggest a secondary vent opened on the northern flank of the eastern cone from which CO4a erupted. This supports previous findings which indicate vents are more likely to open in close proximity to the two pre-existing faults within the caldera and are more likely to form close to previous vents (Clarke, 2020; Hunt et al., 2019). This can have the effect of obscuring deposits or giving the appearance of a single vent and should be considered when assessing the source of eruptions. In addition, this is significant for assessing the probabilistic and spatial risk of new vents opening on the flanks of Chabbi.

In contrast to Chabbi, explosive eruptions generating widespread pumice fall deposits (e.g., Bedded Pumice and WKYP) and localised dilute PDCs (e.g., CC_D; See Section 2.3.3) dominate on Urji. Some of the earliest activity recorded on Urji is the deposition of several ash-rich PDC units, some of which (US_B; Figure 2.10) have previously been attributed to phreatomagmatic activity (Rapprich et al., 2016). Previous work has suggested the presence of a lake within part of the caldera, likely during a high stand period of Lake Hawassa (Altaye, 1984; Lamb et al., 2002). Whilst the location of this lake is uncertain, the widespread occurrence of ash-rich PDCs may indicate a phreatomagmatic components; however further work is needed to identify more evidence of phreatomagmatic activity. One important observation is the scarcity of these PDCs at distal locations outside the caldera walls indicating flows are unlikely to have large run out distances however, future similar PDC-generating eruptions could pose a significant risk to the local population living within the caldera. The population within the caldera is estimated to be over 14,000 people based on the number of homes observed in satellite images (2,836) and a rural occupancy rate of 5 (Ethiopian Public Health Institue (EPHI), 2021); however, anecdotal evidence suggests the population is far greater than this estimate. Further work is required to fully delimit the risk posed by PDCs within the caldera (Clarke, 2020).

The Wendo Koshe Cone, as identified by Rapprich et al. (2016), is the youngest cone on the flanks of Urji and has previously been attributed as the source for the WKYP eruption. However, we find evidence which challenges this hypothesis. Throughout the central caldera, exposures of the Bedded Pumice unit (Section 2.3.3 & 2.3.4) show the classic architecture of a pumice cone eruption (SI A.6). Close to the vent, beds are coarse-grained and chaotically bedded. At proximal locations, interbedded pumice fall and dilute to granular PDC deposits dominate, whilst distal deposits are massive pumice fall horizons (Clarke, 2020). The sequence in the central caldera consistently shows the Bedded Pumice horizon overlain by a paleosol and capped with a coarse-grained, obsidian bearing pumice (CC_B). This succession is so frequently observed we can confidently correlate it across multiple locations, including in exposures on the flanks of the Wendo Koshe Cone (Figures 2.8 & 2.10). The occurrence of the Bedded Pumice unit on the flanks of the Wendo Koshe Cone, in conjunction with the fact it has the classic architecture of a pumice cone eruption, strongly suggests that the Bedded Pumice unit was emplaced during the formation of the Wendo Koshe Cone. The eruption followed the typical sequence of pumice cone forming eruptions as set out by Clarke (2020), with an initial phase emplacing large blocks at proximal locations before establishing a highly unsteady plume that underwent periodic collapse, generating numerous dilute PDCs (SI A.6). The deposition of massive pumice fall horizons at distal locations indicates the plume was established for a period, but localised PDCs may have continued. The eruption may have concluded with the emplacement of a now buried lava, as is characteristic of pumice cone eruptions; however, this was not observed in the field or remote sensing imagery and is possibly buried by subsequent deposits.

One feature of the Wendo Koshe Cone is the absence of the WKYP on its flanks, despite deposits being seen at proximal locations (Figure 2.10). The WKYP lacks the characteristics of a pumice cone eruption, and there is little evidence of the passage of PDCs indicating the plume was stable and sustained, depositing tephra over a large area (Fontijn et al., 2018; Rapprich et al., 2016). An outflow sheet on the northern flank of the Wendo Koshe Cone (Figure 2.2F) has previously been attributed to the WKYP eruption (Rapprich et al., 2016) and appears to outcrop above the WKYP deposits. This raises two possible scenarios; (1) both the Bedded Pumice and the WKYP erupted from the same vent after a period of quiescence, (2) the Wendo Koshe Cone represents the remains of two cones, the first erupting the Bedded Pumice unit and the second forming in very close proximity first, erupting the WKYP and undergoing a flank collapse. Since pumice cones in the MER are thought to be monogenetic (Clarke, 2020; Clarke et al., 2019) and we see evidence of vents

in close proximity to one another (e.g., Eruption of CO4a from a vent near the Eastern Cone; Figure 2.12), we consider the second scenario to be the more likely. Whilst there is uncertainty surrounding this scenario, it does explain the nature of the observed deposits and highlights the discrete areas within the caldera where they have formed. It should be noted that further work is needed to fully understand the dynamics of pumice cone forming eruptions and whether they are in fact monogenetic.

Following the deposition of the WKYP, two other (smaller-scale) explosive eruptions occurred (CC_H & CG_E; Figure 2.5); however, the origin of these eruptions have not been determined due to spatially inconsistent outcrops. They may be related to the more recent eruptions on Chabbi (CO5, CO5a, CO5b and CO6; Figure 2.11) as they are only seen proximally to Chabbis edifice. Further work investigating the nature of these eruptions is required.

2.5.2.1 Biftu Tuff Cone

The Biftu Tuff Cone is one of the few vents not associated with the two main edifices, Urji and Chabbi. Its location outside the caldera wall (Figure 2.2A) and away from the identified pre-existing faults makes it an apparently unique event at Corbetti. Investigation of the NW shore of Lake Hawassa revealed the presence of large, fully-dilute PDC deposits (see Section 2.3.6), which are inferred to relate to the formation and collapse of the Biftu Tuff Cone. These deposits contain abundant reworked shells and display complex and varied sedimentary structures. Based on ^{14}C dating of M. tuberculata shells within an associated dilute PDC deposit on the Northwest shore of Lake Hawassa, the timing of the eruption can be broadly constrained to < 7375 ± 54 cal BP (Table 2.8). Previous studies have hypothesised a phreatomagmatic origin of the eruption resulting from the interaction with lake water during a relative high stand of Lake Hawassa (Clarke, 2020; Rapprich et al., 2016). M. tuberculata shells record negative δ^{13}C values (-1.4-3.5 ‰) and positive δ^{18}O values (3.12-3.97 ‰) suggesting a wet climate (Leng et al., 1999; Lamb et al., 2002). Dating and stable isotope analysis of organic matter from Lake Hawassa show similar isotopic values (negative δ^{13}C and positive δ^{18}O values) around 7375 cal BP (Lamb et al., 2002). M. tuberculata shells are known to be a good proxy for climatic conditions in Lake Hawassa (Leng et al., 1999), therefore this provides good evidence that around the time of the Biftu Tuff Cone eruption, Lake Hawassa was likely at a high-stand. In addition, studies on the nearby Ziway-Shalla basin have found evidence for multiple phases of shoreline retreat and advance during the late Pleistocene and early Holocene (Benvenuti et al., 2002;

Gillespie et al., 1983; Olaka et al., 2010) reflecting changes in climate. Similarly, evidence from M. tuberculata shells from the Ziway-Shalla basin suggests higher precipitation levels in the rift during the early Holocene compared with today, which would contribute to rises in lake levels (Leng et al., 1999).

It is proposed that the eruption of the Biftu Tuff cone occurred at a time of high lake levels resulting in a phreatomagmatic eruption generating large quantities of ash and extensive, fully-dilute, PDCs. These PDCs likely travelled across the lake and subaqueously, incorporating lake sediment and shells as the flows travelled from the vent. Overlying the PDC at one locality (Site 12; Figure 2.3.6) is a thin sequence of lake sediment capped with a shell bearing horizon. The ages of these shells are older than those in the underlying deposit. This 'upside down' age sequence likely occurred due to the reworking of old deposits which were emplaced during a period of high stand at Lake Hawassa. This supports observations of the continued fluctuations in the lake's water level during the early Holocene.

2.5.3 Recurrence rate and Hazard Implications

This field investigation identified 5-6 explosive and effusive eruptions at Corbetti over the last 2301 ± 120 cal BP (Figure 2.5). Based on this, the recurrence rate over this period is approximately one eruption every 300-400 years, with four of these eruptions occurring on Chabbi. This evidence suggests volcanism is comparable with the approximated recurrence rate for Aluto (Fontijn et al., 2018; Hutchison et al., 2016c) and among the highest rates in the MER. These data, coupled with the active deformation occurring at the caldera, demonstrate the potential volcanic hazard Corbetti poses. A key question is understanding how any future volcanism will manifest itself at Corbetti. The contrasting styles of past volcanism across both Urji and Chabbi present two different hazards compared with the hazards posed by other MER volcanoes. Urji, like post-caldera vents at Aluto, shows a propensity to generate ash-rich PDCs which are likely to inundate densely populated areas within the caldera whilst the eruption of obsidian flows from Chabbi presents a more localised risk. This highlights the need for further hazard-based studies to fully constrain the ramifications of any future volcanism within the complex. This is especially important given the high population density and proposed development of a geothermal power plant within the caldera.

2.6 Conclusions

Here we have presented a detailed stratigraphy of activity at Corbetti over the course of its eruptive history, highlighting major explosive events and the range of volcanism experienced within the complex. Development of the edifice has been centred around eruptions from multiple vents emplacing large rhyolite lavas and pumice cones. We find previously undocumented evidence of lithic lag breccias and ignimbrites which may be associated with this eruption, recording the precursory and syn-phases of edifice collapse. However, questions are raised over the number and relative timing of caldera forming eruptions at Corbetti. It may be that Corbetti has undergone multiple phases of caldera collapse; however further investigation to evaluate this hypothesis is needed. The most recent activity at Corbetti centres around Urji and Chabbi, two low relief shields built up by eruptions from numerous vents. The styles of volcanism recorded at each edifice vary between the generation of multiple, highly localised PDCs and the eruption of obsidian lavas. Re-evaluation of the obsidian lavas on Chabbi has led to the identification of three additional units (CO4a, CO5a, CO5b), which were previously attributed to one of the larger deposits.

We propose that the most recent cone on Urji, the Wendo Koshe Cone, represents the remains of two cones, the first erupting the Bedded Pumice unit and the second erupting the WKYP. These are the two most well constrained post-caldera eruptions from Corbetti and are the most extensive deposits throughout the caldera. We find several locations on the post-caldera edifices that show vents opening close to older vents. We have constrained the age of the Biftu Tuff Cone eruption to $< 7375 \pm 54$ cal BP through ^{14}C dating of shells incorporated into an associated PDC deposit. Carbon and oxygen isotope data from these shells also indicate the eruption likely occurred during a high-stand period at Lake Hawassa, raising the possibility of the lake water interacting with the eruption, resulting in the generation of the large-scale dilute PDCs observed.

Based on the new observations of eruptive deposits, we have determined a recurrence rate of between 300-400 years, highlighting that Corbetti has been one of the most active volcanoes within the MER during the Late Holocene. Corbetti is also seen to have a propensity to generate dilute, highly localised PDCs. The frequency with which these deposits are seen within the caldera highlights that PDCs are a significant hazard for future eruptions. Therefore, we recommend further investigating the PDC-related hazards, especially considering plans to develop a geothermal powerplant within the caldera.

2.7 Acknowledgements

This work was supported by the Natural Environment Research Council via grant NE /L013932/1 (RiftVolc) and an Oxford DTP studentship (NE /L002612/1) to D.C. We would like to thank Seid Abubaker of Ethioder and guide Hamiyou Bekera for their support in the field and for ensuring a safe and productive field trip. Fieldwork and sample export was kindly permitted by the authroities of the Oromia region and Ministry of Mines and Petroleum of Ethiopia, respectively. We would also like to thank Owen Green for his help with sample preparation and Activation Laboratories and Beta Analytic for conducting the geochemical analysis and carbon dating respectively. We thank Vladislav Rapprich and Stéphane Scaillet for their reviews which have helped to improve this paper.

Chapter 3

Magma storage conditions beneath a peralkaline caldera in the Main Ethiopian Rift

David J Colby[a], David M Pyle[a], Karen Fontijn[b], Tamsin A Mather[a], Abate A Melaku[c]., Million A Mengesha[d]., Gezahegn Yirgu[d]

[a] *Department of Earth Science, University of Oxford, United Kingdom*

[b] *Laboratoire G-Time, Department of Geosciences, Environment, and Society, Université libre de Bruxelles, Belgium*

[c] *School of Earth and Environmental Sciences, University of St. Andrews, United Kingdom*

[d] *School of Earth Sciences, Addis Ababa University, Ethiopia*

This work has been submitted to the Journal of Volcanology and Geothermal Research and is currently in review

Abstract

The numerous volcanic centres in the Main Ethiopia Rift (MER) present significant but poorly understood hazards to local populations. It is also an important site to gain insights into tectonic processes as it captures the transition from continental rifting (to the south) to incipient seafloor spreading (to the north). Peralkaline magmas account for around 90% of the volcanic products found in the MER. Determining the conditions under which these magmas evolve is critical to understanding rift-related volcanism and its associated hazards. Corbetti caldera has an extensive record of large-scale, predominantly aphyric, peralkaline rhyolite eruptions. However, little is known about the mafic magmas from which these highly evolved melts have developed. Here we present data from the only basaltic deposit found within the caldera, coupled with whole rock, glass and mineral analysis of the peralkaline products, to investigate magma storage conditions at Corbetti. We demonstrate that magma mixing played a role in the evolution of the basaltic magmas and use RhyoliteMELTS modelling to show Corbetti's peralkaline magmas likely evolved at pressures between 100 and 250 MPa, from a magma with an initial water content of 0.5 - 1 wt.%, at or below the QFM buffer. Mineral thermometry and hygrometry on the sparse crystal populations corroborate the RhyoliteMELTS modelling: indicating that the basaltic magma had 0.1-1.2 ± 0.32 wt.% H_2O, and the peralkaline magmas ~3-7.9 ± 0.75 wt.% H_2O. These results match the best fit runs from RhyoliteMELTS (~5 wt.% H_2O) and melt inclusion data for Corbetti and other peralkaline systems. These results add to our understanding of the storage conditions of peralkaline magmas within a continental rift setting and highlight the hydrous nature of Corbetti's magmas and the role that H_2O plays during explosive eruptions.

3.1 Introduction

Understanding the nature of magmatic systems and the processes governing magma evolution is critical when investigating the surface expression of volcanism and unpicking signals of unrest. This is particularly true for regions such as the Main Ethiopian Rift (MER), which has a high density of volcanic centres that have shown historical unrest and have erupted highly differentiated peralkaline magmas in the past (Biggs et al., 2021).

The MER is a key natural laboratory to study the evolution of peralkaline magmas due to its high density of peralkaline centres along a differentially mature rift (Ebinger, 2005). Studies investigating the nature of volcanism within the rift (Hutchison et al., 2016c; Rapprich et al., 2016; Martin-Jones et al., 2017; Fontijn et al., 2018; Tadesse et al., 2019, 2022; Colby et al., 2022) and the processes governing magma evolution in the MER (Gleeson et al., 2017; Hutchison et al., 2018; Iddon et al., 2019; Tadesse et al., 2019, 2023) have highlighted the bimodal nature of eruptive compositions and the dominance of peralkaline rhyolites (molar $(Na_2O + K_2O)/Al_2O_3 > 1$; Shand 1927). It is generally accepted that the peralkaline products of the MER are differentiated through progressive fractional crystallisation of an alkali basalt at shallow pressures and reducing conditions (Scaillet and MacDonald, 2003; Di Carlo et al., 2010; Gleeson et al., 2017); although, some centres show signatures of a minor amount of crustal contamination (Peccerillo et al., 2003; Giordano et al., 2014; Hutchison et al., 2018). The compositional hiatus between 52-64 wt.% SiO_2, known as the Daly gap, is observed throughout the MER (Peccerillo et al., 2003; Ronga et al., 2009; Rooney et al., 2012; Hutchison et al., 2016c; Gleeson et al., 2017; Tadesse et al., 2019). This compositional gap is a poorly understood feature of magma evolution within the MER. It has been attributed to various processes, including, high silica activity between 52-64 wt.% SiO_2, resulting in fast differentiation towards rhyolitic compositions (White et al., 2009; Iddon et al., 2019) and magma mixing (Ferla and Meli, 2006); however, further investigation is required to constrain the processes governing the absence of these compositions.

The peralkaline rhyolites of the MER range from comendites ($Fe/Al^* = 1.33 \times FeOT / (Al_2O_3\text{-}4.4) < 1$; White et al.2023) to pantellerites ($Fe/Al^* > 1$) and are erupted both explosively and effusively from large silicic centres, usually associated with calderas (Fontijn et al., 2018), which are distributed along the rift axis (Figure 3.1). Eruptive products of basaltic compositions are rarely found within large silicic calderas. Basalts are more generally found at off-edifice locations, and appear primarily controlled by rift-related structures

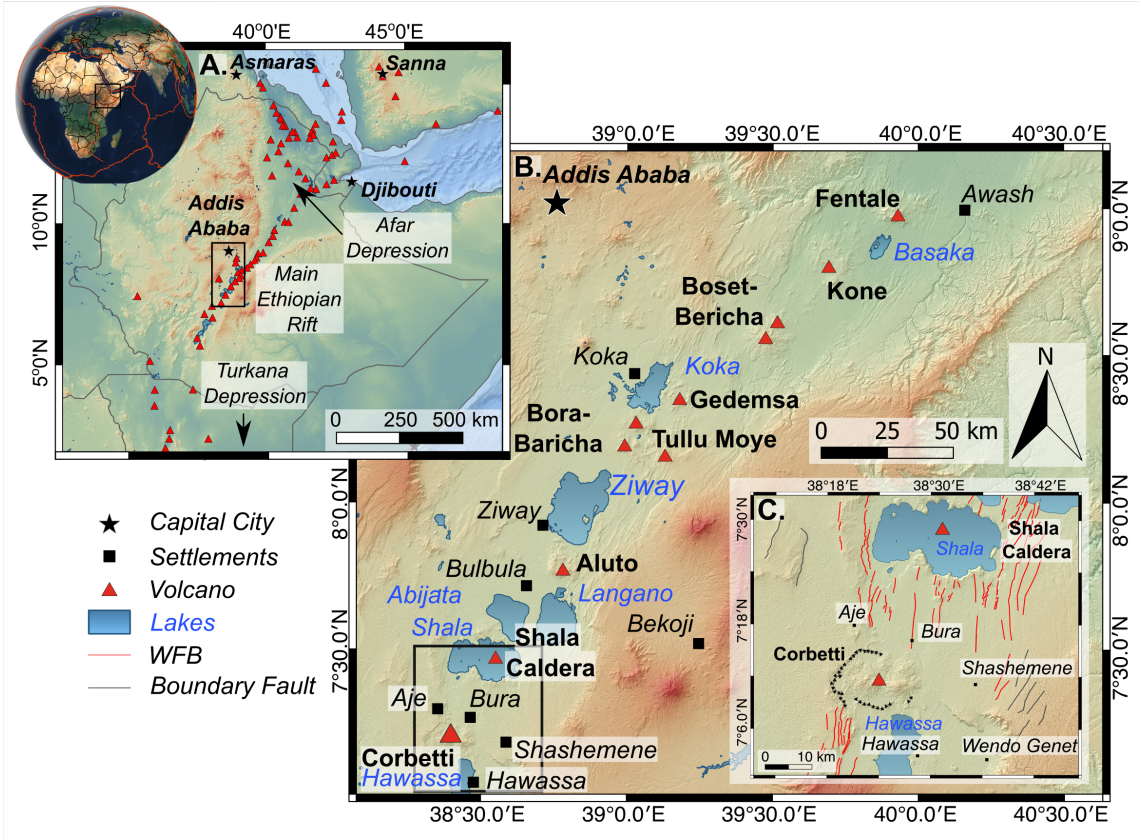

Figure 3.1: A) Regional map of the East African Rift, highlighting the area in B. B) Central and Southern section of the Main Ethiopian Rift, showing the location of Corbetti Caldera, and other major silicic centres. C) Overview map of Corbetti Caldera highlighting regional faults and the Wonji Fault Belt (WFB). Faults after Agostini et al. (2011)

.

such as the Wonji Fault belt (e.g., Wonji Basalts at Gedemsa (Peccerillo et al., 2003) and scoria cones found near Aluto Hutchison et al.2016c). Samples of basaltic composition have been reported from Aluto, Tullu Moye and Bora-Baricha calderas (Hutchison et al., 2016c; Tadesse et al., 2019, 2022).

3.1.1 Geological Setting of Corbetti Caldera

Here we investigate one restless caldera system, Corbetti caldera (Lloyd et al., 2018a,b), a large silicic centre in the southernmost part of MER erupting predominantly aphyric, peralkaline rhyolites. Corbetti has followed a similar evolutionary pattern to other silicic centres in the MER (Hutchison et al., 2016c), undergoing an initial shield-building phase, followed by at least one caldera-forming eruption, dated to ~182 ka and subsequent development of

post-caldera edifices (Hutchison et al., 2016b; Vidal et al., 2022a). Post-caldera volcanism has centred around three edifices: Artu, Urji and Chabbi. Artu is heavily eroded, with little known about its eruptive history. Urji and Chabbi have both erupted geochemically-similar peralkaline rhyolite magmas, with Urji dominated by pumice-cone-forming eruptions and Chabbi dominated by the eruption of large obsidian lava flows (Rapprich et al., 2016; Fontijn et al., 2018; Colby et al., 2022). Over the last 2.3 ka, Corbetti has experienced explosive and effusive eruptions, with a recurrence rate of around one eruption per 300-400 years (Fontijn et al., 2018; Colby et al., 2022). Geophysical observations show that Corbetti continues to display restless deformation signals. Steady uplift has been occurring at Corbetti between 2015-2020 at a rate of ~ 4.6 cm/yr^{-1} which has been interpreted as continual pressurization of a large magmatic reservoir (Albino and Biggs, 2021; Albino et al., 2022).

This study seeks to understand the magma storage conditions at Corbetti caldera in the MER. We investigate two endmember compositions, an alkali basaltic tuff and a welded peralkaline ignimbrite, to offer an insight into how Corbetti's magma likely evolved. We employ RhyoliteMELTS modelling and compare these results to petrological findings to test the validity of using RhyoliteMELTS on peralkaline systems. We also look in detail at the only recorded basaltic eruption at Corbetti and provide insights into the magmatic processes occurring before its eruption.

3.1.2 Overview of studied units

NCW_H is a basaltic, stratified ash-rich tuff found within the northern caldera wall (Site 4; Figure 3.2B and Figure 3.3.2.1C & D) deposited by dilute pyroclastic density currents (PDCs). Hereafter the unit is referred to as the 'basaltic tuff'. NCW_F underlies the basaltic tuff (Site 3; Figure 3.2B, 3.3.2.1C & B) and is a massive green eutaxitic lapilli tuff deposited by a PDC, hereafter referred to as the 'welded ignimbrite'. Colby et al. (2022) outlines detailed descriptions and interpretations of these units. These two endmember compositions form the basis for our petrological investigation and comparison with the results of our RhyoliteMELTS simulations.

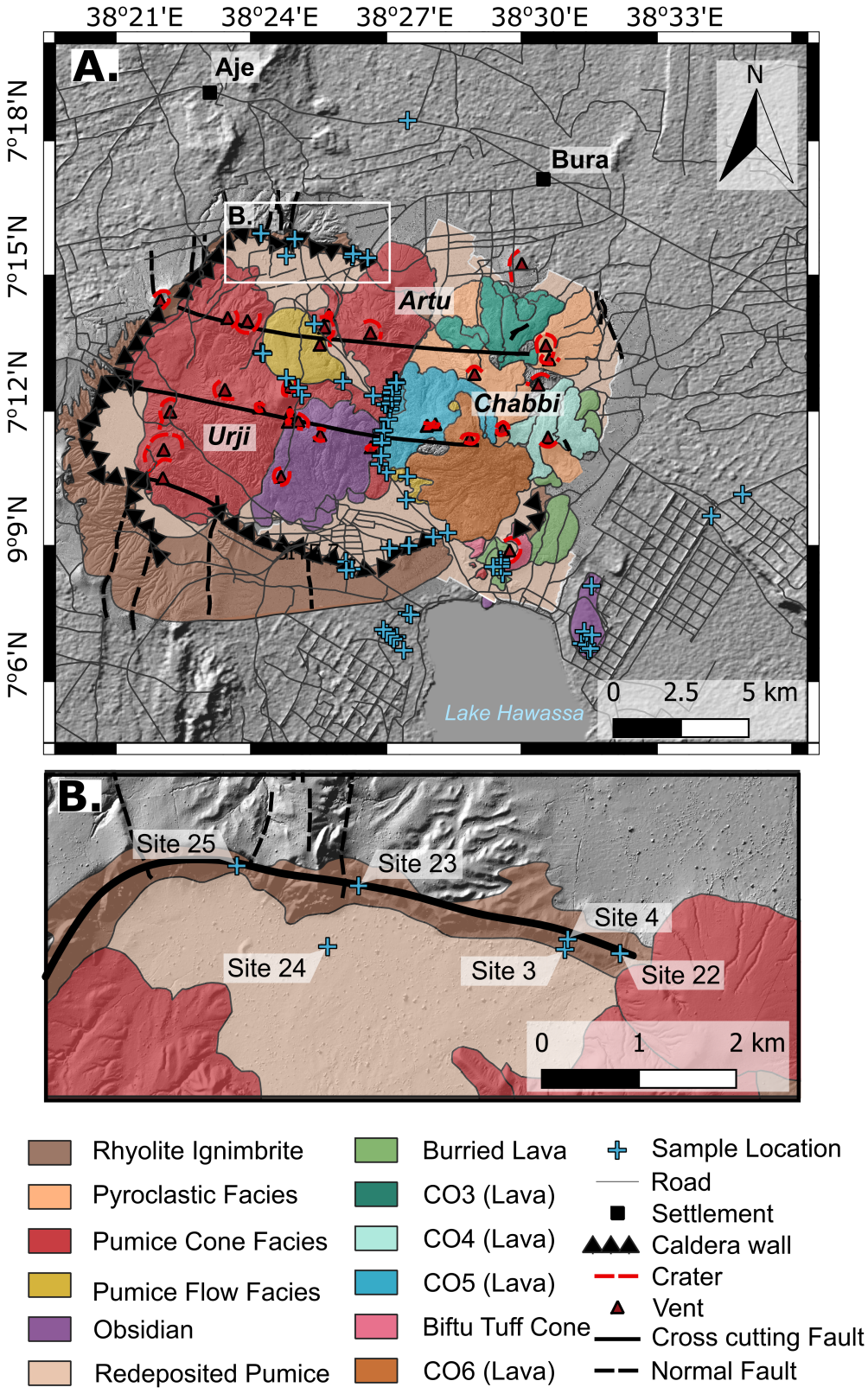

(Caption on next page.)

Figure 3.2: Geological map of Corbetti Caldera highlighting the sample locations (after Hunt et al. 2019 & Colby et al. 2022). B) Detail of the northern caldera walls showing sample sites of samples analysed in this study.

In addition to these units, only a few deposits at Corbetti contain crystalline material. Phenocrysts are almost exclusively restricted to large rhyolitic lava flows, which comprise significant parts of the northern and southern caldera walls, the ignimbrite associated with the caldera-forming eruption (NCW_E) and sparse crystalline portions of obsidian lavas (Colby et al., 2022). None of these latter units returned suitable glass and mineral data for thermometry and hygrometry analysis to be conducted.

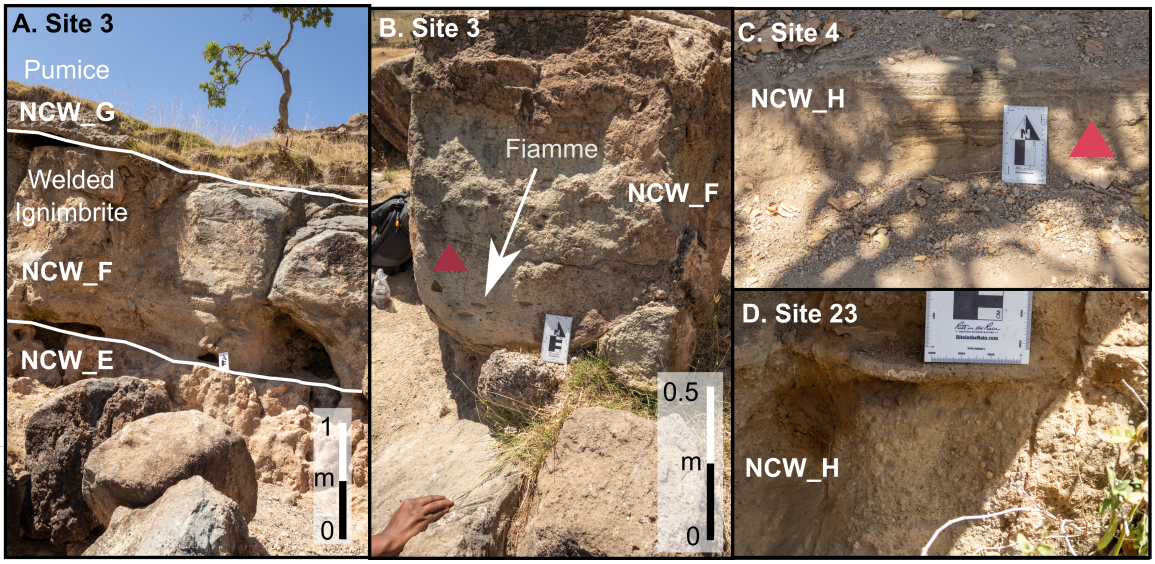

Figure 3.3: Field photos of deposits in north caldera walls (Site 3 & 4; Figure 3.2B) highlighting outcrops of the welded ignimbrite (NCW_F) and basaltic tuff (NCW_H). Adapted from Colby et al. 2022

3.2 Methods

3.2.1 Whole Rock, Glass and Mineral Geochemistry

Glass and mineral major element compositions were analysed by Electron Probe Micro-Analysis at the Department of Earth Sciences, Oxford. 5 spectrometers were used; PET (K, Ti), TAP (Na, Mg), LPET (Ca, P, Zr), TAP (Si, Al) and LLIF (Mn, Fe). Beam conditions were set at 15 kV, 10 nA, with a beam size of 10 μm for both glass and mineral phases.

Analysis of mineral phases in the enclave found in sample NCW_F required a smaller beam size of 5 μm. The probe was calibrated on in house primary standards (Si, Al and Na on Albite, Ca on Wollastonite, Mn on Mn, Fe on Fayalite, K on Sanidine, Ti on Rutile, Mg on MgO, P on Durango Apatite and Zr on Zircon). Secondary standards were not used. Two standard deviations for each of the elements are as follows: Si 0.83 wt.%, Al 0.33 wt.%, Ca 0.06 wt.% Mn 0.07 wt.%, Fe 0.16 wt%, K 0.26 wt.%, Ti 0.06 wt.%, Na 0.37 wt.%, Mg 0.06 wt.%, P, 0.05 wt.%. Alkali elements were measured first to minimise Na loss. Analytical totals below 97 wt% for the alkali basalt glass and below 95 wt.% for the peralkaline ignimbrite were rejected. Glass compositions were normalised to an anhydrous composition. Lower totals for the peralkaline ignimbrite are likely due to high water contents in the glass. Mineral data consistently recorded totals better than 99 wt.%. Any analysis with totals below 99 wt.% were rejected.

For whole rock analysis, samples were cleaned, oven-dried, crushed, and powered in an agate ball mill and analysed using ICP-OES for major elements and ICP-MS for trace elements at Activation Laboratories, Canada (Details and data presented in 2).

3.2.2 $^{87}Sr/^{86}Sr$ Isotope Analysis

Strontium isotope ratios were determined for 10 samples representing a range of pre-, syn- and post-caldera eruptions. These samples include two of the most well-characterised eruptions, the Bedded Pumice and WKYP eruptions (Rapprich et al., 2016; Fontijn et al., 2018; Colby et al., 2022), as well as samples from Chabbi (CO6) and the Biftu Tuff cone which sits outside of the caldera walls (Figure 3.2). Ratios were determined using the NU Plasma II MC-ICP-MS at the Laboratoire G-Time, Université libre de Bruxelles (Brussels, Belgium). Powdered samples were dissolved in a mix of 3 ml HNO_3 (14M) and 1 ml HF (23M) in a Teflon Savillex container on a hot plate for a minimum of 48 hours before being allowed to dry on the hot plate. Powders were then redissolved in 3 mL of HCl (6M) on a hot plate for at least 24 hours and then dried on a hot plate. A 100 mg strontium resin was added to HNO_3 (7M) was added into each container and placed in the ultrasonic bath for 20 minutes to complete the third and final dissolution. The resin is then rinsed with 5 $\times$ 1 ml of HNO_3 (7M) to eliminate unwanted elements. The Sr fraction was collected in 6 $\times$ 1 ml of HNO_3 (0.05M) in a new Savillex container and dried on a hotplate. Sample SCW_A2 required a second purification step due to a high Rb/Sr ratio. Two measurements were taken for each sample and an average reported. The average values have a 2SD of less than 0.000041. Samples were analysed alongside secondary standard NBS987 (Weis et al.,

2006) and an in-house carbonate sample. Measured values for the standards were within 0.001% of expected values (See supplementary information for details).

3.2.3 RhyoliteMELTS

Thermodynamic modelling of Corbetti's magmas was undertaken using RhyoliteMELTS v1.02 (Gualda et al., 2012) using the easyMELTS GUI (Suikkanen, 2020). Isobaric fractional crystallisation of an alkali basalt starting melt was modelled at various pressures (50-250 MPa at 50 MPa intervals), oxygen fugacities (+2 to -2 QFM at 1 log unit intervals) and initial water contents (0.5 and 1-4 wt.% at 1 wt.% interval). These parameters are consistent with other studies investigating the petrogenesis of peralkaline magmas in the MER (Gleeson et al., 2017; Romano et al., 2020; Scaillet and Macdonald, 2001). The starting composition was chosen to be the most primitive of the glass shards of the basaltic tuff, with 6.2 wt.% MgO (section 3.3.1). The starting composition for each run was normalised (to 100%) depending on the initial H_2O content and oxygen fugacity (FeOt was recalculated to FeO and Fe_2O_3 based on the starting fO_2 condition). The modelled compositions of differentiated melts were compared with natural whole-rock compositions (Chapter 2) using the least-squared approach of Gleeson et al. (2017) to find the best fit. Each fractionation point is compared to the target composition and a residual calculated. The 15 fractionation steps with the lowest calculated residual represent the closest fits to the target compostion and are then averaged to provide the overall residual for that run. The RhyoliteMELTS run with the lowest calculated residual is determined to be the best fit for the target compositon. RhyoliteMELTS has been used to investigate magma storage conditions at a variety of peralkaline centres (e.g. Peccerillo et al. 2003; Ronga et al. 2009; Gleeson et al. 2017); however, it should be noted that RhyoliteMELTS is not calibrated for peralkaline magmas and does not accurately model hydrous phases such as amphibole (Gualda et al., 2012; Rooney et al., 2012). Whilst this phase has not been reported in Corbetti's eruptive products, it has been found at other MER volcanoes (Gibson, 1974; Peccerillo et al., 2007; Giordano et al., 2014; Tadesse et al., 2023) and in peralkaline melts more generally, and it will likely affect the modelling of intermediate compositions. In addition, RhyoliteMELTS does not accurately model phases such as aenigmatite and apatite which is commonly found in peralkaline melts (Di Carlo et al., 2010; Rooney et al., 2012). To overcome some of these limitations, we compare results with petrological data to test the validity of the modelling.

3.2.4 Thermobarometry and Hygrometry

3.2.4.1 Basaltic Tuff (NCW_H)

The basaltic tuff (NCW_H) was emplaced as a PDC (Colby et al., 2022). It is, therefore, likely that a portion of minerals in the sample will not be in equilibrium with the erupted glass; hence, only olivine and plagioclase phenocrysts hosted in fresh glass were considered for analysis. All thermometry and hygrometry calculations were conducted using the Thermobar python package (Wieser et al., 2022). For olivine-liquid pairs, the proportion of Fe_2O_3 in the liquid was determined using the method of Kress and Carmichael (1991) at the QFM buffer, which is in line with the results from the thermodynamic modelling (see section 3.3.5) and previous studies (Gleeson et al., 2017). The core and rim compositions of olivine-liquid pairs were tested for equilibrium using the method of Roeder and Emslie (1970) (threshold set at $Kd^{Ol-liq}_{(Fe-Mg)}0.3 \pm 0.03$) however other equilibrium tests which are included in the Thermobar package were in good agreement. Equilibrium olivine-liquid pairs were used to estimate temperatures using Equation 22 of Putirka (2008) and were calculated at five pressures (50 - 250 MPa at 50 MPa intervals) to reflect the proposed depths of magma storage within the MER (Gleeson et al., 2017) and in line with the results of the thermodynamic modelling (see section 3.3.5).

Plagioclase-liquid thermometry and hygrometry were also conducted using plagioclase phenocrysts hosted in glass. Temperatures and H_2O contents were calculated iteratively (using 30 iterations) across the same pressure intervals (50-250 MPa at 50 MPa steps) using Equation 24a of Putirka (2008) to calculate temperature and the method of Waters and Lange (2015) to calculate H_2O contents. Results were filtered to exclude plagioclase phenocrysts which were not in equilibrium with their host glass, using the An-Ab test of Putirka (2008).

3.2.4.2 Peralkaline Rhyolite Ignimbrite (NCW_F)

Temperatures and water contents were also calculated for the peralkaline welded ignimbrite (NCW_F), which outcrops below the basaltic tuff (Colby et al., 2022) in Corbetti's northern caldera wall (Figure 3.3.2.1). Liquid compositions were matched with every feldspar composition and temperatures calculated using Equation 24b of (Putirka, 2008) in Thermobar (Wieser et al., 2022) across the same pressure intervals (50-250 MPa). The calculated temperatures were then used to estimate water contents using the K-feldspar - liquid hygrometer

of Mollo et al. (2015). This hygrometer is calibrated for high alkali compositions, which makes it the most appropriate for our samples. As the calculated temperatures (Section 3.3.3) do not vary significantly with pressure (~0.1 K), we used temperatures calculated at 100 MPa to estimate the water contents. The results were filtered using the equilibrium test proposed by Mollo et al. (2015) based on the measured vs predicted Or-Ab partitioning between the K-feldspar and the melt (when ${}^{Ksp-melt}Kd_{Or-Ab}$ 'Measured' versus 'Predicted' is plotted, the equilibrium field lies along the 1:1 line ± 0.05).

Temperatures and pressures were also estimated for a crystalline enclave found within NCW_F. As no glass compositions could be collected, we used two-feldspar thermometry (equation 27b of Putirka 2008), and the clinopyroxene-only thermometry and barometer using the random forest model developed by Jorgenson et al. (2022).

3.3 Results

3.3.1 Geochemistry and $^{87}Sr/^{86}Sr$ Ratios

The basaltic tuff within the northern caldera wall (NCW_H) is the only example of a deposit from a basaltic eruption so far found within the complex (Colby et al., 2022). The composition of individual glass shards is broadly homogenous; however, there is significant variation between individual shards which range from basaltic (46.3 wt.% SiO_2) to basaltic andesite (54 wt.% SiO_2) (Figures 3.4 & 3.5). In addition, obsidian lithics were also found encased in basaltic glass. These were highly silicic, ranging from 74.95 to 76.75 wt.% SiO_2 (Figure 3.4B), weakly peralkaline comendites (Peralkalinity Index = 1.01-1.13).

Glass compositions from the basaltic tuff record a fractional crystallisation trend; however, a bimodal distribution in SiO_2, CaO and K_2O is observed. In addition, there is significant scatter in the observed MnO, Na_2O and P_2O_5 concentrations above 50 wt.% SiO_2. As the cause of this chemical diversity is unclear, we only consider samples < 50 wt.% SiO_2 for comparison with the RhyoliteMELTS modelling which is outlined in Section 3.3.5.

Whole rock trace element geochemistry published in (Colby et al., 2022) (See 2) is presented in Figures 3.6 & 3.7, highlighting the incompatible trace element trends and the mean trace element composition of units normalised to primitive mantle compositions (McDonough and Sun, 1995). There is little variation between peralkaline eruptive units,

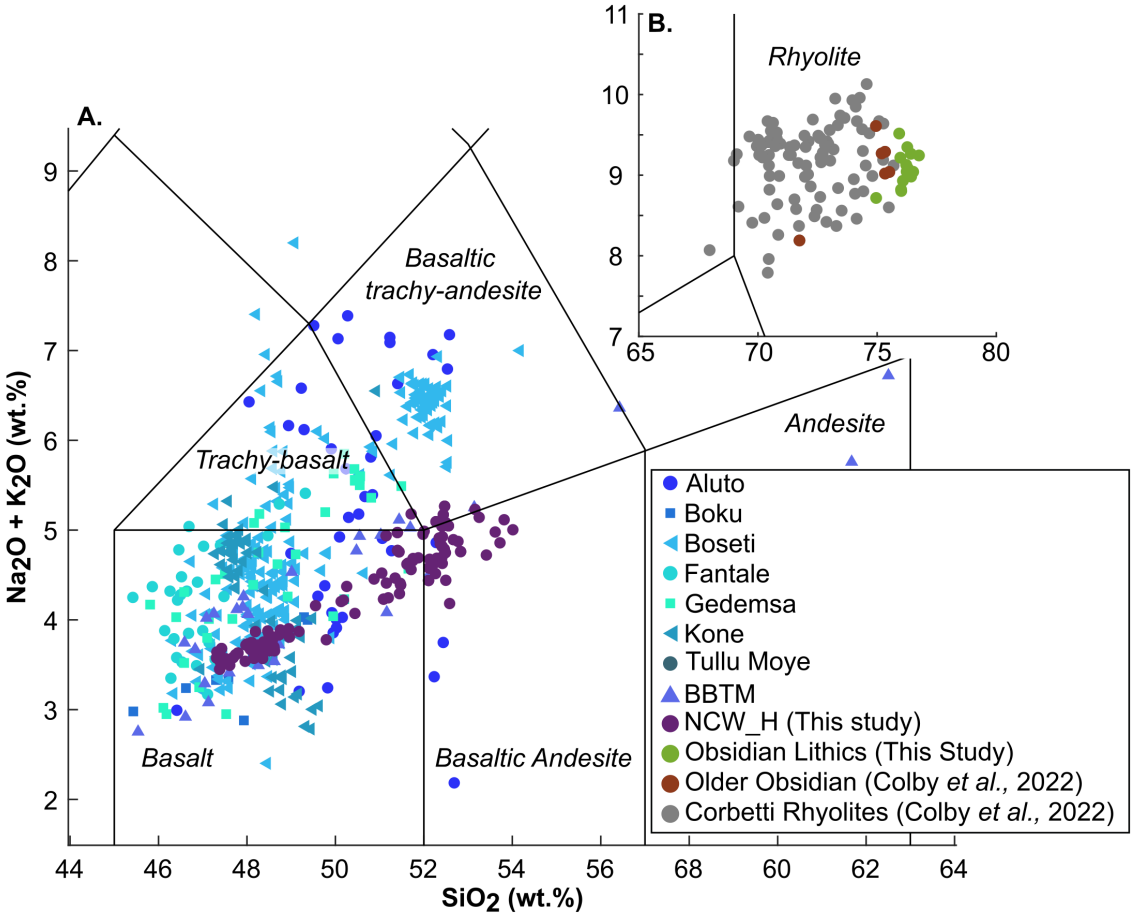

Figure 3.4: A) Total Alkali-Silica plot comparing the glass compositions reported here with glass (G) and whole-rock (WR) basaltic compositions reported at other calderas within the MER. Aluto; Teklemariam et al. (1996) (WR); Hutchison et al. (2016c) (WR); Fontijn et al. (2018) (G), Boku: Tadesse et al. (2019) (WR), Boset: Brotzu et al. (1980) (WR); Furman et al. (2006) (WR); Fontijn et al. (2018) (WR), Fantale: Furman et al. (2006) (WR); Rooney et al. (2007) (WR); Giordano et al. (2014) (WR), Gedemsa: Chernet and Hart (1999) (WR); Peccerillo et al. (2003) (WR); Rooney et al. (2007) (WR); Giordano et al. (2014) (WR), Kone: Rooney et al. (2007)(WR); Fontijn et al. (2018)(G), Tullu Moye: Fontijn et al. (2018) (G), BBTM: Tadesse et al. (2023) (WR). B) TAS plot (Axis the same as A) showing the composition of the obsidian lithics compared with WR peralkaline rhyolite samples from Corbetti.

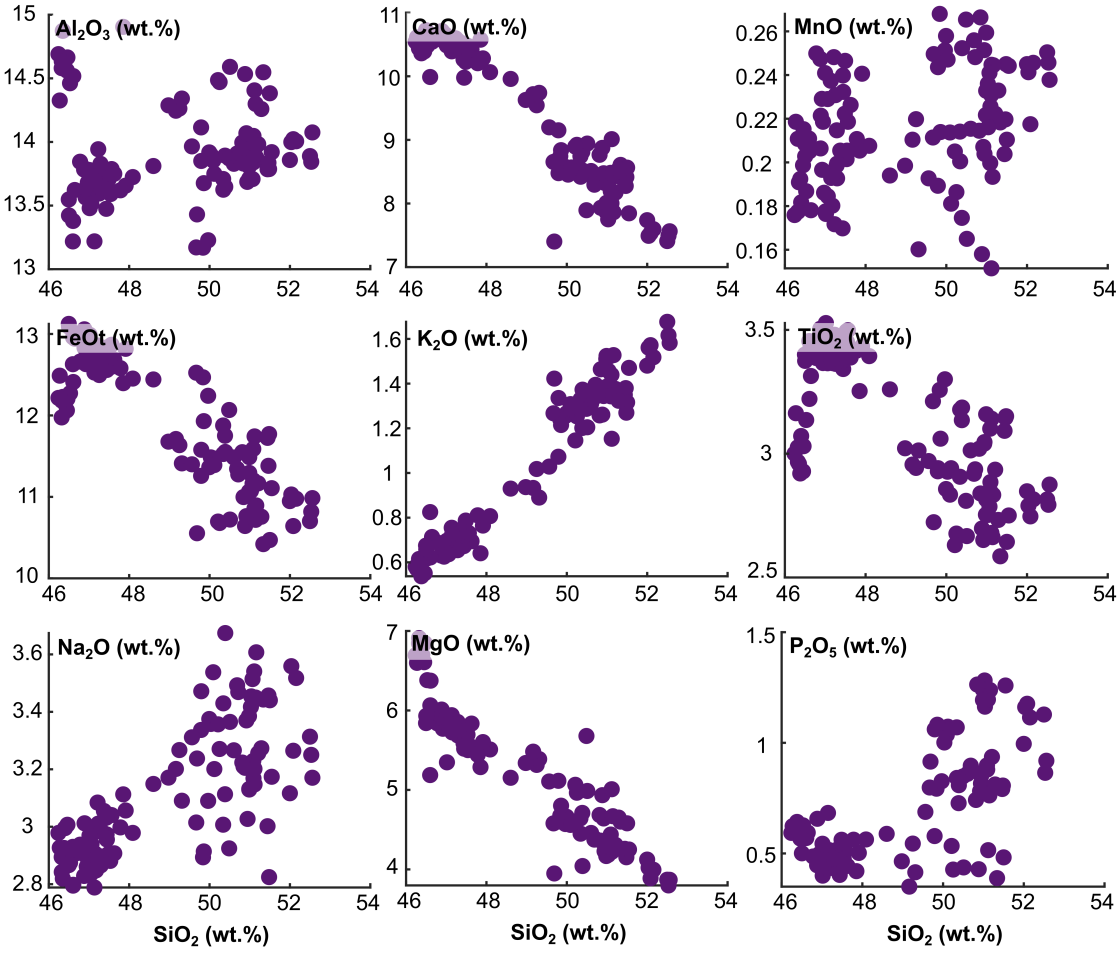

Figure 3.5: Harker diagrams showing the variation of basaltic glass compositions recorded within the basaltic tuff (NCW_H). Samples above 50 wt.% SiO_2 show increased scatter in MnO, FeOt, TiO_2 and Na_2O. High P_2O_5 values are unusual, however, similar P_2O_5 values in alkali basalts are also reported at Aluto and may be due to the late fractionation of apatite (Hutchison et al., 2016c). Although not observed in Corbettis erupted products, apatite is likely to be present through the crystallisation sequence (Field et al., 2012).

Table 3.1: $^{87}Sr/^{86}Sr$ ratios and Sr concentrations for selected samples. Sample locations are highlighted in Colby et al. (2022).

Correlation[1]	Material	Location[1]	Sr (ppm)	$^{87}Sr/^{86}Sr$	2SD[2]
SCW_A2	Lava	Site 7B	2	0.705029	0.000041
NCW_E	Ignimbrite	Site 2B	9	0.706223	0.000004
NCW_F	Ignimbrite	Site 3B	4	0.704972	0.000013
NCW_H	Ash	Site 4A1	354	0.704324	0.000007
US_A	Lava	Site 66B	3	0.705031	0.000009
Bedded Pumice	Pumice	Site 40C1	3	0.704487	0.000026
Biftu PDC	Ash	Site 9D	17	0.705184	0.000002
WKYP	Pumice	Site 34B	3	0.705184	0.000018
Urji Lava	Lava	Site 37	3	0.704474	0.000013
CO6	Lava	Site 58A	3	0.704507	0.000005

1. See Colby et al. (2022) for information on units and sample locations.
2. 2SD = Two standard deviations.

especially between post-caldera deposits, making differentiation between units based on composition alone challenging (Fontijn et al., 2018; Colby et al., 2022). The peralkaline magmas show characteristic depletion with respect to the primitive mantle in Ba and Sr, reflecting extensive alkali feldspar fractionation. Whilst most samples show the expected trends of a highly differentiated peralkaline magma, Figure 3.6 highlights some examples, which span several stratigraphic units, that have a lower Zr/Nb ratio. These samples also have high Zr/Hf ratios (57-72) compared with the rest of the dataset (40-52), which are expected to remain constant through fractionation and are also slightly depleted in Ta (Figure 3.6).

$^{87}Sr/^{86}Sr$ isotope values for selected samples are reported in Table 4.1 with comparison with other $^{87}Sr/^{86}Sr$ data for the MER presented in Figure 3.8. All but one of the samples has values which range from 0.7043-0.7051, in good agreement with previous $^{87}Sr/^{86}Sr$ data for Corbetti (Rapprich et al., 2016). One sample, NCW_E, shows a more elevated isotopic signature of 0.7062 and matches the value for the caldera-forming ignimbrite reported by Rapprich et al. (2016).

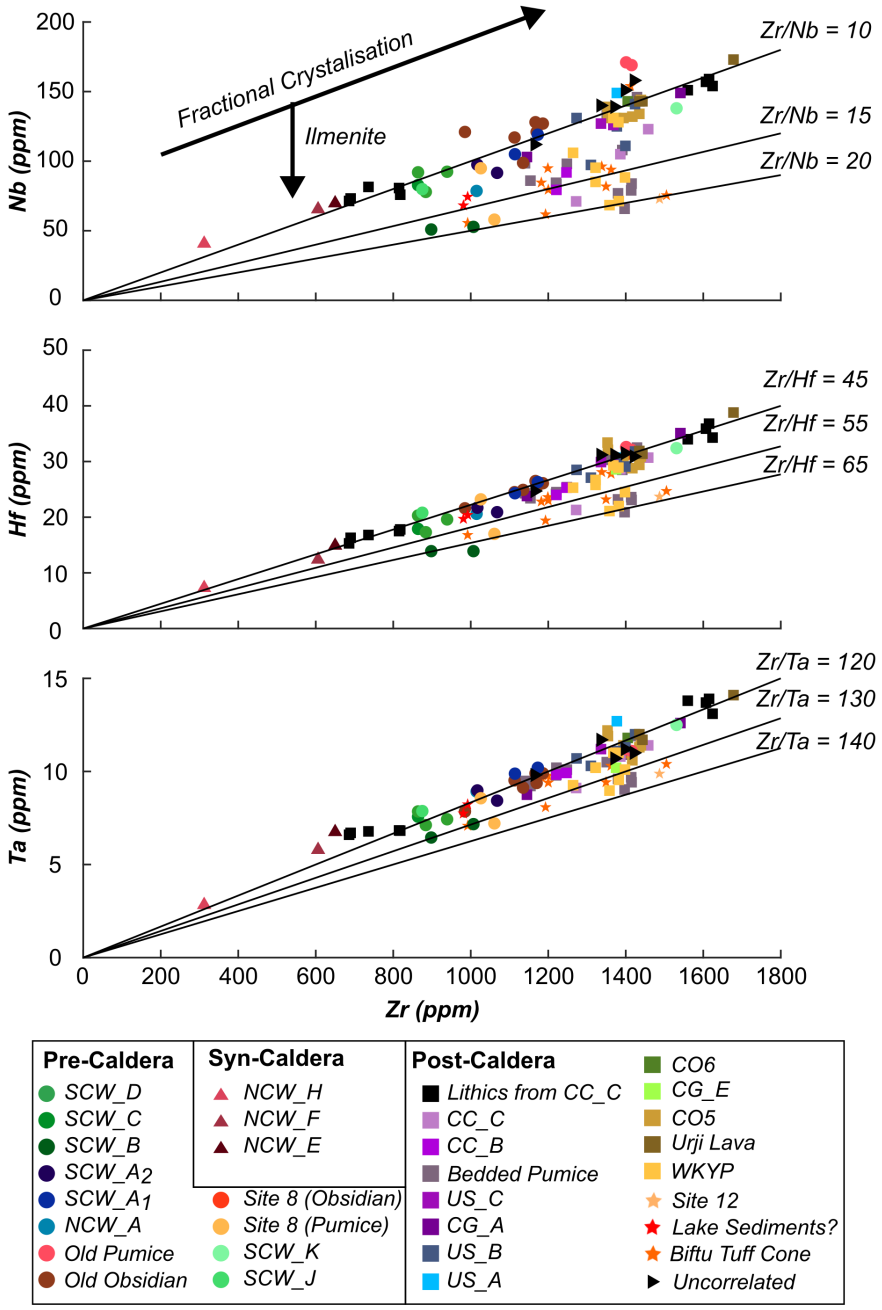

Figure 3.6: Selected incompatible whole rock trace element data plots which show fractional crystallisation trends. Black lines highlight the trends of different ratios of Zr to respective elements.

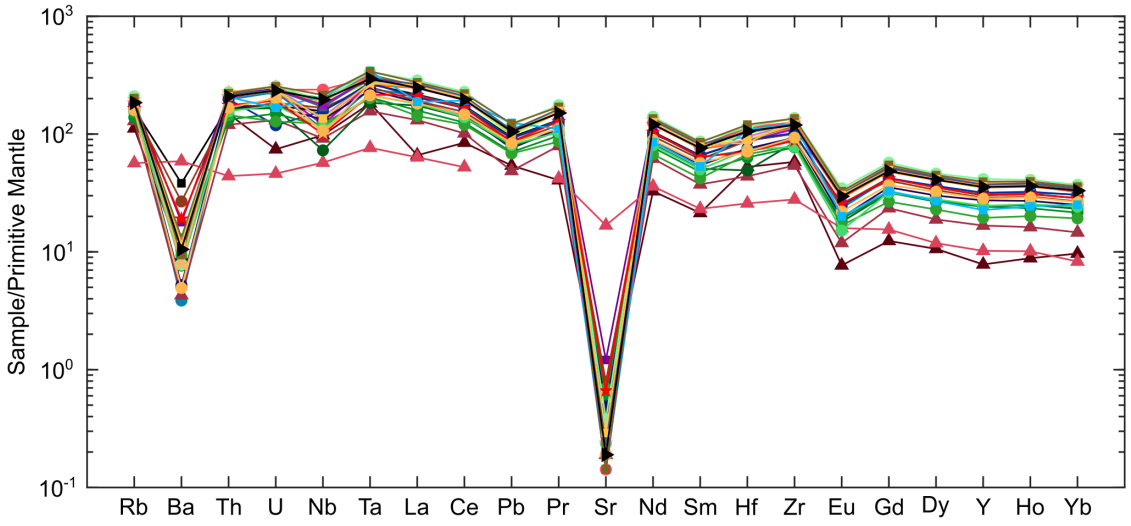

Figure 3.7: Spider diagrams showing the mean whole rock trace element variation for selected units at Corbetti normalised to the primitive mantle (McDonough and Sun, 1995)- symbols as in Figure 3.6. The least fractionated sample is the basaltic tuff (NCW_H)

3.3.2 Mineralogy

The eruptive products products at Corbetti are crystal-poor, with only a few samples containing phenocrysts. Here we outline the mineral assemblage of crystal-bearing samples in Table 3.2 and highlight features of the mineral populations. Details on specific phases present in the the basaltic tuff (NCW_H) and the peralkaline endmember (welded ignimbrite; NCW_E) focused on in this study, are outlined below.

3.3.2.1 Olivine

The Basaltic Tuff (NCW_H) contains olivine as individual grains and phenocrysts encased in glass (Figure 3.9A-D). Olivines are predominantly euhedral to anhedral with some showing signs of dis-equilibrium in the form of patchy zoning (Figure 3.9). They range in composition from Fo_{75-85} (Figure 3.10), and most are normally zoned; however, the degree of zonation varies considerably. Some phenocrysts show a less than 0.1 wt.% variation in MgO between the core and the rim, whilst others show $\sim$ 2 wt.% variations. There are rare instances of reverse-zoned phenocrysts. Some olivine phenocrysts contain Fe-Ti oxide inclusions.

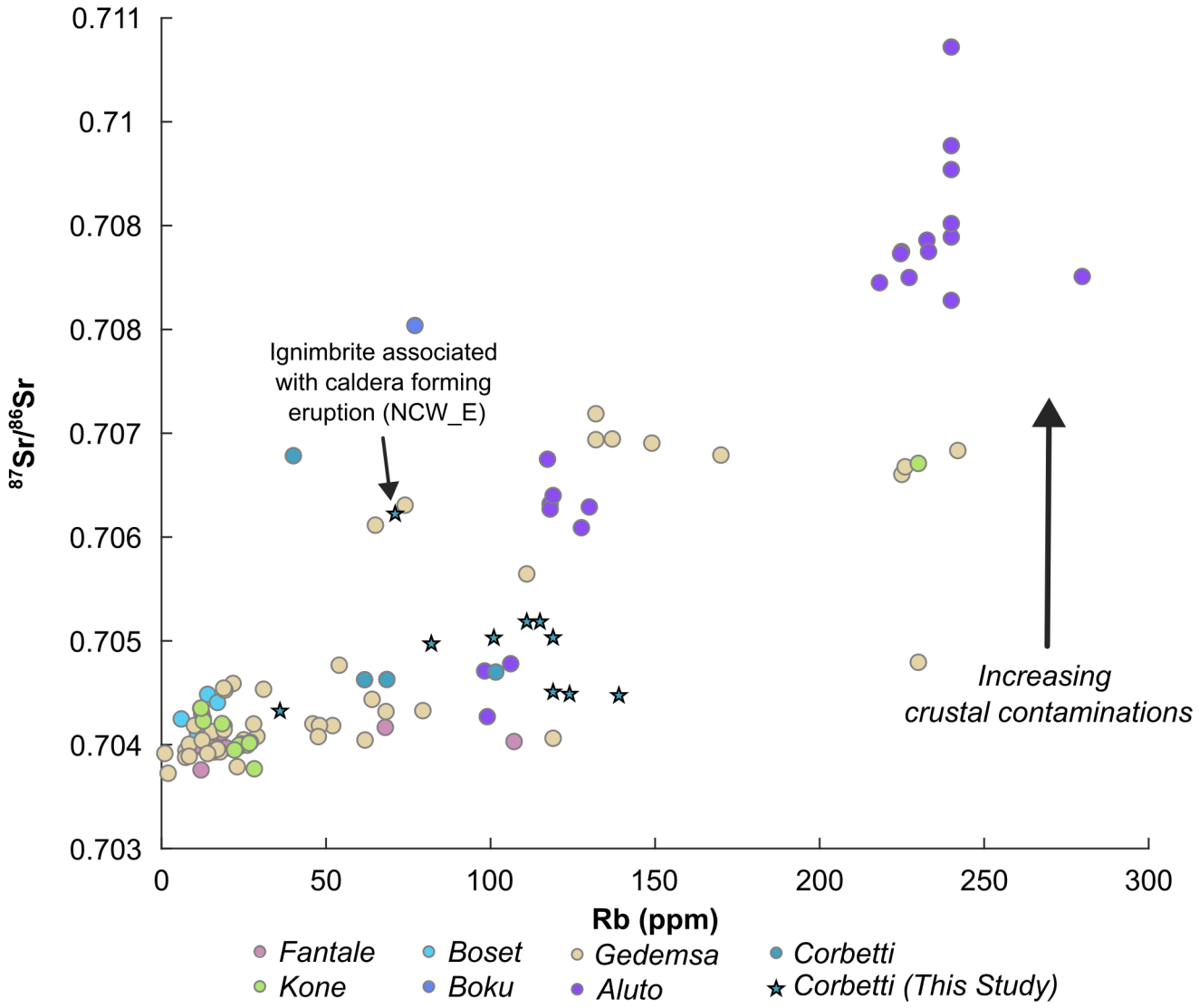

Figure 3.8: Variation in $^{87}Sr/^{86}Sr$ ratio values reported across the MER in comparison to the values in this study. One of Corbetti's eruptive units (NCW_E) records an elevated $^{87}Sr/^{86}Sr$ ratio indicating a degree of crustal contamination that may result from the incorporation of country rock during eruption or through assimilation of country rock due to a higher magma flux in the lead up to the development of this magma body. Other samples from Corbetti show similar values with some slight elevations observed with may indicate a minor degree of crustal contamination but are in line with other samples from the MER. Data downloaded from the the GeoRoc database (Downloaded on 1st Dec 2023 `https://georoc.eu/`). Fantale:Furman et al. (2006); Giordano et al. (2014); Ayalew et al. (2016); Kone: Furman et al. (2006); Peccerillo et al. (2007); Ayalew et al. (2016); Boset: Furman et al. (2006); Ronga et al. (2009); Ayalew et al. (2016); Boku: Boccaletti et al. (1995); Gedemsa: Boccaletti et al. (1995); Barberio et al. (1999); Peccerillo et al. (2003); Giordano et al. (2014); Ayalew et al. (2016); Castillo et al. (2020); Aluto: Deniel (2009); Corbetti: Rapprich et al. (2016)

Table 3.2: Overview of minerals present in crystalline samples from Corbetti Caldera. Mineral abbreviations after Whitney and Evans (2010). Ol: Olivine, Pl: Plagioclase, Aeg: Aegirine Augite, Afs: Alkali-feldspar, Fa: Fayalite, Qz: Quartz, CPX: Clinopyroxene.

Sample	Material	Groundmass	Minerals	Notes
NCW_H	Basaltic Tuff	Glass shards	Ol, Pl, Fe-Ti Oxides	Aeg and Afs also found in dis-equilibrium with glass
NCW_F	Welded Ignimbrite	Welded Glass	Qz, Afs, Aeg	Enclave present containing Pl, Afs, CPX, Fe-Ti oxides
NCW_E	Ignimbrite	Glass	Qz, Afs, rare Aeg and Fa	Qz phenocrysts highly fractured
SCW_B	Lithics from Breccia	Flow-banded glass	Qz, Afs,	Glomerocrysts of Qz and Afs
SCW_D	Lithics from Breccia	Glass	Qz, Afs, Aeg	Glomerocrysts of Qz, rare Afs with Granophyre texture. Lithic fragments from other rocks also present
SCW_A2	Lava	Devitrified glass	Qz, Afs, rare Aeg	Qz phenocrysts commonly have embayments. Aeg shows signs of breakdown and resorption
NCW_A	Lava	Devitrified glass	Sparse Aeg	Matrix glass has spherulite texture
Older Obsidians	Obsidian Lava	Glass, Afs microlites	Qz, Afs, Fe-Ti Oxides, rare aegirine-augite	Microlites aligned in flow direction

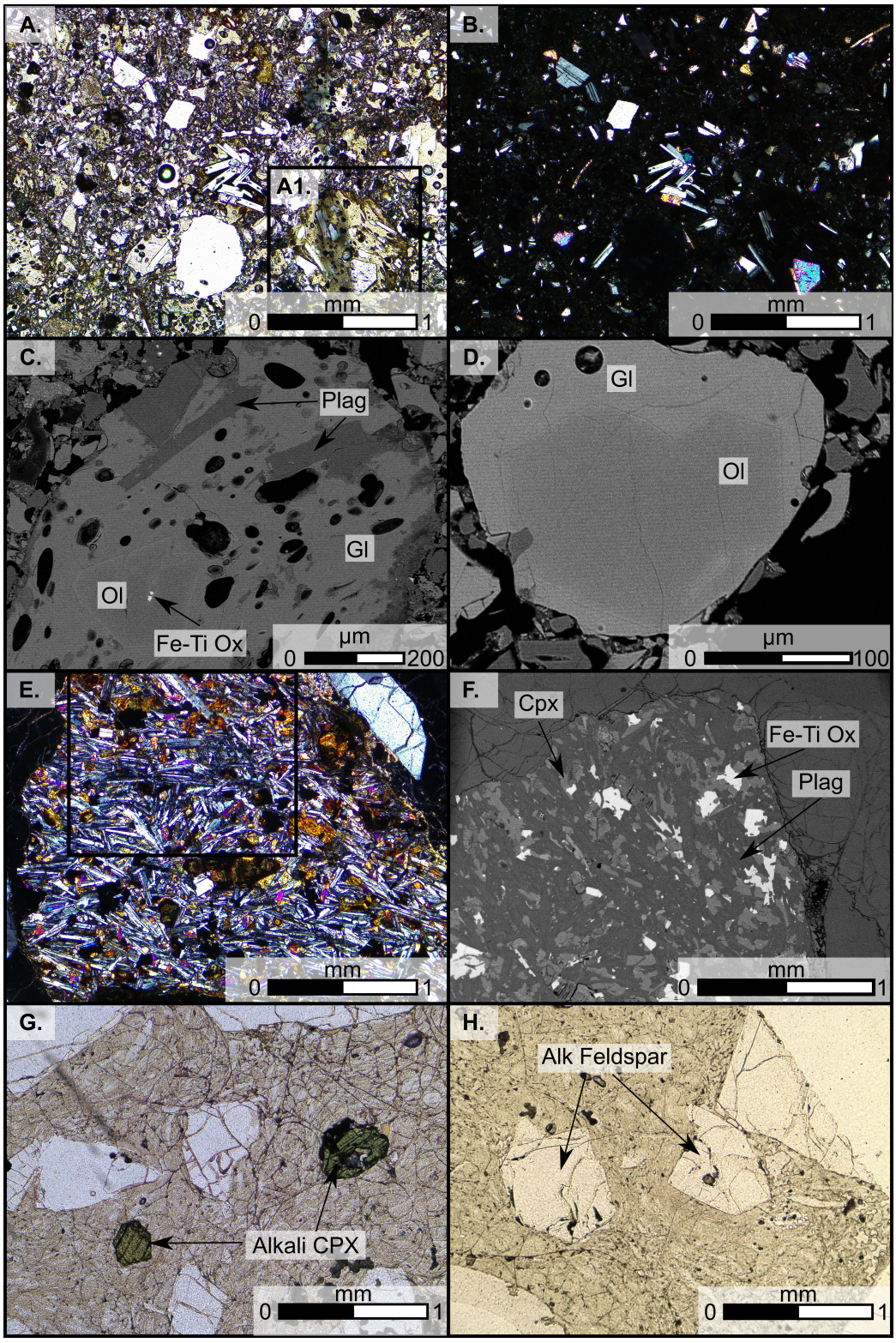

(Caption on next page.)

Figure 3.9: A) and B) are thin section images of NCW_H in plain and cross-polarised light. Olivine and plagioclase can be seen hosted in glass. C) shows the area highlighted in A1 in BSE (View of area is rotated ~45° clockwise): presence of plagioclase and olivine hosted in a basaltic glass with visible vesicles. The olivine phenocryst contains Fe-Ti Oxide inclusions. D) Olivine phenocrysts hosted in glass. E) Cross-polarised image of crystalline enclave found within NCW_F showing dense concentration of feldspars, clinopyroxenes, and Fe-Ti Oxides. F) BSE image of area highlighted in E (View rotated ~90° clockwise). G and H) plain polarised images of NCW_F glass and mineral phases.

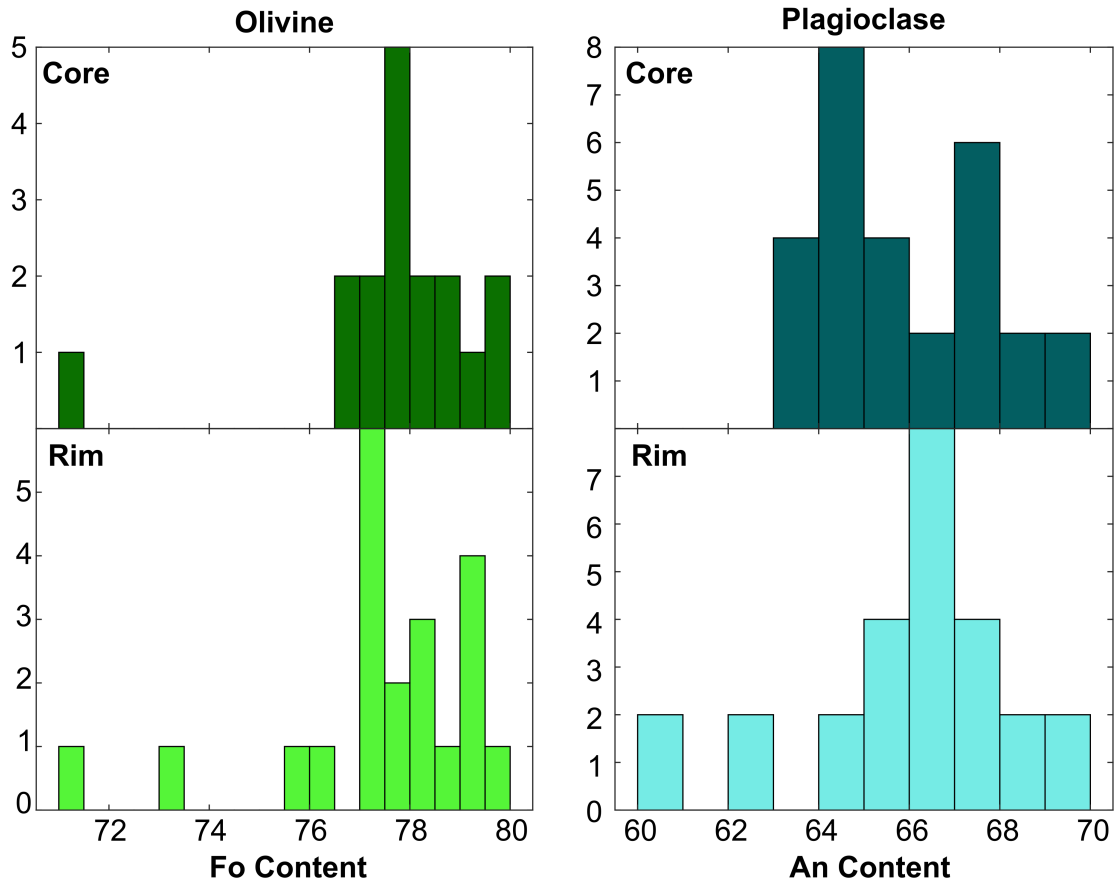

Figure 3.10: Range in Fo contents for the core and rims of analysed olivine phenocrysts and range in An content of plagioclase phenocrysts from the basaltic tuff (NCW_H)

3.3.2.2 Feldspars

The Basaltic Tuff (NCW_H) also contains plagioclase phenocrysts (Figure 3.9). Core compositions range between An_{63-70}. However, Figure 3.10 shows two peaks in the data around An_{64-65} and An_{67-68}. Rim compositions range between An_{60-70}; however, most phenocryst rims have a An concentration around An_{66-67} (Figures 3.10 & 3.11). Rare alkali feldspars (Or_{36-41}) are also recorded (Figure 3.11). These alkali feldspars are likely scavenged from older, evolved batches of melt (Iddon et al., 2019) or accidentally entrained during eruption.

The welded ignimbrite (NCW_F) contains abundant alkali feldspars, which range in composition between Or_{36-45}. A highly crystalline enclave within this sample contains abundant feldspar ranging in composition from An_{11-58} (Figure 3.10 & 3.11).

3.3.2.3 Clinopyroxene

Clinopyroxenes, whilst scarce, are found within the welded ignimbrite and crystalline enclave and range in composition from Wo_{36-40} & Fs_{39-44}. Alkali clinopyroxenes are also recorded in large rhyolite flows within the caldera wall (SCW_A1; Colby et al. 2022) however show signs of breakdown, likely due to devitrification of the ground glass.

Rare clinopyroxenes are found within the basaltic tuff (NCW_H) however, these are not in equilibrium with glass preserved in the sample and are likely scavenged from a more evolved melt or accidentally entrained during the eruption.

3.3.2.4 Other Phases

Quartz is common in all crystalline rhyolitic samples, with phenocrysts in the rhyolitic lavas (SCW_A1) showing embayment's. Glomerocrysts of feldspar and quartz are also recorded in the caldera-forming ignimbrite. These are thought to form near the roof of magma systems and are seen in the deposits of other eruptions in the MER (Hutchison et al., 2016c). Fe-Ti Oxides are found in a small number of samples as individual grains and inclusions within other phases (olivines). A single phenocryst of fayalite was found in NCW_E (ignimbrite associated with the caldera-forming eruption).

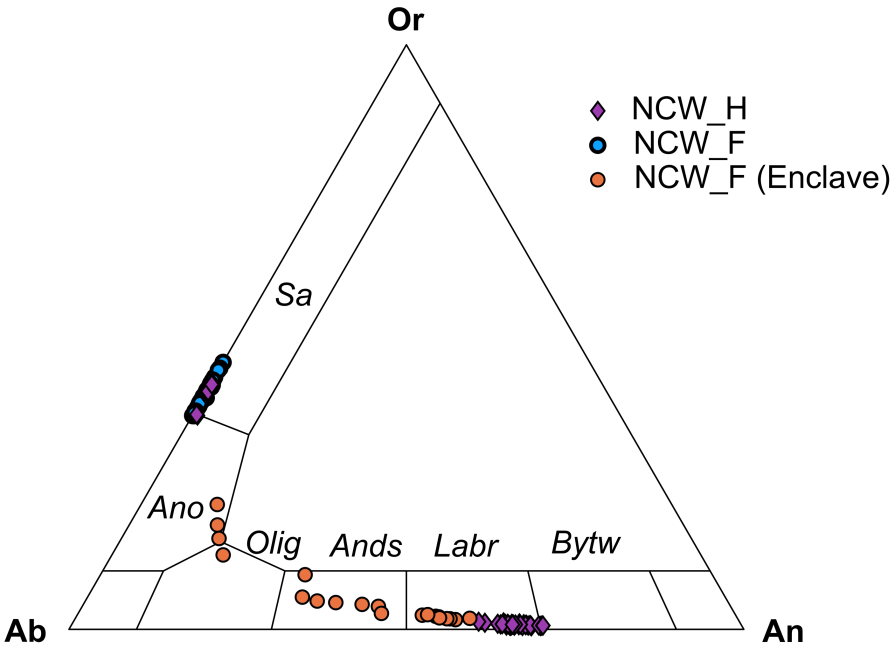

Figure 3.11: Tri-plot showing the range of feldspar compositions recorded in the basaltic tuff (Purple), peralkaline ignimbrite (Blue) and enclave (Orange). Shows some alkali-feldspars are present within the basaltic tuff and are likely antecrystic.

3.3.3 Thermobarometry and Hygrometry

Figure 3.12 shows the rim and core Fo contents of olivine phenocrysts compared with the Mg# of their host glass. A large proportion of olivines are not in equilibrium with their host glass and have high Fo contents suggesting they formed in more primitive melts and have been mixed with a more evolved melt prior to eruption.

Calculated temperatures based on olivine-liquid and plagioclase-liquid thermometry are presented in Figure 3.13. Whilst pressure impacts the calculated temperature; the variation is within the error of the models. Due to the low number of equilibrium mineral-liquid pairs, liquid-only thermometry was also conducted (Figure 3.13). These results agree with the mineral-liquid estimates and indicate that equation 14 of (Putirka, 2008) can be readily applied to alkali basalts where suitable equilibrium mineral-liquid pairs are unavailable.

Due to the lack of crystalline phases, and therefore melt inclusions, in Corbetti's eruptive products, there is minimal information on the pre-eruptive H_2O contents of Corbetti's magmas (Iddon and Edmonds, 2020). We have sought to add to this limited dataset through mineral-liquid hygrometry. Based on equilibrium plagioclase-liquid pairs (using

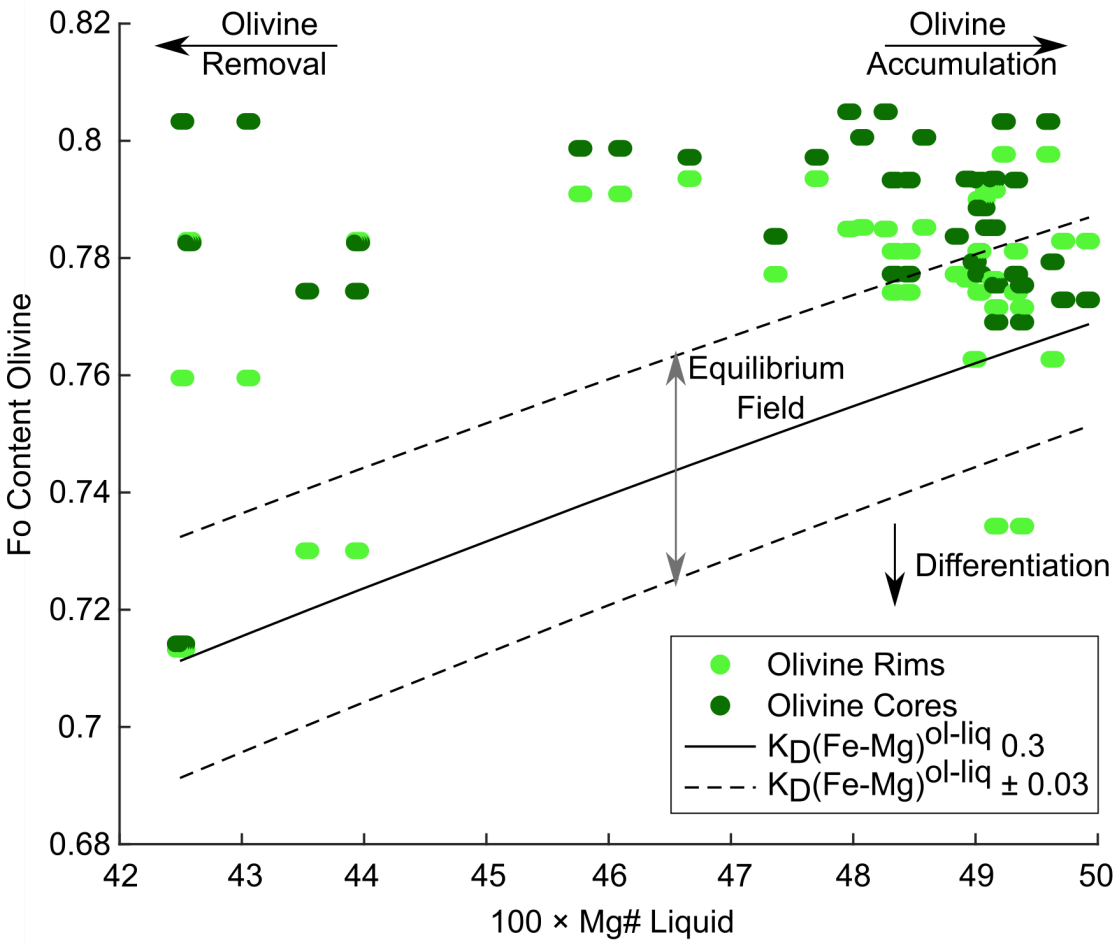

Figure 3.12: Equilibrium plot showing Fo contents of the rims and cores of olivines plotted against the Mg# of the host glass. Olivines in equilibrium with their host glass will fall within the equilibrium field $Kd_{(Fe-Mg}{}^{ol-liq}$ 0.3 ± 0.3 defined after (Roeder and Emslie, 1970). Rim and core compositions from the same olivivne phenocrysts are compared to the glass composition they are hosted in. Where there is an offset between the rim and core Fo values it indicates a degree of zonation.

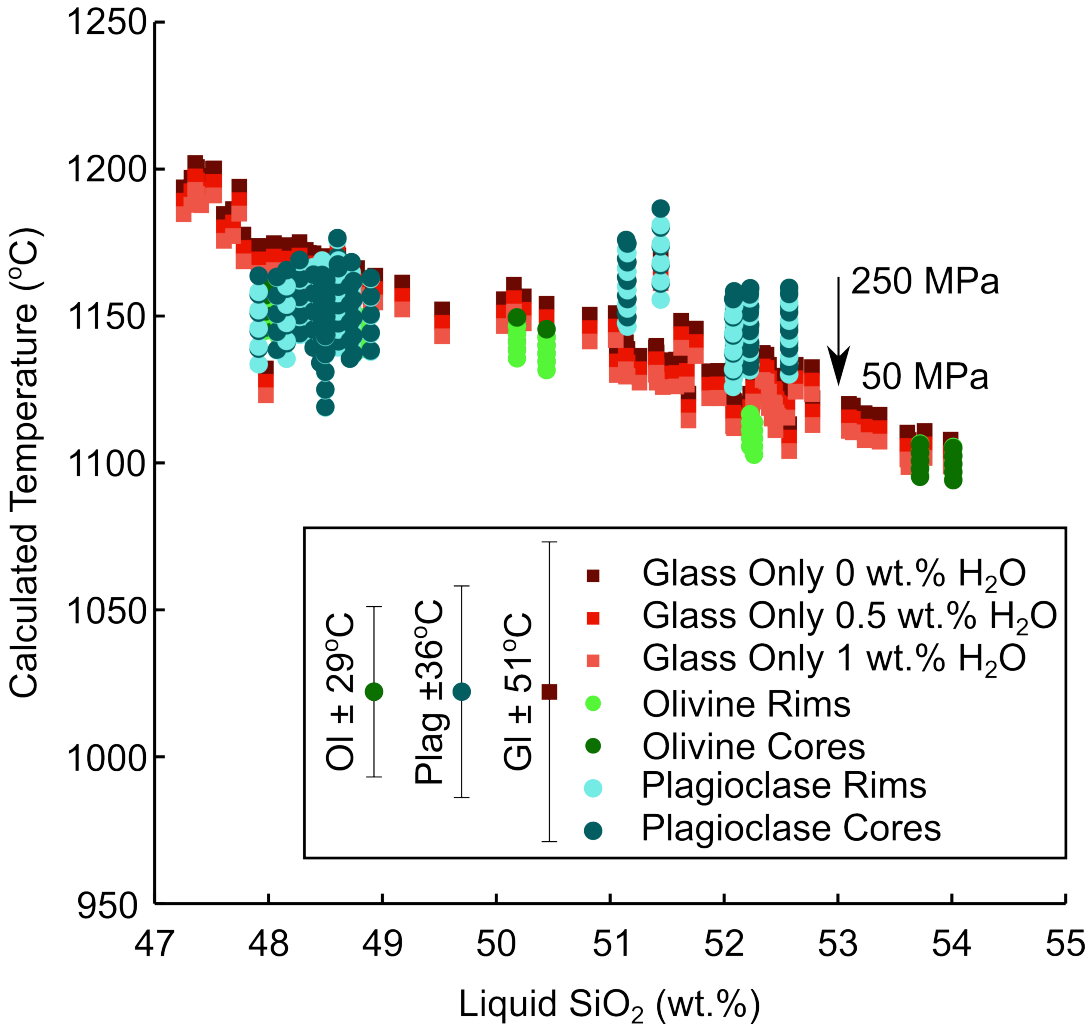

Figure 3.13: Temperatures calculated using glass-only thermometry, olivine-liquid pairs, and plagioclase-liquid pairs. Glass-only thermometry was calculated at 3 different H_2O contents, from anhydrous to 1 wt.% H_2O. Olivine and Plagioclase temperatures were determined at a range of pressures (250 MPa to 50 MPa at 50 MPa steps).

the An-Ab test of Putirka 2008), we calculated water contents of 0-1.2 ± 0.72 wt.% for Corbetti's basaltic magma. The range in concentrations reflects plagioclase phenocrysts crystallising at different stages of melt differentiation and temperatures (see section 3.3.3). These calculated water contents match well with the estimated initial water contents for the basaltic magma from the RhyoliteMELTS modelling (section 3.3.5).

Calculated temperatures for equilibrium alkali feldspar-liquid pairs (Mollo et al., 2015) for NCW_F range from 793 to 614 °C (Figure 3.14). Temperatures below 620 °C were excluded as these are anticipated to be below the solidus (Scaillet and Macdonald, 2001). These temperatures were calculated over a range of pressures (50-250 MPa) to be consistent with the input parameters used in the RhyoliteMELTS modelling (section 3.3.5). However, variation in pressure had a minimal effect on the calculated temperatures, which is smaller than the model error. Therefore, for simplicity, we have only presented temperatures calculated at 100 MPa.

Temperatures for the crystalline enclave were calculated using two-feldspar thermometry across five pressure intervals (50-250 MPa). Plagioclase phenocrysts were only in equilibrium with three alkali feldspar phenocrysts. Calculated temperatures ranged from 879 to 711.9 ± 30 °C, varying by ~ 12 °C across the pressure range for a given pair.

The welded ignimbrite (NCW_F) water contents were also calculated using K-feldspar - liquid hygrometry. The concentrations ranged from ~ 1 - 7.9 ± 0.75 wt.% (Figure 3.14). The large range in calculated H_2O concentrations results from the hygrometer's sensitivity to the composition of the alkali - feldspars. To test if the maximum recorded water content is a reasonable estimate, we calculated the solubility of H_2O in the melt as a function of composition, temperature and pressure using the method of Allabar et al. (2022). These results demonstrate up to ~7.5 wt.% H_2O can be dissolved in a peralkaline melt at 250 MPa. This matches the pressure conditions estimated from RhyoliteMELTS based on the glass chemistry of the ignimbrite.

3.3.4 Pressure Estimates

Pressure estimates depend on the availability and quality of clinopyroxene phenocrysts, which, ideally, are in equilibrium with their host liquid. Clinopyroxene phenocrysts from the welded ignimbrite (NCW_F) were not in equilibrium with their host liquids. In addition, they had an abundance of Fe cations and a deficiency in Al cations, which resulted in them

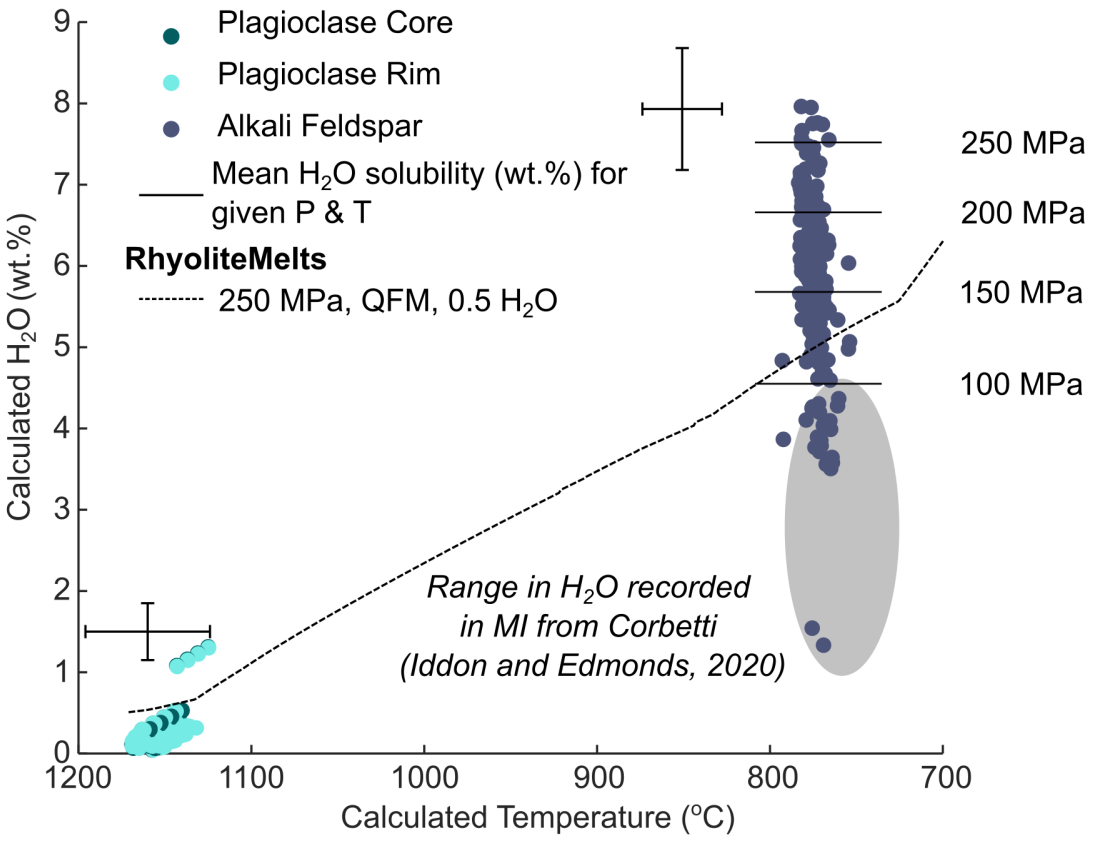

Figure 3.14: Calculated temperatures and water contents of plagioclase-liquid pairs and alkali feldspar liquid pairs. Data overlain with RhyoliteMELTS output which best match the natural composition of the welded ignimbrite. Grey region shows the range in H_2O contents found in quartz-hosted melt inclusions from Corbetti (Iddon and Edmonds, 2020). The gap between the melt inclusion data and the petrological hygrometry likely suggests melt inclusion volatile contents may have been reset prior to eruption. Solid lines reflect H_2O solubility in a rhyolitic melt calculated using the method of Allabar et al. (2022).

being excluded from the analysis as the model is not calibrated for these compositions are regards them as bad analyses.

Clinopyroxenes in the crystalline enclave found in NCW_F did pass the quality check; however, no liquid compositions from the enclave could be analysed. Therefore, we conducted clinopyroxene-only barometry using Jorgenson et al. (2022) random forest machine learning algorithm. Mean temperatures and pressures were calculated and ranged from 1065 to 1110 ± 72.715 °C and 70 to 220 ± 320 MPa, respectively. The large error associated with the pressure estimates results from the calibration set used in the model (Jorgenson et al., 2022) and uncertainties associated with clinopyroxene-only thermobarometers. Tadesse et al. (2023) note that the clinopyroxene-only thermometer of (Jorgenson et al., 2022) overestimates temperatures in peralkaline systems compared with other thermometers however, the results here are in good agreement with other estimates of pressure (Gleeson et al., 2017). Further experimental work on alkali clinopyroxenes in peralkaline melts would greatly improve the calibration datasets for these models.

3.3.5 RhyoliteMelts

The results from each RhyoliteMELTS simulation are compared with the natural whole-rock compositions reported in Colby et al. (2022) and the samples of Fontijn et al. (2018) using the methodology of Gleeson et al. (2017). This allowed us to constrain the likely conditions under which Corbetti's magmas have evolved (Table 3.3 & Figure 3.15). Based on the best fit models, pressures ranged from 100-250 MPa, with most samples evolving at 250 MPa. Redox conditions for pre-caldera deposits varied at or above the QFM buffer however, the redox conditions of post-caldera units were found to be at or below the QFM buffer. Initial H_2O concentrations are consistent at around 0.5 wt.%. There is a considerable variation in the calculated residuals for each target composition, which reflects the deficiencies RhyoliteMELTS has in resolving certain oxide concentrations in these extreme peralkaline systems (Fowler and Spera, 2010; Rooney et al., 2012). This also may reflect that the basaltic compositions recorded within the tuff are not reflective of the parental magma source for the peralkaline magmas at Corbetti.

The outputs of these simulations were also compared to the glass compositions recorded in the basaltic tuff (NCW_H) using the same approach. However, the methodology of Gleeson et al. (2017) assumes the target compositions are all from the same unit and therefore have a relatively similar composition with a small standard deviation. When

Table 3.3: Results of RhyoliteMELTS simulations showing the likely conditions under which magmas at Corbetti evolved and their associated residual. The residual is calculated using the method of Gleeson et al. (2017) $\sum_X^m(\sum_i^n(X_i - \hat{X})^2/X_{SD})_X$, where n is the number of natural samples that represent the target composition, m is the number of oxides considered, X_i is the concentration of oxide X of sample i, $\hat{X}$ is the concentration of oxide X predicted by RhyoliteMELTS at a particular temperature, X_{SD} is the standard deviation of oxide X of all empirically determined compositions of natural samples representing the target composition.

Sample	**Pressure (MPa)**	**fO_2**	**Initial H_2O (wt.%)**	**Residual**
CO5	200	QFM-1	0.5	54.38
WKYP	150	QFM-1	0.5	67.96
Bedded Pumice	250	QFM	0.5	40.28
Biftu Tuff Cone	250	QFM	0.5	42.77
CC_B	250	QFM-2	0.5	23.05
CC_C	250	QFM-1	0.5	17.02
CG_A	250	QFM	0.5	5.24
CG_E	100	QFM	0.5-2	546.38
US_B	200	QFM-1	0.5	27.65
US_C	250	QFM-1	0.5	80.71
Urji Lava	250	QFM-1	0.5	34.42
Site 8	250	QFM+1	0.5	27.46
SCW_A	250	QFM	0.5	24.73
Older Obsidian	250	QFM+1	0.5	25.96
Older Pumice	250	QFM+1	0.5	27.46
Fontijn et al. (2018) Glass compositions	250	QFM	0.5	227.42

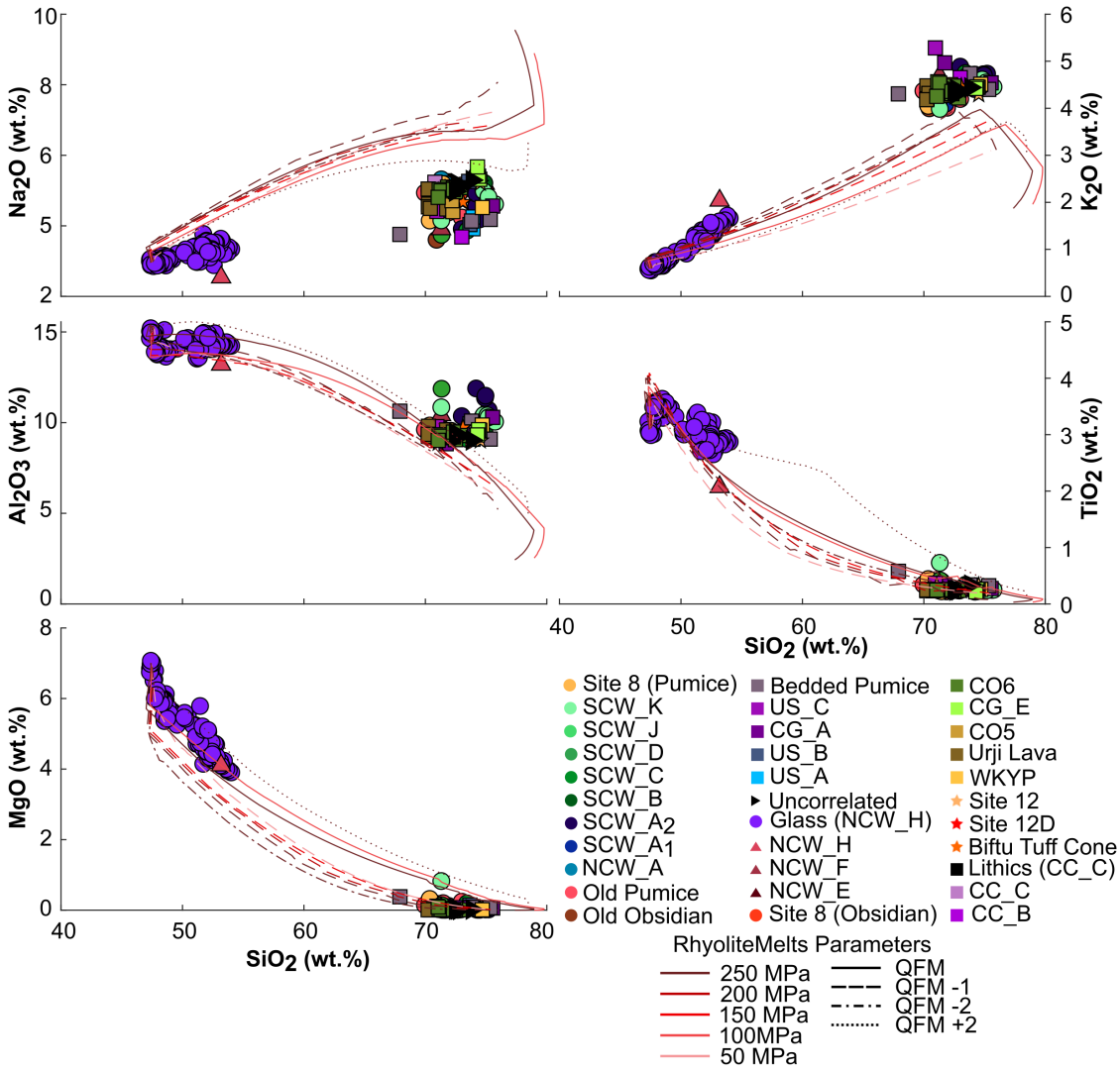

Figure 3.15: Comparing the output of the RhyoliteMELTS runs which most closely match the natural compositions found at Corbetti. RhyoliteMELTS provides a good fit for certain oxdies; however consistently under-predicts the concentration of Na_2O and over estimates K_2O compared with natural samples. This may suggest that this basaltic composition is not reflective of the parental basalts from which the peralklaine products are differentiated.

considering the wide range of compositions within the basaltic tuff, a decision must be made on whether to treat the dataset as a whole or subdivide it. Based on the glass chemistry, it is clear there is a high chemical diversity (section 3.3.1) which, if the dataset was treated as a whole, would yield a high standard deviation and a poor fit. As samples above ~ 50 wt.% SiO_2 show considerable scatter which may be associated with processes such as magma mixing or crustal contamination, these have not been compared with the outputs of the RhyoliteMELTS modelling. Glass shards with < 50 wt.% SiO_2 evolved at one log unit below the QFM buffer, with an initial H_2O content of 0.5 wt.% stored at 100 MPa.

3.4 Discussion

3.4.1 Basaltic Eruption

The basaltic tuff (NCW_H) is the only basaltic eruption product currently recorded within Corbetti Caldera. The eruption was phreatomagmatic, likely interacting with groundwater or a pre-existing intra-caldera lake (Colby et al., 2022). This generated multiple dilute PDCs, forming laminated deposits, some of which are preserved in the northern caldera wall. The weakly peralkaline obsidian chips found within the sample have a very similar composition to the obsidian flows found outside the caldera wall (Older Obsidians of Colby et al. 2022; Figure 3.4). This suggests the magma likely erupted through an obsidian dome/flow emplaced during the pre-caldera phase of activity. Glass shards vary from basaltic to basaltic-andesite, with limited variation in composition within individual shards. The compositions recorded in the basaltic tuff reflect a fractional crystallisation trend (Figure 3.5), however, evolved samples (> ~50 wt.% SiO_2) show increased scatter in certain oxides (Na_2O, CaO, TiO_2 and MnO; Figure 3.5). The cause of this variation is unclear. It may be due to analytical issues, however there is no discernible decrease in Na_2O concentration with decreasing analytical totals indicating Na loss is unlikely the cause. These compositions may reflect magma stored in distinct melt lens which has undergone some mixing or contamination prior to eruption. Figure 3.4 shows an overview of basaltic compositions from a selection of the calderas within the MER. It demonstrates some heterogeneity in erupted compositions across the rift, especially with respect to total alkali content. Corbetti's basaltic compositions have a slightly lower overall alkali content compared with some rift volcanoes, however are comparable with those erupted from Aluto and Gedemsa. These lower alkali contents may explain the observed discrepancy between

modelled Na_2O and K_2O concentrations from RhyoliteMELTS and natural samples (Figure 3.15). This discrepancy was not observed by Gleeson et al. (2017) and therefore may reflect that this basaltic unit does not accurately reflect the parental basalt from which the peralkaline products are derived. In the absence of other basaltic eruptions recorded at Corbetti, this is difficult to test; however, the lower concentration of alkali elements in this unit compared with other basalt's from the MER may support this hypothesis. Further field investigation would be necessary to attempt to identify additional basaltic eruptions within the caldera to explore this hypothesis further.

A variable degree of zonation is observed in most olivine phenocrysts with around 2 wt.% variations in MgO between the rim and the core (Figure 3.12). This may indicate that some magma mixing occurred before the eruption. It is likely that two basaltic magma bodies, at different stages of differentiation, experienced some mixing. Most olivine rims have started to equilibrate with the co-erupted glass suggesting the mixing was progressive and occurred sometime before the eruption. Some phenocrysts show no zoning but are not in equilibrium with their host glass, suggesting they were incorporated into the system immediately before eruption and quenching. There are rare instances of reversely zoned olivines suggesting limited transfer between the more evolved region and the more primitive melt. In addition, a bimodal distribution in An contents in plagioclase phenocryst cores is observed (Figure 3.10), whilst the rim compositions have a more consistent An content. This suggests plagioclase phenocrysts may have initially crystallised in two batches of melt, which were then mixed and began to equilibrate towards an average An content. These two magma bodies did not fully mix, thus preserving a fractional crystallisation trend and a bimodal distribution of SiO_2 contents (Figure 3.5). It is possible there was an injection of more mafic magma immediately before the eruption, as recorded in rare phenocrysts in showing no zonation and in disequilibrium with the co-erupted glass; however, there are insufficient minerals recording this to provide conclusive evidence. In addition to this, the presence of alkali feldspars and alkali clinopyroxenes suggests scavenging or entrainment of felsic phases into the melt, potentially from a crystalline mush, before the eruption. Temperatures determined from olivine-liquid pairs, plagioclase-liquid pairs and glass-only thermometry, show a gradual decrease in melt temperature from 1200 °C to ~1100 °C, consistent with a cooling and fractional crystallisation trend. These estimates also agree with olivine crystallisation temperatures in the MER (Wong et al., 2022).

The water contents determined for Corbetti's basaltic magma (0 - 1.2 wt.% H_2O) add to the sparse dataset on H_2O contents in basaltic magmas from volcanoes in the MER. These data are consistent with estimates from olivine-hosted melt inclusion from Kone and

Butajira (0.2 - 1.5 wt.%) (Iddon and Edmonds, 2020) and with H_2O contents in transitional basaltic melts and alkali basalts from Pantelleria, Italy (White et al., 2009; Gioncada and Landi, 2010; Neave et al., 2012; Gleeson et al., 2017) . This hygrometry also supports the results of the RhyoliteMELTS modelling (section 3.3.5, Table 3.2), which indicated an initial H_2O content of 0.5-1 wt.% and is consistent with the results of RhyoliteMELTS modelling on other silicic systems in the MER (Gleeson et al., 2017). This demonstrates that whilst RhyoliteMELTS has limitations when investigating peralkaline melts (Gleeson et al., 2017; Romano et al., 2020), it does offer a good approximation of the initial starting H_2O composition. This finding helps to support previous studies which have exclusively used RhyoliteMELTS to infer the initial water content of alkali basaltic magmas (Gleeson et al., 2017).

The estimated storage depth of the basaltic magma (100 MPa) from RhyoliteMELTS modelling is significantly shallower than geophysical estimates of the depth of alkali basalt injection into the Corbetti magma system (Gottsmann et al., 2020). This may relate to the limitations of RhyoliteMELTS, and in the absence of mafic melt inclusions or a suitable barometer to validate this finding, we anticipate this pressure estimate to be an underestimate.

In summary, our findings indicate basaltic pre-eruptive temperatures at Corbetti are consistent with other estimates for the MER and peralkaline systems elsewhere. Glass compositions recorded a fractional crystallisation trend; however, a portion of the more evolved glass shards (> 50 wt.% SiO_2) likely underwent a degree of magma mixing or crustal contamination resulting in lower Na_2O, MnO and P_2O_5 concentrations. Evidence from olivine and plagioclase phenocrysts and the presence of more felsic phases (alkali clinopyroxenes and alkali feldspars) indicate some degree of magma mixing and/or scavenging of phenocrysts from portions of melt at different stages of differentiation. The presence of olivines with high Fo contents (Fo_{80}), which do not display any zoning, could indicate that a batch of primitive magma was injected into the system shortly before it erupted. In addition, we constrained the H_2O content of the alkali basalt to around 0.5 wt.%, which is consistent with estimates from olivine-hosted melt inclusions from the MER and with RhyoliteMELTS modelling presented in this study and previous studies on calderas in the MER (Gleeson et al., 2017).

3.4.2 Peralkaline Magmas

Our RhyoliteMELTS observations support those of previous studies, indicating ~90% fractional crystallisation is needed to reach these peralkaline compositions (Gleeson et al., 2017). Estimated temperatures (~793 °C) are in good agreement with pre-eruptive temperatures for peralkaline magmas at other centres in the MER (Gleeson et al., 2017; Tadesse et al., 2023). The characteristic depletion in Ba and Sr is observed (Figure 3.7), indicating the fractionation of alkali feldspars, a key component of peralkaline melts (Carmichael and MacKenzie, 1963; Macdonald et al., 2021; White et al., 2023). Incompatible trace element plots highlight the role of fractional crystallisation in the evolution of Corbetti's magmas (Figure 3.6). However, Figure 3.6 shows a considerable scatter in the concentration of Nb, with some samples showing elevated Zr/Nb ratios of up to 20. For instance, samples from the WKYP unit show relatively constant Zr values but decreasing Nb (Figure 3.6). In addition, samples with high Zr/Nb ratios also exhibit higher Zr/Hf ratios. In general, Zr/Hf ratios for Corbetti (40-52) are slightly elevated relative to the average for the rift (~40); however, samples with a high Zr/Nb ratio also display the highest Zr/Hf ratios (57-72).

High Zr/Nb values have been attributed to the crystallisation of ilmenite (Hutchison et al., 2018); however, these data may indicate a differing source composition when viewed alongside the high Zr/Hf ratios. This may indicate some heterogeneity in source compositions at Corbetti, where basaltic magmas have variable initial Nb, Hf and Ta concentrations and have followed different liquid lines of descent to reach a near-homogenous, in terms of major element compositions, endpoint.

The trace element data presented here (Figure 3.6) indicates that fractional crystallisation was the dominant evolutionary mechanism, with crustal assimilation unlikely to play a role. This is supported by Sr isotope analysis (Table 3.3) on samples that span the major pre- and post-caldera eruptions, which do not indicate that crustal assimilation occurred during these magmas' evolution. The only exception is the ignimbrite associated with the caldera-forming eruption (NCW_E), which shows an elevated signature ($^{87}Sr/^{86}Sr$ 0.706) likely due to contamination by country rock during the eruption. It also may reflect a higher rate of magma flux in the lead up to this eruption, transferring more heat into the upper crust and leading to a higher degree of assimilation of the country rock. This could also explain the lower incompatible trace element compositions reported for this unit (Figure 3.7). This elevated $^{87}Sr/^{86}S$ ratio is observed by Rapprich et al. (2016), who proposed this is the result of 0.5 % contamination by the Ethiopian basement ($^{87}Sr/^{86}Sr \sim 0.731$; Peccerillo et al. 1998). Other samples show a slight variation in isotopic ratios (between $^{87}Sr/^{86}Sr$ 0.704 and

0.705), which may indicate some heterogeneity in magma compositions or a small degree of crustal assimilation; however, these values fall within the MER's expected range and aligns with the previous data (Figure 3.8). It should be noted however, that whole rock analysis for $^{87}Sr/^{86}Sr$ ratios in peralkaline rhyolites can return heterogeneous results for a single sample even in fresh aphyric samples (Deniel, 2009). Deniel (2009) proposed that small changes in $^{87}Sr/^{86}Sr$ ratios may reflect interaction with magmatic fluids prior to eruption as opposed to a crustal signature. The small hetrogenaities seen in Corbetti's eruptive products may reflect interaction with fluids rather than crustal contamination however, further investigation is required to evaluate this hypothesis.

As our understanding of the evolutionary conditions of peralkaline magmas has increased, it is clear these extreme compositions can be achieved under varying storage conditions. Geophysical and petrological investigations in the rift highlight storage zones at multiple depths in the crust where peralkaline magmas can be generated (Gleeson et al., 2017; Iddon and Edmonds, 2020; Samrock et al., 2021). This has been explained in calc-alkaline systems through the role of reactive flows where a melt in a low melt fraction mush is buffered by the surrounding crystalline phases (Dufek and Bachmann, 2010; Blundy, 2022). As the melt evolves it is extracted from the system via buoyant rise or compaction and erupted. This process could explain the scarcity of minerals in most of Corbetti's products. Similarly, it would explain the evidence presented for the scavenging of alkali feldspars from melts at different stages of differentiation (Iddon et al., 2019). Further experiments are required on peralkaline melts at various pressure and temperature conditions to fully evaluate this hypothesis. There is a need to apply the advances made on calc-alkaline melts to peralkaline systems specifically related to the evolution of the magmas and extraction of predominantly crystal-free material. This requires expanding the underpinning experimental datasets, which are currently limited compared with calc-alkaline systems, through further work on peralkaline systems specifically investigating the products of the MER.

We also demonstrate that the peralkaline magmas at Corbetti may have had a pre-eruptive water content of up to 8 wt.% H_2O (Figure 3.15). This is higher than previous estimates of water contents at Corbetti obtained from melt inclusions which suggest H_2O contents of between 0.95-4.2 wt.% and CO_2 concentrations of < 330 ppm (Iddon and Edmonds, 2020). This range was determined with a small number of quartz-hosted melt inclusions, which likely underwent degassing before entrapment. Similarly, quartz-hosted melt inclusions can undergo H^+ loss via diffusion through the crystal host (Tollan et al., 2019). Although this has not been extensively studied, evidence suggests that quartz-hosted inclusions can undergo H_2O loss if they are reheated (Severs et al., 2007; Tollan et al.,

2019) lowering the measured concentration. Therefore the the low water contents reported in melt inclusions may be the result of slightly reheating after entrapment. Therefore it is likely that these inclusions were reset after entrapment in response to changes in the magma storage conditions (Stock et al., 2018). This demonstrates that whilst melt inclusions are a useful tool, they are prone to alteration from secondary processes and should be used in conjunction with other independent estimates of volatile contents.

To test the feasibility of Corbetti's magmas containing up to 8 wt.% H_2O, we calculated the solubility of H_2O (using the method of Allabar et al. 2022 for this sample at 4 different pressures, using the temperatures calculated from our thermometry (section 3.3.3). It demonstrates that up to 7.5 wt.% H_2O can be dissolved in a melt of this composition when stored at 250 MPa (Figure 3.15) and is in good agreement with other estimates of solubility from experimental studies (Schmidt and Behrens, 2008). This matches the results of the RhyoliteMELTS modelling (section 3.3.5), which indicate the magma which fed this eruption likely evolved at 250 MPa. In addition, these water contents match those of other peralkaline systems in the MER, with melt inclusions from Aluto recording a maximum of 8 wt.% H_2O (Iddon and Edmonds, 2020).

In summary, the rarity of melt inclusions in Corbetti's eruptive products makes it challenging to understand the magma storage system, particularly when no primitive or intermediate melt inclusions are recorded. Therefore, using alkali-feldspar hygrometry provides insight into the likely hydrous nature of these melts. In the case of Corbetti, the high-water contents are likely the main driving force behind volcanic eruptions, as the shallow storage region would result in the majority of CO_2 being degassed before an eruption.

3.4.3 Depth of Magma Storage

Determining the magma storage depth at Corbetti through petrological analysis is challenging due to the lack of suitable crystal phases and the significant error associated with single-phase thermobarometry. As outlined in section 3.3.4, clinopyroxene-only barometry determined pressures of between 70 to 220 ± 320 MPa. These estimates are similar to clinopyroxene-only barometry calculations at Bora Baricha - Tullu Moye with estimated storage depths of < 200 MPa (Tadesse et al., 2023). In addition, they agree with our findings from RhyoliteMELTS modelling (section 3.3.5), which suggest magma at Corbetti has been stored at pressures ranging from 100-250 MPa, with most magma likely stored at depths

greater than 200 MPa (Table 3.3). This corresponds to depths of 3.6-9.1 km using a density of 2800 gm^{-3} (Wilks et al., 2017). This is slightly deeper than previously determined for other peralkaline systems in the rift using RhyoliteMELTS (e.g., ~150 MPa at Aluto; Gleeson et al. 2017; however, it does cover the range of the pressure estimates for Aluto (50-300 MPa) determined from quartz-hosted melt inclusions (Iddon and Edmonds, 2020). Magma is likely stored across the depth range within a crystalline mush at a resolution which currently cannot be determined through petrological techniques.

Comparing our findings with geophysical observations from Corbetti shows a good alignment between the various techniques (Figure 3.16 & Table B.2). Geophysical and magnetotelluric observations have also shown a shallow hydrothermal system at ~1-2 km depth and multiple structures beneath the caldera (Lloyd et al., 2018a). The two most prominent are an east-west striking strike-slip fault, thought to predate the caldera (Lloyd et al., 2018a), and a 0.5-1 km thick clay cap at ~0.2 km depth and deepening to the north of the caldera (Gíslason et al., 2015). These features likely influence the migration of fluids and magma at shallow depth (Lloyd et al., 2018a).

Magnetotelluric data have also shown the presence of a hot conductive layer around 5-15 km deep (Gíslason et al., 2015; Wilks et al., 2017; Lloyd et al., 2018a) interpreted as a region of partial melt (Figure 3.16; Gíslason et al. 2015). In addition, numerical modelling investigating the causes of the observed uplift at Corbetti (Lloyd et al., 2018a) concluded that the injection of mafic magma at ~7 km depth could explain the observed deformation (Gottsmann et al., 2020). Similarly, analysis of CO_2 and H_2O concentrations in quartz-hosted, peralkaline melt inclusions from Corbetti found they were likely trapped at pressures of 100 - 150 MPa (Iddon and Edmonds, 2020).

Whilst the data on storage depths at Corbetti is limited and, in some cases, has high associated uncertainties, we show that the methods employed in this study align well with other independent petrological and geophysical observations (Figure 3.16) demonstrating the importance of shallow pressures in the evolution of peralkaline systems. It also demonstrates the need for further experimental studies to focus specifically on peralkaline products from the MER to gain a better petrological understanding of the phase relationships and storage conditions at silicic volcanoes in the MER.

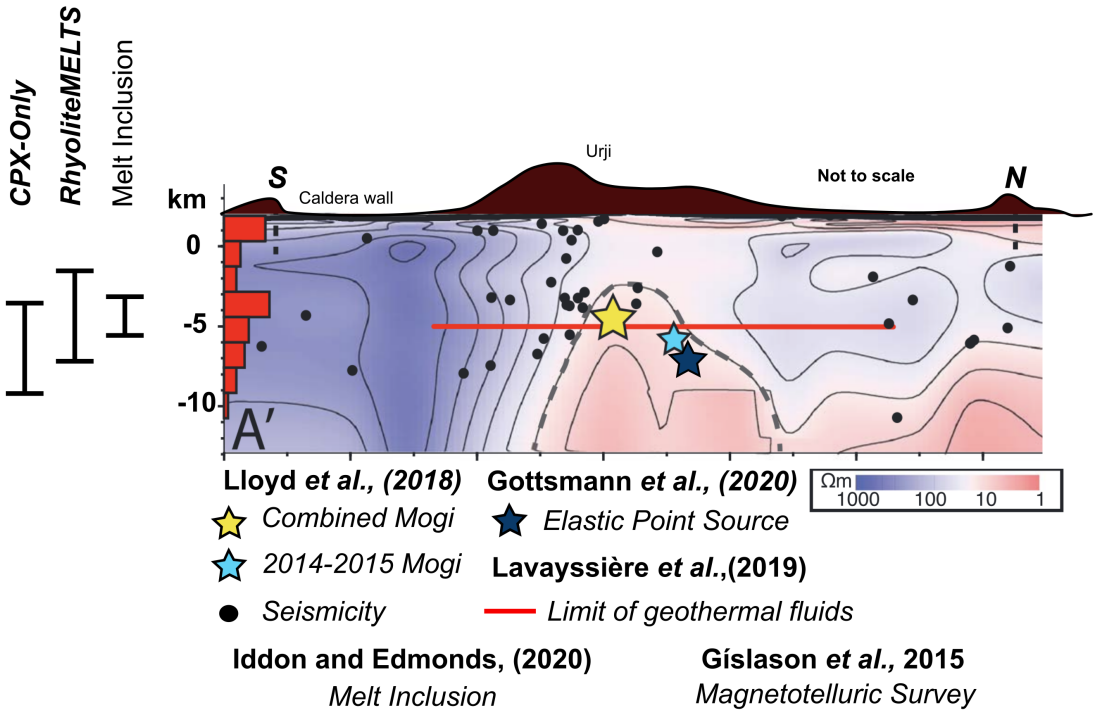

Figure 3.16: Schematic overview of estimated magma storage depths at Corbetti combining petrological and geophysical techniques. Details can be found in Table B.2. CPX-only barometry has a high associated error or 320 MPa; however, results are in good agreement with geophysical observations. The magnetotelluric survey places the top of the conductive hot zone at around 5 km (Gíslason et al., 2015). Seismic surveys also suggest the presence of geothermal fluids at < 5km depth in the crust (Lavayssière et al., 2019). Figure adapted from Lloyd et al. (2018a) with data from this study and recent geophysical studies overlain.

3.5 Conclusion

Here we report the results of RhyoliteMELTS modelling and petrological investigation of the endmember compositions at Corbetti Caldera in the MER. We demonstrate that the erupted basaltic magmas were likely tapped from two melt regions at different differentiation stages that underwent some mixing. The more evolved lens also likely underwent some alteration affecting the concentration of Na in the melt. RhyoliteMELTS modelling and hygrometry agree that the initial water content of this melt was between 0.5-1 wt.%. RhyoliteMELTS modelling and trace element geochemistry indicate that Corbetti's magmas likely evolved through progressive fractionation, and $^{87}Sr/^{86}Sr$ isotope values rule out the role of crustal assimilation. Temperatures were estimated for the basaltic tuff using olivine-liquid thermometry, which yielded results in agreement with other studies in the MER (Wong et al., 2022).

Hygrometry on the peralkaline end member estimated water contents of up to ~8 wt.%. Although higher than previous estimates for Corbetti, it does agree with other data from peralkaline systems in the MER and globally. Although further constraints on the volatile contents of Corbetti's magmas are needed, particularly regarding the halogen contents, this data does highlight the hydrous nature of Corbetti's magmas and demonstrates the important role H_2O plays in the explosive eruption of these magmas.

Overall, the scarcity of crystalline phases at Corbetti hampers efforts to petrologically resolve the magmatic processes governing evolution compared with other silicic centres in the MER. However, it highlights the efficacy of crystal-melt segregation processes in these highly differentiated systems. Further work is required to investigate these processes in peralkaline systems.

There are still considerable uncertainties surrounding estimating magma storage depth within peralkaline systems using standard modelling or petrological techniques. Currently, geophysical estimates provide the best insight into magma storage beneath Corbetti, with further experimental work needed to refine the current barometers to apply to these shallow magmatic systems with a particular focus required on the products of the MER.

3.6 Acknowledgements

This work was supported by the Natural Environment Research Council via grant NE/L013932/1 (RiftVolc) and an Oxford DTP studentship (NE/L002612/1) to D.C. K.F. acknowledges Fonds National de la Recherche Scientifique (F.R.S.-FNRS) MIS grant F.4515.20. K.F., D.P. and T.M. acknowledge the Wiener Anspach Foundation grant "The Magmatic Evolution of Geothermally Active Calderas in Ethiopia". We would like to thank Seid Abubaker of Ethioder and guide Hamiyou Bekera for their support in the field and for ensuring a safe and productive field trip. Fieldwork and sample export were kindly permitted by the authorities of the Oromia region and the Ministry of Mines and Petroleum of Ethiopia, respectively. We would also like to thank Owen Green for his help with sample preparation and microscopy, Matthew Beverley Smith for making the thin sections of selected samples, Dr Andrew Matzen for his help and support in setting up and using the EMPA, Activation Laboratories for undertaking the whole rock geochemical analysis, and Wendy Debouge and Jeroen de Jong for Sr isotope analysis.

Chapter 4

Diversity in Peralkaline Magmas across the Main Ethiopian Rift

Abstract

Peralkaline magmas dominate the eruptive products of the Main Ethiopian Rift (MER), making it an ideal place to study the chemical variability of these enigmatic compositions. Previous work on Corbetti Caldera has demonstrated that its eruptive products occupy a very narrow compositional range compared with other silicic centres in the MER. Here we explore the chemical variability of peralkaline magmas erupted from several large caldera systems in the MER using the parameter Qz* (Qz* = 100*Qz_n/[Qz_n+Or_n+Ab_n] where Qz_n, Or_n and Ab_n are the CIPW norm components). We define the major trends and compile information on the mineral phases present in the eruptive products. We demonstrate that peralkaline magmas occupy a diverse compositional space, and we identify several trends in major element data. We employ mass balance modelling to determine the mineralogical control of these trends and compare this with naturally observed assemblages. We highlight how using traditional discrimination diagrams and discretely classifying peralkaline products at pantellerite or comendite can mask important features of a magma's liquid line of descent. We also investigate these magmas through the lens of the Qz-Or-Ab-Ns-Ac residua system and demonstrate that data project onto two different experimentally determined cotectics. We conduct mass balance modelling to define the mineralogical control on the observed trends in the data and show the composition and quantity of alkali-feldspar fractionating alongside the presence or absence of alkali-clinopyroxene compositions will dictate which cotectic the magma will follow. This work draws out key variations in peralkaline compositions across the MER, the mineralogical control on observed geochemically trends, and demonstrates that further experimental investigation of products from the MER is necessary to fully understand the phase relationships and differing liquid lines of descent found within these systems.

4.1 Introduction

Peralkaline volcanism involving magmas or melts with molar $(Na_2O+K_2O)/Al_2O_3 > 1$ account for up to 90% of the erupted products within the Main Ethiopian Rift (MER) (Trua et al., 1999; Macdonald et al., 2021), making it an ideal location to study the processes governing the evolution of these enigmatic magma compositions. As an eruption at a peralkaline volcano has not currently been witnessed, our understanding of the nature of these enigmatic magmas is based upon the study of eruptive deposits (e.g Hutchison et al. 2016c, Fontijn et al. 2018, McNamara et al. 2018, Clarke et al. 2019, Colby et al. 2022, Tadesse et al. 2022), investigation of the rheology of these magmas (Di Genova et al., 2013; Hughes et al., 2017), their geochemical variation (Hutchison et al., 2018; Jeffery and Gertisser, 2018; Macdonald et al., 2021) and experiments and modelling of the processes behind their generation (e.g Peccerillo et al. 2007, Di Carlo et al. 2010, Rooney et al. 2012,Romano et al. 2018, Tadesse et al. 2019,Romano et al. 2020, Tadesse et al. 2023). A characteristic feature of calderas across the MER is the dominance of peralkaline rhyolites with minor occurrences of alkali basalts and rare intermediate compositions recorded in enclaves (Peccerillo et al., 2003, 2007; Rooney et al., 2012; Hutchison et al., 2016c; Fontijn et al., 2018; Iddon et al., 2019; Tadesse et al., 2019, 2023). Despite erupted products being restricted to basaltic and rhyolitic compositions, the peralkaline magmas found across the rift show a high degree of geochemical diversity, highlighted in Figure 4.2 and Figure 4.3. However, considerable variation exists in the range of erupted compositions found within the different volcanic centres. Recent work on the eruptive history and storage conditions at one silicic centre, Corbetti caldera (Figure 4.1), has revealed a lack of geochemical diversity in its eruptive products over its > 182 ka eruptive history (Fontijn et al., 2018; Colby et al., 2022, Chapter 3). Like many MER calderas, Corbetti is dominated by peralkaline rhyolite compositions, with only a single basaltic eruption recorded (Mohr, 1966; Macdonald and Gibson, 1969; Di Paola, 1972; Rapprich et al., 2016; Fontijn et al., 2018; Colby et al., 2022, Chapter 3). However, the peralkaline products at Corbetti have a considerable lack of diversity compared with similarly well-sampled systems such as Gedemsa and Boset.

Major and trace element data, in conjunction with isotopic data and RhyoliteMELTS modelling, indicate that the progressive fractionation crystallisation of alkali basalt is the primary control on magma evolution in the rift (Peccerillo et al., 2007; Rooney et al., 2012; Hutchison et al., 2016c; Gleeson et al., 2017, Chapter 3). Some centres show a minor degree of crustal assimilation influencing magma evolution (Peccerillo et al., 2003; Giordano et al., 2014; Hutchison et al., 2018); however, it is not thought to have a

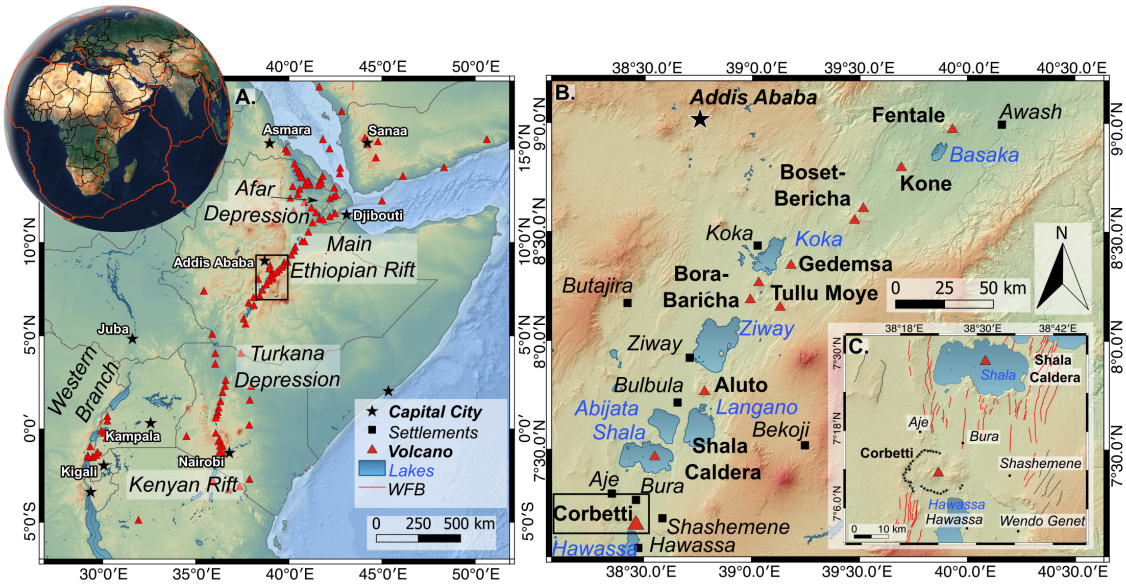

Figure 4.1: (A) Map showing the location of the MER, which forms part of the wider East African Rift system, and (B) the location of peralkaline complexes, which form the focus of this study.(WFB after Agostini et al. 2011
).

dominant impact. Studies investigating the storage conditions of peralkaline magmas in the rift using petrological methods, thermodynamic modelling and experimental studies have demonstrated the necessity for shallow storage depths (100 - 250 MPa) (Di Carlo et al., 2010; Hutchison et al., 2016c; Gleeson et al., 2017; Romano et al., 2020; Tadesse et al., 2023) and redox conditions at or below the QFM buffer. This is consistent with geophysical observations, which have identified shallow conductive zones at 5-7 km depth (~150-200 MPa) beneath several silicic calderas (Gíslason et al., 2015; Hutchison et al., 2016c; Lloyd et al., 2018a; Samrock et al., 2021; Nigussie et al., 2023) interpreted as magma bodies.

The dominance of fractional crystallisation allows us to explore the mineralogical controls on the generation of peralkaline magmas and investigate the different liquid lines of descent, resulting in the diversity in compositions observed. Here we focus on the peralkaline products found at several MER volcanoes based on data presented on Corbetti (Colby et al., 2022, Chapter 3) and published data: Fantale, Kone, Boset, Boku, Gedemsa, Bora Baricha, Tullu Moye and Corbetti (Figure 4.1). These centres have undergone a range of explosive and effusive eruptions, with many experiencing at least one large-scale, caldera-forming eruption (Rampey et al., 2010; Hutchison et al., 2016b,c; Fontijn et al., 2018; Colby et al., 2022; Tadesse et al., 2022; Vidal et al., 2022a).

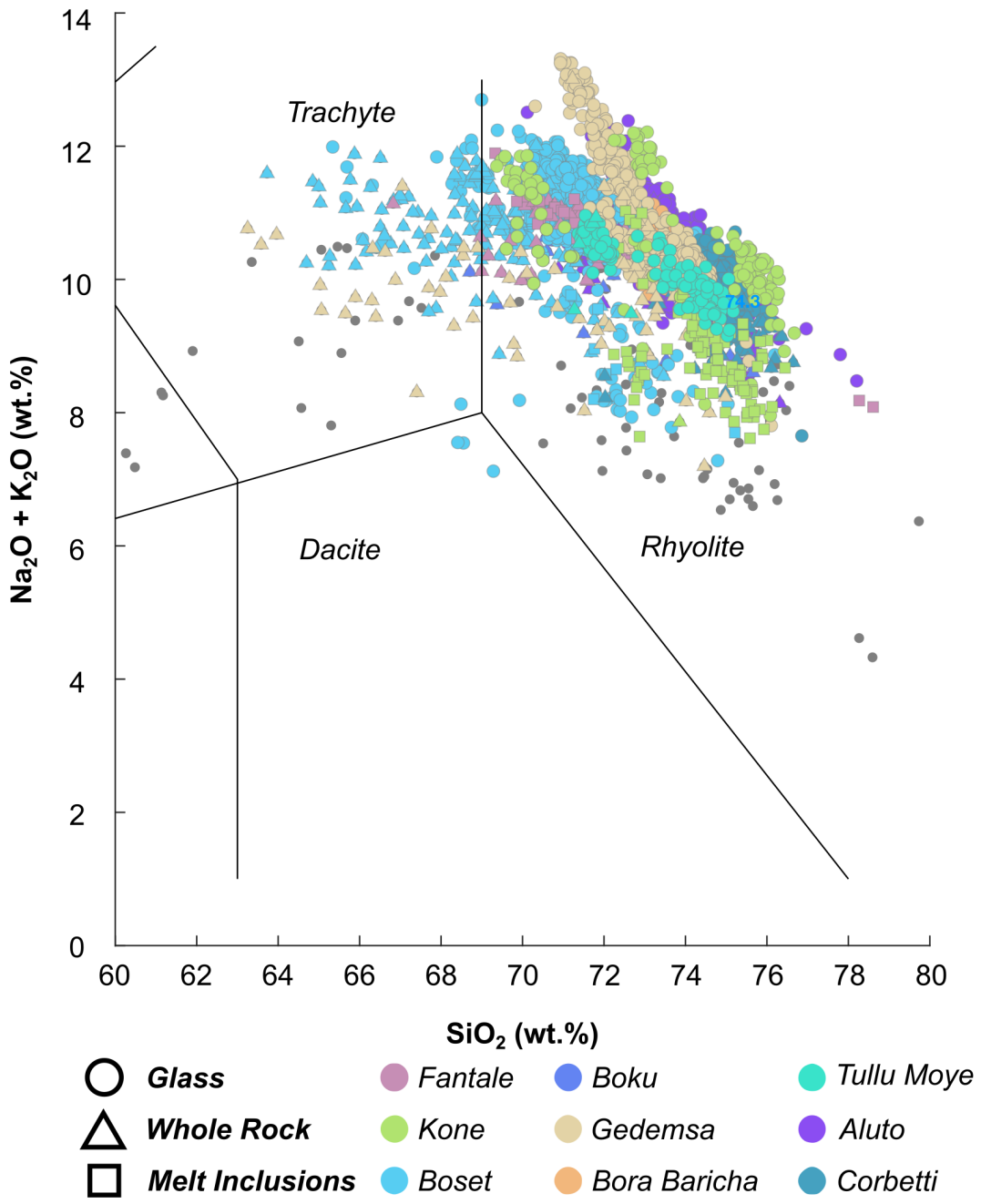

Figure 4.2: Total alkali-silica diagram showing the range in evolved peralkaline compositions across the MER. Fentale: Gibson (1972); Webster et al. (1993); Giordano et al. (2014), Kone: Peccerillo et al. (2007); Fontijn et al. (2018); Iddon and Edmonds (2020), Boset: Brotzu et al. (1980); Ronga et al. (2009); Macdonald et al. (2012); Fontijn et al. (2018), Boku: Boccaletti et al. (1995); Tadesse et al. (2023), Gedemsa: Boccaletti et al. (1995); Barberio et al. (1999); Yirgu et al. (1999); Peccerillo et al. (2007); Giordano et al. (2014); Fontijn et al. (2018), Bora Baricha Fontijn et al. (2018), Tullu Moye: Di Paola (1972); Trua et al. (1999); Fontijn et al. (2018), Aluto Teklemariam et al. (1996); Trua et al. (1999); Hutchison et al. (2016c); Gleeson et al. (2017); Fontijn et al. (2018), Corbetti: Macdonald and Gibson (1969); Di Paola (1972); Rapprich et al. (2016); Fontijn et al. (2018); Colby et al. (2022)

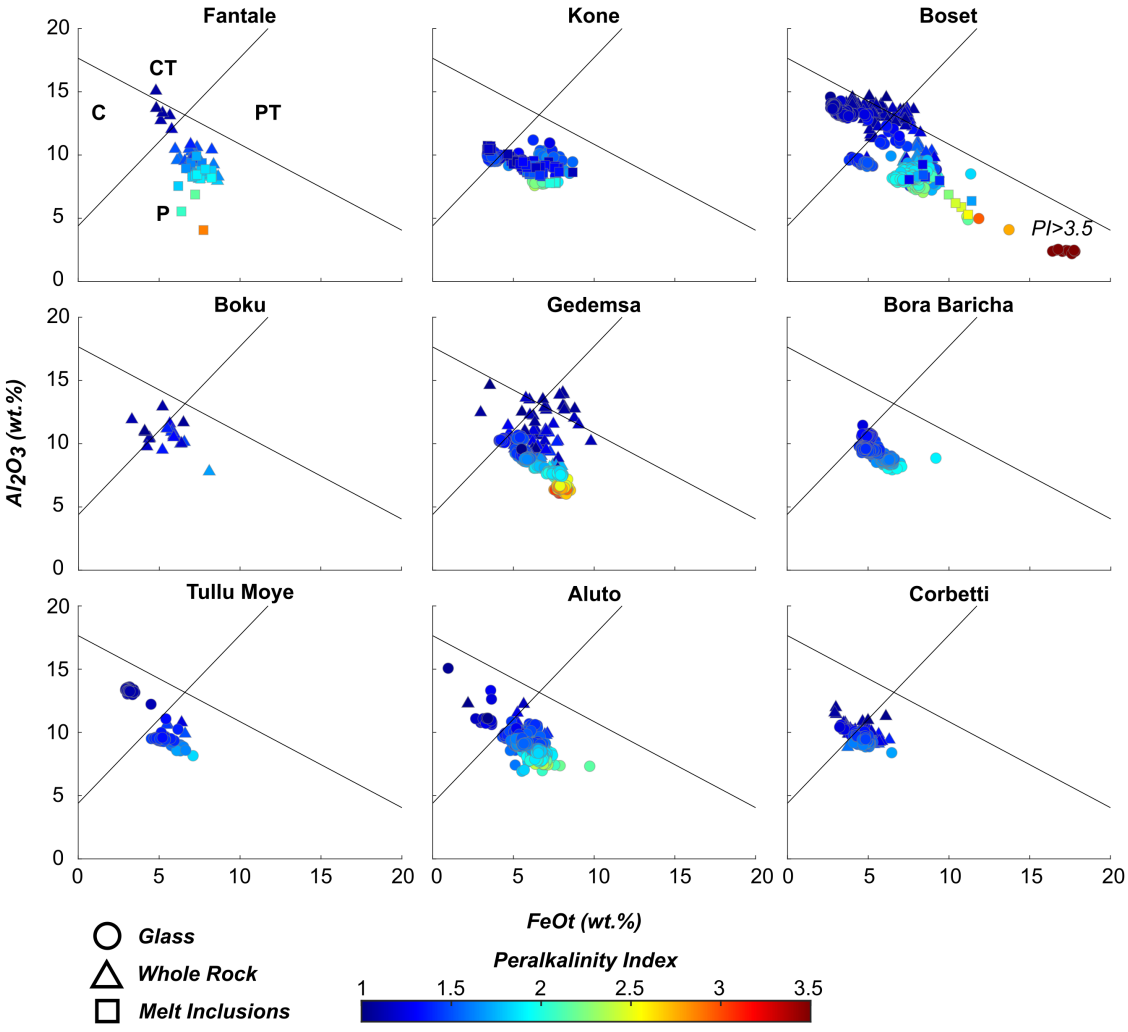

Figure 4.3: Classification plot after Macdonald (1974) of whole rock, glass, and melt inclusion data showing the range in peralkaline compositions reported across the MER and within individual volcanic centres. Plots (top left to bottom right) are ordered from north to south along the rift. PT: Trachytic pantellerite, CT: Trachytic comendite, P: Pantellerite, C: Comendite. The symbols are coloured by their peralkalinity index (molar $(Na_2O+K_2O)/Al_2O_3$).

4.1.1 Peralkaline Magmas

Peralkaline magmas have traditionally been subdivided into comendites and pantellerites based on their respective concentrations of Al_2O_3 and FeOt (Figure 4.3; Macdonald 1974). While the trends of compositional data from individual volcanic centres on Al_2O_3-FeOt plots record differing liquid lines of descent (Figure 4.3) and the crystallisation of different mineral phases (Macdonald et al., 2011; Liszewska et al., 2018; Macdonald et al., 2021), the boundary between these compositions is arbitrary. Where it is reasonable that comendite and pantellerites belong to the same magmatic lineage, as is likely the case in the MER, discrete classification into these two categories is not always beneficial as it hides important information on the degree of differentiation the magma has undergone.

All peralkaline magmas have the potential to reach highly peralkaline compositions (PI >3) and evolve towards the effective minimum composition (EMC). This is the proposed high FeOt (~ 13 wt.%), low Al_2O_3 (~5 wt.%) endpoint for peralkaline magmas (Macdonald et al., 2021; White et al., 2023). While it is feasible for magmas to evolve past this point, they are unlikely to erupt because they are likely to be rheologically locked in the crystal mush (Macdonald et al., 2021; White et al., 2023). This evolution towards extreme peralkaline compositions depends on continued fractional crystallisation and suitable thermal conditions. In particular, alkali-feldspar fractionation is highly influential and will increase the melt's peralkalinity index. However, this increase in peralkalinity can be damped or halted by the crystallisation of Na-rich phases such as acmite ($NaFe(SiO_3)_2$) or sodic amphibole (Scaillet and Macdonald, 2006).

The fractionation of alkali feldspars in felsic magmas can be traced in the quartz (SiO_2; Qz) - orthoclase ($KAlSi_3O_8$; Or) - albite ($NaAlSi_3O_8$; Ab) residua system (where Qz, Or and Ab are the CIPW norm endmembers), with melts evolving along a 'thermal valley' towards a low-temperature point on the feldspar-quartz cotectic (Figure 4.4; Carmichael and MacKenzie, 1963; Tuttle and Bowen, 1958). The 'thermal valley' refers to the pathway a cooling magma will follow from the feldspar minima to the feldspar-quartz cotectic under fractional crystallisation (Figure 4.4). However, the Qz-Or-Ab residua system is inappropriate for peralkaline magmas (Bailey and Schairer, 1964) as the progressive fractionation of alkali feldspars causes the residual melt to become enriched in Na and increases the melt's peralkalinity, an effect which is hidden in the Qz-Or-Ab projection. This has been demonstrated in experimental results and studies of natural samples (Macdonald et al., 2012). Bailey and Schairer (1964) showed that the quartz (Qz) - orthoclase (Or) - albite

(Ab) - acmite ($NaFe(SiO_3)_2$; Ac) - sodium silicates (Na_2SiO_3; Ns) residua system better represented the evolutionary pathways of peralkaline magmas. Figure 4.4A shows a sketch of the Qz-Or-Ab-Ac-Ns ternary after Carmichael and MacKenzie (1963); Bailey and Schairer (1964). The location of the quartz-feldspar cotectic and thermal valley is shown after the experiments of Carmichael and MacKenzie (1963), for the 8.3% acmite (Ac) + 8.3% sodium silicates (Ns) plane at PH_2O = 100 MPa. Isotherms show that a cooling felsic magma crystalising alkali feldspars will track along the thermal valley towards the feldspar-quartz cotectic. Figure 4.4B shows the isobaric projection of Figure 4.4A in the cartesian system (Wilke et al., 2017) with the feldspar-quartz cotectic as defined from the experiments of Carmichael and MacKenzie (1963), and Di Carlo et al. (2010) and Romano et al. (2020). Recent work has used this residua system to investigate the liquid lines of descent at Pantelleria, Italy, combining this with experimental data to demonstrate that peralkaline magmas can evolve along several distinct liquid lines of descent towards non-unique endpoints Macdonald et al. (2012); Liszewska et al. (2018); White et al. (2023).

Here we investigate the chemical variability of eruptive products from MER, identify differing trends in major element data and project these data onto the Qz-Or-Ab-Ac-Ns residua system. We compare the observed trends from Corbetti to several peralkaline silicic centres in the MER, highlight the key differences, and incorporate this with a review of the mineralogy of peralkaline products of the MER and conduct mass balance modelling to investigate potential liquid lines of descent.

4.2 Methodology

We have compiled whole rock, glass, and melt inclusion data for nine silicic centres (Fentale, Kone, Bora Baricha, Corbetti, Aluto, Boku, Gedemsa, Tullu Moye, Boset Baricha; Figure 4.1) within the Main Ethiopian Rift from the GeoRoc database (Downloaded on 30th March 2023 `https://georoc.eu/`) (Macdonald and Gibson, 1969; Di Paola, 1972; Brotzu et al., 1974; Webster et al., 1993; Boccaletti et al., 1995; Yirgu et al., 1999; Trua et al., 1999; Peccerillo et al., 2003, 2007; Ronga et al., 2009; Macdonald et al., 2012; Giordano et al., 2014; Hutchison et al., 2016c; Rapprich et al., 2016; Fontijn et al., 2018; Tadesse et al., 2019; Iddon and Edmonds, 2020; Colby et al., 2022). The data was filtered to remove samples labelled to have undergone secondary alteration and recalculated to anhydrous compositions, normalised to 100 wt.%. CIPW norm mineral components were calculated using the R package shiny:NORRRM (González-Guzmán, 2016). Where trace element

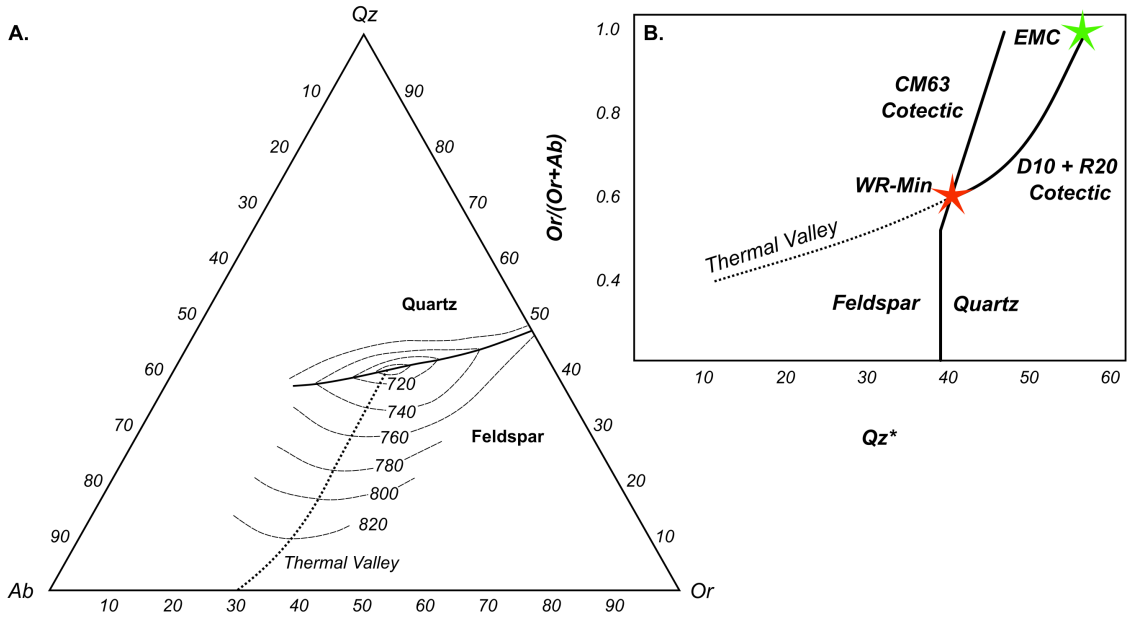

Figure 4.4: A) Sketch of the Qz-Ab-Or-Ac-Ns residua system at PH2O = 1000 bar; after Carmichael and MacKenzie (1963). The solid line shows the location of the Quartz-Feldspar cotectic in the acmite (Ac) 8.3% + Ns 8.3% system. The dotted line shows the location of the thermal valley based on experiments by Carmichael and MacKenzie (1963). Dashed lines show isotherms in °C. B) Sketch of the isobaric projection of the Qz-Ab-Or system in a cartesian form showing the change in the proportion of Or with increasing Qz*. Cotectic of Carmichael and MacKenzie (1963) (CM63) and Di Carlo et al. (2010) & Romano et al. (2020) (D10+R20) are shown for comparison (White et al., 2023). The location of the whole rock minimum (WR-Min; lowest Al_2O_3 and highest FeOt compositions of whole rock data) and effective minimum composition (EMC; Macdonald et al. 2012, Macdonald et al. 2021, White et al. 2023) is also shown.

and halogen (Cl and F) data were reported, these were included in the CIPW calculations; however these have a negligible affect on the calculated mineral components. Fe^{2+}/Fe^{3+} was recalculated using the method of (Le Maitre, 1976). We employ the term Qz* (= 100 $\times$ Qz_n/[Qz_n+Or_n+Ab_n]) where Qz_n, Or_n and Ab_n are the CIPW norm components reported in wt.% as a differentiation index (Blundy and Cashman, 2008; White et al., 2023) and to trace the crystallisation of alkali feldspar in the Qz-Or-Ab-Ac-Ns system. In addition, we also reviewed the literature, collating information on the mineral assemblages of peralkaline products from the MER and, where possible, the composition of the host rock. We have also compiled data on the reported mineral chemistry for peralkaline products from the GeoRoc database (`https://georoc.eu/`).

To investigate the mineralogical control on the liquid lines of descent at each volcanic centre, we undertake mass balance modelling using the approach of Janoušek and Moyen (2014), adapting it to use the non-negative least squares model of Lawson and Hanson (1995) through the nnls R package. This ensures that all returned mass fractions are positive. The R script used for this modelling is supplied in the supplementary information. Mass balance modelling does not provide a unique solution as results depend on the composition of the mineral phases tested and the parent-daughter compositions. Therefore, it is key to carefully select appropriate mineral assemblages and the composition of minerals to reflect the likely crystallising phases.

Similarly, selecting parent-daughter compositions is also important; therefore, we focus on data suites likely to be from the same magmatic lineage (i.e., from the same stratigraphic unit). We compiled a list of the mineral phases in the eruptive deposits and their typical compositions for each tested volcanic centre. Where mineral phases were known to occur (Table 4.2), but no analyses are reported for that centre (i.e., for phases such as apatite, Fe-Ti oxides or fayalite), we used representative compositions from a comparable system (stated in the supplementary information). For phases such as alkali-feldspar and clinopyroxene, where a range of compositions are reported, we include several compositions to reflect this range. Table 4.2 provides an overview of the inputs and parameters used in the mass balance modelling. Parent and daughter compositions are also important to consider. For parent compositions, we select the samples with the lowest FeOt or lowest Qz* value, and for the daughter compositions, we use samples with the highest FeOt, highest Qz* or highest proportion of normative Or (Or/[Or+Ab]). We select multiple parent and daughter compositions for a single unit and test every combination. Similarly, to avoid bias when selecting the likely mineral assemblages for the modelling, we implemented a routine which took selected parent-daughter pairs and tested every combination of minerals (Table 4.2),

Table 4.1: Overview of the input parameters used for the mass balance modelling and the mineral phases used.

Parent	Daughter	Minerals[1]	Results	Residual
All Major Elements Included. Parent compositions selected as having the lowest FeOt or lowest Qz* value	All Major Elements Included. Highest FeOt or Qz* value	Alkali Feldspar Quartz Clinopyroxene Fayalite Aenigmatite Apatite Biotite Amphibole Ilmenite Magnetite	Mass fraction of each mineral component	Sum of the squared residual between the known daughter composition and the modelled daughter composition

1. Several compositions for Alkali-feldspar, clinopyroxene and aenigmatite were used and details can be found in supplementary information.

starting with a two-mineral component system to a six-mineral component system. We then chose the model with the lowest residual value and the smallest number of mineral components. Mineral assemblages were then compared with the naturally observed mineral assemblages to ensure the results were feasible.

The modelled trends are shown across Figures 4.5-4.8 and 4.13 where they can be easily observed. Detailed results of the modelling are provided in the Appendix C

4.3 Results

Normative mineral components and Qz* were calculated for whole rock, glass and melt inclusion data from 9 silicic centres across the MER (See supplementary information). Figures C.2 to C.3 demonstrate the diversity of peralkaline magma compositions across the MER and within individual volcanic centres. Boset and Gedemsa, and to a lesser degree Aluto, show the highest diversity in peralkaline compositions with the widest ranges of Qz* values from ~ 5 to 70, Boset and Gedemsa have erupted some of the most differentiated peralkaline magmas recorded in the rift, with compositions approaching the effective minimum composition (EMC) (Macdonald et al., 2012). Corbetti is notable due to its lack of geochemical diversity in its' eruptive products despite being a relatively well-sampled system (Rapprich et al., 2016; Fontijn et al., 2018; Colby et al., 2022, Chapter 3). Qz*

values at Corbetti vary between ~30 to 45, with similarly restricted ranges in compositions observed at Bora Baricha; however, this system is comparatively undersampled.

Whilst using Zr concentrations is the best method for estimating the degree of crystallisation (e.g. Hutchison et al. 2018) due to the incompatibility of this element in peralkaline magmas, the dataset here comprises mostly glass compositions which have not been analysed for Zr. For whole-rock samples, Zr increase with increasing Qz* up to the whole-rock minimum composition (White et al., 2023) at Qz* 40, when Zr increases with very little change in Qz* (See supplementary information Figure C.1); however, glass data from Pantelleria shows a continued increase in Zr with increasing Qz* (White et al., 2023). Therefore, without Zr glass data, Qz* becomes a good alternative. One advantage of using Qz* as an index for differentiation is that it is a more robust parameter when investigating the evolution of peralkaline systems compared with SiO_2. It has been well-documented that SiO_2 concentrations can decrease in extreme peralkaline compositions due to the increased dominance of quartz in the fractionating assemblage (Blundy and Cashman, 2008; Wilke et al., 2017; White et al., 2023). Using Qz* allows us to identify trends in a fractionating magma that we would not otherwise be able to observe.

Previous work on peralkaline melts has demonstrated a strong negative correlation between Qz* and Al_2O_3 (wt.%) for whole rock and glass compositions (White et al., 2023). Figure C.2 demonstrates this relationship between Al_2O_3 and Qz* at several silicic peralkaline centres across the MER plotted with the regression for samples from Pantelleria for comparison. This observation allowed White et al. (2023) to propose the parameter Fe/Al* ($= 1.33 \times \text{FeOt}/(Al_2O_3\text{-}4.4)$ to track a magma's evolution through FeOt-Al_2O_3 space. Fe/Al* will increase as a peralkaline magma becomes progressively more differentiated due to decreasing concentrations of Al_2O_3 in the melt with increasing degrees of differentiation (Figure C.2). This parameter has been used to distinguish between comendite (Fe/Al* < 1) and pantellerite (Fe/Al* > 1) compositions; however, as previously noted, this distinction is arbitrary. Nevertheless, the Fe/Al* parameter may be useful in identifying potential liquid lines of descent and the compositional variability of the parental alkali basalts. Figure 4.5 plots the parameter Fe/Al* against the differentiation index, Qz*. By plotting against Qz* instead of SiO_2, we can clearly see the evolutionary pathways these magmas take. Peralkaline magmas evolve from a low Fe/Al* value towards higher Fe/Al* values with continued fractional crystallisation, and across the rift, we observe this trend; however, this trend is not linear and uniform across the different peralkaline centres. Glass compositions from Gedemsa and Boset show a progressive increase in Fe/Al* with increasing differentiation. Data from Kone, on the other hand, demonstrate that low Fe/Al* (< 1) magmas can occur at

high degrees of differentiation, up to Qz* values of 41.5. These highly differentiated, low Fe/Al* magmas are also observed at Aluto, Boset and Corbetti. Similarly, we also observe less differentiated magmas, with higher Fe/Al* values at Kone (Figure 4.5).

Figure 4.6 shows that the melt peralkalinity index (PI) is generally positively correlated with Qz*. Gedemsa, Bora Baricha and Corbetti show an increase in PI with increasing Qz*, albeit to differing degrees. This is expected, as the progressive removal of quartz and alkali feldspar during fractional crystallisation of a mildly peralkaline magma will drive the melt to increasingly more peralkaline compositions. Aluto also shows an overall positive correlation; however, there is a significant range in recorded PI for a given Qz*. In contrast, centres like Kone and Boset show a much more diverse range in PI and do not display a clear positive correlation (Figure 4.6). Boset records the most extreme peralkaline compositions currently recorded within the rift (PI = 7). Some data from these systems show weakly peralkaline samples at high differentiation (40-50 Qz*). This is observed at Kone and, to a lesser degree, at Gedemsa.

The variation in SiO_2 with Qz* also varies considerably across the rift (Figure 4.7). We generally observe an overall positive correlation; however, individual centres have interesting features. Corbetti and Aluto show a broad increase in SiO_2 with increasing Qz*; however, there is some scatter in the data. Data from Gedemsa shows a clear increase in SiO_2 with Qz* up to Qz* values of ~ 40, where we observe a reversal in the trend with SiO_2 progressively decreasing. This is also observed at Boset, but at a slightly higher degree of differentiation (Qz* $\sim$ 48), Kone shows a much more complex trend with melt inclusion data recording various SiO_2 contents at relatively constant Qz* values (Figure 4.7).

Figure 4.8 shows the variation in TiO_2 with Qz*. Here we can observe complex trends between the individual centres. Where geochemically distinct units have been identified, we see a range of TiO_2 concentrations at relatively constant Qz* values. This is seen in the glass data from Gedesma, Tullu Moye and Bora Baricha. From this data, it is difficult to discern an overall trend. Previous studies on peralkaline systems have shown decreased TiO_2 content with increasing Qz* up to a value of ~40, with strongly peralkaline samples above this point showing an increase in TiO_2 with increasing Qz* (White et al., 2023). Boset shows the most complex trends in TiO_2 of all of these systems. Three trends can be identified: (1) a decrease in TiO_2 between ~5 - 25 Qz*, (2) a decrease in TiO_2 between 30 - 40 Qz*, (3) an increase in TiO_2 between 30-60 Qz*. Samples following trend 3 are the most peralkaline samples with compositions approaching the EMC.

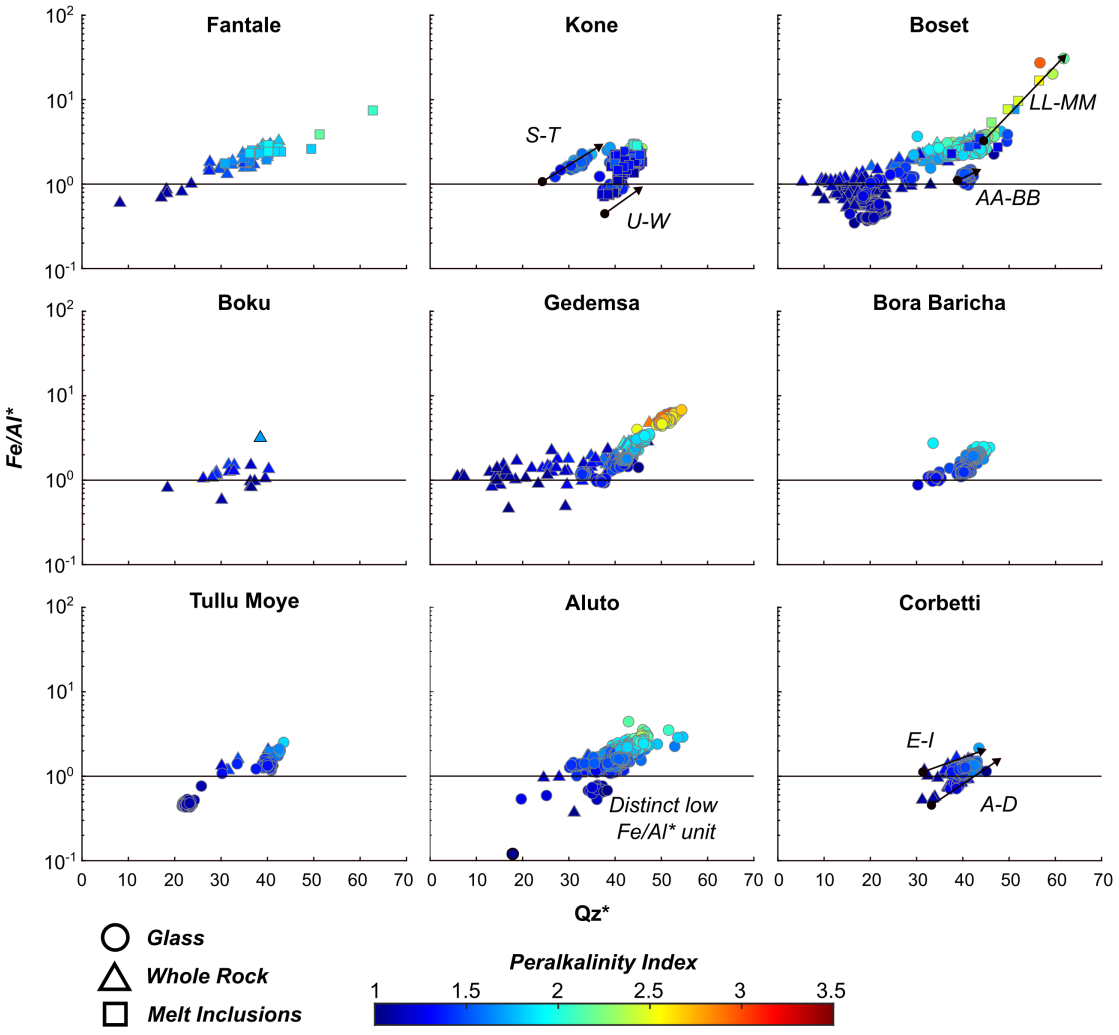

Figure 4.5: Qz* vs Fe/Al* (=1.33×FeOt/[Al_2O_3-4.4]). Arrows indicate trends of magma lineages which are potentially sourced from different parental magmas. Arrows denote the trends modelled trends in Section 4.4 (Tables 4.4.1, 4.4.3, 4.4.4). Where these trends can be clearly observed in other figures they are denoted. Data with Fe/Al* < 1 is classified as comendite and Fe/Al* > 1 is classified as pantellerite (White et al., 2023).

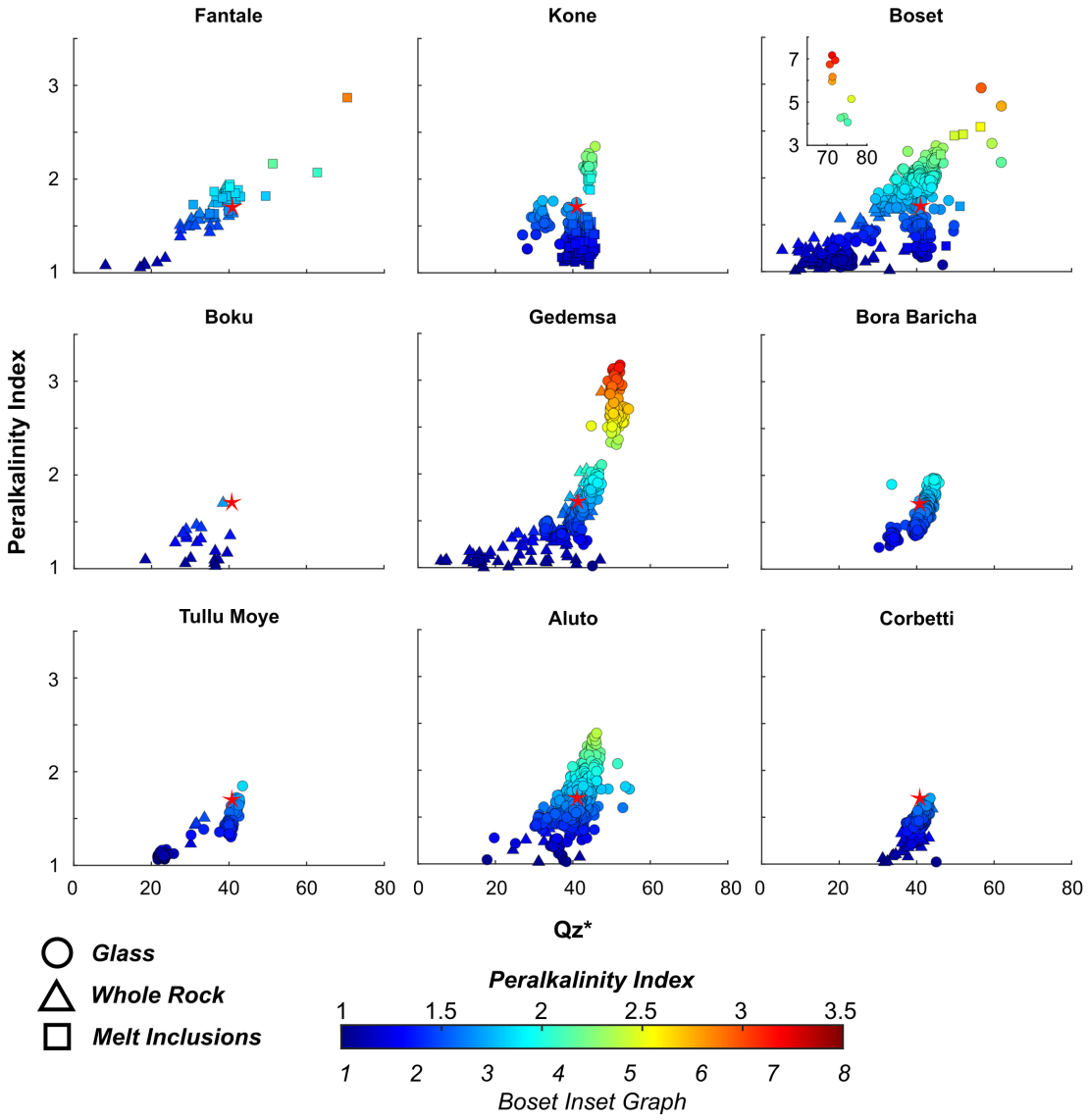

Figure 4.6: Variation in peralkalinity index (PI = molar(Na_2O+K_2O)/Al_2O_3) with Qz* across the MER. The red star indicates the 'thermal valley' projected location with the feldspar-quartz cotectic calculated from data on the Green Tuff, Pantelleria (Carmichael and MacKenzie, 1963; White et al., 2023).

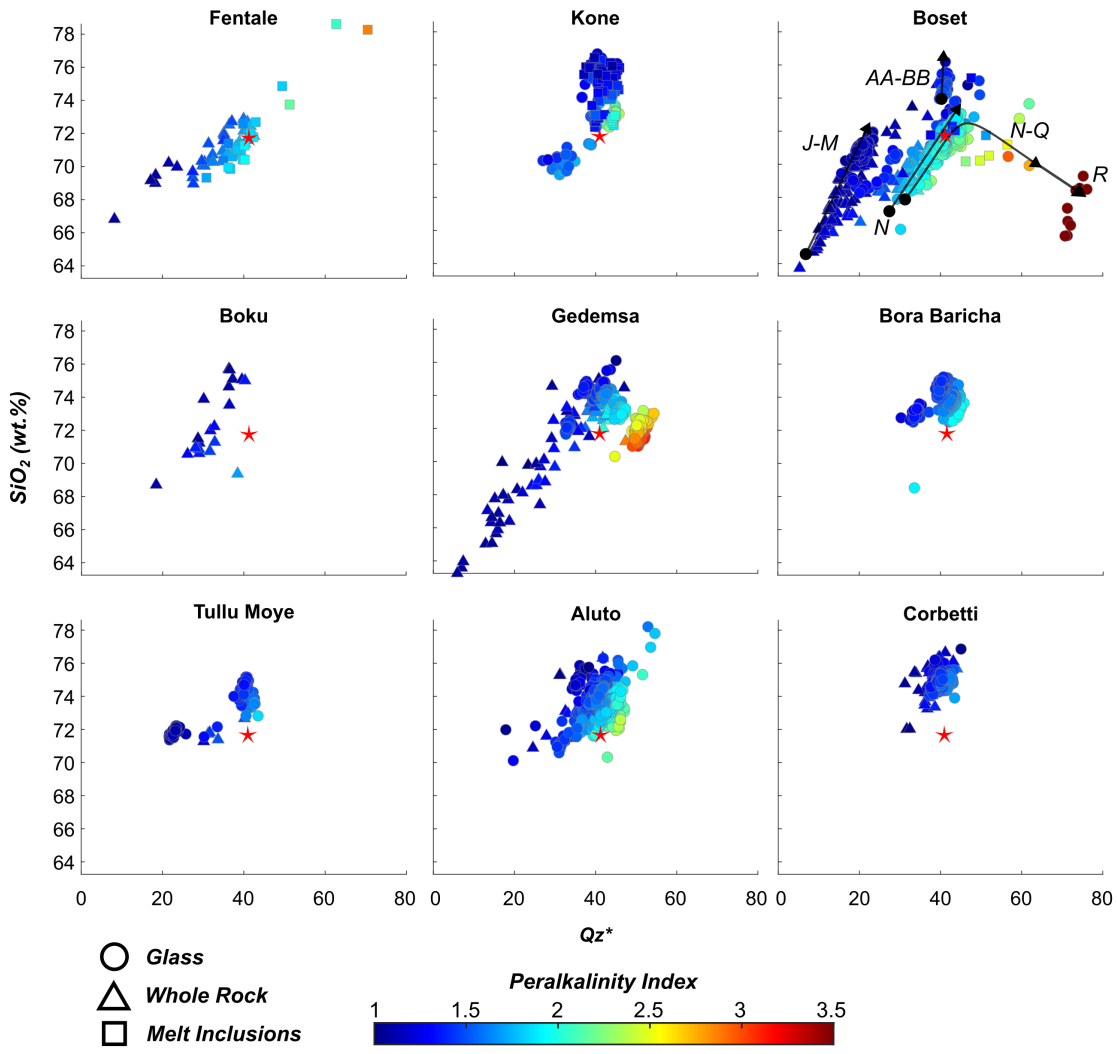

Figure 4.7: Variation in SiO_2 with increasing Qz* across the MER. Arrows denote the modelled trends investigated in Section 4.4 (Results in tables 4.4.1, 4.4.3, 4.4.4). Boset and Gedmesa show the greatest variation in SiO_2 contents with Qz* of the studided systems. We observe a decrease in SiO_2 concentration with Qz* values > 40 which may reflec the onset of the cyrstalisation of quartz.

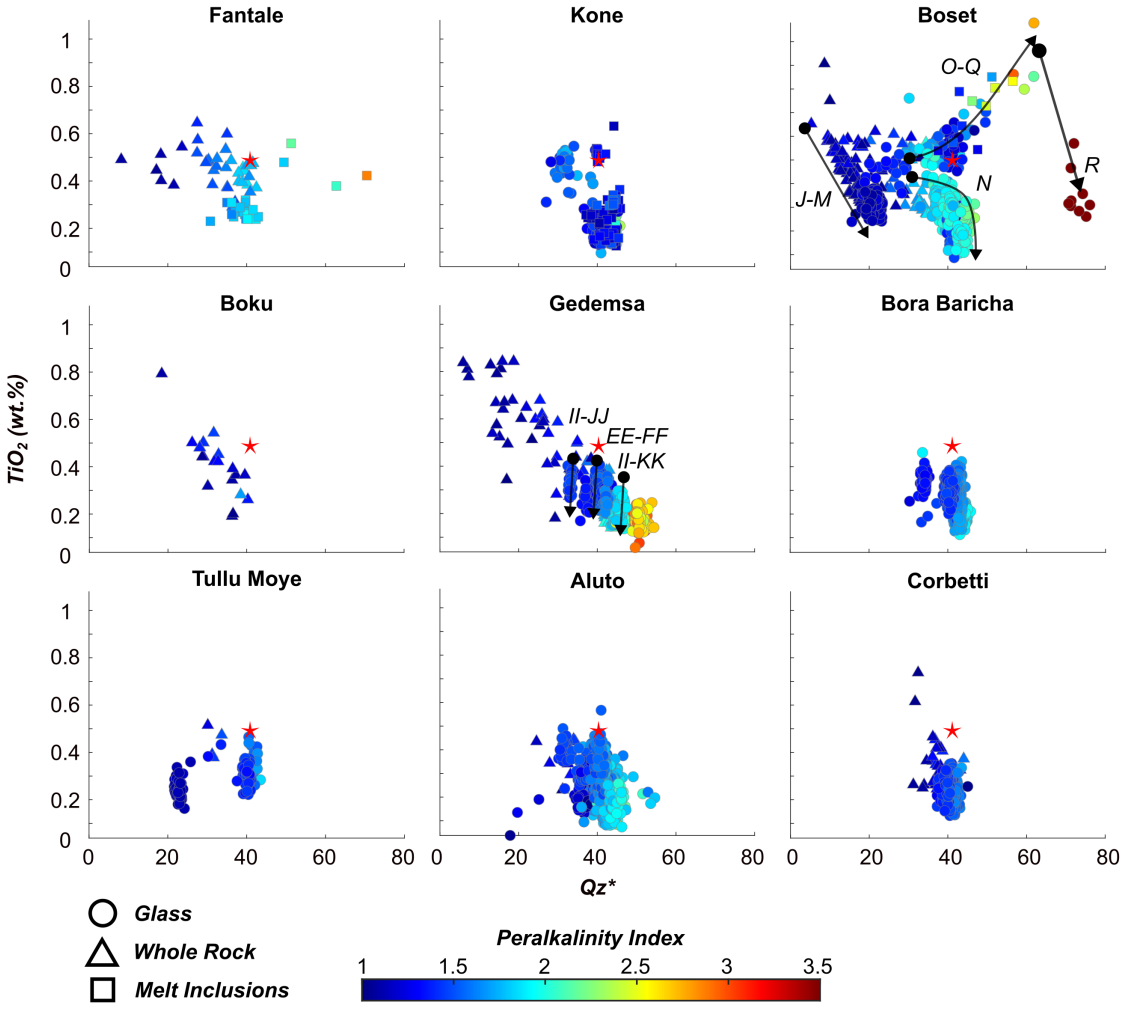

Figure 4.8: Variation in TiO_2 content across the rift with Qz*. Demonstrates a decrease in TiO_2 with increasing Qz* and a sharp decrease in TiO_2 at constant Qz* within geochemically distinct units. Arrows highlight the direction of the modelled trends (letters) investigated in Section 4.4 (Results in tables 4.4.1, 4.4.3, 4.4.4)

As with other major oxides, CaO varies widely in peralkaline magmas (Figure C.3). There is overall a negative correlation with Qz*; however, some highly differentiated samples from Boset (Qz* > 50) show a slight increase in CaO. When this is associated with a decrease in SiO_2, it is inferred to show the diminishing role of clinopyroxene in the crystallising assemblage. As noted previously, only Gedemsa and Boset show a decrease in SiO_2 at high Qz* values; however, progressively more differentiated samples from Gedemsa continue to show an overall decrease in CaO concentrations.

4.3.1 Mineral Assemblages

In Appendix C we compile the mineral assemblages reported from comendites and pantellerite samples across the MER.

The minerals reported across the MER are reasonably consistent between volcanic centres. Assemblages are dominated by alkali feldspar and quartz. Alkali-feldspars in peralkaline samples range from ~Or_{10} to ~Or_{60} (Figure 4.9), with plagioclase occasionally recorded in peralkaline samples or mafic enclaves. Assemblages frequently include clinopyroxenes (sodic ferro-hedenbergite, aegirine-augite & augite) and aenigmatite, with aegirine-augite and aenigmatite commonly occurring together (Appendix C and Figure 4.11). Figure 4.10 shows the range in clinopyroxenes compositions reported across the MER. Mafic clinopyroxenes are also reported in some samples. These more mafic mineral phases are thought to play an important role in magmas evolution towards the EMC (White et al., 2023).

Fe-Ti oxides (ilmenite and Ti-magnetite) are commonly reported as individual grains or inclusions in other mineral phases. Other phases, such as fayalite, are found across the rift; however, their occurrence in individual samples is rare, often in low proportions, and commonly restricted to more trachytic samples. Similarly, amphiboles (arfvedsonite and other sodic amphiboles) are also reported across the rift but are relatively low in abundance. Biotite, apatite and orthopyroxene are also reported, but these are rare and often restricted to individual centres.

Macdonald et al. (2021) noted that few studies report sample mineral assemblages and compositions. We have compiled data on sample composition (glass or whole rock) and mineral assemblage, where both these data are reported and presented in Figure 4.11. From this, we can observe that aenigmatite is restricted to compositions greater than ~28 Qz* and

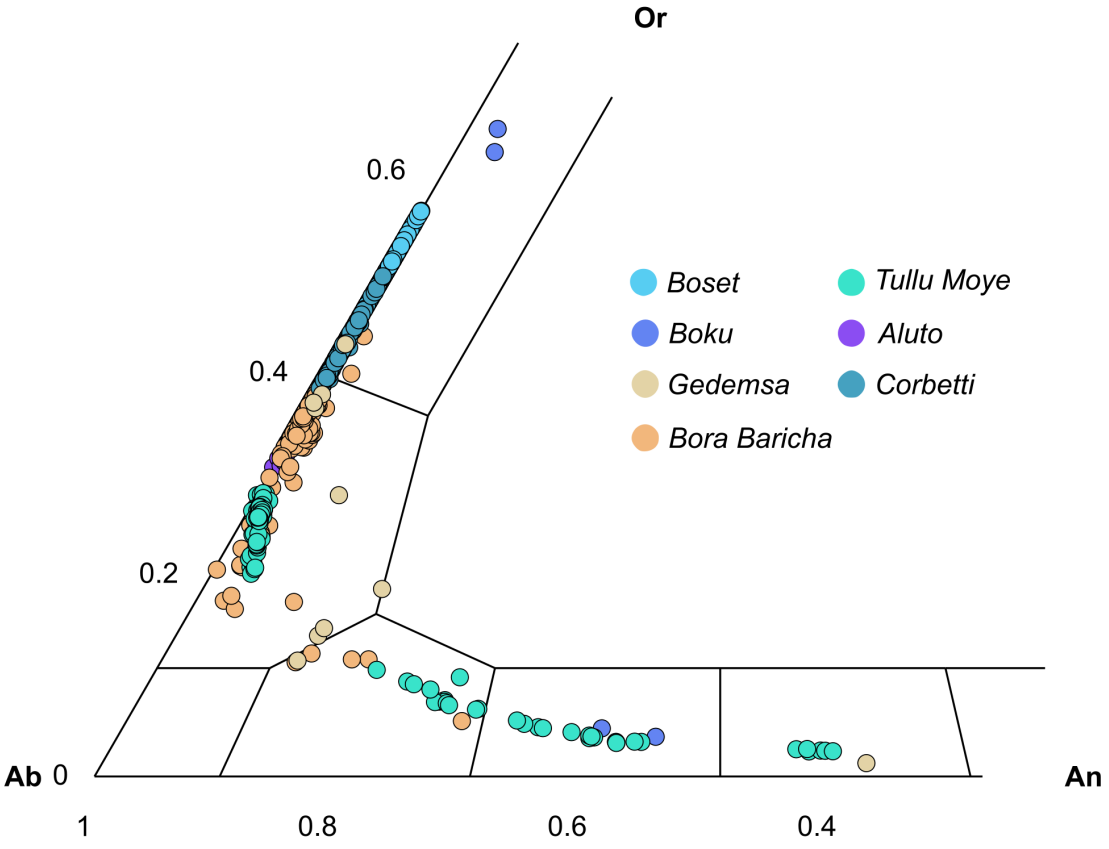

Figure 4.9: Subset of Ab-Or-An ternary plot showing the variation in reported feldspar compositions found in rhyolite/trachyte rocks at different silicic centres across the MER. Data from: Brotzu et al. (1980); Boccaletti et al. (1995); Peccerillo et al. (2003); Ronga et al. (2009); Macdonald et al. (2012). Plotted using MinPlot after Walters (2022).

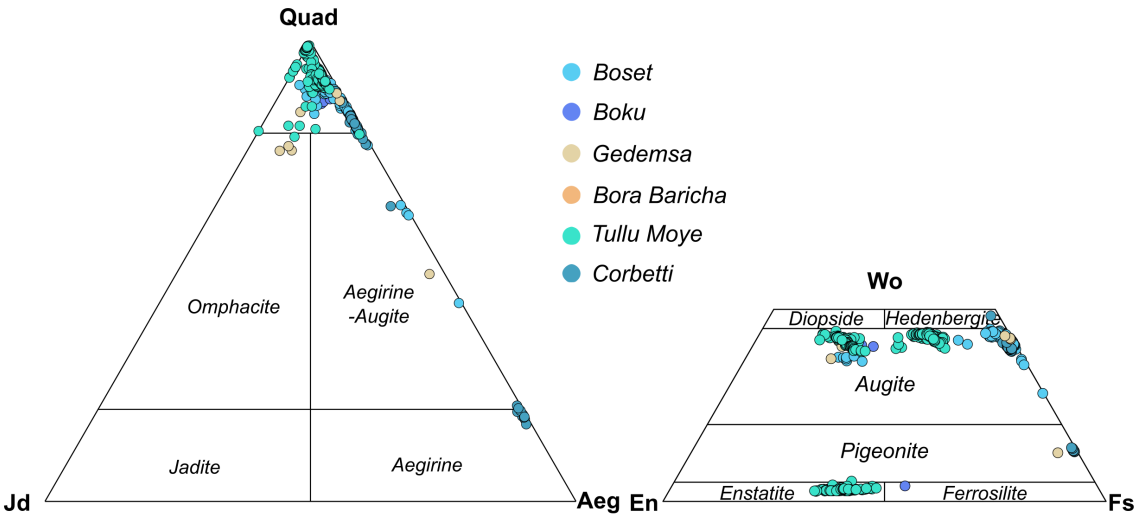

Figure 4.10: Variation in the composition of pyroxenes across the MER. Colours as in Figure 4.2. Quad = quadrilateral, Jd = Jadite, Aeg = Aegirine, En = Enstatie, Fs = Ferrosilite, Wo = Wollastonite (Morimoto, 1989). Data from Brotzu et al. (1974); Boccaletti et al. (1995); Peccerillo et al. (2003); Ronga et al. (2009); Macdonald et al. (2012). Plotted using MinPlot after Walters (2022)

samples with a peralkalinity index greater than 1, and fayalite is not reported in samples with Qz*> ~40. (Figure 4.11). We also observe that whilst Aegirine augite is common in peralkaline rocks, it is slightly restricted to samples with a lower peralkalinity index and Qz* values of < 40. Figure 4.11 also highlights the lack of petrological and chemical data for samples with Qz* values of > ~45. Filling this gap in the data will provide more insight into the mineralogical control on the differentiation of extreme peralkaline compositions.

4.4 Discussion

4.4.1 Geochemical Diversity

Data compiled here show the diversity of peralkaline compositions observed across the MER and highlight the diversity in magmatic processes and liquid lines of descent that lead to their generation. It is widely accepted that fractional crystallisation exerts the main control on peralkaline magmas evolution in the MER, with only minor examples of crustal contamination contributing to generating peralkaline compositions (Rooney et al., 2012; Gleeson et al., 2017; Hutchison et al., 2018). What is clear from the data presented here is that although the evolutionary processes are similar between each of the silicic centres, the

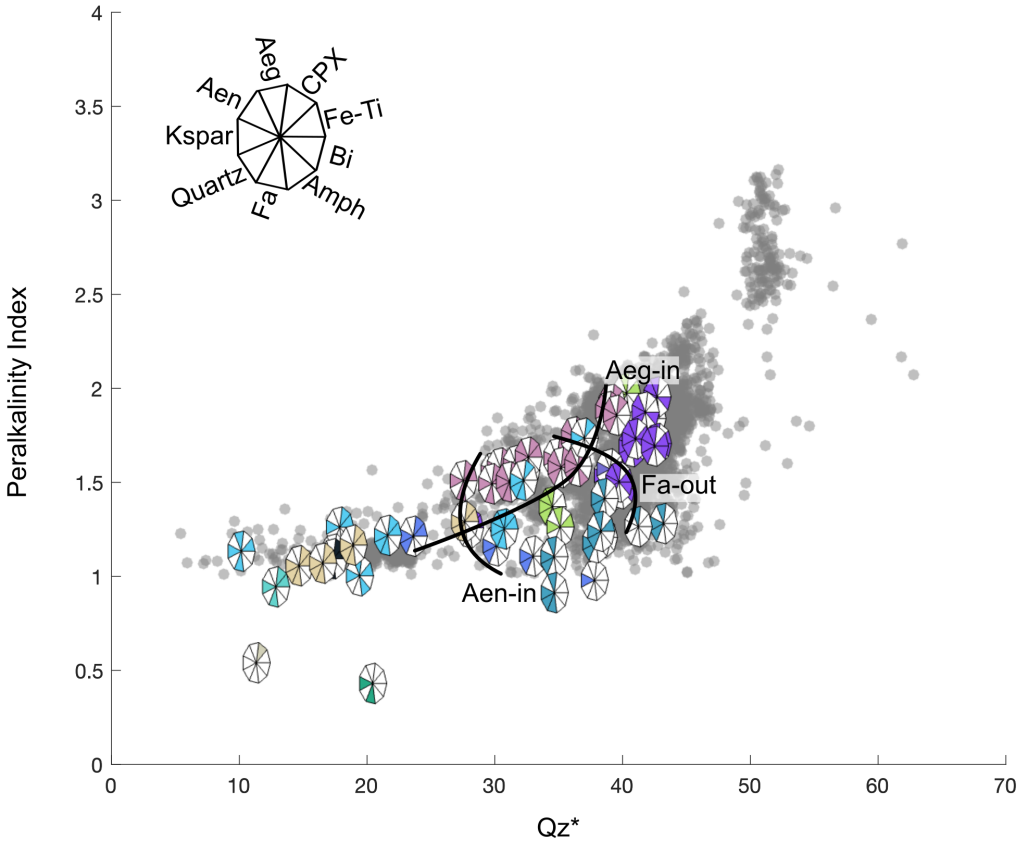

Figure 4.11: Mineral assemblages found in trachyte and peralkaline rocks within the MER. The colours are as in Figure 4.2. Grey data shows the compositional range of peralkaline products used in this study. CPX = clinopyroxene, Aeg = aegirine augite, Aen = aenigmatite, Kspar = alkali-feldspar, Fa = fayalite, Amph = amphibole, Bi = biotite, Fe-Ti = Fe-Ti oxide

liquid lines of descent differ widely. This is true both between the silicic centres and within the products of a given volcanic complex.

Most centres within the MER do not erupt samples with Qz* > 50 except Boset and Gedemsa and sparse melt inclusions from Fantale, recording Qz* values up to 70. Notably, these centres with these highly differentiated samples and the most extreme peralkaline compositions are restricted to the northern section of the MER (Boset and Gedemsa; Figure 4.1), whereas Corbetti in the south displays one of the most restricted compositional ranges (Figures Figure 4.6-C.3). This may be linked to the respective stages of rift evolution or to the thermal state of the sub-volcanic system; however, there are two exceptions. Kone shows a much more restricted compositional space than Boset and Gedemsa, and samples are generally less peralkaline (Figure 4.6). The lower degree of peralkalinity may be due to alkali-rich clinopyroxenes in the crystallising assemblage (See supplementary information). Conversely, Aluto in the southern section of the MER shows a much higher compositional diversity and a higher degree of peralkalinity (Figures 4.6-C.3). However, this may be a function of how well sampled some centres are, as some centres, such as Boku and Fantale, have considerably less data than Boset. This limits the conclusions that can be drawn from these centres. Despite this, centres such as Corbetti, with a large sample population, continually display a monotony in compositional variability.

This difference in geochemical diversity may also be linked to magma flux rates (Weber et al., 2020). Recent work has highlighted how a high magma flux can result in a higher diversity in erupted compositions (Weber et al., 2020; Weber and Sheldrake, 2022), whereas lower fluxes of smaller batches of melt produce a more restricted compositional range. Low flux rates into cold crust result in a large thermal gradient between the crust and intruded magma, causing rapid cooling of magma and rapid fractionation to rhyolitic compositions (Annen, 2009; Jackson et al., 2018; Weber et al., 2020) Higher flux rates allow the crust to mature thermally and establish a sustained mush system where mafic and intermediate melt compositions can reside (Weber et al., 2020). Centres like Boset likely experienced a higher magma flux rate, resulting in the observed range of erupted compositions. This is supported by a high rate of post-caldera volcanism, with Boset experiencing cyclic activity with low volume mafic eruptions occurring on 10 ka timescales and felsic on 100 ka timescales (Siegburg et al., 2017; Fontijn et al., 2018). This high rate of volcanism and a large diversity of erupted compositions supports the assertion that activity at Boset is fed through a high magma flux rate, either through decompression melting of the mantle caused by rifting or through a hotspot (Siegburg et al., 2017).

In contrast to this, centres such as Fantale and Gedemsa have low volumes of post-caldera activity (< 1km^3; Hunt et al. 2019) but display a large range of erupted compositions; and Gedemsa, in particular, shows distinct chemical signatures between eruptive units (Fontijn et al., 2018) recent volcanism at Gedemsa and Fentale has been mafic in nature(Siegburg et al., 2023) supporting the hypothesis of a well developed magma system. The low post-caldera eruptive volumes may indicate a hiatus in magma supply, ineffective mobilisation of melt, or be the result from our comparatively poor understanding of their eruptive histories.

Corbetti has one of the most restricted ranges in magma composition of any well-sampled silicic centre in the MER. With only one basaltic eruption reported, the eruptive products are relatively monotonous peralkaline rhyolites. However, Corbetti has experienced a large amount of post-caldera volcanism (14.5 km^3; Hunt et al. 2019) over the last 182 ka. This large volume of erupted material indicates a continued magma supply into the Corbettis' system which may occur in the form of episodic injections of melt that evolves rapidly towards peralkaline rhyolite and is then erupted. This could account for the lack of intermediate and mafic compositions observed and the monotonous nature of the eruptive deposits (Weber et al., 2020). Weber et al. (2020) showed that frequent injection of low volumes of magma into the crust will result in a extraditable composition that occupies a very narrow compositional range. Alternatively, the high post-caldera volumes could indicate high magma fluxes into a relatively underdeveloped magmatic system and reflect the young age of the complex. Gottsmann et al. (2020) inferred the recently observed uplift at Corbetti (Lloyd et al., 2018a; Biggs et al., 2021) was in response to the injection of mafic magma at a rate of $\sim 10^{11}$ kg yr^{-1} which is an order or magnitude higher than the mean mass eruption rate. This may supported the hypothesis that Corbettis' magmatic system is less thermally mature in comparison to other centres in the northern section of the MER. In either case, it is anticipated that as the magmatic system at Corbetti develops, in response to the development of the rift, a wider range of erupted compositions are likely to be observed; however this will occur on the order of tens to hundreds of thousands of years.

Due to challenges around finding datable material within the MER, it is difficult to link the age of silicic systems to their geochemical diversity. Boset is one of the younger calderas (119 ± 6 ka Siegburg et al. 2017) but has a somewhat unqiue history and, unlike many silicic centres in the MER, has gone through a period of stratovolcano development. This suggests a long lived magmatic system, which is supported by evidence of activity around 1.6 Ma (Morbidelli et al., 1975; Siegburg et al., 2017). In the case of other centres, the ages of the onset of activity are poorly constrained.

Overall, there does appear to be a trend towards higher magma diversity and a larger proportion of mafic volcanism at calderas in the northern section of the MER, which likely reflects a more developed rift and magmatic systems. Southern silicic centres, in particular Corbetti, display a very restricted range, likely owing to a lower magma flux in a less developed segment of the rift (Weber et al., 2020).

The wide variation in the degree of peralkalinity observed across the rift is likely a function of two factors; the composition of the alkali basalt from which the magmas are derived and the minerals which have crystallised in the magma as it progressively fractionates, which in turn, is a function of the P-T-fO_2-H_2O conditions. As demonstrated in Figure 4.6, peralkalinity will increase with continued fractionation of alkali-feldspars. Where this trend is not observed, it indicates that mineral phases are dampening the effect of feldspar fractionation on peralkalinity. Although the general trend is that peralkalinity increases with increasing differentiation (as measured by Qz*; Figure 4.6), this is not linear, and we observed multiple examples where samples with Qz* values of $\sim$ 40 report lower peralkalinity indexes than some samples at lower Qz* (i.e., Kone, Boset, Aluto). Therefore, using peralkalinity as an indicator of fractionation can be misleading. The fractionation of Na-rich mineral phases such as sodic-amphiboles and alkali-clinopyroxenes may dampen or prevent increases in peralkalinity as magmas evolve (Scaillet and Macdonald, 2006). Mass balance modelling of weakly peralkaline but highly differentiated samples from Kone (Figure 4.5; Trend 2) predicts Na-rich clinopyroxene and aenigmatite fractionation (Supplementary Information; Model S-W). This would explain the weakly peralkaline nature of these samples compared to the wider rift. It should also be noted that centres with a large range in erupted compositions, (namely Boset and Gedemsa), also record some of the highest peralkalinity indexes. This range is likely linked to higher magma flux rates into sufficiently long lived magma systems allowing for the development of extreme compositions prior to extraction and eruption.

Across the rift, TiO_2 generally decreases with increasing Qz*. Boset shows several unique trends, which are outlined in Figure 4.8. Using mass balance modelling, we can show that Trend 1 represents the fractionation of Fe-Ti oxides (ilmenite/magnetite) or aenigmatite in conjunction with feldspar, clinopyroxene, amphibole and a minor amount of apatite (Table 4.4.1; Models J-M). However, in natural samples, aenigmatite is rarely observed in magmas with Qz* < 28 (Figure 4.11); therefore, it is likely that the crystallisation of Fe-Ti Oxides (magnetite or ilmenite) has the dominant control. Trend 2 records a progressive decrease in TiO_2 between Qz* 30-50 (Figure 4.8). This trend reflects the fractionation of aenigmatite, feldspar, and clinopyroxene with the occasional addition of fayalite (Appendix C; Model N).

Highly differentiated samples with increasing TiO_2 (Trend 3; Figure 4.8) can be explained by fractionating fayalite, feldspar, quartz, clinopyroxene and a minor amount of magnetite (See supplementary information; Model O-P). Magnetite will likely have a negligible effect as it occurs in such low proportions. This demonstrates that at low degrees of differentiation (Qz* < 20), decreases in TiO_2 can be explained through the crystallisation of Fe-Ti oxides. At Qz* above ~ 30, the presence or absence of aenigmatite and clinopyroxene has the most dominant control on the variation in TiO_2 concentrations.

Previously, observed decreases in SiO_2 with increasing Qz* at peralkaline centres have been mirrored with increasing CaO, reflecting the increasing dominance of quartz in the crystallising assemblage compared with clinopyroxene (Macdonald et al., 2021; White et al., 2023). This is observed at Boset in samples with Qz* > 50, decreasing in SiO_2 (Figure 4.7) and increasing in CaO (Figure C.3). However, SiO_2 concentrations at Gedemsa decrease with increasing Qz*, but there is no associated increase in CaO. This may indicate that fractionation of clinopyroxene plays a much greater role in generating extreme peralkaline magmas at Gedemsa than Boset.

Continued fractional crystallisation of a weakly peralkaline magma will increase Qz* and Fe/Al* values. Magmas with the same alkali-basalt source and liquid line of descent will follow the same trend from a low Fe/Al* value to a higher value. Figure 4.5 shows that multiple trends exist at different degrees of differentiation within a given centre. Using this data, we have identified subtle differences in the evolutionary pathway of Corbetti's erupted products, showing slight variations in the liquid lines of descent. This is likely to be controlled by slight variations in P-fO_2-H_2O storage conditions. Variations in parental source compositions cannot be fully ruled out, however, there is little evidence to support this (Colby et al., 2022, Chapter 3). We use mass balance modelling to test if there are any variations in the mineralogical control of these trends. We demonstrate that both these trends can be explained predominantly through the fractionation of alkali-feldspars and quartz (Table 4.4.1; Model A-I). Models agree with petrological evidence from Corbetti and indicate the fractionation of minor amounts of clinopyroxene (Na-rich and Na-poor phases), fayalite, and Fe-Ti oxides also occurs. Modelling also suggests that minor amounts of apatite and aenigmatite may also fractionate; however, these are not observed in natural samples at Corbetti (Appendix C). One notable feature is the fractionation of Na-rich and Na-poor clinopyroxenes in Corbetti's assemblage. These occur in relatively low abundances compared with other MER systems, although at Corbetti, Na-poor clinopyroxene phases are predicted to occur more frequently than other MER systems. The absence of predicted mineral phases (i.e. apatite & aenigmatite) from naturally observed assemblages at Corbetti

may result from the crystal-poor nature of Corbettis' eruptive deposits. However, in the case of apatite and other accessory phases, these are rarely found in other more crystal-rich systems.

Kone also displays some well-defined trends in Figure 4.5 which link to geochemically distinct units associated caldera and post-caldera activity (Fontijn et al., 2018). Like Corbetti, these trends likely reflect variations in the compositions of the alkali basalt source. Peralkaline products at low Qz* with a high Fe/Al* value predominantly fractionate alkali-feldspar and quartz with minor fayalite and clinopyroxene. More differentiated samples fractionate Na-rich clinopyroxenes in addition to minor aenigmatite or fayalite (see supplementary information; Models S-W).

This data shows that magmas with low Fe/Al* values (< 1) do not occur above Qz* values of 41, whereas magmas with high Fe/Al* values can occur from Qz* values of 5 through to ~ 70 (Figure 4.5). Notably, a single sample suite from Aluto that is highly differentiated but records a low Fe/Al* value shows a decrease in peralkalinity with ongoing differentiation (highlighted A in Figure 4.5). This is the only example we observe in the rift. It may indicate a change in storage conditions or magma mixing, causing mineral phases to resorb and the melt to become less peralkaline as it undergoes fractional crystalisation.

Table 4.2: Mass balance model results investigating the mineralogical control on highlighted trends in major element data. Mass fractions equal 1. Kspar: alkali-feldspar, Q: auartz, CPX: clinopyroxene, Aen: aenigmatite, Fa: fayalite, Mg, magnetite, Il: ilmenite, Ap: apatite, Amph: amphibole, f/c%: percentage of fractional crystallisation predicted by the model, r: model residual (squared sum of the squared residuals between the known and modelled daughter compositions). The reference figure shows the direction of the trend modelled. Mineral proportions represent the percentage within the fractionating assemblage.

Model	Reference Figure	Parent	Daughter	Kspar[2]	Q	CPX[3]	Aen	Fa	Mg	Il	Ap	Amph	f/c%	r
Corbetti		Qz*												
A	4.5	33.580	41.179	0.659	0.285	0.041	-	0.012	-	0.004	-	-	74.093	0.000
B	4.5	33.580	43.144	0.682	0.282	0.024	-	0.005	0.008	-	-	-	70.136	0.000
C	4.5	33.949	41.179	0.659	0.277	0.036	0.028	-	-	-	-	-	67.334	0.000
D	4.5	36.671	41.179	0.065	0.276	0.046	-	0.020	-	0.004	-	-	39.436	0.001
E	4.5	36.910	42.180	0.829	0.100	0.050	-	-	0.015	-	0.006	-	15.792	0.003
F	4.5	36.910	42.314	0.652	0.226	0.036	0.067	0.027	-	-	-	-	30.703	0.013
G	4.5	36.910	41.186	0.708	0.163	0.039	-	0.080	-	0.009	0.010	-	16.708	0.006
H	4.5	36.234	42.180	0.638	0.283	0.021	-	0.036	0.007	-	-	0.015	48.760	0.006
I	4.5	36.234	41.186	0.619	0.293	0.028	-	0.053	0.009	-	-	-	47.951	0.003
Boset														
J	4.8	8.622	23.162	0.750	-	0.043	-	-	0.048	-	0.100	0.149	55.632	0.002
K	4.8	5.275	23.016	0.728	-	0.126	-	-	-	0.005	0.001	0.135	82.223	0.047
L	4.8	9.275	23.270	0.700	-	0.102	0.035	0.003	-	-	-	0.154	67.275	0.058
M	4.8	9.478	23.016	0.697	-	0.168	0.035	-	-	-	-	0.092	68.447	0.126
N	4.8	36.212	42.704	0.524	-	0.196	0.220	0.041	-	-	-	-	19.550	0.119
O	4.8	38.860	56.470	0.700	0.223	0.013	-	0.054	0.005	-	-	-	44.331	0.005
P	4.8	38.860	59.423	0.829	0.104	0.039	-	-	-	-	-	-	34.844	0.073
Q	4.8	37.781	56.600	0.883	0.115	-	-	-	-	-	-	-	32.317	0.031

Continued on next page

Table 4.2 – continued from previous page

Model	Figure	Parent	Daughter	Kspar[2]	Q	CPX[3]	Aen	Fa	Mg	Il	Ap	Amph	f/c%	r
R	4.8	59.423	76.093	0.551	0.423	-	-	-	-	0.023	-	-	39.735	0.687
Kone														
S	4.5	27.023	33.360	0.975	0.066	-	-	-	-	-	-	-	17.483	0.093
T	4.5	28.238	34.039	0.686	0.214	0.017	-	0.058	0.017	-	0.003	-	41.475	0.099
U	4.5	37.124	41.748	0.624	0.297	-	0.049	0.021	-	-	-	-	45.287	0.001
V	4.5	37.610	41.748	0.604	0.335	0.021	-	0.020	0.012	-	-	-	64.949	0.000
W	4.5	37.610	41.441	0.667	0.281	0.026	-	-	0.011	-	-	-	35.140	0.000

1. The specific composition of the feldspar predicted by the models is given in the supplementary information.

2. The specific composition of the clinopyroxene phase predicted by the model is given in the supplementary information.

Plotting the data in this way, compared with the traditional FeOt-Al_2O_3 discrimination diagram (Figure 4.3), allows for a more robust assessment of a magmatic suite's degree of differentiation, the potential liquid lines of descent, and the variability of the source components across a given centre. It also highlights that if the classification of (Macdonald, 1974) were employed, we would potentially miss key information on the amount of differentiation a magma has undergone to reach these compositions and sample suites which follow similar trends could wrongly be assumed to fall within the same magmatic lineage. It should be noted, however, that the Fe/Al* ($1.33 \times FeOt/(Al_2O_3\text{-}4.4)$ scheme is not appropriate for classifying extremely peralkaline samples with $Al_2O_3 < 4.4$ wt.% as the returned value is negative.

Here we have explored the major element variation in peralkaline magmas across the MER. We have highlighted the variation in the degree of differentiation of erupted products across the rift and the diversity of erupted compositions. We demonstrate subtle differences in feldspar and clinopyroxene compositions can explain differences in the observed geochemical trends within major element data. By using mineral compositions which are known to have erupted at a given centre (where data exist), we are confident the mass balance modelling provide a good fit to natural data. For systems where detailed mineral data is currently unavailable we used a range of mineral compositions known to have erupted at comparable centres. Further work on these systems is needed to fully constrain the range of minerals compositions erupted within eruptive products.

We also draw a link between the geochemical diversity of the silicic centres across the MER and the rate of magma supply. Centres within the northern section of the rift typically exhibit a larger range in erupted compositions compared to centres in the southern section of the rift, in particular Corbetti. This is likely linked to higher rates of magma supply over a longer time period to magmatic segments in the northern section of the rift. It is likely that as the rift continues to mature, silicic centres in the southern section of the rift will begin erupting a more diverse compositional range.

We further explore this further by projecting data onto the Qz-Or-Ab-Ac-Ns residua system to further investigate the mineralogical controls on the generation of peralkaline melts.

4.4.2 The Qz-Or-Ab-Ac-Ns residua system

Alkali-feldspar is one of the most important and dominant phases to fractionate in peralkaline melts and is a key phase in driving melts to extreme peralkaline compositions (Carmichael and MacKenzie, 1963; Bailey and Schairer, 1964; White et al., 2023). The fractionation of alkali-feldspar can be traced by projecting data onto the Qz-Or-Ab (8.3% Ac + 8.3% Ns at PH_2O = 1000) residua system. Figure 4.12 shows the data from the MER projected onto this residua system, and we plot the thermal valley and location of the alkali-feldspar-quartz cotectic are plotted after Carmichael and MacKenzie (1963). Figure 4.13 shows this projection plotted in the cartesian form (Qz* vs Or/(Or+Ab)) primarily for simplicity and easier viewing of the trends across all datasets. Figures Figure 4.12 and Figure 4.13 demonstrate that a cooling felsic magma will track along the 'thermal valley' towards its intersection with the alkali-feldspar-quartz cotectic. The orange star in these plots highlights where the 'thermal valley' intersects with the feldspar quartz cotectic at Qz* 40.5 $Or_{34.5}$ Ab_{25} (White et al., 2023). Magmas can move past this point, continuing to crystallise feldspar and project into the 'thermal delta' rather than following the cotectic. Magmas crystallising along the thermal valley will increase in Qz* and gradually increase in the proportion of Or with respect to Ab, reflecting the tendency for melts to become more K_2O-rich with continued fractionation of alkali-feldspars. When data from the MER is projected onto this diagram, two distinct trends are observed at the low-temperature intersection of the 'thermal valley' and the feldspar-quartz cotectic. Data either follow the cotectic of Carmichael and MacKenzie (1963), remaining relatively constant in Qz* but dramatically increasing the proportion of Or, or they will follow the cotectic defined by Di Carlo et al. (2010) and Romano et al. (2020) (Figure 4.3), increasing in Qz* and more gradually in the proportion of Or towards the EMC.

Here we explore the mineralogical control on these two observed trends and compare this with observations on known mineral assemablages and major element data.

4.4.3 Carmichael and MacKenzie Cotectic

Kone, Boset, Aluto and Gedemsa all have at least one stratigraphic unit that shows a near-constant Qz* value but a wide range in the proportion of Or, resulting in the vertical trends seen in Figure 4.13. In the case of Boset, the samples are associated with deposits from the caldera-forming eruption (MER120; Fontijn et al. 2018) whilst, at Gedemsa, each of

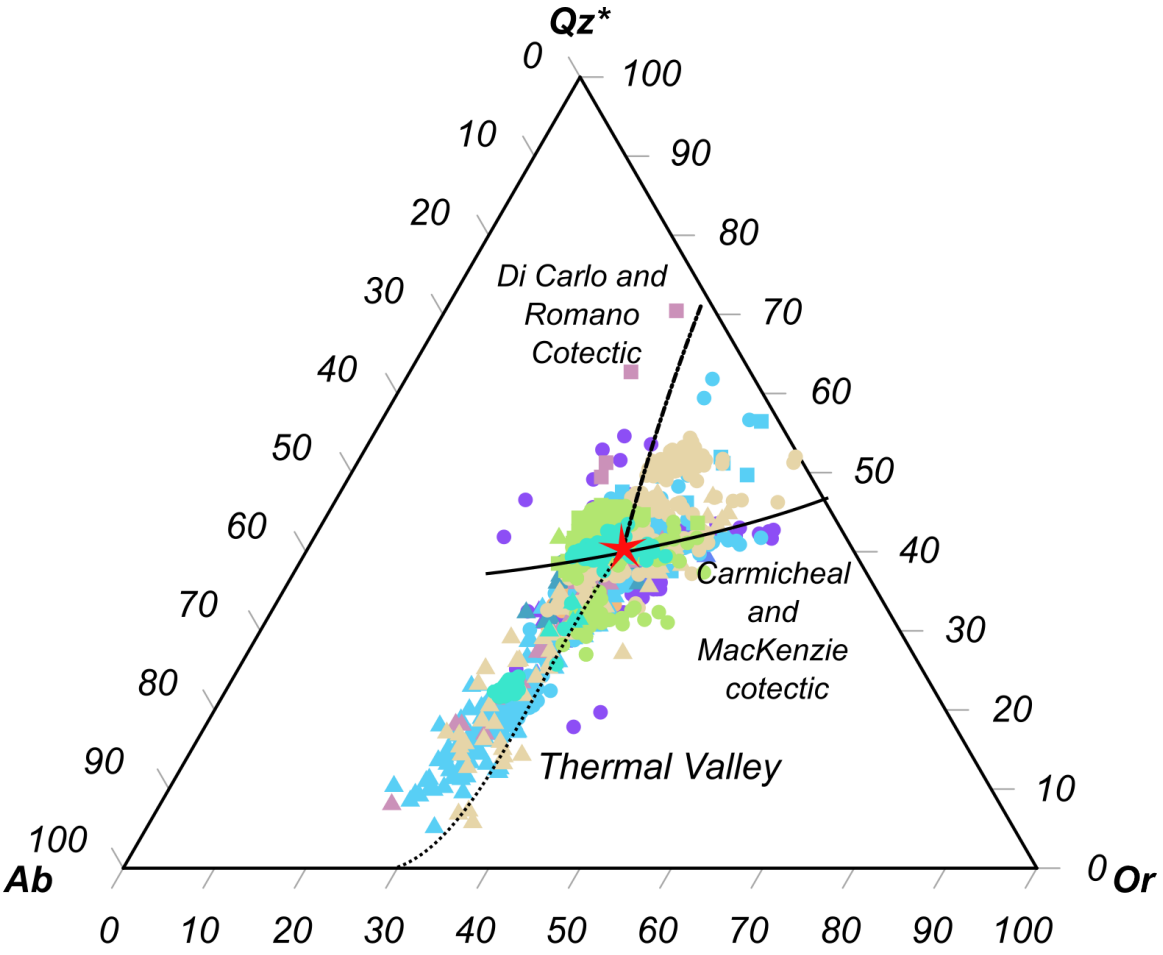

Figure 4.12: Tri-plot of normative Qz*-Or-Ab CIPW components projected onto the Qz-Or-Ab-Ns-Ac residua system at PH_2O = 100 MPa. Cotectic after Carmichael and MacKenzie (1963) (Solid line) and the cotectic of Di Carlo et al. (2010) and Romano et al. (2020) (Dashed line). The red star indicates where the thermal valley intersects with the feldspar-quartz cotectic. Colours as in Figure 4.2.

the geochemically distinct units identified by Fontijn et al. (2018) show a vertical trend at different Qz* values. In all cases, samples which follow this trend have a near-constant PI and SiO_2 content. To determine the mineralogical control of this trend, we conduct mass balance using mineral compositions found at each of these centres. For the samples from Aluto mass balance showed that the crystallisation of alkali-feldspar ($Or_{28.66}$; 0.509), quartz (0.377), clinopyroxene (aegirine augite; 0.066) and aenigmatite (0.045) provided the best-fit model (Table 4.4.3; model CC, r = 0.0351). Testing different parent-daughter melt combinations from the same sample suite yielded similar results, with some models indicating that adding fayalite and removing clinopyroxene from the assemblage produced similarly good fits. Similarly, mass balance on samples from the caldera-forming eruption at Boset showed that the fractionation of alkali-feldspar ($Or_{34.34}$; 0.604), quartz (0.305), clinopyroxene (aegirine augite; 0.054) and a minor amount of aenigmatite (0.026) gave a reasonable solution to the mass balance model (Table 4.4.3; Model AA, residual = 0.224). This demonstrates that this trend can be explained through the fractionation of Na-rich phases such as aegirine-augite and aenigmatite, which likely prevents the melt from further increasing peralkalinity despite the continued fractionation of anorthoclase (Scaillet and Macdonald, 2006).

Gedemsa has a much more complex picture. Samples associated with the syn-caldera activity (Fontijn et al., 2018) fall at the projected location of the intersection of the thermal valley with the feldspar-quartz cotectic (40.5 Qz*). Like samples from Boset and Aluto, they follow the cotectic of Carmichael and MacKenzie (1963), recording a sharp increase in the proportion of Or. Fractionation of alkali-feldspar ($Or_{39.9}$; 0.678), quartz (0.282), ilmenite (0.013) and two Na-rich clinopyroxene phases (0.021 & 0.009) give a good solution for this trend (Table 4.4.3; Model FF, r=0.0164). A good fit is also achieved (Table 4.4.3; Model EE, r = 0.0914) with only a single clinopyroxene phase (0.022), fayalite (0.014) and magnetite (0.007), in addition to alkali feldspar and quartz. In this case, the increase in the proportion of Or is likely due to the fractionation of Na-rich feldspars and Na-rich clinopyroxene phases, with the clinopyroxene dampening any increase in peralkalinity.

Other pre-and post-caldera samples from Gedemsa show a similar increase in the proportion of Or at near constant Qz* values; however, these occur at Qz* values lower than the projected cotectic at PH_2O = 100 MPa (Figure 4.13). Mass balancing on these datasets shows the dominance of alkali feldspars ($Or_{10.7}$ - $Or_{39.9}$) and quartz with minor fractionation of Na-rich clinopyroxene and aenigmatite (Table 4.4.3; Models EE, FF, II-KK). These models give a very good fit (r «0.1). The prediction of quartz and feldspar at lower Qz*

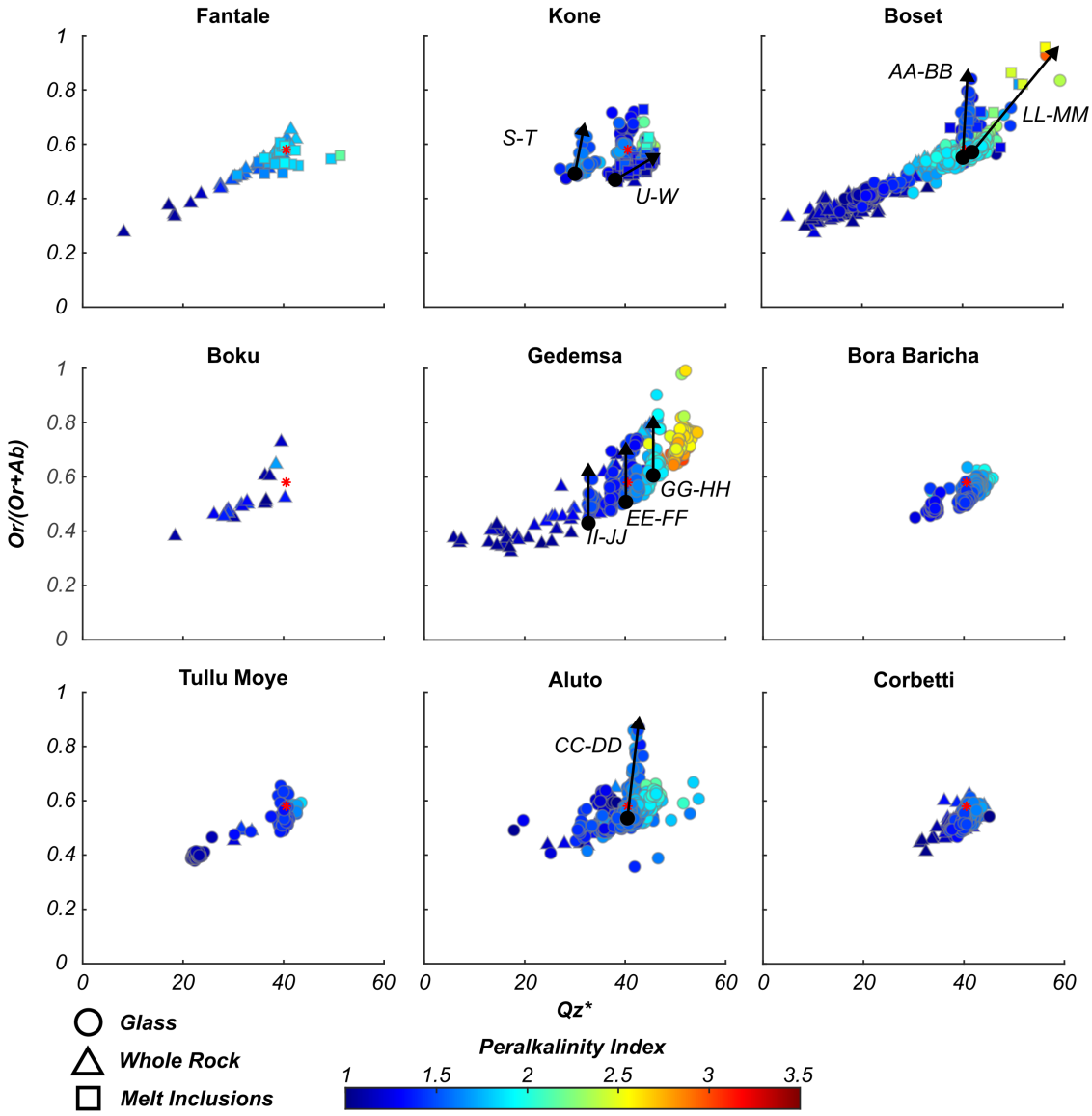

Figure 4.13: Cartesian, isobaric projection of Figure 4.12. The red star indicates the 'thermal valley' location intersecting with the feldspar-quartz cotectic. A key feature of Boset, Gedemsa and Aluto are the units which show a sharp increase in the proportion of Or with a relatively constant Qz* value. Arrows indicate direction of the trends modelled and are presented in Tables 4.4.3 and 4.4.4. The multiple data clusters showing a vertical trend at Gedemsa relate to the geochemically distinct units identified by Fontijn et al. (2018)

values that the projected cotectic suggests that these magmas were fractionated at varying pressures, which altered the location of the cotectic (Blundy and Cashman, 2001).

Table 4.3: Mass balance model results investigating the mineralogical control on trends observed in the Qz-Or-Ab-Ac-Ns residua system focusing on samples following the cotectic of Carmichael and MacKenzie (1963). Kspar: Alkali-feldspar, Q: Quartz, CPX: Clinopyroxene, Aen: Aenigmatite, Fa: Fayalite, Mg, Magnetite, Il: Ilmenite, Ap: Apatite, Amph: Amphibole, f/c%: percentage of fractional crystallisation predicted by the model, r: model residual (squared sum of the squared residuals between the known and modelled daughter compositions) Mineral proportions represent the percentage within the fractionating assemblage. Figure 4.13 shows the direction of the modelled trends.

Model	Parent	Daughter	Kspar[1]	Q	CPX[2]	Aen	Fa	Mg	Il	Ap	Amph	f/c%	r
Boset	Qz*												
AA	39.805	40.46	0.604	0.305	0.054	0.026	-	-	-	-	-	35.190	0.224
BB	39.805	42.01	0.617	0.276	0.074	0.017	-	-	-	-	-	31.500	0.530
Aluto													
CC	42.301	41.67	0.509	0.377	0.066	0.045	-	-	-	-	-	17.300	0.035
DD	42.124	41.67	0.508	0.384	0.073	0.028	-	-	-	-	-	31.940	0.018
Gedemsa													
EE	39.420	42.74	0.691	0.256	0.022	-	0.014	0.007	-	-	-	59.660	0.091
FF	39.420	41.91	0.678	0.282	0.030	-	-	-	0.013	-	-	36.870	0.016
GG	45.68	49.82	0.595	0.283	0.125	-	-	-	-	-	-	27.750	0.027
HH	44.57	46.52	0.495	0.354	0.026	0.139	-	-	-	-	-	15.680	0.049
II	33.62	33.20	0.611	0.379	-	-	-	-	-	-	-	8.490	0.032
JJ	33.62	33.60	0.679	0.313	-	-	-	-	-	0.006	-	8.260	0.020
KK	32.61	33.20	0.618	0.322	-	0.071	-	-	-	-	-	11.920	0.126

1. The specific composition of the feldspar predicted by the models is given in the supplementary information.

2. The specific composition of the clinopyroxene phase predicted by the model is given in the supplementary information.

4.4.4 Di Carlo and Romano Cotectic

Samples from Boset (Figure 4.13) (Macdonald et al., 2012) follow the projected cotectic Di Carlo et al. (2010) & Romano et al. (2020). Using the whole rock composition of sample B350 (Ronga et al., 2009) as the parental melt and the most differentiated glass composition of B350 as an endpoint, we found that large-scale fractionation of alkali-feldspar (Or_{19}; 0.935) with minor fractionation of aenigmatite (0.055), aegirine-augite (0.014) and sodic amphibole (0.011) provided the best result (Table 4.4.4; Model LL, r = 0.0444). Similarly, using the least differentiated glass composition yielded similar results but did not fractionate amphibole (Table 4.4.4; Model MM, r = 0.2041). Notably, quartz is not needed to fractionate to the daughter composition. In addition, the proportion of alkali-feldspar predicted is much higher compared with samples from Boset which follow the vertical trend of Carmichael and MacKenzie (1963). We also use the most FeOt-rich glass composition of sample B375 as the daughter melt. We found that fractionation of alkali feldspar ($Or_{33.5}$ $Ab_{66.6}$; 0.709), quartz (0.181), fayalite (0.021), Fe-Ti oxides (Magnetite; 0.029) and alkali-poor clinopyroxene (0.019) results in the generation of the extreme compositions observed (Table 4.4.4; Model NN, r = 0.0451). These findings broadly agree with previous studies, highlighting the generalised assemblage of alkali feldspar + fayalite + hedenbergite + oxide ± quartz needed to reach these extreme compositions (White et al., 2009; Macdonald et al., 2012).

Overall, the mineralogical control of these two trends can be explained through the composition and quantity of fractionating alkali feldspar in addition to Na-rich or Na-poor mineral phases. Fractionating towards extreme compositions requires the large-scale fractionation of alkali-feldspars with minor Na-poor clinopyroxenes. Samples following the vertical cotectic of Carmichael and MacKenzie (1963) fractionate lower proportions of Na-rich feldspars and higher quantities of Na-rich clinopyroxene and aenigmatite.

Table 4.4: Mass balance model results investigating the mineralogical control on trends observed in the Qz-Or-Ab-Ac-Ns residua system (Figure 4.13) following the cotectic of Di Carlo et al. (2010) & Romano et al. (2020). Kspar: alkali-feldspar, Q: quartz, CPX: clinopyroxene, Aen: aenigmatite, Fa: fayalite, Mg: magnetite, Il: ilmenite, Ap: apatite, Amph: amphibole, f/c%: percentage of fractional crystallisation predicted by the model, r: model residual (squared sum of the squared residuals between the known and modelled daughter compositions). Mineral proportions represent the percentage within the fractionating assemblage.

Model	Parent	Daughter	Kspar[1]	Q	CPX[2]	Aen	Fa	Mg	Il	Ap	Amph	f/c%	r
		Qz*											
LL	36.999	56.48	0.935	-	0.014	0.055	-	-	-	-	0.011	27.011	0.044
MM	39.380	56.48	0.942	-	0.014	0.048	-	-	-	-	-	25.078	0.204
NN	30.738	75.17	0.709	0.181	0.019	-	0.021	0.029	-	-	-	67.353	0.045

1. The specific composition of the feldspar predicted by the models is given in the supplementary information.

2. The specific composition of the clinopyroxene phase predicted by the model is given in the supplementary information.

4.4.5 Location of the quartz-feldspar cotectic in peralkaline systems

The location of the feldspar-quartz cotectic lies at the termination of the 'thermal valley' in the Qz-Or-Ab residua system. Studies have sought to parameterise this intersection to define the composition of the melt as it reaches this point. White et al. (2023) used data from the Green Tuff in Pantelleria to achieve this, and we have plotted these results in Figures Figure 4.6 to C.3 for comparison. It is clear from the data presented here that the composition of a given magma at the intersection of the thermal valley with the quartz-feldspar cotectic varies significantly across the rift. This is particularly true for SiO_2 and TiO_2 concentrations. The diversity of the compositional space that magma can occupy at the cotectic again highlights the diversity of the liquid lines of descent that generate peralkaline magma.

The vertical trends in glass data from Gedemsa in Figure 4.13 likely reflect a shift in the location of the feldspar-quartz cotectic. Experimental data shows a shift in the location of the feldspar-quartz cotectic with increasing pressure. At higher pressures, up to 150 MPa, feldspar and quartz are present at lower degrees of differentiation ($\sim$ 30 Qz*) than experiments run at lower pressures (50 to 100 MPa). However, there is a lack of experimental data conducted at > 150 MPa meaning only limited conclusions can be drawn. Further experimental investigation of the Qz-Or-Ab-Ac-Ns residua system is needed to fully constrain how the location of the cotectic varies with both pressure and redox conditions. Similarly, another important consideration is the volatile concentration of peralkaline melts. It has been shown that high concentrations of F and H_2O can increase the size of the quartz field in the Qz-Or-Ab system, causing it to appear earlier in the fractionating assemblage (Manning, 1981; Manning et al., 1981; Wilke et al., 2017; Macdonald et al., 2021). Whilst data on volatile concentrations in the MER are limited, data does show these magmas are likely rich in H_2O (Iddon and Edmonds, 2020). Similarly, data from Aluto shows volcanic samples can have up to 8200 ppm F (Regenspurg et al., 2022) and whole rock samples from Gedemsa report F concentrations of between 92 and ~3100 ppm. Further experimental investigation on the influence of volatile phases on the phase relationships in peralkaline rocks is required to constrain this further.

4.5 Conclusion

Here we have explored the geochemical variation in peralkaline magmas and the mineralogical control of these trends, comparing data with known mineral assemblages observed

at peralkaline centres. Corbetti shows one of the most restricted compositional ranges in the rift, whereas centres in the northern section, such as Boset and Gedemsa, tend to erupt some of the most extreme and diverse peralkaline compositions reported. Using the parameter Qz* to measure the degree of differentiation, we can trace the chemical variability in peralkaline magmas as they evolve and identify differing liquid lines of descent. Using Qz*, we provide a robust overview of the MER's compositional variability of peralkaline magmas. This has highlighted how traditional discrimination diagrams and the discrete classification of peralkaline products into comendite and pantellerite can mask important information on a magma's degree of differentiation and the evolutionary pathway that it has followed. When investigating peralkaline magmas, it is important to account for the broad compositional space they occupy to assess liquid lines of descent fully.

We demonstrate the variation in peralkaline products across the MER and note how the most significant diversity is observed at silicic centres in the northern section of the MER (such as Boset and Gedemsa). These centres likely experienced higher magma flux rates, establishing more developed magmatic systems where mafic and intermediate compositions can survive longer within the mush and do not fractionate quickly towards rhyolitic compositions due to a lower thermal gradient between the magma and the surrounding crust. Centres which show slight variations in geochemistry are typically under-sampled; however, Corbetti has been demonstrated to erupt geochemically similar magmas over its > 182 ka yr eruptive history (Fontijn et al., 2018; Colby et al., 2022, Chapter 3). Whilst we observe some slight variation in major element compositions at Corbetti, the general monotony of Corbetti's magmas is likely the result of similar P-T-H_2O-fO_2 conditions during magma evolution leading to only slightly differing liquid lines of descent. This coupled with a lower magma flux and potentially some degree of magma mixing (Chapter 3, may be the cause of the restricted compositional range.

We also investigate the role of alkali-feldspar fractionation on the evolution of peralkaline magmas through the lens of the Qz-Or-Ab-Ns-Ac residua system. Here we observe two distinctive trends where data either plot along the cotectic defined by Carmichael and MacKenzie (1963) or the cotectic defined by Di Carlo et al. (2010) and Romano et al. (2020). Some samples from Boset, Aluto and Gedemsa follow the cotectic of Carmichael and MacKenzie (1963), and show a sharp increase in the proportion of normative Or, which can be explained through the fractionation of Na-rich feldspar and Na-rich clinopyroxene and/or aenigmatite. This results in a melt with a higher proportion of K_2O than Na_2O. We also observe samples at Boset following the cotectic of Di Carlo et al. (2010) and Romano et al. (2020), which trends towards the EMC. This requires fractionating a higher proportion

of alkali-feldspar and Na-poor clinopyroxenes. Notably, quartz does not necessarily need to fractionate to reach these extreme peralkaline compositions. This results in a melt with a higher proportion of Na_2O relative to K_2O. In addition, data from Gedemsa shows potential shifting in the location of the cotectic to lower Qz* values, which is likely the result of magma storage at different pressures or differences in the concentration of halogens, in particular F, in the melt, which increase the size of the quartz field (Scaillet and Macdonald, 2006).

Overall, future experimental studies should seek to expand the pressure range of current phase relationship experiments and investigate how this influences the location of the quartz-feldspar cotectic. In addition, further consideration needs to be given to the influence of volatile phases, particularly fluorine, and their effects on the quartz field in peralkaline melts.

Chapter 5

Conclusions

This thesis has explored the physical volcanology of a restless caldera within the Main Ethiopian Rift (MER) and used a variety of physical and chemical data to develop insights into past eruptions, investigate magma storage conditions, and consider the chemical variability of the peralkaline magmas found in the MER and the mineralogical control on their evolution. Here I outline the main findings of this work, outline the wider implications and highlight potential areas of future investigation that would further our understanding of Corbetti and, more widely, the processes governing the evolution of peralkaline magmas and their associated hazards.

5.1 Physical Volcanology

One of the aims of this thesis was to provide a comprehensive overview of the stratigraphy and eruptive history of Corbetti encompassing pre-, syn-, and post-caldera activity. This was achieved through a detailed field campaign conducted in Jan-Feb 2020. We developed a composite stratigraphy (Figure 5.1) by identifying key marker horizons and correlating them across multiple sites within the caldera. The key findings can be summarised as follows:

1. Corbetti has followed a similar evolutionary pattern to other calderas in the MER with an initial shield-building stage, followed by caldera collapse dated to $\sim$ 182 ka (Hutchison et al., 2016b; Vidal et al., 2022a) and post-caldera volcanism.

2. The pre-caldera activity was dominated by the eruption of multiple large rhyolite lava flows likely to have erupted from numerous vents. We also find evidence of units which may record proximal pumice cone facies within the caldera wall, supporting our assessment that activity originated from numerous vents across the pre-caldera shield.

3. We find previously undocumented lithic lag breccias in the southernmost section of the caldera wall, likely forming part of precursory activity associated with the emplacement of pyroclastic density currents in the lead-up to caldera collapse.

4. Post-caldera activity has centred around 3 edifices: Artu, Urji and Chabbi. These edifices have been built up over numerous eruptions from various vents, with eruptions from Urji being predominantly explosive, whilst eruptions at Chabbi have generated extensive obsidian lavas.

5. We have compiled a relative chronology of activity by correlating stratigraphic units across the caldera and established a recurrence rate of one eruption every 300-400 years over the past 2.3 ka.

6. We have constrained the date of the Biftu Tuff Cone eruption to < 7375 ± 54 cal BP based on ^{14}C dating of shells found within associated PDC deposits.

7. Oxygen and Carbon isotopes from shells found within the PDC deposits of the Biftu tuff cone indicate the eruption occurred during a high-stand period at Lake Hawassa, raising the possibility of a phreatomagmatic eruption. The ash-rich nature of the deposits supports this.

8. We have re-evaluated the obsidian flows on Chabbi, leading to 3 additional units being identified (Figure 5.2).

9. We note that eruptions from Corbetti are commonly associated with the emplacement of localised PDC deposits, which, should an eruption occur, would pose a significant risk to the > 14,000 people living within the caldera.

5.2 Magma Storage Conditions

Using samples collected from fieldwork, we conducted an extensive geochemical investigation of Corbetti's erupted products using whole-rock, glass and mineral data to investigate

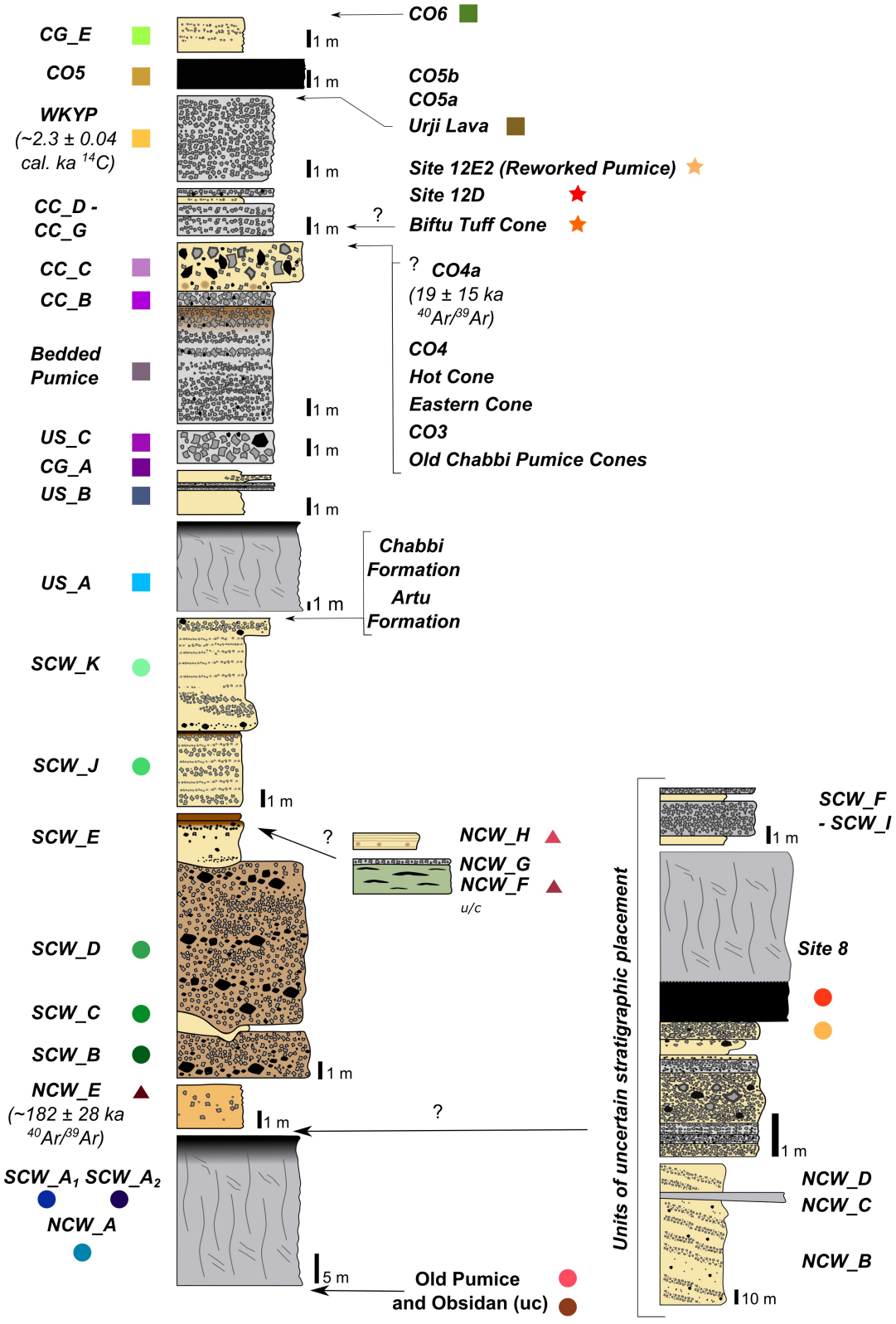

Figure 5.1: Composite stratigraphy of Corbetti caldera (From Chapter 2), highlighting the major stratigraphic units outlined in Chapter 2 and areas of uncertainty in the placement of certain stratigraphic units.

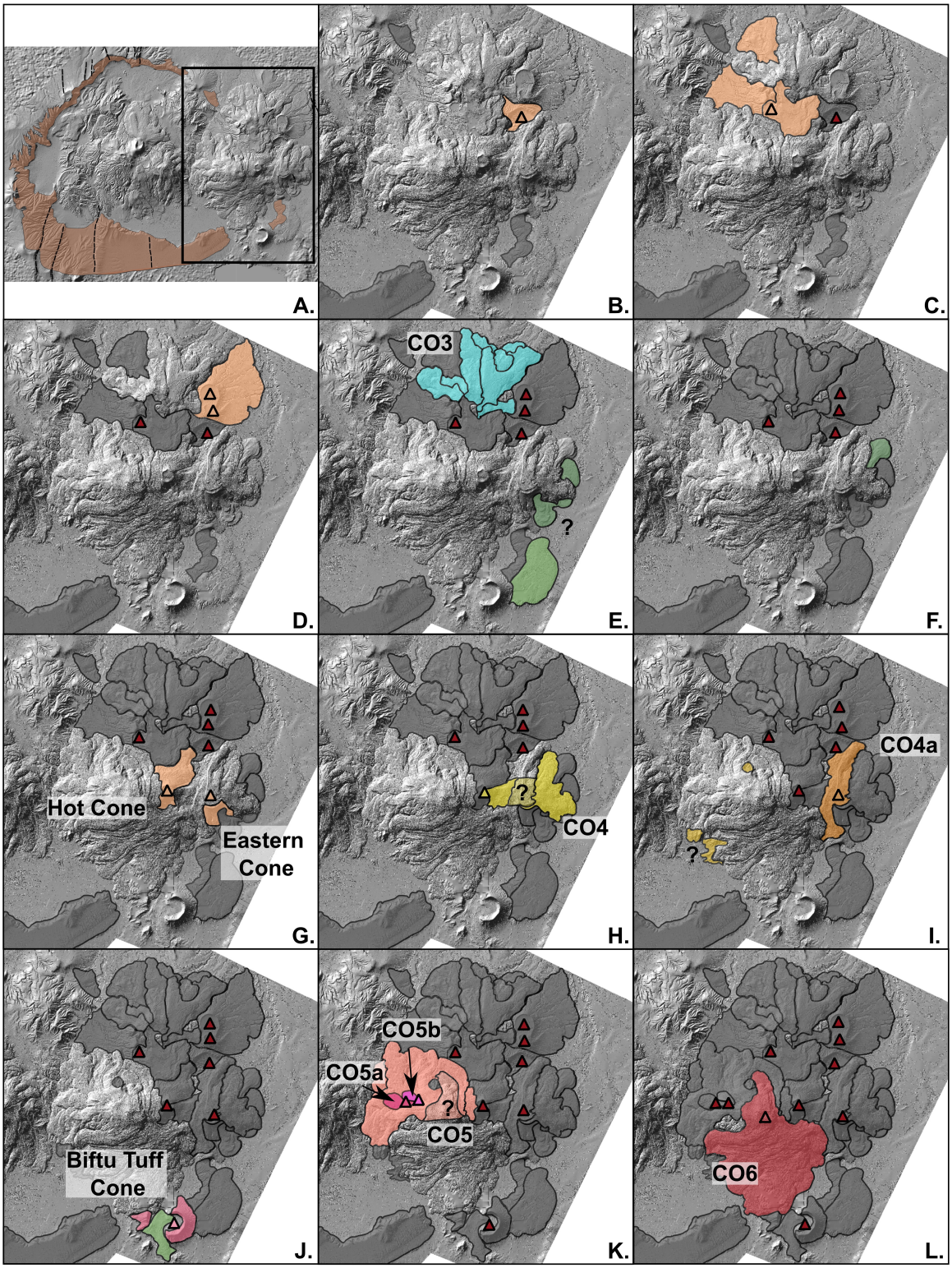

Figure 5.2: Relative chronology of lava flows from Chabbi as presented in Chapter 2, including the 3 new flows identified in this study (CO4a, CO5a and CO5b). For full explanation see Figure 2.11

the magma storage conditions beneath Corbetti Caldera. Due to a lack of mineral phases in Corbetti's erupted products, we also employed RhyoliteMELTS modelling (Gualda et al., 2012) to determine the P-H_2O-fO_2 conditions Corbetti's magmas were likely stored at. Then we compared these to the results of our petrographic analysis. Of significance, we found:

1. The eruption of peralkaline rhyolites dominates the volcanic products at Corbetti, and these erupted products occupy a narrow compositional range making it difficult to discriminate between units based solely on their glass or whole rock geochemistry.

2. In agreement with previous studies, we demonstrate through trace element data and Sr isotopes that Corbetti's magmas are differentiated through progressive fractionation crystallisation.

3. We present glass and mineral data on the only basaltic eruption recorded at Corbetti.

4. Through RhyoliteMELTS modelling, we estimate that magmas at Corbetti are stored at ~150 MPa to 250 MPa prior to eruption, evolving at or below the QFM buffer, and the alkali-basalt source has an initial water content of ~0.5 wt.%

5. Glass data collected from the basaltic tuff recorded a range of compositions from 46 to 52 wt.% SiO_2. We used olivine and plagioclase phenocrysts to conduct thermometry and hygrometry on this sample, yielding estimated temperatures of 1200 - 1100 °C and water contents between 0 - 1.2 wt.% (Figure 5.3).

6. In addition to this, we use glass and mineral data from one of the peralkaline eruptions to estimate temperatures ~760 °C and water contents of up to 7.5 wt.% (Figure 5.3).

7. Clinopyroxene-only barometry yielded an estimated pressure of 50-190 MPa however, the error associated with the barometer exceeds the estimate (± 320 MPa).

8. We also found evidence in the products of the basaltic tuff of magma mixing, suggesting that mixing occurred for some time before the eruption.

9. We found good agreement between estimates using petrographic techniques and RhyoliteMELTS modelling, suggesting that although RhyoliteMELTS is not calibrated for peralkaline compositions, it is a suitable method when more robust methods, such as mineral-liquid barometry, are not possible due to the absence of suitable phases.

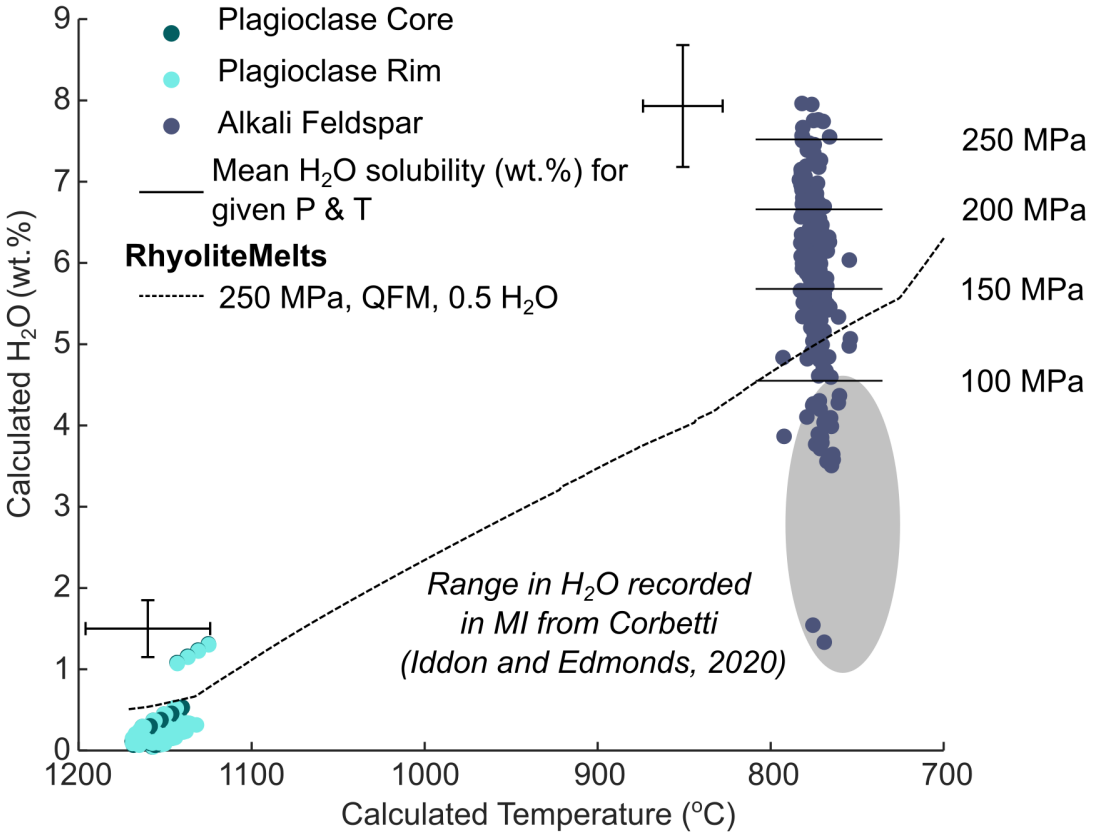

Figure 5.3: Temperature and H_2O content of the basaltic tuff and peralkaline rhyolite estimated from plagioclase-liquid and alkali-feldspar-liquid thermometry and hygrometry as presented in Chapter 3

10. Estimates of magma storage depths from barometry and RhyoliteMELTS modelling matched well with independent estimates from geophysical studies on Corbetti (Gíslason et al., 2015; Lavayssière et al., 2019; Gottsmann et al., 2020; Iddon and Edmonds, 2020) and other studies investigating storage conditions at other MER calderas (Gleeson et al., 2017; Tadesse et al., 2023).

11. We present a compilation of geophysical and petrological data for Corbetti showing the likely depths of magma storage (Figure 5.4)

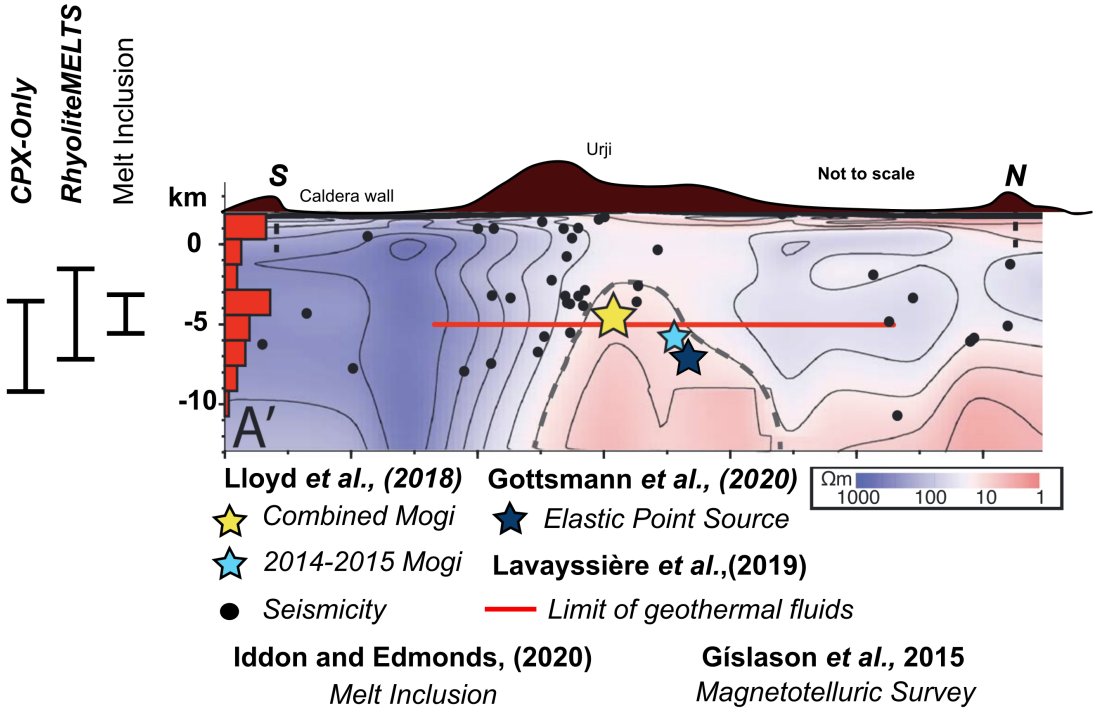

Figure 5.4: Overview of geophysical and petrological data available for Corbetti. Figure adapted from Lloyd et al. (2018a) incorporating data from this study and recent geophysical studies. Demonstrates that magma is likely stored in a conductive hot zone ~7 km beneath Corbetti with lenses of shallower melt or geothermal fluids nearer the surface. We see good agreement between the estimates of storage depths from this study and geophysical surveys.

5.3 Diversity in Peralkaline Magmas

Findings from Chapters 2 and 3 have demonstrated a lack of geochemical diversity in Corbettis' peralkaline magmas. In Chapter 4, we compared the lack of diversity observed at Corbetti with other major caldera systems in the MER. We provided an overview of the variation in peralkaline compositions reported across the rift, the minerals found within eruptive deposits and the mineralogical controls on the development of peralkaline magmas.

1. We demonstrate a wide variation in peralkaline compositions reported across the MER and identify multiple liquid lines of descent, varying from one centre to another.

2. We have shown that well sampled centres in the northern section of the MER show a much larger diversity in magmatic compositions compared to similarly well sampled systems in the southern section of the rift. Previous studies have linked a high diversity of erupted compositions to a high magma flux and a developed magmatic system (Weber et al., 2020). We propose that the diversity in compositions observed at Boset and Gedemsa relates to higher magma fluxes over sustained periods of time, resulting in a mature magmatic system where mafic and intermediate compositions can survived, and be extracted and erupted at the surface.

3. Centres such as Corbetti which display a very monotonous range in compositions, likely have less developed magmatic systems owing to a lower magma flux. However, the high post-caldera eruptive volumes at Corbetti ($\sim$ 14.5 km^3; Hunt et al. 2019) suggest a consistent, supply of magma. It is therefore likely that Corbetti experiences episodic injection of magma into its magma system, however due to the crust being less thermally mature, it quickly fractionates to peralkaline rhyolitic compositions before being erupted (Weber et al., 2020).

4. As the magmatic system beneath Corbetti develops, along with this section of the rift, it is likely a greater diversity in eruptive compositions will be observed, similar to those in the northern, more mature, section of the MER.

5. We identify trends in major element data (SiO_2, TiO_2, CaO, and peralkalinity index), and investigate the mineralogical controls on these trends through mass balance modelling.

6. We highlight that discrete classification of peralkaline compositions under the comendite, pantellerite nomenclature poses the risk of masking important geochemical characteristics of a dataset. We demonstrate that using the Qz* parameter (=100*Qz_n/[Qz_n + Or_n + Ab_n]) to investigate the broad compositional space that a peralkaline magma can occupy provides a more robust approach.

7. We compiled a dataset of mineral assemblages reported in natural samples across the rift and compared these to reported whole rock and glass data for the same samples. From this, we find systematic mineral/chemical variations within the comendites and pantellerites of the MER. For example, aenigmatite is only present in samples with Qz* values > 28 and fayalite is absent in assemblages with a Qz* value of > 40.

8. By projecting data onto the Qz-Or-Ab-Ns-Ac residua system, we are able to identify differing trends in the location and nature of the alkali-feldspar quartz cotectic.

9. Data from several centres follows two distinct trends, which follow either the quartz feldspar cotectic of Carmichael and MacKenzie (1963) or Di Carlo et al. (2010) & Romano et al. (2020).

10. We show that these differing trends can be explained through the fractionation of different quantities and compositions of feldspar (Na-rich or K-rich) and the presence or absence of Na-rich clinopyroxenes.

11. We also highlight how the location of the quartz-feldspar cotectic appears to shift to lower Qz* values at Gedemsa, which may be a consequence of differing storage pressures or high F concentrations, increasing the quartz field size Scaillet and Macdonald (2006).

12. We strongly encourage the need for further experimental studies to investigate phase relationships at higher pressures and investigate the role of F on the quartz-feldspar cotectic.

5.4 Future Work

5.4.1 Palaeomagnetism

Palaeomagnetism has been used to determine the emplacement temperature of the deposits of pyroclastic density currents (Hoblitt and Kellogg, 1979; McClelland et al., 2004; Porreca

et al., 2008). This is achieved through the acquisition of a partial thermal remanent magmatism. For instance, when a lava dome is emplaced and cooled, magnetic minerals will be orientated in the direction of the magnetic field. If a subsequent eruption was to remobilise and incorporate clasts into a PDC, an investigation of the magnetic orientation of these clasts can provide clues to the emplacement temperature of the PDC. Should emplacement temperatures exceed the curie point (~ 570 °C), the original magnetic alignment will be wiped from the sample, and all the clasts will have a new alignment in the direction of the present-day magnetic field. Similarly, if emplacement temperatures are similar to the ambient air temperature (~30 °C), clasts will have random orientations in the deposit when analysed. However, if clasts are heated during transport to temperatures less than the curie point, once they are emplaced and begin to cool, a portion of the magnetism will be overwritten by the present-day magnetic field, leaving two magnetic orientations in the sample. Once the natural remnant magnetism has been measured, samples undergo thermal demagnetisation to determine the maximum emplacement temperature (Porreca et al., 2008).

During our 3-week field campaign, we collected orientated samples of lithic clasts from two large lithic lag breccias within the southern caldera wall (SCW_B & SCW_D; Figure 5.1). These samples will determine the emplacement temperatures of the two lithic lag breccias. One drawback is that samples could only be collected from the top of deposit SCW_B and base of SCW_D due to the limited exposure and accessibility of the outcrop. However, this technique is anticipated to provide useful insight into the deposition of these deposits and the nature of lithic lag breccias in peralkaline systems.

5.4.2 Volcanic Risk

One area currently lacking at Corbetti is a hazard assessment (Martin-Jones et al., 2017). This work has highlighted the propensity for Corbetti to generate localised, ash-rich pyroclastic density currents, which would pose a significant risk to the > 14,000 population who live within the caldera (Colby et al., 2022). Similarly, the proximity of 2 major settlements, Hawassa and Shashemene, would place them at risk in the event of an eruption similar to the WKYP, which emplaced up to 50 cm on pumice in Shashemene (Fontijn et al., 2018). One challenge in assessing risk at Corbetti is the difference in eruptive styles between Urji and Chabbi and the nature of the hazard posed by any eruption. This study has demonstrated that the extrusion of obsidian lavas will likely dominate future eruptions from Chabbi; however, one area of uncertainty is whether these eruptions are purely effusive or have an explosive

component. In our field study, we identified pumice fall deposits which may be associated with eruptions from Chabbi; however, this is still highly uncertain. An eruption from Urji will likely be a significantly more explosive, pumice cone-forming eruption generating localised PDCs.

To assess the future volcanic risk, a probabilistic approach should be taken, similar to studies conducted at Aluto (McNamara et al., 2018; Clarke, 2020; Tierz, 2020; Tierz et al., 2020); however, this should be integrated with an assessment of population vulnerability, taking into account factors such as the routes locals would take to evacuate, disruption to local to regional infrastructure (e.g. geothermal wells, Hawassa airport and quarrying operations within the caldera), transport networks and damage to electricity lines which run through the caldera. This is particularly important as there are limited access routes into the caldera, meaning they would act as pinch points during any evacuation. Similarly, the main road, which runs through the caldera's centre, would likely be blocked in the event of an eruption from Urji or Chabbi.

A novel way of conducting this assessment would be through fuzzy logic. It can be employed to deal with partial truths where, for instance, a true value may vary between 0 and 1, whereas in Boolean logic, the truth value must be 1 or 0. This allows for imprecise or non-numerical data to be incorporated into an assessment. Fuzzy logic has been employed in assessing landslide and seismic risk (e.g. Pourghasemi et al. 2012, Pradhan 2012, Gheshlaghi et al. 2020) as these phenomena, like volcanic hazards, contain a significant amount of uncertainty or lack of quantifiable data to use a purely probabilistic approach. Incorporating this with other factors, such as possible evacuation routes, access to emergency facilities and access to sanitation and water, would provide a robust picture of what a volcanic crisis might look like and highlight areas that need improvement to minimise the risk to life.

Any hazard assessment must be coupled with effective and equitable outreach to the local communities. Presently, little to no information is provided about volcanic risk within the caldera (or more generally in Ethiopia), and there is distrust between the local populations and outside stakeholders. The current geothermal project within the caldera has reportedly sought to improve relations with local communities. As this develops, this could be a useful route for engaging local groups on ideas of volcanic unrest and hazards.

5.4.3 Peralkaline Magmas

Further experimental investigation of the phase relationships of peralkaline magmas is required. Currently, the experimental dataset is limited compared with calc-alkaline systems, limiting our ability to interpret phase assemblages and understand evolutionary conditions in peralkaline. No phase relationship experiments have been conducted on peralkaline magmas at pressures greater than 150 MPa limiting the extent to which we can constrain models of peralkaline magma evolution. Geophysical evidence, thermodynamic modelling and petrological data suggest that peralkaline magmas can be stored up to 250 MPa and potentially deeper. Experimental investigation would help validate these findings and improve our ability to assess storage depths in these systems. In addition, further experimental studies should also focus on using products from the MER to probe the diversity in compositions across the rift and the differences between the type locality, Pantelleria. In addition, expanding the experimental database will also enable the effective calibration of mineral-liquid thermobarometers to peralkaline systems, which is currently lacking. This is particularly relevant to clinopyroxene thermobarometers as there is a lack of data on the extreme compositions frequently found within peralkaline systems. Similarly, our findings outlined in Chapter 4 indicate that the location of the alkali-feldspar-quartz cotectic in the Qz-Or-Ab-Ns-Ac residua system varies at several centres in the MER, which may indicate crystallisation under different pressures. Further experimental studies on this residua system are needed to confirm this and to investigate the role of halogens on the timing of quartz crystallisation.

As new paradigms are developed surrounding the processes governing magma evolution (Cashman et al., 2017; Jackson et al., 2018; Sparks et al., 2019; Hu et al., 2022; Gleeson et al., 2023), and models developed to determine P-H_2O-fO_2 conditions (i.e., CHOMPI; Blundy 2022) consideration needs to be given to how these could be applied to peralkaline systems. Although peralkaline magmas are less common than calc-alkaline magmas, they are regionally significant in areas such as the East African Rift; and globally are often associated with mineralisation (e.g. Tadesse 2001). These theories and models have not been applied to peralkaline systems, primarily due to a lack of calibration data. These models have the potential to be hugely influential on our understanding of peralkaline and rift-related volcanism however, significantly more experimental work is needed to calibrate them effectively. This also offers a unique opportunity to probe the structure of subvolcanic reservoirs at these large caldera systems and the processes and timescales leading up to caldera-forming eruptions (Caricchi et al., 2014; Weber et al., 2020; Caricchi et al., 2021;

Weber and Sheldrake, 2022). Similarly, at Corbetti, further work should be conducted to establish the controls on eruptive style between Urji and Chabbi. In particular, how sub-volcanic structure (Lloyd et al., 2018b) influences the distribution of melt and volatiles, resulting in two very different eruptive styles.

5.5 Concluding Remarks

Reflecting on the overarching aims of this study, we have presented a detailed account of eruptive activity at Corbetti, the variation in eruptive styles and offered a hypothesis to the origin of large-scale explosive eruptions. We have outlined the lack of geochemical variability at Corbetti, confirmed the dominant role of fractional crystallisation on the generation of peralkaline melts and offered estimates for H_2O contents of the erupted magmas. We have also compared Corbetti with other silicic systems in the MER and identified the key mineralogical controls on generating the observed peralkaline compositions. Overall, this thesis has reaffirmed the diverse nature of volcanism experienced in the MER, highlighted potential hazards faced by local populations and demonstrated that further work on peralkaline magmas is crucial to furthering our understanding of these enigmatic compositions.

Bibliography

A. Agostini, M. Bonini, G. Corti, F. Sani, and F. Mazzarini. Fault architecture in the Main Ethiopian Rift and comparison with experimental models: Implications for rift evolution and Nubia-Somalia kinematics. *Earth and Planetary Science Letters*, 301 (3-4):479–492, 2011. ISSN 0012821X. doi: 10.1016/j.epsl.2010.11.024. URL http://dx.doi.org/10.1016/j.epsl.2010.11.024. Publisher: Elsevier B.V.

F. Albino and J. Biggs. Magmatic Processes in the East African Rift System: Insights From a 2015–2020 Sentinel-1 InSAR Survey. *Geochemistry, Geophysics, Geosystems*, 22(3):e2020GC009488, 2021. ISSN 1525-2027. doi: 10.1029/2020GC009488. URL https://onlinelibrary.wiley.com/doi/abs/10.1029/2020GC009488. _eprint: https://onlinelibrary.wiley.com/doi/pdf/10.1029/2020GC009488.

F. Albino, J. Biggs, M. Lazecký, and Y. Maghsoudi. Routine Processing and Automatic Detection of Volcanic Ground Deformation Using Sentinel-1 InSAR Data: Insights from African Volcanoes. *Remote Sensing*, 14(22):5703, Jan. 2022. ISSN 2072-4292. doi: 10.3390/rs14225703. URL https://www.mdpi.com/2072-4292/14/22/5703. Number: 22 Publisher: Multidisciplinary Digital Publishing Institute.

A. Allabar, P. L. Petri, D. Eul, and M. Nowak. An empirical H2O solubility model for peralkaline rhyolitic melts. *Contributions to Mineralogy and Petrology*, 177(5): 52, Apr. 2022. ISSN 1432-0967. doi: 10.1007/s00410-022-01915-8. URL https://doi.org/10.1007/s00410-022-01915-8.

E. Altaye. Geology and surface alteration of the Corbetti Caldera. Technical report, Geothermal Institute University of Auckland, Auckland, 1984.

C. Annen. From plutons to magma chambers: Thermal constraints on the accumulation of eruptible silicic magma in the upper crust. *Earth and Planetary Science Letters*, 284(3-4):409–416, 2009. ISSN 0012821X. doi: 10.1016/j.epsl.2009.05.006. URL http://dx.doi.org/10.1016/j.epsl.2009.05.006. Publisher: Elsevier B.V.

W. P. Aspinall, M. Auker, T. Hincks, S. Mahony, F. Nadim, J. Pooley, R. S. J. Sparks, and E. Syre. Volcano Hazard and Exposure in GFDRR Priority Countries and Risk Mitigation Measures-GFDRR, Volcano risk Study. Technical report, Bristol University Cabot Institute and Norwegian Geotechnical Institute (NGI) for the World Bank, Oslo, 2011. Publication Title: Bristol: Bristol University Cabot Institute and NGI Norway for the World Bank: NGI Report 20100806.

D. Ayalew, S. Jung, R. L. Romer, F. Kersten, J. A. Pfänder, and D. Garbe-Schönberg. Petrogenesis and origin of modern Ethiopian rift basalts: Constraints from isotope and trace element geochemistry. *Lithos*, 258-259:1–14, Aug. 2016. ISSN 00244937. doi: 10.1016/j.lithos.2016.04.001. URL `http://dx.doi.org/10.1016/j.lithos.2016.04.001`. Publisher: The Authors ISBN: 2519114088.

D. K. Bailey and J. F. Schairer. Feldspar-liquid equilibria in peralkaline liquids; the orthoclase effect. *American Journal of Science*, 262(10):1198–1206, Dec. 1964. ISSN 0002-9599. doi: 10.2475/ajs.262.10.1198. Publisher: American Journal of Science (AJS).

M. R. Barberio, C. Donati, P. Donato, G. Yirgu, A. Peccerillo, and T. W. Wu. Petrology and geochemistry of Quaternary magmatism in the northern sector of the Ethiopian Rift between Debre Zeit and Awash Park. *Acta Vulcanologica*, 11:69–82, 1999.

I. D. Bastow, D. Keir, and E. Daly. The Ethiopia Afar Geoscientific Lithospheric Experiment (EAGLE): Probing the transition from continental rifting to incipient seafloor spreading. *Geological Society of America Bulletin*, 478:51–76, June 2011. ISSN 978-0-8137-2478-2. doi: 10.1130/2011.2478(04).

M. Benvenuti, S. Carnicelli, G. Belluomini, N. Dainelli, S. Di Grazia, G. A. Ferrari, C. Iasio, M. Sagri, D. Ventra, B. Atnafu, and S. Kebede. The Ziway-Shala lake basin (main Ethiopian rift, Ethiopia): A revision of basin evolution with special reference to the Late Quaternary. *Journal of African Earth Sciences*, 35(2):247–269, 2002. ISSN 08995362. doi: 10.1016/S0899-5362(02)00036-2.

J. Biggs, I. D. Bastow, D. Keir, and E. Lewi. Pulses of deformation reveal frequently recurring shallow magmatic activity beneath the Main Ethiopian Rift. *Geochemistry, Geophysics, Geosystems*, 12(9):1–11, 2011. ISSN 15252027. doi: 10.1029/2011GC003662. ISBN: 1525-2027.

J. Biggs, A. Ayele, T. P. Fischer, K. Fontijn, W. Hutchison, E. Kazimoto, K. Whaler, and T. J. Wright. Volcanic activity and hazard in the East African Rift Zone. *Nature Communications*, 12(1):6881, Nov. 2021. ISSN 2041-1723. doi: 10.1038/s41467-021-27166-y. URL https://www.nature.com/articles/s41467-021-27166-y. Number: 1 Publisher: Nature Publishing Group.

J. Blundy. Chemical Differentiation by Mineralogical Buffering in Crustal Hot Zones. *Journal of Petrology*, 63(7):egac054, July 2022. ISSN 0022-3530, 1460-2415. doi: 10.1093/petrology/egac054. URL https://academic.oup.com/petrology/article/doi/10.1093/petrology/egac054/6612964.

J. Blundy and K. V. Cashman. Ascent-driven crystallisation of dacite magmas at Mount St Helens, 1980–1986. *Contributions to Mineralogy and Petrology*, 140(6):631–650, Mar. 2001. ISSN 1432-0967. doi: 10.1007/s004100000219. URL https://doi.org/10.1007/s004100000219.

J. Blundy and K. V. Cashman. Petrologic Reconstruction of Magmatic System Variables and Processes. *Reviews in Mineralogy and Geochemistry*, 69(1):179–239, Jan. 2008. ISSN 1529-6466. doi: 10.2138/rmg.2008.69.6. URL https://doi.org/10.2138/rmg.2008.69.6.

M. Boccaletti, A. Getaneh, R. Mazzuoli, L. Tortorici, and T. Trua. Chemical variations in a bimodal magma system: the Plio-Quaternary volcanism in the Dera Nazret area (Main Ethiopian Rift, Ethiopia). *Africa Geoscience Review*, 2(1):37–60, 1995.

S. C. Boone, B. P. Kohn, A. J. W. Gleadow, C. K. Morley, C. Seiler, and D. A. Foster. Birth of the East African Rift System: Nucleation of magmatism and strain in the Turkana Depression. *Geology*, 47(9):886–890, 2019. ISSN 0091-7613. doi: 10.1130/g46468.1.

M. J. Branney and P. Kokelaar. *Pyroclastic Density Currents and the Sedimentation of Ignimbrites*, volume 27. Geological Society of London, 2002. ISBN 978-1-86239-124-6. doi: 10.1144/GSL.MEM.2003.027. Publication Title: Geological Society, London, Memoirs ISSN: 9781862394025.

P. Brotzu, L. Morbidelli, E. M. Piccirillo, and G. Traversa. Petrological features of boseti mountains, a complex volcanic system in the axial portion of the main Ethiopian rift. *Bulletin Volcanologique*, 38(1):206–234, 1974. ISSN 0366483X. doi: 10.1007/BF02597811.

P. Brotzu, L. Morbidelli, E. M. Piccirillo, and G. Traversa. Volcanological and magmatological evidence of the Boseti volcanic complex (Main Ethiopian Rift). *Acc Naz Lincei (Roma)*, 47:317–362, 1980.

R. J. Brown, M. Branney, C. Maher, and P. Davila-Harris. Origin of accretionary lapilli within ground-hugging density currents: Evidence from pyroclastic couplets on Tenerife. *Geological Society of America Bulletin*, 122(1-2):305–320, Jan. 2010. ISSN 0016-7606. doi: 10.1130/B26449.1. URL https://pubs.geoscienceworld.org/gsabulletin/article/122/1-2/305-320/125507.

R. J. Brown, C. Bonadonna, and A. J. Durant. A review of volcanic ash aggregation. *Physics and Chemistry of the Earth*, 45-46:65–78, 2012. ISSN 14747065. doi: 10.1016/j.pce.2011.11.001. Publisher: Elsevier Ltd ISBN: 1474-7065.

L. Caricchi, C. Annen, J. Blundy, G. Simpson, and V. Pinel. Frequency and magnitude of volcanic eruptions controlled by magma injection and buoyancy. *Nature Geoscience*, 7(2):126–130, 2014. ISSN 17520894. doi: 10.1038/ngeo2041. Publisher: Nature Publishing Group.

L. Caricchi, M. Townsend, E. Rivalta, and A. Namiki. The build-up and triggers of volcanic eruptions. *Nature Reviews Earth & Environment*, 2(7):458–476, July 2021. ISSN 2662-138X. doi: 10.1038/s43017-021-00174-8. URL https://www.nature.com/articles/s43017-021-00174-8. Number: 7 Publisher: Nature Publishing Group.

I. S. E. Carmichael and W. S. MacKenzie. Feldspar-liquid equilibria in pantellerites; an experimental study. *American Journal of Science*, 261(4):382–396, Apr. 1963. doi: 10.2475/ajs.261.4.382. URL https://ajs.scholasticahq.com/article/58990. Publisher: American Journal of Science.

M. Casey, C. J. Ebinger, D. Keir, R. Gloaguen, and F. Mohamed. Strain accommodation in transitional rifts: extension by magma intrusion and faulting in Ethiopian rift magmatic segments. *Geological Society Special Publication*, 259(2003):143–163, 2006. ISSN 03058719. doi: 10.1144/GSL.SP.2006.259.01.13.

K. V. Cashman, R. S. J. Sparks, and J. D. Blundy. Vertically extensive and unstable magmatic systems: A unified view of igneous processes. *Science*, 355(6331):eaag3055, Mar. 2017. doi: 10.1126/science.aag3055. URL https://www.science.org/doi/full/10.1126/science.aag3055. Publisher: American Association for the Advancement of Science.

P. R. Castillo, X. Liu, and P. Scarsi. The geochemistry and Sr-Nd-Pb isotopic ratios of high 3He/4He Afar and MER basalts indicate a significant role of the African Superplume in EARS magmatism. *Lithos*, 376-377:105791, Dec. 2020. ISSN 0024-4937. doi: 10.1016/j.lithos.2020.105791. URL https://www.sciencedirect.com/science/article/pii/S002449372030428X.

T. Chernet and W. K. Hart. Petrology and geochemistry of volcanism in the northern Main Ethiopian Rift-southern Afar transition region. *Acta Vulcanologica*, 11:21–42, 1999.

B. Clarke. *Post-caldera eruptions and pyroclastic density current hazard in the Main Ethiopian Rift*. PhD thesis, The University of Edinburgh, 2020. URL https://www.researchgate.net/publication/338793244_Post-caldera_eruptions_and_pyroclastic_density_current_hazard_in_the_Main_Ethiopian_Rift/.

B. Clarke, E. S. Calder, F. Dessalegn, K. Fontijn, J. A. Cortés, M. Naylor, I. Butler, W. Hutchison, and G. Yirgu. Fluidal pyroclasts reveal the intensity of peralkaline rhyolite pumice cone eruptions. *Nature Communications*, 10(1):2010, 2019. ISSN 2041-1723. doi: 10.1038/s41467-019-09947-8. URL http://www.nature.com/articles/s41467-019-09947-8. Publisher: Springer US.

B. Clarke, P. Tierz, E. Calder, and G. Yirgu. Probabilistic Volcanic Hazard Assessment for Pyroclastic Density Currents From Pumice Cone Eruptions at Aluto Volcano, Ethiopia. *Frontiers in Earth Science*, 8(August):1–19, Aug. 2020. ISSN 2296-6463. doi: 10.3389/feart.2020.00348. URL https://www.frontiersin.org/article/10.3389/feart.2020.00348/full.

D. J. Colby, D. M. Pyle, K. Fontijn, T. A. Mather, A. A. Melaku, M. A. Mengesha, and G. Yirgu. Stratigraphy and eruptive history of Corbetti Caldera in the Main Ethiopian Rift. *Journal of Volcanology and Geothermal Research*, 428:107580, Aug. 2022. ISSN 03770273. doi: 10.1016/j.jvolgeores.2022.107580. URL https://linkinghub.elsevier.com/retrieve/pii/S0377027322001111.

J. W. Cole. Gariboldi volcanic complex, Ethiopia. *Bulletin Volcanologique*, 33(2):566–578, June 1969. ISSN 1432-0819. doi: 10.1007/BF02596525. URL https://doi.org/10.1007/BF02596525.

G. Corti. Continental rift evolution: From rift initiation to incipient break-up in the Main Ethiopian Rift, East Africa. *Earth-Science Reviews*, 96(1-2):1–53, 2009. ISSN 00128252. doi: 10.1016/j.earscirev.2009.06.005. URL http://dx.doi.org/10.1016/j.earscirev.2009.06.005. Publisher: Elsevier B.V.

G. Corti, D. Maestrelli, and F. Sani. Large-to Local-Scale Control of Pre-Existing Structures on Continental Rifting: Examples From the Main Ethiopian Rift, East Africa. *Frontiers in Earth Science*, 10(January):1–18, 2022. ISSN 22966463. doi: 10.3389/feart.2022.808503.

F. Costa, T. Shea, and T. Ubide. Diffusion chronometry and the timescales of magmatic processes. *Nature Reviews Earth & Environment*, 1(4):201–214, 2020. doi: 10.1038/s43017-020-0038-x. Publisher: Springer US.

G. R. Davies and R. Macdonald. Crustal influences in the petrogenesis of the naivasha basalt - comendite complex: Combined trace element and Sr-Nd-Pb isotope constraints. *Journal of Petrology*, 28(6):1009–1031, 1987. ISSN 00223530. doi: 10.1093/petrology/28.6.1009.

C. Deniel. Heterogeneous initial Sr isotope compositions of highly evolved volcanic rocks from the Main Ethiopian Rift, Ethiopia. *Bulletin of Volcanology*, 71(5):495–508, July 2009. ISSN 1432-0819. doi: 10.1007/s00445-008-0228-8. URL https://doi.org/10.1007/s00445-008-0228-8.

I. Di Carlo, S. G. Rotolo, B. Scaillet, V. Buccheri, and M. Pichavant. Phase equilibrium constraints on pre-eruptive conditions of recent felsic explosive volcanism at Pantelleria Island, Italy. *Journal of Petrology*, 51(11):2245–2276, 2010. ISSN 00223530. doi: 10.1093/petrology/egq055.

D. Di Genova, C. Romano, K. U. Hess, A. Vona, B. T. Poe, D. Giordano, D. B. Dingwell, and H. Behrens. The rheology of peralkaline rhyolites from Pantelleria Island. *Journal of Volcanology and Geothermal Research*, 249:201–216, 2013. ISSN 03770273. doi: 10.1016/j.jvolgeores.2012.10.017. Publisher: Elsevier B.V.

G. M. Di Paola. The Ethiopian Rift Valley (between 7° 00' and 8° 40' lat. north). *Bulletin Volcanologique*, 36(4):517–560, 1972. ISSN 0366483X. doi: 10.1007/BF02599823.

T. H. Druitt. Vent Evolution and Lag Breccia Formation during the Cape Riva Eruption of Santorini, Greece. *The Journal of Geology*, 93(4):439–454, July 1985. ISSN 0022-1376. doi: 10.1086/628965. URL https://www.jstor.org/stable/30078316.

J. Dufek and O. Bachmann. Quantum magmatism: Magmatic compositional gaps generated by melt-crystal dynamics. *Geology*, 38(8):687–690, Aug. 2010. ISSN 1943-2682. doi: 10.1130/G30831.1. URL

http://pubs.geoscienceworld.org/geology/article/38/8/687/130302/Quantum-magmatism-Magmatic-compositional-gaps.

W. A. Duffield, C. R. Bacon, and G. R. Roquemore. Origin of reverse-graded beddeing in air-fall pumice, Coso Range, California. *Journal of Volcanology and Geothermal Research*, 5:35–48, 1979.

C. J. Ebinger. Continental break-up: The East African perspective. *Astronomy and Geophysics*, 46(2):2.16–2.21, 2005. ISSN 1366-8781. doi: 10.1111/j.1468-4004.2005.46216.x. ISBN: 1366-8781.

C. J. Ebinger and M. Casey. Continental breakup in magmatic provinces: An Ethiopian example. *Geology*, 29(6):527–530, 2001. ISSN 00917613. doi: 10.1130/0091-7613(2001)029<0527:CBIMPA>2.0.CO;2.

Ethiopian Public Health Institue (EPHI). Ethiopia Mini Demographic and Health Survey 2019: Final Report. Technical report, EPHI and ICF, Rockville, Maryland, USA, 2021. ISBN: 2511127547.

Ethiopian Statistics Agency. Population Projection, 2022. URL http://www.statsethiopia.gov.et/population-projection/. Snapshot:/Users/davidcolby/Zotero/storage/BVYLXE7X/population-projection.html:text/html.

P. Ferla and C. Meli. Evidence of Magma Mixing in the 'Daly Gap' of Alkaline Suites: a Case Study from the Enclaves of Pantelleria (Italy). *Journal of Petrology*, 47(8):1467–1507, Aug. 2006. ISSN 1460-2415, 0022-3530. doi: 10.1093/petrology/egl015. URL https://academic.oup.com/petrology/article-lookup/doi/10.1093/petrology/egl015.

L. Field, J. Blundy, R. A. Brooker, T. Wright, and G. Yirgu. Magma storage conditions beneath Dabbahu Volcano (Ethiopia) constrained by petrology, seismicity and satellite geodesy. *Bulletin of Volcanology*, 74(5):981–1004, 2012. ISSN 02588900. doi: 10.1007/s00445-012-0580-6.

K. Fontijn, K. McNamara, A. Z. Tadesse, D. M. Pyle, F. Dessalegn, W. Hutchison, T. A. Mather, and G. Yirgu. Contrasting styles of post-caldera volcanism along the Main Ethiopian Rift: Implications for contemporary volcanic hazards. *Journal of Volcanology and Geothermal Research*, 356:90–113, 2018. ISSN 03770273. doi: 10.1016/j.jvolgeores.2018.02.001. Publisher: Elsevier B.V.

S. J. Fowler and F. J. Spera. A metamodel for crustal magmatism: Phase equilibria of giant ignimbrites. *Journal of Petrology*, 51(9):1783–1830, 2010. ISSN 00223530. doi: 10.1093/petrology/egq039.

B. R. Frost and C. D. Frost. A geochemical classification for feldspathic igneous rocks. *Journal of Petrology*, 49(11):1955–1969, 2008. ISSN 00223530. doi: 10.1093/petrology/egn054.

T. Furman, J. Bryce, T. O. Rooney, B. Hanan, G. Yirgu, and D. Ayalew. Heads and Tails: 30 million years of the Afar plume. *The Afar Volcanic Province within the East African Rift System*, 259:95–119, 2006.

H. A. Gheshlaghi, B. Feizizadeh, and T. Blaschke. GIS-based forest fire risk mapping using the analytical network process and fuzzy logic. 0568, 2020. doi: 10.1080/09640568.2019.1594726. Publisher: Routledge.

I. L. Gibson. A pantelleritic welded ash-flow tuff from the Ethiopian Rift Valley. *Contributions to Mineralogy and Petrology*, 28(2):89–111, 1970. ISSN 00107999. doi: 10.1007/BF00404992.

I. L. Gibson. The chemistry and petrogenesis of a suite of pantellerites from the ethiopian rift. *Journal of Petrology*, 13(1):31–44, 1972. ISSN 00223530. doi: 10.1093/petrology/13.1.31.

I. L. Gibson. A Review of the Geology, Petrology and Geochemistry of the Volcano Fantale. *Bulletin of Volcanology*, (38):791–802, 1974.

R. Gillespie, F. A. Street-perrott, and R. Switsur. Post-glacial arid episodes in Ethiopia have implications for climate prediction. *Nature*, 306(5944):680–683, 1983. ISSN 00280836. doi: 10.1038/306680a0.

A. Gioncada and P. Landi. The pre-eruptive volatile contents of recent basaltic and pantelleritic magmas at Pantelleria (Italy). *Journal of Volcanology and Geothermal Research*, 189(1):191–201, Jan. 2010. ISSN 0377-0273. doi: 10.1016/j.jvolgeores.2009.11.006. URL https://www.sciencedirect.com/science/article/pii/S0377027309004387.

F. Giordano, M. D'Antonio, L. Civetta, S. Tonarini, G. Orsi, D. Ayalew, G. Yirgu, F. Dell'Erba, M. A. Di Vito, and R. Isaia. Genesis and evolution of mafic and felsic magmas at Quaternary volcanoes within the Main Ethiopian Rift: Insights from

Gedemsa and Fanta 'Ale complexes. *Lithos*, 188:130–144, 2014. ISSN 00244937. doi: 10.1016/j.lithos.2013.08.008. Publisher: Elsevier B.V.

G. Gíslason, H. Eysteinsson, G. Björnsson, and V. Harðardóttir. Results of Surface Exploration in the Corbetti Geothermal Area, Ethiopia. *World Geothermal Congress 2015*, (April):1–10, 2015.

M. L. Gleeson, M. J. Stock, D. M. Pyle, T. A. Mather, W. Hutchison, G. Yirgu, and J. Wade. Constraining magma storage conditions at a restless volcano in the Main Ethiopian Rift using phase equilibria models. *Journal of Volcanology and Geothermal Research*, 337:44–61, 2017. ISSN 03770273. doi: 10.1016/j.jvolgeores.2017.02.026. Publisher: Elsevier B.V.

M. L. M. Gleeson, C. J. Lissenberg, and P. M. Antoshechkina. Porosity evolution of mafic crystal mush during reactive flow. *Nature Communications*, 14(1):3088, May 2023. ISSN 2041-1723. doi: 10.1038/s41467-023-38136-x. URL https://www.nature.com/articles/s41467-023-38136-x. Number: 1 Publisher: Nature Publishing Group.

R. González-Guzmán. NORRRM: A Free Software to Calculate the CIPW Norm. *Open Journal of Geology*, 06(01):30–38, 2016. ISSN 2161-7570, 2161-7589. doi: 10.4236/ojg.2016.61004. URL http://www.scirp.org/journal/doi.aspx?DOI=10.4236/ojg.2016.61004.

J. Gottsmann, J. Biggs, R. Lloyd, Y. Biranhu, and E. Lewi. Ductility and Compressibility Accommodate High Magma Flux Beneath a Silicic Continental Rift Caldera: Insights From Corbetti Caldera (Ethiopia). *Geochemistry, Geophysics, Geosystems*, 21(4), 2020. ISSN 1525-2027. doi: 10.1029/2020gc008952. URL https://doi.org/10.1029/2020GC008952.

P. Grosse and M. Kervyn. Morphometry of terrestrial shield volcanoes. *Geomorphology*, 304:1–14, 2018. ISSN 0169555X. doi: 10.1016/j.geomorph.2017.12.017. URL https://doi.org/10.1016/j.geomorph.2017.12.017. Publisher: Elsevier B.V.

G. A. R. Gualda, M. S. Ghiorso, R. V. Lemons, and T. L. Carley. Rhyolite-MELTS: a Modified Calibration of MELTS Optimized for Silica-rich, Fluid-bearing Magmatic Systems. *Journal of Petrology*, 53(5):875–890, May 2012. ISSN 0022-3530. doi: 10.1093/petrology/egr080. URL https://doi.org/10.1093/petrology/egr080.

R. P. Hoblitt and K. S. Kellogg. Emplacement temperatures of unsorted and unstratified deposits of volcanic rock debris as determined by paleomagnetic techniques. *Geological Society of America Bulletin*, 90(7):633, 1979. ISSN 0016-7606. doi: 10.1130/0016-7606(1979)90<633:ETOUAU>2.0.CO;2. URL https://pubs.geoscienceworld.org/gsabulletin/article/90/7/633-642/202482.

H. Hu, M. D. Jackson, and J. Blundy. Melting, Compaction and Reactive Flow: Controls on Melt Fraction and Composition Change in Crustal Mush Reservoirs. *Journal of Petrology*, 63(11):egac097, Nov. 2022. ISSN 0022-3530, 1460-2415. doi: 10.1093/petrology/egac097. URL https://academic.oup.com/petrology/article/doi/10.1093/petrology/egac097/6718125.

E. C. Hughes, D. A. Neave, K. J. Dobson, P. J. Withers, and M. Edmonds. How to fragment peralkaline rhyolites: Observations on pumice using combined multi-scale 2D and 3D imaging. *Journal of Volcanology and Geothermal Research*, 336:179–191, 2017. ISSN 03770273. doi: 10.1016/j.jvolgeores.2017.02.020. URL http://dx.doi.org/10.1016/j.jvolgeores.2017.02.020. Publisher: The Authors.

J. A. Hunt, A. Z. Tadesse, T. A. Mather, D. M. Pyle, and P. H. Barry. Spatially Variable CO2 Degassing in the Main Ethiopian Rift: Implications for Magma Storage, Volatile Transport, and Rift-Related Emissions. *Geochemistry, Geophysics, Geosystems*, 18(10):3714–3737, 2017. ISSN 15252027. doi: 10.1002/2017GC006975.

J. A. Hunt, D. M. Pyle, and T. A. Mather. The geomorphology, structure, and lava flow dynamics of peralkaline rift volcanoes from high-resolution digital elevation models. *Geochemistry, Geophysics, Geosystems*, 2019. ISSN 15252027. doi: 10.1029/2018GC008085. URL http://doi.wiley.com/10.1029/2018GC008085. ISBN: 0000000226639.

W. Hutchison, T. A. Mather, D. M. Pyle, J. Biggs, and G. Yirgu. Structural controls on fluid pathways in an active rift system: A case study of the Aluto volcanic complex. *Geosphere*, 11(3):542–562, 2015. ISSN 1553040X. doi: 10.1130/GES01119.1.

W. Hutchison, J. Biggs, T. A. Mather, D. M. Pyle, E. Lewi, G. Yirgu, S. Caliro, G. Chiodini, L. E. Clor, and T. P. Fischer. Causes of unrest at silicic calderas in the East African Rift: New constraints from InSAR and soil-gas chemistry at Aluto volcano, Ethiopia. *Geochemistry, Geophysics, Geosystems*, 17(8):3008–3030, Aug. 2016a. ISSN 15252027. doi: 10.1002/2016GC006395. URL http://doi.wiley.com/10.1002/2016GC006395. ISBN: 0148-0227.

W. Hutchison, R. Fusillo, D. M. Pyle, T. A. Mather, J. D. Blundy, J. Biggs, G. Yirgu, B. E. Cohen, R. A. Brooker, D. N. Barfod, and A. T. Calvert. A pulse of mid-Pleistocene rift volcanism in Ethiopia at the dawn of modern humans. *Nature Communications*, 7: 1–12, 2016b. ISSN 20411723. doi: 10.1038/ncomms13192. URL http://dx.doi.org/10.1038/ncomms13192. Publisher: Nature Publishing Group ISBN: 2041-1723 (Electronic) 2041-1723 (Linking).

W. Hutchison, D. M. Pyle, T. A. Mather, G. Yirgu, J. Biggs, B. E. Cohen, D. N. Barfod, and E. Lewi. The eruptive history and magmatic evolution of Aluto volcano: new insights into silicic peralkaline volcanism in the Ethiopian rift. *Journal of Volcanology and Geothermal Research*, 328:9–33, Dec. 2016c. ISSN 03770273. doi: 10.1016/j.jvolgeores.2016.09.010. URL https://linkinghub.elsevier.com/retrieve/pii/S0377027316303535. Publisher: The Authors.

W. Hutchison, T. A. Mather, D. M. Pyle, A. J. Boyce, M. L. M. Gleeson, G. Yirgu, J. D. Blundy, D. J. Ferguson, C. Vye-Brown, I. L. Millar, K. W. W. Sims, and A. A. Finch. The evolution of magma during continental rifting: New constraints from the isotopic and trace element signatures of silicic magmas from Ethiopian volcanoes. *Earth and Planetary Science Letters*, 489(May):203–218, May 2018. ISSN 0012821X. doi: 10.1016/j.epsl.2018.02.027. URL https://doi.org/10.1016/j.epsl.2018.02.027. Publisher: Elsevier B.V.

F. Iddon and M. Edmonds. Volatile-Rich Magmas Distributed Through the Upper Crust in the Main Ethiopian Rift. *Geochemistry, Geophysics, Geosystems*, 21(6), 2020. ISSN 15252027. doi: 10.1029/2019GC008904. URL https://doi.org/10.1029/2019GC008904.

F. Iddon, C. Jackson, W. Hutchison, K. Fontijn, D. M. Pyle, T. A. Mather, G. Yirgu, and M. Edmonds. Mixing and Crystal Scavenging in the Main Ethiopian Rift Revealed by Trace Element Systematics in Feldspars and Glasses. *Geochemistry, Geophysics, Geosystems*, 20(1):230–259, Jan. 2019. ISSN 1525-2027. doi: 10.1029/2018GC007836. URL https://onlinelibrary.wiley.com/doi/abs/10.1029/2018GC007836.

InfraCo Africa. Corbetti – InfraCo Africa, 2023. URL https://infracoafrica.com/project/corbetti/.

M. D. Jackson, J. Blundy, and R. S. J. Sparks. Chemical differentiation, cold storage and remobilization of magma in the Earth's crust. *Nature*, 564(7736):405–409, 2018. ISSN 14764687. doi: 10.1038/s41586-018-0746-2. Publisher: Springer US.

V. Janoušek and J. F. Moyen. Mass Balance Modelling of Magmatic Processes in GCDkit. In S. Kumar and R. N. Singh, editors, *Modelling of Magmatic and Allied Processes*, Society of Earth Scientists Series, pages 225–238. Springer International Publishing, Cham, 2014. ISBN 978-3-319-06471-0. doi: 10.1007/978-3-319-06471-0_11. URL https://doi.org/10.1007/978-3-319-06471-0_11.

A. J. Jeffery and R. Gertisser. Peralkaline Felsic Magmatism of the Atlantic Islands. *Frontiers in Earth Science*, 6(145), Nov. 2018. ISSN 2296-6463. doi: 10.3389/feart.2018.00145. URL https://www.frontiersin.org/article/10.3389/feart.2018.00145/full.

N. J. Jordan, S. G. Rotolo, R. Williams, F. Speranza, W. C. McIntosh, M. J. Branney, and S. Scaillet. Explosive eruptive history of Pantelleria, Italy: Repeated caldera collapse and ignimbrite emplacement at a peralkaline volcano. *Journal of Volcanology and Geothermal Research*, 349:47–73, 2018. ISSN 03770273. doi: 10.1016/j.jvolgeores.2017.09.013. URL https://doi.org/10.1016/j.jvolgeores.2017.09.013. Publisher: Elsevier B.V.

C. Jorgenson, O. Higgins, M. Petrelli, F. Bégué, and L. Caricchi. A Machine Learning-Based Approach to Clinopyroxene Thermobarometry: Model Optimization and Distribution for Use in Earth Sciences. *Journal of Geophysical Research: Solid Earth*, 127(4):e2021JB022904, 2022. ISSN 2169-9356. doi: 10.1029/2021JB022904. URL https://onlinelibrary.wiley.com/doi/abs/10.1029/2021JB022904. _eprint: https://onlinelibrary.wiley.com/doi/pdf/10.1029/2021JB022904.

J. M. Kendall, G. W. Stuart, C. J. Ebinger, I. D. Bastow, and D. Keir. Magma-assisted rifting in Ethiopia. *Nature*, 433(7022):146–148, 2005. ISSN 00280836. doi: 10.1038/nature03161.

V. C. Kress and I. S. Carmichael. The compressibility of silicate liquids containing Fe2O3 and the effect of composition, temperature, oxygen fugacity and pressure on their redox states. *Contributions to Mineralogy and Petrology*, 108(1-2):82–92, 1991. ISSN 00107999. doi: 10.1007/BF00307328.

T. Kurz, R. Gloaguen, C. Ebinger, M. Casey, and B. Abebe. Deformation distribution and type in the Main Ethiopian Rift (MER): A remote sensing study. *Journal of African Earth Sciences*, 48(2-3):100–114, 2007. ISSN 1464343X. doi: 10.1016/j.jafrearsci.2006.10.008.

A. L. Lamb, M. J. Leng, H. F. Lamb, R. J. Telford, and M. U. Mohammed. Climatic and non-climatic effects on the δ18O and δ13C compositions of Lake Awassa, Ethiopia, during the last 6.5 ka. *Quaternary Science Reviews*, 21(20-22):2199–2211, 2002. ISSN 02773791. doi: 10.1016/S0277-3791(02)00087-2.

A. Lavayssière, T. Greenfield, D. Keir, A. Ayele, and M. J. Kendall. Local seismicity near the actively deforming Corbetti volcano in the Main Ethiopian Rift. *Journal of Volcanology and Geothermal Research*, June 2019. ISSN 03770273. doi: 10.1016/j.jvolgeores.2019.06.008. URL https://linkinghub.elsevier.com/retrieve/pii/S0377027319301684. Publisher: Elsevier B.V.

C. L. Lawson and R. J. Hanson. *Solving least squares problems*. SIAM, 1995.

R. W. Le Maitre. Some problems of the projection of chemical data into mineralogical classifications. *Contributions to Mineralogy and Petrology*, 56(2):181–189, Jan. 1976. ISSN 1432-0967. doi: 10.1007/BF00399603. URL https://doi.org/10.1007/BF00399603.

M. J. Leng, A. L. Lamb, H. F. Lamb, and R. J. Telford. Palaeoclimatic implications of isotopic data from modern and early Holocene shells of the freshwater snail Melanoides tuberculata, from lakes in the Ethiopian Rift Valley. *Journal of Paleolimnology*, 21(1): 97–106, 1999. ISSN 09212728. doi: 10.1023/A:1008079219280.

K. M. Liszewska, J. C. White, R. Macdonald, and B. Bagiński. Compositional and Thermodynamic Variability in a Stratified Magma Chamber: Evidence from the Green Tuff Ignimbrite (Pantelleria, Italy). *Journal of Petrology*, 59(12):2245–2272, Dec. 2018. ISSN 0022-3530, 1460-2415. doi: 10.1093/petrology/egy095. URL https://academic.oup.com/petrology/article/59/12/2245/5146341.

R. Lloyd, J. Biggs, Y. Birhanu, M. Wilks, J. Gottsmann, M. J. Kendall, A. Ayele, E. Lewi, and H. Eysteinsson. Sustained Uplift at a Continental Rift Caldera. *Journal of Geophysical Research: Solid Earth*, 123(6):5209–5226, 2018a. ISSN 21699356. doi: 10.1029/2018JB015711. URL https://doi.org/10.1029/2018JB015711.

R. Lloyd, J. Biggs, M. Wilks, A. Nowacki, M. J. Kendall, A. Ayele, E. Lewi, and H. Eysteinsson. Evidence for cross rift structural controls on deformation and seismicity at a continental rift caldera. *Earth and Planetary Science Letters*, 487:190–200, 2018b. ISSN 0012821X. doi: 10.1016/j.epsl.2018.01.037. Publisher: Elsevier B.V. ISBN: http://rub.ruc.dk/soeg/kviksoeg/?query=8759308893.

S. C. Loughlin, R. S. J. Sparks, S. K. Brown, S. F. Jenkins, and C. Vye-Brown. *Global Volcanic Hazards and Risk*. Cambridge University Press, 2015. ISBN 978-1-316-27627-3.

R. Macdonald. Nomenclature and petrochemistry of the peralkaline oversaturated extrusive rocks. *Bulletin Volcanologique*, 38(2):498–516, June 1974. ISSN 0258-8900. doi: 10.1007/BF02596896. URL http://link.springer.com/10.1007/BF02596896.

R. Macdonald and I. L. Gibson. Pantelleritic obsidians from the volcano Chabbi (Ethiopia). *Contributions to Mineralogy and Petrology*, 24(3):239–244, 1969. ISSN 0010-7999. doi: 10.1007/BF00376050. URL http://link.springer.com/10.1007/BF00376050.

R. Macdonald, B. Baginski, P. T. Leat, J. C. White, and P. Dzierzanowski. Mineral stability in peralkaline silicic rocks: Information from trachytes of the Menengai volcano, Kenya. *Lithos*, 125(1-2):553–568, 2011. ISSN 00244937. doi: 10.1016/j.lithos.2011.03.011.

R. Macdonald, B. Bagiński, F. Ronga, P. Dzierzanowski, M. Lustrino, A. Marzoli, and L. Melluso. Evidence for extreme fractionation of peralkaline silicic magmas, the Boseti volcanic complex, Main Ethiopian Rift. *Mineralogy and Petrology*, 104(3-4):163–175, 2012. ISSN 09300708. doi: 10.1007/s00710-011-0184-4.

R. Macdonald, J. C. White, and H. E. Belkin. Peralkaline silicic extrusive rocks: magma genesis, evolution, plumbing systems and eruption. *Comptes Rendus. Géoscience*, 353(S2):7–59, 2021. ISSN 1778-7025. doi: 10.5802/crgeos.97. URL https://comptes-rendus.academie-sciences.fr/geoscience/item/CRGEOS_2021__353_S2_7_0/.

D. Maestrelli, G. Corti, M. Bonini, D. Montanari, and F. Sani. Caldera collapse and tectonics along the Main Ethiopian Rift: reviewing possible relationships. *Comptes Rendus. Géoscience*, 353(S2):91–109, Jan. 2022. ISSN 1778-7025. doi: 10.5802/crgeos.63. URL https://comptes-rendus.academie-sciences.fr/geoscience/articles/10.5802/crgeos.63/.

P. K. H. Maguire, C. J. Ebinger, G. W. Stuart, G. D. Mackenzie, K. A. Whaler, J.-M. Kendall, M. A. Khan, C. M. R. Fowler, S. L. Klemperer, G. R. Keller, S. Harder, T. Furman, K. Mickus, L. Asfaw, A. Ayele, and B. Abebe. Geophysical project in Ethiopia studies continental breakup. *Eos, Transactions American Geophysical Union*, 84(35):337–343, 2003. ISSN 2324-9250. doi: 10.1029/2003EO350002. URL https://onlinelibrary.wiley.com/doi/abs/10.1029/2003EO350002. _eprint: https://onlinelibrary.wiley.com/doi/pdf/10.1029/2003EO350002.

P. K. H. Maguire, G. Keller, S. Klemperer, G. Mackenzie, K. Keranen, S. Harder, B. O'Reilly, H. Thybo, L. Asfaw, M. Khan, and M. Amha. Crustal structure of the northern Main Ethiopian Rift from the EAGLE controlled-source survey; a snapshot of incipient lithospheric break-up. *Geological Society, London, Special Publications*, 259 (1):269–292, Jan. 2006. doi: 10.1144/GSL.SP.2006.259.01.21. URL https://www.lyellcollection.org/doi/abs/10.1144/GSL.SP.2006.259.01.21. Publisher: The Geological Society of London.

G. A. Mahood. Pyroclastic rocks and calderas associated with strongly peralkaline magmatism. *Journal of Geophysical Research*, 89(B10):8540, 1984. ISSN 0148-0227. doi: 10.1029/JB089iB10p08540. URL http://doi.wiley.com/10.1029/JB089iB10p08540.

G. A. Mahood and J. A. Stimac. Trace-element partitioning in pantellerites and trachytes. *Geochimica et Cosmochimica Acta*, 54(8):2257–2276, 1990. ISSN 00167037. doi: 10.1016/0016-7037(90)90050-U.

D. A. C. Manning. The effect of fluorine on liquidus phase relationships in the system Qz-Ab-Or with excess water at 1 kb. *Contributions to Mineralogy and Petrology*, 76 (2):206–215, May 1981. ISSN 1432-0967. doi: 10.1007/BF00371960. URL https://doi.org/10.1007/BF00371960.

D. A. C. Manning, D. L. Hamilton, C. M. B. Henderson, and M. J. Dempsey. The probable occurrence of interstitial Al in hydrous, F-bearing and F-free aluminosilicate melts. *Contributions to Mineralogy and Petrology*, 75(3):257–262, Sept. 1981. ISSN 1432-0967. doi: 10.1007/BF01166765. URL https://doi.org/10.1007/BF01166765.

C. M. Martin-Jones, C. S. Lane, N. J. Pearce, V. C. Smith, H. F. Lamb, F. Schaebitz, F. Viehberg, M. C. Brown, U. Frank, and A. Asrat. Recurrent explosive eruptions from a high-risk Main Ethiopian Rift volcano throughout the Holocene. *Geology*, 45(12):1127–1130, 2017. ISSN 0091-7613. doi: 10.1130/G39594.1. URL http://pubs.geoscienceworld.org/geology/article/doi/10.1130/G39594.1/519598/Recurrent-explosive-eruptions-from-a-highrisk-Main. ISBN: 0091-7613.

F. Mazzarini, G. Corti, P. Manetti, and F. Innocenti. Strain rate and bimodal volcanism in the continental rift: Debre Zeyt volcanic field, northern MER, Ethiopia. *Journal of African Earth Sciences*, 39(3-5):415–420, 2004. ISSN 08995362. doi: 10.1016/j.jafrearsci.2004.07.025.

E. McClelland, C. J. N. Wilson, and L. Bardot. Palaeotemperature determinations for the 1.8-ka Taupo ignimbrite, New Zealand, and implications for the emplacement history of a high-velocity pyroclastic flow. *Bulletin of Volcanology*, 66(6):492–513, Aug. 2004. ISSN 1432-0819. doi: 10.1007/s00445-003-0335-5. URL https://doi.org/10.1007/s00445-003-0335-5.

W. F. McDonough and S. s. Sun. The composition of the Earth. *Chemical Geology*, 120 (3):223–253, Mar. 1995. ISSN 0009-2541. doi: 10.1016/0009-2541(94)00140-4. URL https://www.sciencedirect.com/science/article/pii/0009254194001404.

K. McNamara, K. V. Cashman, A. C. Rust, K. Fontijn, F. Chalié, E. L. Tomlinson, and G. Yirgu. Using Lake Sediment Cores to Improve Records of Volcanism at Aluto Volcano in the Main Ethiopian Rift. *Geochemistry, Geophysics, Geosystems*, 19(9):3164–3188, 2018. ISSN 15252027. doi: 10.1029/2018GC007686.

P. Mohr, J. G. Mitchell, and R. G. H. Raynolds. Quaternary volcanism and faulting at O'A caldera, central ethiopian rift. *Bulletin Volcanologique*, 43(1):173–189, 1980. ISSN 0366483X. doi: 10.1007/BF02597619.

P. A. Mohr. Chabbi Volcano (Ethiopia). *Bulletin Volcanologique*, (July 1897):797–815, 1966.

S. Mollo, M. Masotta, F. Forni, O. Bachmann, G. De Astis, G. Moore, and P. Scarlato. A K-feldspar–liquid hygrometer specific to alkaline differentiated magmas. *Chemical Geology*, 392:1–8, Jan. 2015. ISSN 0009-2541. doi: 10.1016/j.chemgeo.2014.11.010. URL https://www.sciencedirect.com/science/article/pii/S0009254114005282.

L. Morbidelli, M. Nicoletti, C. Petrucciani, and E. M. Piccirillo. Ethiopian South-Eastern Plateau and related escarpment: K/Ar ages of the main volcanic events (Main Ethiopian Rift from $8^{o}10'$ to $9^{o}0'$ Lat. North). In *Afar Depression of Ethiopia.*, pages 362–370. Schweizerbart'sche Verlagsbuchhandlung (Ngele u. Obermiller), Stuttgart, 1975.

N. Morimoto. Nomenclature of pyroxenes. *Mineralogical Journal*, 14(5):198–221, 1989. doi: 10.2465/minerj.14.198.

D. A. Neave, G. Fabbro, R. A. Herd, C. M. Petrone, and M. Edmonds. Melting, differentiation and degassing at the pantelleria volcano, Italy. *Journal of Petrology*, 53(3):637–663, 2012. ISSN 00223530. doi: 10.1093/petrology/egr074.

W. Nigussie, K. Mickus, D. Keir, A. Alemu, Y. Muhabaw, A. A. Muluneh, E. Yehualaw, and Z. Demissie. Subsurface structure of magmatic segments during continental breakup: Perspectives from a gravity data analysis along the Main Ethiopian Rift. *Frontiers in Earth Science*, 10, 2023. ISSN 2296-6463. URL https://www.frontiersin.org/articles/10.3389/feart.2022.1092759.

L. A. Olaka, E. O. Odada, M. H. Trauth, and D. O. Olago. The sensitivity of East African rift lakes to climate fluctuations. *Journal of Paleolimnology*, 44(2):629–644, 2010. ISSN 09212728. doi: 10.1007/s10933-010-9442-4.

A. Peccerillo, B. Mandefro, G. Solomon, G. Hambisa, H. Bedru, and K. Tesfaye. The Precambrian Rocks From Southern Ethiopia - Petrology, Geochemistry and Their Interaction With the Recent Volcanism From the Ethiopian Rift Valley. *Neues Jahrbuch Fur Mineralogie-Abhandlungen*, 173(c):237–262, 1998. doi: 10.1127/njma/173/1998/237.

A. Peccerillo, M. R. Barberio, G. Yirgu, D. Ayalew, M. Barbieri, and T. W. Wu. Relationships between Mafic and Peralkaline Silicic Magmatism in Continental Rift Settings: a Petrological, Geochemical and Isotopic Study of the Gedemsa Volcano, Central Ethiopian Rift. *Journal of Petrology*, 44(11):2003–2032, Nov. 2003. ISSN 1460-2415. doi: 10.1093/petrology/egg068. URL https://academic.oup.com/petrology/article-lookup/doi/10.1093/petrology/egg068.

A. Peccerillo, C. Donati, A. P. Santo, A. Orlando, G. Yirgu, and D. Ayalew. Petrogenesis of silicic peralkaline rocks in the Ethiopian rift: Geochemical evidence and volcanological implications. *Journal of African Earth Sciences*, 48(2-3):161–173, 2007. ISSN 08995362. doi: 10.1016/j.jafrearsci.2006.06.010. ISBN: 1362-4962 (Electronic)\r0305-1048 (Linking).

A. Pizzi, M. Coltorti, B. Abebe, L. Disperati, G. Sacchi, and R. Salvini. The Wonji fault belt (Main Ethiopian Rift): structural and geomorphological constrains and GPS monitoring. In G. Yirgu, C. J. Ebinger, and P. K. H. Maguire, editors, *The Afar Volcanic Province within the East African Rift System*, pages 191–207. Geological Society of London, Special Publications, 2006.

M. Porreca, M. Mattei, C. MacNiocaill, G. Giordano, E. McClelland, and R. Funiciello. Paleomagnetic evidence for low-temperature emplacement of the phreatomagmatic Peperino Albano ignimbrite (Colli Albani volcano, Central Italy). *Bulletin of Volcanology*, 70(7):877–893, May 2008. ISSN 1432-0819. doi: 10.1007/s00445-007-0176-8. URL https://doi.org/10.1007/s00445-007-0176-8.

H. R. Pourghasemi, B. Pradhan, and C. Gokceoglu. Application of fuzzy logic and analytical hierarchy process (AHP) to landslide susceptibility mapping at Haraz watershed, Iran. *Natural Hazards*, 63(2):965–996, Sept. 2012. ISSN 1573-0840. doi: 10.1007/s11069-012-0217-2. URL https://doi.org/10.1007/s11069-012-0217-2.

B. Pradhan. Application of an advanced fuzzy logic model for landslide susceptibility analysis. *International Journal of Computational Intelligence Systems*, Mar. 2012. ISSN 1875-6891. URL https://www.tandfonline.com/doi/abs/10.1080/18756891.2010.9727707. Publisher: Taylor & Francis Group.

P. G. Purcell. Re-imagining and re-imaging the development of the East African Rift. *Petroleum Geoscience*, 24(1):21–40, 2018. ISSN 13540793. doi: 10.1144/petgeo2017-036.

K. D. Putirka. Thermometers and barometers for volcanic systems. *Reviews in Mineralogy and Geochemistry*, 69:61–120, 2008. ISSN 15296466. doi: 10.2138/rmg.2008.69.3. ISBN: 9780939950836.

M. L. Rampey, C. Oppenheimer, D. M. Pyle, and G. Yirgu. Caldera-forming eruptions of the Quaternary Kone Volcanic Complex, Ethiopia. *Journal of African Earth Sciences*, 58(1):51–66, 2010. ISSN 1464343X. doi: 10.1016/j.jafrearsci.2010.01.008. URL http://dx.doi.org/10.1016/j.jafrearsci.2010.01.008. Publisher: Elsevier Ltd.

V. Rapprich, V. Žáček, K. Verner, V. Erban, T. Goslar, Y. Bekele, F. Legesa, T. Hroch, and P. Hejtmánková. Wendo Koshe Pumice: The latest Holocene silicic explosive eruption product of the Corbetti Volcanic System (Southern Ethiopia). *Journal of Volcanology and Geothermal Research*, 310:159–171, 2016. ISSN 03770273. doi: 10.1016/j.jvolgeores.2015.12.008.

S. Regenspurg, L. Virchow, F. D. H. Wilke, M. Zimmer, E. Jolie, A. Hachenberger, G. Yirgu, E. F. Gebru, A. Vieth-Hillebrand, and B. Gizaw. Origin and migration of fluoride in the area of the Aluto Volcanic Complex (Main Ethiopian Rift). *Applied Geochemistry*, 146:105403, Nov. 2022. ISSN 0883-2927. doi: 10.1016/j.apgeochem.2022.105403. URL https://www.sciencedirect.com/science/article/pii/S0883292722002074.

P. J. Reimer, W. E. Austin, E. Bard, A. Bayliss, P. G. Blackwell, C. Bronk Ramsey, M. Butzin, H. Cheng, R. L. Edwards, M. Friedrich, P. M. Grootes, T. P. Guilderson, I. Hajdas, T. J.

Heaton, A. G. Hogg, K. A. Hughen, B. Kromer, S. W. Manning, R. Muscheler, J. G. Palmer, C. Pearson, J. Van Der Plicht, R. W. Reimer, D. A. Richards, E. M. Scott, J. R. Southon, C. S. Turney, L. Wacker, F. Adolphi, U. Büntgen, M. Capano, S. M. Fahrni, A. Fogtmann-Schulz, R. Friedrich, P. Köhler, S. Kudsk, F. Miyake, J. Olsen, F. Reinig, M. Sakamoto, A. Sookdeo, and S. Talamo. The IntCal20 Northern Hemisphere Radiocarbon Age Calibration Curve (0-55 cal kBP). *Radiocarbon*, 62(4):725–757, 2020. ISSN 00338222. doi: 10.1017/RDC.2020.41.

E. A. Robertson, J. Biggs, K. V. Cashman, M. A. Floyd, and C. Vye-Brown. Influence of regional tectonics and pre-existing structures on the formation of elliptical calderas in the Kenyan Rift. *Geological Society Special Publication*, 420(1):43–67, 2016. ISSN 03058719. doi: 10.1144/SP420.12.

P. L. Roeder and R. F. Emslie. Olivine-Liquid Equilibrium. *Contributions to Mineralogy and Petrology*, 29:275–289, 1970.

P. Romano, J. Andújar, B. Scaillet, N. Romengo, I. di Carlo, and S. G. Rotolo. Phase Equilibria of Pantelleria Trachytes (Italy): Constraints on Pre-eruptive Conditions and on the Metaluminous to Peralkaline Transition in Silicic Magmas. *Journal of Petrology*, 59(3):559–588, Mar. 2018. ISSN 0022-3530. doi: 10.1093/petrology/egy037. URL https://doi.org/10.1093/petrology/egy037.

P. Romano, B. Scaillet, J. C. White, J. Andújar, I. Di Carlo, and S. G. Rotolo. Experimental and thermodynamic constraints on mineral equilibrium in pantelleritic magmas. *Lithos*, 376-377, 2020. ISSN 18726143. doi: 10.1016/j.lithos.2020.105793.

F. Ronga, M. Lustrino, A. Marzoli, and L. Melluso. Petrogenesis of a basalt-comendite-pantellerite rock suite: The Boseti Volcanic Complex (Main Ethiopian Rift). *Mineralogy and Petrology*, 98(1-2):227–243, Mar. 2009. ISSN 09300708. doi: 10.1007/s00710-009-0064-3. URL http://link.springer.com/10.1007/s00710-009-0064-3.

T. Rooney, T. Furman, I. Bastow, D. Ayalew, and G. Yirgu. Lithospheric modification during crustal extension in the Main Ethiopian Rift. *Journal of Geophysical Research: Solid Earth*, 112(10), 2007. ISSN 21699356. doi: 10.1029/2006JB004916.

T. O. Rooney, W. K. Hart, C. M. Hall, D. Ayalew, M. S. Ghiorso, P. Hidalgo, and G. Yirgu. Peralkaline magma evolution and the tephra record in the Ethiopian Rift. *Contributions to Mineralogy and Petrology*, 164(3):407–426, 2012. ISSN 00107999. doi: 10.1007/s00410-012-0744-6.

F. Samrock, A. V. Grayver, O. Bachmann, Ö. Karakas, and Saar. Integrated magnetotelluric and petrological analysis of felsic magma reservoirs: Insights from Ethiopian rift volcanoes. *Earth and Planetary Science Letters*, 559:116765, 2021. ISSN 0012821X. doi: 10.1016/j.epsl.2021.116765. URL https://doi.org/10.1016/j.epsl.2021.116765. Publisher: Elsevier B.V.

B. Scaillet and R. Macdonald. Phase Relations of Peralkaline Silicic Magmas and Petrogenetic Implications. *Journal of Petrology*, 42(4):825–845, Apr. 2001. ISSN 14602415. doi: 10.1093/petrology/42.4.825. URL https://academic.oup.com/petrology/article-lookup/doi/10.1093/petrology/42.4.825.

B. Scaillet and R. MacDonald. Experimental constraints on the relationships between peralkaline rhyolites of the Kenya Rift Valley. *Journal of Petrology*, 44(10):1867–1894, 2003. ISSN 00223530. doi: 10.1093/petrology/egg062.

B. Scaillet and R. Macdonald. Experimental constraints on pre-eruption conditions of pantelleritic magmas: Evidence from the Eburru complex, Kenya Rift. *Lithos*, 91(1-4): 95–108, 2006. ISSN 00244937. doi: 10.1016/j.lithos.2006.03.010.

B. C. Schmidt and H. Behrens. Water solubility in phonolite melts: Influence of melt composition and temperature. *Chemical Geology*, 256(3):259–268, Nov. 2008. ISSN 0009-2541. doi: 10.1016/j.chemgeo.2008.06.043. URL https://www.sciencedirect.com/science/article/pii/S0009254108002672.

M. J. Severs, T. Azbej, J. B. Thomas, C. W. Mandeville, and R. J. Bodnar. Experimental determination of H2O loss from melt inclusions during laboratory heating: Evidence from Raman spectroscopy. *Chemical Geology*, 237(3):358–371, Mar. 2007. ISSN 0009-2541. doi: 10.1016/j.chemgeo.2006.07.008. URL https://www.sciencedirect.com/science/article/pii/S0009254106005171.

S. J. Shand. On the Relations between Silica, Alumina, and the Bases in Eruptive Rocks, considered as a Means of Classification. *Geological Magazine*, 64(10):446–449, Oct. 1927. ISSN 0016-7568. doi: 10.1017/S0016756800103760.

M. Siegburg, T. M. Gernon, J. M. Bull, D. Keir, D. N. Barfod, R. N. Taylor, B. Abebe, and A. Ayele. Geological evolution of the Boset-Bericha Volcanic Complex, Main Ethiopian Rift: 40Ar/39Ar evidence for episodic Pleistocene to Holocene volcanism. *Journal of Volcanology and Geothermal Research*, 351:115–133, 2017. ISSN 03770273. doi: 10.1016/j.jvolgeores.2017.12.014. URL https://doi.org/10.1016/j.jvolgeores.2017.12.014. Publisher: The Authors.

M. Siegburg, T. M. Gernon, D. Keir, J. M. Bull, R. N. Taylor, E. J. Watts, T. Greenfield, and E. F. Gebru. Temporal clustering of fissural eruption across multiple segments within the Ethiopian Rift. *Frontiers in Earth Science*, 11, 2023. ISSN 2296-6463. URL https://www.frontiersin.org/articles/10.3389/feart.2023.1169635.

J. M. Simmons, R. A. Cas, T. H. Druitt, and C. B. Folkes. Complex variations during a caldera-forming Plinian eruption, including precursor deposits, thick pumice fallout, co-ignimbrite breccias and climactic lag breccias: The 184 ka Lower Pumice 1 eruption sequence, Santorini, Greece. *Journal of Volcanology and Geothermal Research*, 324: 200–219, 2016. ISSN 03770273. doi: 10.1016/j.jvolgeores.2016.05.013. URL http://dx.doi.org/10.1016/j.jvolgeores.2016.05.013. Publisher: Elsevier B.V.

R. S. J. Sparks, C. Annen, J. D. Blundy, K. V. Cashman, A. C. Rust, and M. D. Jackson. Formation and dynamics of magma reservoirs. *Philosophical Transactions of the Royal Society A: Mathematical, Physical and Engineering Sciences*, 377(2139):20180019, Jan. 2019. doi: 10.1098/rsta.2018.0019. URL https://royalsocietypublishing.org/doi/full/10.1098/rsta.2018.0019. Publisher: Royal Society.

M. J. Stock, M. C. S. Humphreys, V. C. Smith, R. Isaia, R. A. Brooker, and D. M. Pyle. Tracking Volatile Behaviour in Sub-volcanic Plumbing Systems Using Apatite and Glass: Insights into Pre-eruptive Processes at Campi Flegrei, Italy. *Journal of Petrology*, 59(12): 2463–2492, Dec. 2018. ISSN 0022-3530, 1460-2415. doi: 10.1093/petrology/egy020. URL https://academic.oup.com/petrology/article/59/12/2463/4955202.

E. Suikkanen. easyMelts-GUI, 2020. URL https://magmasource.caltech.edu/gitlist/easyMelts.git/tree/master/.

A. Tadesse, K. Fontijn, A. Melaku, E. Gebru, V. Smith, E. Tomlinson, D. Barfod, P. Gopon, F. Bégué, L. Caricchi, P. Laha, H. Terryn, S. Gudbrandsson, G. Yirgu, and D. Ayalew. Eruption frequency and magnitude in a geothermally active continental rift: The Bora-Baricha-Tullu Moye volcanic complex, Main Ethiopian Rift. *Journal of Volcanology and Geothermal Research*, page 107471, 2022. ISSN 03770273. doi: 10.1016/j.jvolgeores.2022.107471. URL https://doi.org/10.1016/j.jvolgeores.2022.107471. Publisher: Journal of Volcanology and Geothermal Research.

A. Z. Tadesse, D. Ayalew, R. Pik, G. Yirgu, and K. Fontijn. Magmatic evolution of the Boku Volcanic Complex, Main Ethiopian Rift. *Journal of African Earth Sciences*, 149(June 2017):109–130, 2019. ISSN 18791956. doi: 10.1016/j.jafrearsci.2018.08.003. URL https://doi.org/10.1016/j.jafrearsci.2018.08.003. Publisher: Elsevier.

A. Z. Tadesse, K. Fontijn, L. Caricchi, F. Bégué, S. Gudbrandsson, V. C. Smith, P. Gopon, V. Debaille, P. Laha, H. Terryn, G. Yirgu, and D. Ayalew. Pre-eruptive storage conditions and magmatic evolution of the Bora-Baricha-Tullu Moye volcanic system, Main Ethiopian Rift. *Lithos*, 442-443:107088, Apr. 2023. ISSN 0024-4937. doi: 10.1016/j.lithos.2023.107088. URL https://www.sciencedirect.com/science/article/pii/S0024493723000725.

S. Tadesse. Epithermal gold occurrences in the lakes district of the Main Ethiopian Rift and Tendaho area of the Afar Rift: discovery of a metallogenic province. *SINET: Ethiopian Journal of Science*, 24(1):69–91, 2001. ISSN 2520-7997. doi: 10.4314/sinet.v24i1.18176. URL https://www.ajol.info/index.php/sinet/article/view/18176.

M. Teklemariam, S. Battaglia, G. Gianelli, and G. Ruggieri. Hydrothermal alteration in the Aluto-Langano geothermal field, Ethiopia. *Geothermics*, 25(6):679–702, Dec. 1996. ISSN 0375-6505. doi: 10.1016/S0375-6505(96)00019-3. URL https://www.sciencedirect.com/science/article/pii/S0375650596000193.

P. Tierz. Long-Term Probabilistic Volcanic Hazard Assessment Using Open and Non-open Data: Observations and Current Issues. *Frontiers in Earth Science*, 8(June 2018):1–11, 2020. ISSN 22966463. doi: 10.3389/feart.2020.00257.

P. Tierz, B. Clarke, E. S. Calder, F. Dessalegn, E. Lewi, G. Yirgu, K. Fontijn, J. M. Crummy, Y. Bekele, and S. C. Loughlin. Event trees and epistemic uncertainty in long-term volcanic hazard assessment of rift volcanoes: the example of Aluto (Central Ethiopia). *Geochemistry, Geophysics, Geosystems*, pages 0–2, Aug. 2020. ISSN 1525-2027. doi: 10.1029/2020GC009219. URL https://doi.org/10.1029/2020GC009219.

P. Tollan, B. Ellis, J. Troch, and J. Neukampf. Assessing magmatic volatile equilibria through FTIR spectroscopy of unexposed melt inclusions and their host quartz: a new technique and application to the Mesa Falls Tuff, Yellowstone. *Contributions to Mineralogy and Petrology*, 174(3):24, Mar. 2019. ISSN 1432-0967. doi: 10.1007/s00410-019-1561-y. URL https://doi.org/10.1007/s00410-019-1561-y.

T. Trua, C. Deniel, and R. Mazzuoli. Crustal control in the genesis of Plio-Quaternary bimodal magmatism of the Main Ethiopian Rift (MER): Geochemical and isotopic (Sr, Nd, Pb) evidence. *Chemical Geology*, 155(3-4):201–231, 1999. ISSN 00092541. doi: 10.1016/S0009-2541(98)00174-0.

C. M. Vidal, K. Fontijn, C. S. Lane, A. Asrat, D. Barfod, E. L. Tomlinson, A. Piermattei, W. Hutchison, A. Z. Tadesse, G. Yirgu, A. Deino, Y. Moussallam, P. Mohr, F. Williams, T. A. Mather, D. M. Pyle, and C. Oppenheimer. Geochronology and glass geochemistry of major Pleistocene eruptions in the Main Ethiopian Rift: Towards a regional tephrostratigraphy. *Quaternary Science Reviews*, 290:107601, Aug. 2022a. ISSN 0277-3791. doi: 10.1016/j.quascirev.2022.107601. URL https://www.sciencedirect.com/science/article/pii/S0277379122002323.

C. M. Vidal, C. S. Lane, A. Asrat, D. N. Barfod, D. F. Mark, E. L. Tomlinson, A. Z. Tadesse, G. Yirgu, A. Deino, W. Hutchison, A. Mounier, and C. Oppenheimer. Age of the oldest known Homo sapiens from eastern Africa. *Nature*, (March), 2022b. ISSN 0028-0836. doi: 10.1038/s41586-021-04275-8.

C. Vye-Brown, R. Sparks, E. Lewi, G. Mewa, A. Asrat, S. Loughlin, K. Mee, and T. Wright. Ethiopian Volcanic Hazards: A Changing Research Landscape. 2015.

J. B. Walters. MinPlot: A mineral formula recalculation and plotting program for electron probe microanalysis. Aug. 2022. URL https://eartharxiv.org/repository/view/3494/. Publisher: EarthArXiv.

L. Waters and R. Lange. An updated calibration of the plagioclase-liquid hygrometer-thermometer applicable to basalts through rhyolites. *American Mineralogist*, 100:2172–2184, Oct. 2015. doi: 10.2138/am-2015-5232.

P. K. Webb and S. D. Weaver. Trachyte shield volcanoes: a new volcanic form from South Turkana, Kenya. *Bulletin Volcanologique*, 39(2):294–312, 1975. ISSN 14320819. doi: 10.1007/BF02597833.

G. Weber and T. E. Sheldrake. Geochemical variability as an indicator for large magnitude eruptions in volcanic arcs. *Scientific Reports*, 12(1):15854, Sept. 2022. ISSN 2045-2322. doi: 10.1038/s41598-022-19902-1. URL https://www.nature.com/articles/s41598-022-19902-1. Number: 1 Publisher: Nature Publishing Group.

G. Weber, G. Simpson, and L. Caricchi. Magma diversity reflects recharge regime and thermal structure of the crust. *Scientific Reports*, 10(1):11867, July 2020. ISSN 2045-2322. doi: 10.1038/s41598-020-68610-1. URL https://www.nature.com/articles/s41598-020-68610-1. Number: 1 Publisher: Nature Publishing Group.

J. D. Webster, R. P. Taylor, and C. Bean. Pre-eruptive melt composition and constraints on degassing of a water-rich pantellerite magma, Fantale volcano, Ethiopia. *Contributions to Mineralogy and Petrology*, 114(1):53–62, 1993. ISSN 00107999. doi: 10.1007/BF00307865.

D. Weis, B. Kieffer, C. Maerschalk, J. Barling, J. de Jong, G. A. Williams, D. Hanano, W. Pretorius, N. Mattielli, J. S. Scoates, A. Goolaerts, R. M. Friedman, and J. B. Mahoney. High-precision isotopic characterization of USGS reference materials by TIMS and MC-ICP-MS. *Geochemistry, Geophysics, Geosystems*, 7(8), 2006. ISSN 1525-2027. doi: 10.1029/2006GC001283. URL https://onlinelibrary.wiley.com/doi/abs/10.1029/2006GC001283. _eprint: https://onlinelibrary.wiley.com/doi/pdf/10.1029/2006GC001283.

J. C. White, D. F. Parker, and M. Ren. The origin of trachyte and pantellerite from Pantelleria, Italy: Insights from major element, trace element, and thermodynamic modelling. *Journal of Volcanology and Geothermal Research*, 179(1-2):33–55, 2009. ISSN 03770273. doi: 10.1016/j.jvolgeores.2008.10.007. Publisher: Elsevier B.V.

J. C. White, R. Macdonald, B. Bagiński, and K. M. Liszewska. Extreme Differentiation along Multiple Liquid Lines of Descent in Strongly Peralkaline Magma Series at Pantelleria (Italy). *Journal of Petrology*, 64(2):egad001, Feb. 2023. ISSN 0022-3530. doi: 10.1093/petrology/egad001.

D. L. Whitney and B. W. Evans. Abbreviations for names of rock-forming minerals. *American Mineralogist*, 95(1):185–187, Jan. 2010. ISSN 0003-004X. doi: 10.2138/am.2010.3371. URL https://pubs.geoscienceworld.org/ammin/article/95/1/185-187/45088.

P. Wieser, M. Petrelli, J. Lubbers, E. Wieser, S. Ozaydin, A. J. Kent, and C. Till. Thermobar: An Open-Source Python3 Tool for Thermobarometry and Hygrometry. July 2022. URL https://eartharxiv.org/repository/view/3455/. Publisher: EarthArXiv.

S. Wilke, F. Holtz, D. A. Neave, and R. Almeev. The Effect of Anorthite Content and Water on Quartz–Feldspar Cotectic Compositions in the Rhyolitic System and Implications for Geobarometry. *Journal of Petrology*, 58(4):789–818, Apr. 2017. ISSN 0022-3530. doi: 10.1093/petrology/egx034. URL https://doi.org/10.1093/petrology/egx034.

M. Wilks, A. Ayele, J.-M. Kendall, and J. Wookey. The 24th January 2016 Hawassa earthquake: Implications for seismic hazard in the Main Ethiopian Rift. *Journal*

of African Earth Sciences, 125(January 2016):118–125, Jan. 2017. ISSN 1464343X. doi: 10.1016/j.jafrearsci.2016.11.007. URL https://linkinghub.elsevier.com/retrieve/pii/S1464343X16303569. Publisher: Elsevier Ltd.

G. WoldeGabriel, J. L. Aronson, and R. C. Walter. Geology, geochronology, and rift basin development in the central sector of the Main Ethiopia Rift. *Geological Society of America Bulletin*, 102(4):439–458, Apr. 1990. ISSN 00167606. doi: 10.1130/0016-7606(1990)102<0439:GGARBD>2.3.CO;2. URL http://www.geosociety.org/pubs/copyrt.htm#gsa.

G. WoldeGabriel, R. C. Walter, J. L. Aronson, and W. K. Hart. Geochronology and distribution of silicic volcanic rocks of Plio-Pleistocene age from the central sector of the Main Ethiopian Rift. *Quaternary International*, 13/14(1):69–76, 1992.

K. Wong, D. Ferguson, S. Matthews, D. Morgan, A. Z. Tadesse, Y. Sinetebeb, and G. Yirgu. Exploring rift geodynamics in Ethiopia through olivine-spinel Al-exchange thermometry and rare-earth element distributions. *Earth and Planetary Science Letters*, 597:117820, Nov. 2022. ISSN 0012-821X. doi: 10.1016/j.epsl.2022.117820. URL https://www.sciencedirect.com/science/article/pii/S0012821X22004563.

G. Yirgu, A. Dereje, A. Peccerillo, C. Donati, and P. Donato. Fluorine and chlorine distribution in the volcanic rocks from the Gedemsa volcano, Ethiopian Rift Valley. *Acta Vulcanologica*, 11:169–176, 1999. URL https://www.semanticscholar.org/paper/Fluorine-and-chlorine-distribution-in-the-volcanic-Yirgu-Dereje/9d6ca93e7b0ecb82c491134cdf344e34ede67c0c.

Appendix A

Appendices for Chapter 2



Figure A.1: Laminated ash horizons observed at Site 23 and correlated with NCW_H.

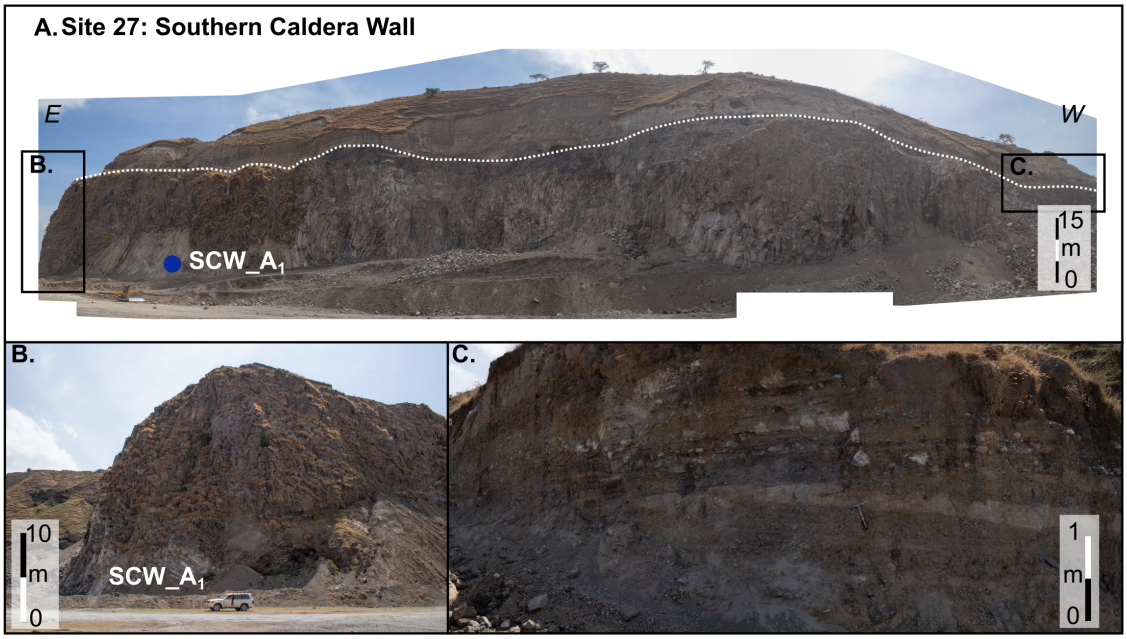

Figure A.2: Overview of Site 27 (Figure 2.2C) B) shows detail of the Jointed rhyolite lava (SCW_A1). C) Shows outcrop of lithic rich PDC deposit above the rhyolitic flow which is likely a different lithofacies of SCW_K however this is unclear.

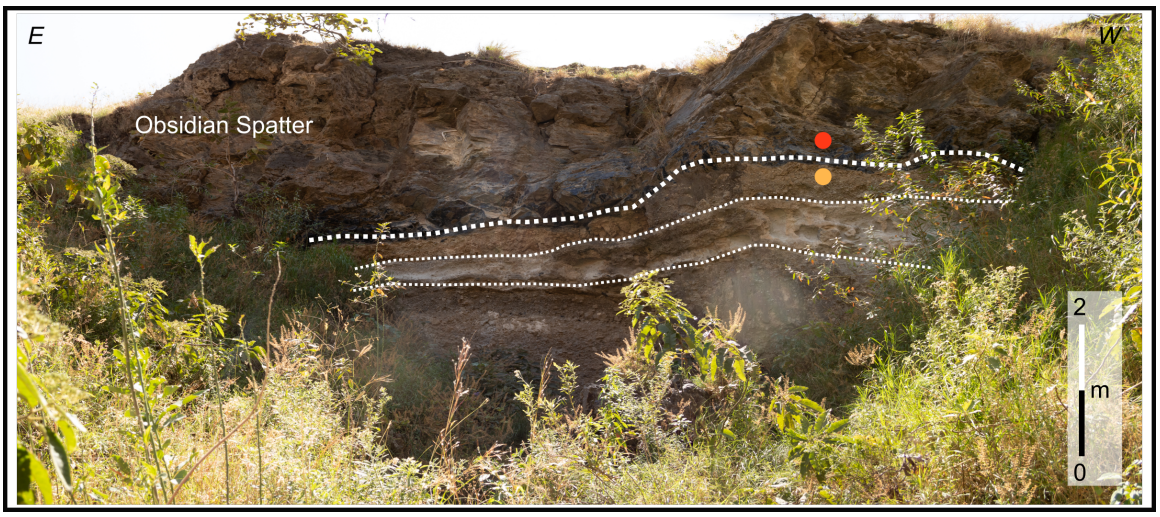

Figure A.3: Outcrop at Site 8 (Figure 2.2C) showing the presence of multiple pumice and ash-rich horizons capped by obsidian. Symbols show location of analysed samples.



Figure A.4: A) Outcrop of CO5 at Site 58 (Figure 2.2C) showing the presence of several welded lenses within the obsidian flow. B) shows detail of folds within the flow front. C) Detail of welded material intermingled with obsidian flow. D) Outcrop of CO6 showing a welded lens similar to CO5.

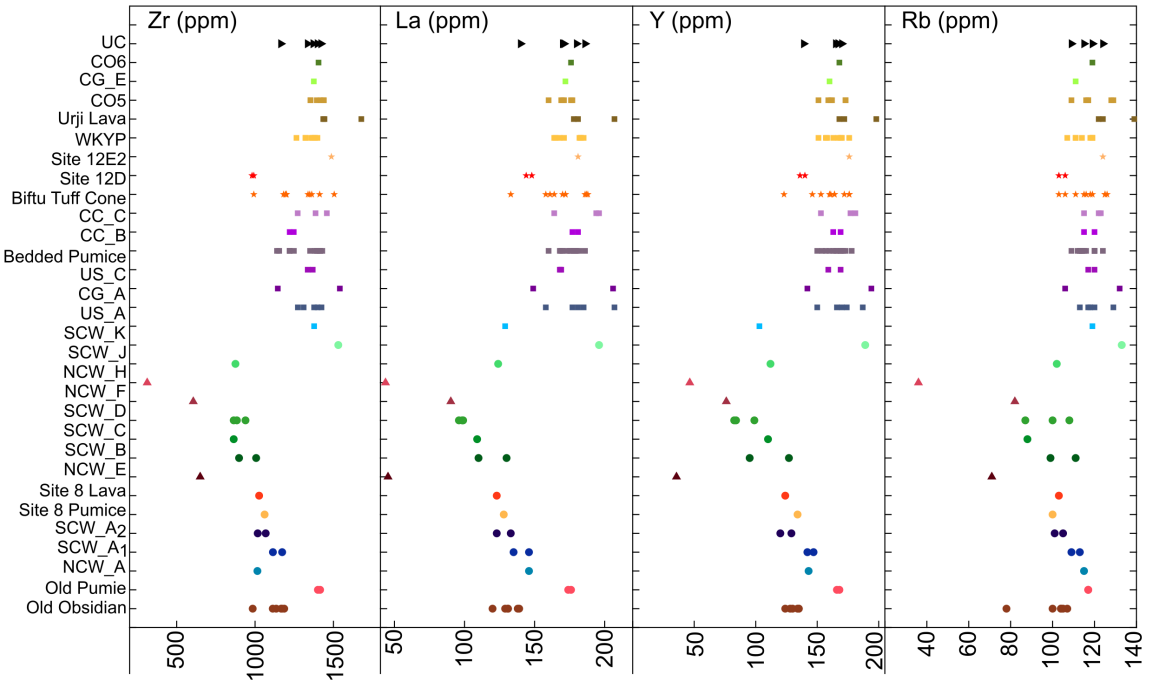

Figure A.5: Variation in selected trace elements with stratigraphic position. Stratigraphic position and uncertainty outlined in Figure 2.5. Different trends can be seen between the pre-and post-caldera deposits, however distinguishing between individual units based solely on the geochemistry is challenging.

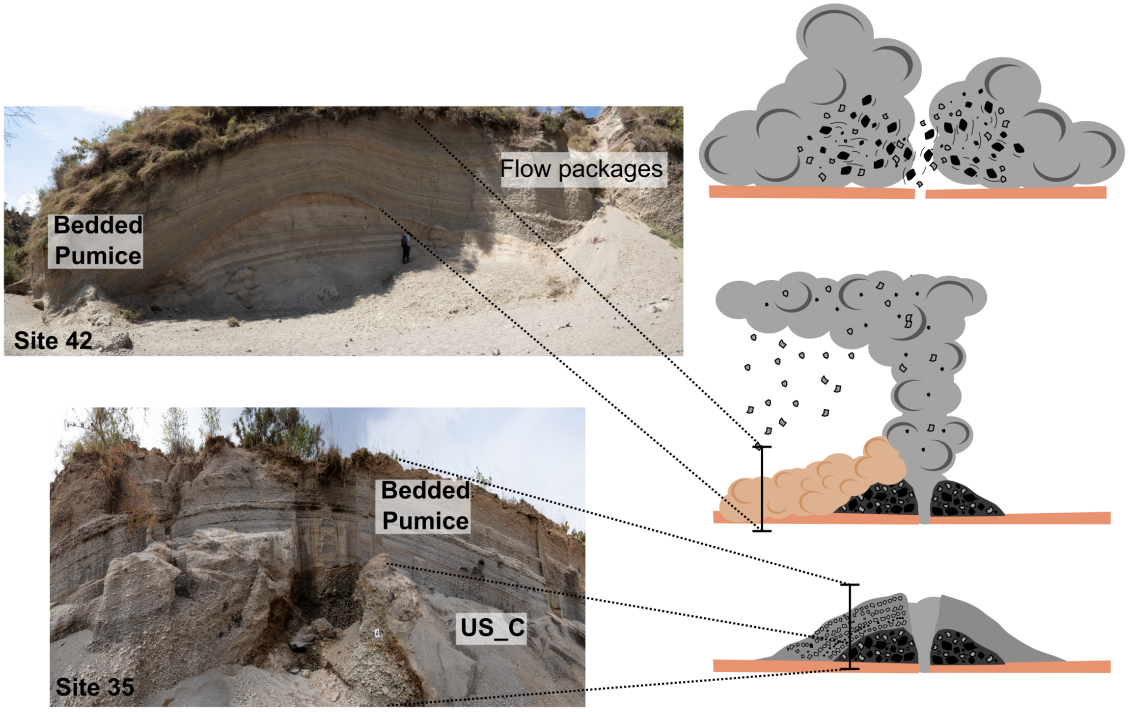

Figure A.6: Conceptual model of pumice cone formation after Clarke (2020) showing the features of the Bedded Pumice observed within the field.

Table A.1: Whole rock major element data. Details on sample locations found in electronic file or Colby et al. (2022). All values given in wt.%

Sample Name	Correlation	SiO_2	Al_2O_3	Fe2O3(T)	MnO	MgO	CaO	Na_2O	K_2O	TiO_2	P_2O_5	LOI	Total
Site 25B	uc	73.63	9	6.2	0.269	0.02	0.21	5.28	4.43	0.34	0.02	0.33	99.74
Site 49A1	uc	72.59	9.21	4.9	0.194	0.01	0.23	5.11	4.35	0.244	<0.01	2.91	99.75
Site 49A2	uc	73.01	9.27	4.86	0.195	0.03	0.25	5.13	4.43	0.247	<0.01	3.06	100.5
Site 52A1	uc	72.53	9.34	4.98	0.2	0.02	0.2	5.2	4.29	0.241	0.01	2.89	99.91
Site 53A2	uc	72.81	9.47	4.82	0.196	0.02	0.2	5	4.38	0.252	<0.01	3.35	100.5
Site 58A	CO6	75.08	9.55	5.01	0.199	<0.01	0.19	5.23	4.44	0.255	<0.01	0.35	100.3
Site 45A1	CG_E	72.65	9.24	4.94	0.195	<0.01	0.2	4.92	4.24	0.247	<0.01	3.19	99.82
Site 16A1	CO5	73.96	9.55	5.03	0.202	<0.01	0.21	5.51	4.42	0.246	<0.01	0.66	99.82
Site 16A1 Dup	CO5	74.10	9.49	5.05	0.203	0.01	0.21	5.46	4.39	0.246	<0.01	0.66	99.82
Site 19B	CO5	74.15	9.99	5.06	0.201	<0.01	0.2	5.23	4.44	0.266	<0.01	0.42	99.97
Site 54	CO5	74.27	9.47	4.96	0.198	<0.01	0.19	5.45	4.51	0.253	0.01	0.37	99.69
Site 55	CO5	74.56	9.59	5.03	0.2	<0.01	0.2	5.53	4.6	0.257	0.02	0.46	100.4
Site 56A1	CO5	75.26	9.55	5.07	0.201	<0.01	0.2	5.22	4.42	0.257	<0.01	0.3	100.5
Site 36A2	UrjiLava	73.35	9.43	5.07	0.201	<0.01	0.19	5.24	4.38	0.253	<0.01	0.36	98.49
Site 36A2 Dup	UrjiLava	73.45	9.49	5.04	0.2	<0.01	0.19	5.34	4.4	0.255	0.02	0.36	98.75
Site 37	UrjiLava	73.24	9.19	5.24	0.208	<0.01	0.19	5.59	4.36	0.212	<0.01	0.36	98.59
Site 15A2	WKYP	72.72	9.27	4.99	0.2	0.01	0.2	5.07	4.21	0.24	<0.01	2.86	99.78
Site 1A	WKYP	70.72	9.08	4.93	0.198	0.04	0.37	5.02	4.34	0.24	<0.01	3.51	98.46
Site 29B	WKYP	70.01	9.18	4.95	0.198	0.02	0.25	4.95	4.49	0.239	<0.01	4.12	98.41
Site 29B Dup	WKYP	70.15	9.1	4.95	0.197	0.02	0.25	4.91	4.46	0.237	<0.01	4.12	98.39
Site 2A1	WKYP	72.62	9.08	4.94	0.199	0.02	0.24	4.98	4.48	0.238	0.02	3.37	100.2
Site 34B	WKYP	70.49	8.95	4.91	0.193	0.09	0.82	4.77	4.22	0.244	0.02	4.49	99.2
Site 41C3	WKYP	71.29	9.08	4.81	0.188	0.02	0.24	5	4.25	0.249	<0.01	3.47	98.59
Site 46A	WKYP	72	9.44	4.84	0.192	<0.01	0.2	5.01	4.34	0.253	0.01	3.27	99.58
Site 12E2	Site12E	71.53	9.11	5	0.198	0.04	0.23	5.06	4.31	0.236	<0.01	4.16	99.87

Continued on next page

Table A.1 – continued from previous page

Sample Name	Correlation	SiO_2	Al_2O_3	Fe2O3(T)	MnO	MgO	CaO	Na_2O	K_2O	TiO_2	P_2O_5	LOI	Total
Site12D2	Site12D2	71.97	9.59	4.33	0.16	0.05	0.3	4.59	4.39	0.237	<0.01	2.86	98.49
Site12D2 Dup	Site12D2	72.1	9.59	4.34	0.16	0.06	0.3	4.61	4.4	0.237	<0.01	2.86	98.64
Site 10A	BiftuPDC	68.99	9.48	5.29	0.201	0.14	0.37	4.87	4.31	0.34	0.03	4.58	98.61
Site 12SL	BiftuPDC	72.12	9.22	5.12	0.203	0.05	0.31	5.1	4.32	0.225	<0.01	3.72	100.4
Site 33A2	BiftuPDC	69.11	9.14	5.11	0.192	0.14	0.42	4.91	4.35	0.295	0.02	4.56	98.25
Site 51A	BiftuPDC	70.89	9.48	4.95	0.193	0.1	0.31	4.72	4.27	0.257	<0.01	4.95	100.1
Site 9B	BiftuPDC	71.72	8.91	4.89	0.193	0.12	0.41	4.37	4	0.277	0.01	4.83	99.74
Site 9C	BiftuPDC	70.08	9.52	5.11	0.191	0.07	0.28	4.95	4.31	0.282	0.01	3.44	98.26
Site 9D	BiftuPDC	70.46	9.4	4.99	0.194	0.03	0.23	4.92	4.33	0.247	<0.01	3.51	98.3
Site 9E	BiftuPDC	70.05	9.46	5	0.193	0.04	0.28	4.94	4.31	0.247	<0.01	3.86	98.39
Site 9F	BiftuPDC	71.6	9.53	5.28	0.225	0.2	0.6	4.51	4.07	0.403	0.07	3.67	100.2
Site 9G	BiftuPDC	72.87	9.48	4.01	0.145	0.24	0.47	4.23	4.19	0.263	0.03	3.89	99.83
Site 17A2L1	CC_C_Lithic	74.8	10.64	3.92	0.154	0.02	0.3	4.28	4.71	0.268	0.01	0.35	99.46
Site 17A3L1	CC_C_Lithic	74.52	11.3	3.31	0.129	0.03	0.4	4.42	4.7	0.26	0.02	0.4	99.48
Site 17A3L2	CC_C_Lithic	74.37	9.4	5.39	0.214	0.01	0.21	5	4.57	0.222	<0.01	0.71	100.1
Site 17A3L3	CC_C_Lithic	74.42	9.58	5.45	0.21	0.02	0.23	4.32	4.48	0.219	0.01	1.4	100.3
Site 17A3L4	CC_C_Lithic	74.4	11.92	3.31	0.13	0.03	0.4	4.57	4.73	0.262	<0.01	0.56	100.3
Site 17A4L1	CC_C_Lithic	75.25	11.53	3.24	0.125	0.02	0.36	4.47	4.72	0.249	0.02	0.39	100.4
Site 17A4L2	CC_C_Lithic	73.36	10.41	3.73	0.133	0.04	0.27	3.93	4.91	0.255	0.01	3.42	100.5
Site 17A4L3	CC_C_Lithic	73.03	9.38	5.28	0.208	<0.01	0.16	4.84	4.34	0.221	0.02	0.96	98.45
Site 17A4L4	CC_C_Lithic	73.51	9.61	5.39	0.212	0.01	0.2	4.13	4.43	0.225	<0.01	1	98.71
Site 15H	CC_C	71.53	9.31	4.9	0.188	0.09	0.35	4.62	4.08	0.287	0.03	4.26	99.66
Site 39D	CC_C	70.94	9.27	4.94	0.199	0.04	0.35	5.06	4.33	0.235	<0.01	4.17	99.53
Site 39F4	CC_C	70.42	9.29	5.02	0.2	0.03	0.39	5.15	4.26	0.249	<0.01	4.08	99.1
Site 15I	CC_B	70.4	9.48	5.01	0.196	0.02	0.23	5.25	4.42	0.261	<0.01	3.45	98.72
Site 18D	CC_B	70.79	9.25	4.91	0.193	0.01	0.21	5.12	4.33	0.246	<0.01	3.72	98.76
Site 13A	BeddedPumice	72.62	9.13	4.93	0.2	<0.01	0.22	4.96	4.26	0.236	<0.01	3.03	99.59

Continued on next page

Table A.1 – continued from previous page

Sample Name	Correlation	SiO_2	Al_2O_3	Fe2O3(T)	MnO	MgO	CaO	Na_2O	K_2O	TiO_2	P_2O_5	LOI	Total
Site 13C	BeddedPumice	73.17	9.33	4.97	0.202	0.02	0.21	5.08	4.24	0.244	<0.01	3.02	100.5
Site 13I	BeddedPumice	70.79	9.4	5	0.196	0.02	0.23	5.16	4.37	0.255	<0.01	3	98.43
Site 13J	BeddedPumice	72.89	9.35	5.09	0.203	0.02	0.21	5.14	4.28	0.246	<0.01	2.52	99.94
Site 15J	BeddedPumice	72.02	9.54	5.08	0.2	0.02	0.24	4.94	4.18	0.258	0.02	3.38	99.88
Site 15L	BeddedPumice	69.95	9.5	5.17	0.193	0.08	0.37	5	4.36	0.331	0.04	3.25	98.26
Site 18C	BeddedPumice	70.76	9.24	4.93	0.196	<0.01	0.2	5.13	4.34	0.24	<0.01	3.42	98.46
Site 20B	BeddedPumice	70.54	9.38	4.85	0.196	0.01	0.2	5.18	4.37	0.246	<0.01	3.62	98.58
Site 29A1	BeddedPumice	70.49	9.22	4.9	0.199	0.01	0.21	5.09	4.34	0.235	<0.01	4.05	98.73
Site 35B3	BeddedPumice	70.41	9.67	5.04	0.189	0.18	0.52	3.58	4.21	0.393	0.07	5.03	99.28
Site 40B	BeddedPumice	69.76	9.53	5.23	0.192	0.22	0.41	4.45	3.96	0.392	0.04	4.83	99.02
Site 40C1	BeddedPumice	71.38	9.2	4.99	0.197	<0.01	0.2	4.93	4.32	0.246	<0.01	4.84	100.3
Site 35 ULP	US_C	72.21	9.16	4.98	0.198	0.02	0.23	4.4	4.46	0.236	0.02	4.02	99.93
Site 35AB2	US_C	71.69	9.15	4.97	0.195	<0.01	0.19	4.68	4.47	0.247	<0.01	3.69	99.3
Site 40A	CG_A	70.85	9.91	4.98	0.176	0.32	0.76	4.18	4.08	0.445	0.1	4.89	100.7
Site 42A	CG_A	71.95	9.08	5.23	0.201	0.02	0.2	5.22	4.27	0.226	<0.01	4.3	100.7
Site 38A	US_B	70.46	9.28	5.06	0.203	<0.01	0.2	4.63	4.49	0.236	<0.01	5.73	100.3
Site 38B	US_B	69.18	9.65	5.03	0.193	0.05	0.31	4.47	4.14	0.256	<0.01	5.2	98.47
Site 38C	US_B	70.48	9.24	4.99	0.198	0.01	0.21	4.5	4.32	0.249	0.01	5.87	100.1
Site 38D1	US_B	70.19	9.35	4.93	0.2	0.01	0.28	5.04	4.18	0.248	<0.01	5.52	99.94
Site 38E	US_B	70.81	9.47	4.63	0.18	0.03	0.21	4.42	4.22	0.252	<0.01	4.45	98.68
Site 66B	US_A	74.02	9.78	5.11	0.194	0.01	0.18	4.48	4.47	0.257	<0.01	0.59	99.11
Site 4A1	NCW_H	52.99	13.15	10.38	0.179	4.09	7.13	2.53	2.03	2.065	0.54	4.57	99.64
Site 3B	NCW_F	70.27	10.27	4.88	0.218	0.06	0.32	3.85	4.62	0.345	0.01	3.73	98.57
Site 2B	NCW_E	70.45	11.72	5.25	0.2	0.14	0.19	3.7	4.26	0.414	0.02	2.4	98.76
Site 8H	Site8	74.67	9.02	5.91	0.264	0.03	0.22	5.22	4.3	0.329	0.01	0.23	100.2
Site 8G	Site8	70.78	8.84	5.76	0.252	0.09	0.26	4.97	4.43	0.326	0.02	3.88	99.61
Site 6I2	SCW_K	69.64	9.01	5.14	0.203	0.04	0.25	5.15	4.33	0.229	0.03	4.35	98.38

Continued on next page

Table A.1 – continued from previous page

Sample Name	Correlation	SiO_2	Al_2O_3	Fe2O3(T)	MnO	MgO	CaO	Na_2O	K_2O	TiO_2	P_2O_5	LOI	Total
Site 6G	SCW_J	73.29	9.44	4.02	0.147	0.07	0.29	3.7	4.67	0.261	0.03	4.51	100.4
Site 6C4	SCW_D	75.49	9.11	5.52	0.205	0.07	0.25	4.19	4.41	0.324	0.02	0.57	100.2
Site 6C4_2	SCW_D	72.61	9.92	5.36	0.229	0.08	0.26	4.07	4.66	0.333	0.01	0.85	98.38
Site 6C5	SCW_D	67.97	10.64	6.39	0.23	0.38	0.54	3.76	4.31	0.58	0.04	5.23	100.1
Site 6B	SCW_C	70.63	9.73	5.41	0.232	0.11	0.35	4.39	5.26	0.368	0.04	3.03	99.55
Site 6A1	SCW_B	75.69	10.31	4.16	0.173	0.06	0.23	4.57	4.55	0.275	<0.01	0.21	100.2
Site 6A2	SCW_B	71.34	8.79	5.82	0.258	0.05	0.25	4.41	4.94	0.326	<0.01	3.3	99.48
Site 7A	SCW_A2	72.46	9.77	5.6	0.236	0.14	0.28	3.97	4.6	0.31	0.01	0.98	98.36
Site 7B	SCW_A2	72.3	9.48	5.47	0.236	0.03	0.2	5.17	4.52	0.306	<0.01	0.56	98.28
Site 27A	SCW_A1	74.14	9.11	6.22	0.27	0.1	0.28	3.93	4.53	0.335	<0.01	1.37	100.3
Site 8Z	SCW_A1	74.07	9.2	6.42	0.288	0.05	0.25	4.26	4.51	0.333	0.01	0.82	100.2
Site 25A	NCW_A	72.37	8.97	6.12	0.309	0.19	0.46	3.81	4.68	0.336	0.15	1.17	98.56
Site 62	OldPumice	72.84	9.31	4.97	0.195	<0.01	0.2	5.05	4.32	0.247	<0.01	3.12	100.3
Site 62 Dup	OldPumice	72.95	9.27	5.07	0.196	0.01	0.2	5.09	4.3	0.248	<0.01	3.12	100.4
Site 59	OlderObsidian	71.74	10.91	5.52	0.157	0.83	1.65	4.18	4.01	0.734	0.26	0.64	100.6
Site 60	OlderObsidian	74.95	10.44	4.01	0.148	<0.01	0.23	4.99	4.62	0.244	0.03	0.49	100.2
Site 62	OlderObsidian	75.33	10.07	3.94	0.144	<0.01	0.22	4.59	4.43	0.248	<0.01	0.64	99.64
Site 63	OlderObsidian	75.51	10.02	3.98	0.146	<0.01	0.22	4.6	4.44	0.251	<0.01	0.51	99.7
Site 64A	OlderObsidian	75.33	10.43	3.99	0.148	<0.01	0.22	4.73	4.56	0.254	0.03	0.63	100.3
Site 65	OlderObsidian	75.19	10.29	3.99	0.146	<0.01	0.23	4.82	4.45	0.243	<0.01	0.65	100

Table A.2: Whole rock trace element data for collected samples in Chapter 2 in ppm

Sample Name	Correlation	Sc	Be	V	Zn	Ga	Ge	Rb	Sr	Y	Zr	Nb	Mo	Ag	In	Sn	Cs	Ba	La
Site 25B	uc	3	8	<5	310	32	2.9	109	<2	139	1165	112	7		0.3	8	1.6	87	187
Site 49A1	uc	2	8	62	330	33	2.8	119	4	167	1371	139	10		0.3	7	1.4	55	181
Site 49A2	uc	2	8	26	340	34	2.6	119	5	170	1398	151	9		0.3	7	1.6	60	186

Continued on next page

Table A.2 – continued from previous page

Sample Name	Correlation	Sc	Be	V	Zn	Ga	Ge	Rb	Sr	Y	Zr	Nb	Mo	Ag	In	Sn	Cs	Ba	La
Site 52A1	uc	2	8	<5	370	34	3.4	124	3	167	1335	140	8		0.3	7	1.2	87	179
Site 53A2	uc	1	8	<5	350	33	2.7	115	4	165	1421	158	7		0.3	6	1.2	88	173
Site 58A	CO6	<1	9	<5	340	33	2.8	119	3	168	1405	143	7		0.3	7	1.3	90	176
Site 45A1	CG_E	2	8	39	300	32	2.5	111	4	160	1375	131	10		0.3	7	1.2	84	168
Site 16A1	CO5	2	9	<5	380	38	3.8	128	3	173	1354	131	9		0.3	7	1.2	88	183
Site 16A1 Dup	CO5	3	9	<5	390	38	3.7	129	3	173	1353	139	9		0.3	6	1.6	131	164
Site 19B	CO5	1	9	<5	340	33	3	117	3	162	1435	134	7		0.3	7	1.3	87	181
Site 54	CO5	<1	9	<5	340	31	2.8	116	3	159	1394	131	7		0.3	7	1.2	93	178
Site 55	CO5	1	9	<5	340	32	3	117	3	161	1439	144	7		0.3	7	1.1	121	170
Site 56A1	CO5	1	9	<5	310	30	2.8	109	3	151	1417	132	6		0.3	10	1.5	89	176
Site 36A2	UrjiLava	<1	9	<5	350	34	3.2	124	3	172	1435	143	8	6	0.3	11	1.5	89	177
Site 36A2 Dup	UrjiLava	<1	9	<5	360	33	3.3	122	3	168	1443	143	7	2.9	0.3	5	<0.1	260	119
Site 37	UrjiLava	<1	10	<5	420	35	3.3	139	3	198	1678	173	7	2.5	0.2	5	0.3	530	104
Site 15A2	WKYP	2	8	<5	310	33	2.7	118	3	167	1398	88.3	10		0.4	10	1.1	49	205
Site 1A	WKYP	2	8	<5	320	31	2.6	111	7	163	1358	68.4	7		0.4	11	0.9	47	214
Site 29B	WKYP	2	9	32	340	33	2.8	119	5	169	1322	95.3	10	2.4	0.3	4	0.4	604	98.3
Site 29B Dup	WKYP	2	9	24	350	33	2.7	119	5	170	1322	85.1	8	2.6	0.3	5	0.4	534	101
Site 2A1	WKYP	2	8	<5	330	34	2.8	119	4	176	1382	71.3	8	2.8	0.2	5	0.9	284	110
Site 34B	WKYP	1	8	<5	330	30	2.8	111	17	157	1381	128	7		0.3	10	1.5	48	182
Site 41C3	WKYP	2	8	42	300	31	2.5	107	5	151	1264	106	10		0.3	9	0.8	49	201
Site 46A	WKYP	<1	8	<5	350	32	3	114	3	158	1368	131	7		0.3	7	1.2	82	182
Site 12E2	Site12E	2	9	<5	340	33	2.6	124	5	176	1487	72.9	9		0.3	7	1.2	85	177
Site12D2	Site12D2	2	7	35	280	31	2.5	106	14	140	992	74.4	6		0.3	8	1.3	87	170
Site12D2 Dup	Site12D2	2	7	38	270	30	2.4	103	14	136	981	68.2	6		0.3	6	1.2	84	171
Site 10A	BiftuPDC	2	9	47	360	33	3	126	20	176	1338	96.2	8		0.3	7	1.2	89	175
Site 12SL	BiftuPDC	1	9	<5	360	33	4.3	125	7	172	1505	75.5	8		0.3	7	0.7	27	146
Site 33A2	BiftuPDC	2	9	52	310	32	3	125	19	176	1362	93.9	9		0.3	7	1.2	26	140

Continued on next page

Table A.2 – continued from previous page

Sample Name	Correlation	Sc	Be	V	Zn	Ga	Ge	Rb	Sr	Y	Zr	Nb	Mo	Ag	In	Sn	Cs	Ba	La
Site 51A	BiftuPDC	2	9	34	310	32	2.6	119	11	161	1412	154	8		0.3	8	0.7	31	146
Site 9B	BiftuPDC	2	8	<5	340	31	2.9	116	15	160	1349	81.8	7		0.3	8	1.3	59	186
Site 9C	BiftuPDC	2	9	<5	320	32	2.8	118	10	164	1199	94.9	7		0.3	8	1.3	63	182
Site 9D	BiftuPDC	2	9	32	320	32	2.7	115	5	164	1182	84.6	9	4.9	0.3	8	1.3	63	183
Site 9E	BiftuPDC	2	9	47	300	30	2.5	111	8	153	1200	79.5	7		0.3	7	1.2	85	185
Site 9F	BiftuPDC	3	7	13	260	31	2.5	106	35	146	1193	61.8	7	3	0.2	5	0.3	64	45.4
Site 9G	BiftuPDC	2	6	5	240	31	3.8	103	22	123	992	55.6	7		0.3	8	1.8	78	188
Site 17A2L1	CC_C_Lithic	2	4	<5	210	30	2.5	78	7	114	818	75.9	<2		0.3	8	1.2	61	164
Site 17A3L1	CC_C_Lithic	3	5	<5	210	30	2.4	79	21	86.4	690	73.2	<2		0.3	10	1.3	74	168
Site 17A3L2	CC_C_Lithic	<1	10	<5	410	36	3.1	133	3	195	1607	157	4		0.3	8	1.2	72	169
Site 17A3L3	CC_C_Lithic	2	10	<5	440	38	4.1	137	3	205	1615	159	3		0.3	7	1.2	140	160
Site 17A3L4	CC_C_Lithic	2	5	<5	170	30	2.2	76	23	85.9	686	71.4	<2		0.3	9	1.3	74	181
Site 17A4L1	CC_C_Lithic	2	5	<5	190	29	2.3	78	20	86.7	736	81.5	<2	5	0.3	9	1.3	75	178
Site 17A4L2	CC_C_Lithic	2	6	<5	220	29	2.4	83	8	100	815	80.7	6		0.4	11	1.6	48	207
Site 17A4L3	CC_C_Lithic	<1	10	<5	400	34	2.9	129	3	176	1624	154	6		0.3	9	1.3	55	207
Site 17A4L4	CC_C_Lithic	<1	11	<5	400	36	2.9	136	3	186	1560	151	4		0.3	8	1.4	91	181
Site 15H	CC_C	2	8	<5	310	32	2.6	115	13	153	1272	71.1	8		0.3	9	1.3	61	177
Site 39D	CC_C	2	9	33	350	33	2.9	122	6	177	1458	123	9		0.3	8	1.3	73	185
Site 39F4	CC_C	2	9	42	340	34	2.7	123	6	181	1386	105	10		0.3	8	1.8	127	158
Site 15I	CC_B	2	9	57	340	34	2.8	120	5	169	1221	79.4	11		0.3	9	1.3	54	194
Site 18D	CC_B	2	8	32	320	33	2.6	115	4	163	1247	91.9	8		0.3	8	1.3	64	196
Site 13A	BeddedPumice	2	8	<5	340	34	2.7	120	3	171	1380	76.9	10	2.1	0.2	4	0.6	30	90.2
Site 13C	BeddedPumice	1	9	<5	310	33	2.6	115	3	165	1397	65.8	7		0.3	7	2.1	199	149
Site 13I	BeddedPumice	2	8	<5	340	34	2.9	116	6	166	1220	84.5	9		0.3	9	1.4	107	169
Site 13J	BeddedPumice	2	9	<5	320	31	2.6	113	3	157	1415	83.9	9		0.3	9	1.4	61	180
Site 15J	BeddedPumice	3	9	5	310	33	2.7	113	5	169	1414	79	9		0.3	7	1.1	103	165
Site 15L	BeddedPumice	2	8	37	330	33	2.9	114	16	160	1154	86	9		0.3	10	1.4	51	206

Continued on next page

Table A.2 – continued from previous page

Sample Name	Correlation	Sc	Be	V	Zn	Ga	Ge	Rb	Sr	Y	Zr	Nb	Mo	Ag	In	Sn	Cs	Ba	La
Site 18C	BeddedPumice	2	8	39	340	34	2.9	120	3	169	1221	83.6	10		0.3	8	1.2	84	172
Site 20B	BeddedPumice	2	8	28	330	33	2.6	112	3	163	1248	98.1	9		0.3	8	1.2	103	168
Site 29A1	BeddedPumice	1	9	38	350	33	2.8	120	4	178	1391	108	9		0.3	9	1.2	84	180
Site 35B3	BeddedPumice	2	8	36	300	32	2.7	109	27	150	1140	98.5	8		0.3	9	1.2	85	186
Site 40B	BeddedPumice	3	8	54	310	31	2.6	114	26	154	1351	133	8	1.1	0.1	2	0.5	411	43.6
Site 40C1	BeddedPumice	1	9	<5	360	33	3.1	124	3	173	1429	146	7		0.3	9	1.6	62	170
Site 35 ULP	US_C	2	9	<5	350	34	3.4	120	3	169	1336	127	8		0.3	10	1.3	87	170
Site 35AB2	US_C	1	9	<5	340	32	2.7	117	3	159	1368	126	7		0.3	9	1.2	85	171
Site 40A	CG_A	4	8	36	280	31	3.2	106	47	142	1145	103	7		0.3	8	1.3	89	169
Site 42A	CG_A	1	9	50	380	35	2.8	132	4	194	1541	149	11		0.3	9	1.3	91	171
Site 38A	US_B	1	9	27	370	35	2.9	129	3	187	1399	111	9		0.3	8	1.2	88	160
Site 38B	US_B	2	9	26	310	33	2.8	117	9	166	1310	97.3	7		0.3	9	1.3	92	176
Site 38C	US_B	<1	9	<5	350	33	2.9	120	4	170	1424	141	7		0.2	6	0.7	236	120
Site 38D1	US_B	<1	9	25	360	33	2.7	118	4	174	1377	125	9		0.3	8	1.1	181	129
Site 38E	US_B	1	8	<5	310	32	2.7	113	6	150	1273	131	6		0.3	7	1.1	174	138
Site 66B	US_A	1	9	<5	380	40	3.3	119	3	103	1377	149	4		0.3	9	1.2	84	174
Site 4A1	NCW_H	22	2	196	130	21	1.6	36	354	46.4	312	40.8	2	5.7	0.3	9	1.2	84	176
Site 3B	NCW_F	3	5	<5	180	31	2	82	4	76.1	606	65.5	4		0.3	7	1.1	172	131
Site 2B	NCW_E	4	4	14	140	37	3.2	71	9	35.6	650	69.8	2		0.3	7	1.1	178	139
Site 8H	Site8	3	7	<5	320	34	3.8	103	<2	124	1026	94.9	7		0.3	8	1.2	182	131
Site 8G	Site8	3	7	5	280	30	2.6	100	4	134	1061	58	7		0.3	9	0.6	67	129
Site 6I2	SCW_K	1	10	<5	380	34	2.7	133	8	189	1531	138	7		0.2	5	0.9	71	110
Site 6G	SCW_J	2	6	8	240	32	3.1	102	5	112	875	79.9	7		0.3	5	1.1	36	130
Site 6C4	SCW_D	5	7	7	230	32	3.7	108	4	82.5	864	92	<2	3	0.3	5	1	72	109
Site 6C4_2	SCW_D	4	7	5	220	29	2.2	100	7	84	884	77.9	<2	3.8	0.2	7	1.3	41	96
Site 6C5	SCW_D	5	6	20	220	29	2.3	87	33	98.9	939	92.4	5	2.9	0.2	5	1.1	34	98.3
Site 6B	SCW_C	4	6	6	250	31	2.3	88	13	110	864	82.8	7	3.1	0.2	6	1.1	121	99

Continued on next page

Table A.2 – continued from previous page

Sample Name	Correlation	Sc	Be	V	Zn	Ga	Ge	Rb	Sr	Y	Zr	Nb	Mo	Ag	In	Sn	Cs	Ba	La
Site 6A1	SCW_B	3	7	<5	190	27	2.3	111	4	95.1	898	50.9	<2	3.8	0.2	7	1	54	124
Site 6A2	SCW_B	3	7	<5	280	30	2.6	99	4	127	1007	52.8	7		0.3	9	1.6	55	196
Site 7A	SCW_A2	3	8	<5	290	32	2.7	105	10	129	1017	97.5	2		0.3	6	0.8	41	133
Site 7B	SCW_A2	3	7	<5	270	30	2.6	101	<2	120	1068	91.6	7		0.3	6	1.1	32	123
Site 27A	SCW_A1	3	8	<5	320	33	3.1	109	10	147	1173	119	2		0.3	5	1.2	35	128
Site 8Z	SCW_A1	4	8	<5	330	35	4	113	8	142	1114	105	3		0.3	7	1.1	34	123
Site 25A	NCW_A	3	8	44	310	33	2.9	115	10	143	1015	78.6	4		0.4	8	0.5	39	135
Site 62	OldPumice	1	8	<5	350	34	2.8	117	3	166	1415	169	7		0.3	7	1.4	80	164
Site 62 Dup	OldPumice	1	9	<5	360	34	2.9	117	3	168	1401	171	7		0.3	7	1.4	78	172
Site 59	OlderObsidian	5	6	52	270	30	2.2	78	75	124	985	121	3		0.3	7	1.3	68	172
Site 60	OlderObsidian	2	7	<5	290	32	3.5	104	5	130	1135	98.8	8		0.3	7	1.3	64	161
Site 62	OlderObsidian	1	7	<5	280	31	2.8	105	5	135	1167	128	7		0.3	5	1.3	105	158
Site 63	OlderObsidian	1	7	<5	280	29	2.8	100	5	128	1170	121	7		0.2	5	1.8	188	133
Site 64A	OlderObsidian	1	7	<5	270	31	2.6	104	5	135	1186	127	7		0.3	6	1.3	133	148
Site 65	OlderObsidian	2	7	<5	290	33	3.6	107	5	134	1113	117	9	3.7	0.3	6	1.3	133	144

Table A.3: Continued whole rock trace element data from Chapter 2 in ppm

Sample Name	Correlation	Ce	Pr	Nd	Sm	Eu	Gd	Tb	Dy	Ho	Er	Tm	Yb	Lu	Hf	Ta
Site 25B	uc	384	46.5	182	37.1	5.55	31.9	5.55	33.5	6.68	19.3	2.85	18.4	2.73	28.1	11.2
Site 49A1	uc	373	45.5	178	36.6	5.39	31.7	5.49	32.8	6.49	18.6	2.78	17.6	2.67	23.7	9.88
Site 49A2	uc	378	45.7	177	36.7	5.34	32.2	5.53	33.5	6.49	18.7	2.74	17.3	2.64	24.7	10.4
Site 52A1	uc	375	44.9	176	35.4	5.26	30.7	5.21	31.9	6.22	17.9	2.68	16.9	2.58	23.2	9.6
Site 53A2	uc	360	43.8	171	34.8	5.13	29.8	5.2	31.1	6.2	17.4	2.61	16.6	2.48	20.9	9.03
Site 58A	CO6	360	44.3	173	34.9	5.09	30.5	5.24	31.8	6.2	17.7	2.69	16.6	2.54	24.2	9.79
Site 45A1	CG_E	345	41.5	163	33.2	4.89	28.5	4.93	30.1	5.79	16.9	2.52	15.9	2.35	23.1	9.42
Site 16A1	CO5	369	45.1	175	35.3	5.25	30.3	5.26	31.3	6.06	17.4	2.58	16.4	2.55	24.5	10.1

Continued on next page

Table A.3 – continued from previous page

Sample Name	Correlation	Ce	Pr	Nd	Sm	Eu	Gd	Tb	Dy	Ho	Er	Tm	Yb	Lu	Hf	Ta
Site 16A1 Dup	CO5	339	40.4	159	32.5	4.9	27.7	4.86	29.2	5.76	16.1	2.39	15.2	2.32	21.3	9.11
Site 19B	CO5	373	44.8	175	35.8	5.19	30.5	5.3	31.6	6.22	17.8	2.65	17	2.63	24	9.83
Site 54	CO5	363	44.3	171	34.8	5.17	30.7	5.29	31.5	6.24	17.5	2.66	16.8	2.56	23.6	9.69
Site 55	CO5	352	42.6	166	33.9	4.99	28.7	4.77	30	5.87	16.2	2.4	15.7	2.35	23.4	9.22
Site 56A1	CO5	365	43.9	172	36.7	5.53	31.4	5.5	33.3	6.48	18.4	2.66	17.4	2.75	32.1	11.9
Site 36A2	UrjiLava	369	44.5	174	36.8	5.62	31.5	5.55	33.9	6.52	18.7	2.73	17.1	2.71	33.4	12.2
Site 36A2 Dup	UrjiLava	231	29.1	114	22.8	3.13	19.4	3.29	19.9	3.98	11.6	1.69	11.6	1.77	17.8	6.82
Site 37	UrjiLava	220	25.3	97.3	20	2.97	16.6	2.76	16.6	3.21	9.35	1.31	9	1.39	16.3	6.7
Site 15A2	WKYP	423	51.1	199	41.2	5.8	35.7	6.05	36.3	7.07	20.4	2.95	19.4	2.97	35.9	13.7
Site 1A	WKYP	437	50.9	198	43.9	6.66	38.8	6.99	42.5	8.19	23.3	3.47	22.6	3.41	36.8	13.9
Site 29B	WKYP	207	24	94.3	18.5	2.82	16	2.67	15.6	3.1	8.82	1.24	8.48	1.3	15.3	6.6
Site 29B Dup	WKYP	216	24.7	97	19.4	2.8	16.3	2.63	16.2	3.15	8.84	1.31	8.57	1.35	16.8	6.78
Site 2A1	WKYP	228	27.1	105	21.1	2.86	18.1	3.02	18.3	3.66	10.8	1.51	10.2	1.58	17.5	6.83
Site 34B	WKYP	396	45.5	176	36.2	5.17	31.6	5.25	32.8	6.45	18.5	2.63	17.5	2.72	34.3	13.1
Site 41C3	WKYP	424	50	193	39.8	5.99	34.7	5.83	35.3	7	20.3	2.92	19.2	2.91	34	13.8
Site 46A	WKYP	375	44.9	175	35.2	5.21	30.3	5.18	32.2	6.26	18	2.62	17.1	2.53	24.5	10.2
Site 12E2	Site12E	363	43.3	170	34.1	4.99	30.5	5.19	30.6	6.04	17.4	2.64	16.7	2.49	25.3	9.92
Site12D2	Site12D2	353	42	166	33.7	5.02	29.1	4.81	30	5.77	17	2.41	15.9	2.41	29.4	11.3
Site12D2 Dup	Site12D2	351	43	169	34.3	5.03	27.8	4.99	29.5	5.86	16.7	2.5	15.8	2.42	21.1	8.97
Site 10A	BiftuPDC	356	43.1	169	34.6	5.08	29.9	5.12	30.7	6.12	17.4	2.55	16.6	2.5	25.4	10.1
Site 12SL	BiftuPDC	304	36	139	28.1	3.95	24.9	4.38	26.8	5.21	15	2.25	15.1	2.26	20.6	8.92
Site 33A2	BiftuPDC	288	34.1	132	27.2	3.81	23.4	4.11	24.8	4.89	14.3	2.08	13.9	2.11	24.7	9.81
Site 51A	BiftuPDC	294	35.7	138	28.4	3.97	25	4.28	26.4	5.25	15	2.17	14.4	2.23	26.3	10.2
Site 9B	BiftuPDC	385	46.3	181	37.3	5.36	31.4	5.41	32.4	6.53	18.4	2.71	17.7	2.69	28.5	10.9
Site 9C	BiftuPDC	374	45	177	36.1	5.34	31.2	5.31	32.3	6.37	18.1	2.71	17	2.59	26.7	10.2
Site 9D	BiftuPDC	376	45.7	179	36.3	5.39	31.7	5.31	32.7	6.43	18.1	2.7	17	2.59	25.8	10.2
Site 9E	BiftuPDC	380	46.2	182	36.8	5.43	30.7	5.33	32.1	6.28	17.8	2.59	17	2.57	22	9.55

Continued on next page

Table A.3 – continued from previous page

Sample Name	Correlation	Ce	Pr	Nd	Sm	Eu	Gd	Tb	Dy	Ho	Er	Tm	Yb	Lu	Hf	Ta
Site 9F	BiftuPDC	150	11.2	44.3	9.5	1.29	7.38	1.29	7.81	1.45	4.28	0.668	4.77	0.811	14.9	6.75
Site 9G	BiftuPDC	384	45.8	181	37	5.31	31.7	5.55	33.6	6.59	18.8	2.76	18	2.67	27.8	10.3
Site 17A2L1	CC_C_Lithic	339	40.7	160	33.3	4.74	28	4.81	28.9	5.61	16.1	2.33	15.6	2.41	28.9	11
Site 17A3L1	CC_C_Lithic	344	41.7	164	34.5	5.04	30.8	5.35	32.2	6.17	17.8	2.68	17	2.62	29.9	11.2
Site 17A3L2	CC_C_Lithic	346	41.4	163	33.5	4.82	28.7	4.86	29.6	5.79	16.6	2.39	15.9	2.4	29.4	11
Site 17A3L3	CC_C_Lithic	332	39.9	155	31.9	4.74	27.9	4.74	28.9	5.67	15.9	2.39	15	2.26	24.3	9.49
Site 17A3L4	CC_C_Lithic	375	45.1	177	36.4	5.3	31.1	5.2	31.5	6.18	17.8	2.56	16.6	2.62	31.9	12
Site 17A4L1	CC_C_Lithic	368	44.3	173	35.9	5.18	30.4	5.09	30.8	5.97	17.4	2.51	16.4	2.56	31.4	11.7
Site 17A4L2	CC_C_Lithic	432	51.4	200	41.2	6.02	36.3	6.08	36.8	7.34	20.7	2.96	20	3.06	38.8	14.1
Site 17A4L3	CC_C_Lithic	413	50.7	198	40.5	5.73	34.6	5.88	35.9	6.93	19.9	2.92	19.1	2.84	29.1	11.3
Site 17A4L4	CC_C_Lithic	369	44.6	179	35.8	5.28	31.1	5.37	31.5	6.17	17.9	2.7	16.9	2.66	27.1	10.3
Site 15H	CC_C	369	43.6	172	35.9	5.16	30.9	5.22	31.7	6.19	17.7	2.55	17.1	2.64	31.8	12
Site 39D	CC_C	381	45.1	178	36.5	5.25	32.1	5.39	32.5	6.49	18.4	2.68	17.4	2.62	29.9	11.1
Site 39F4	CC_C	331	39.6	155	32.1	4.66	27.5	4.54	28.5	5.51	16.3	2.3	15.3	2.33	28.5	10.7
Site 15I	CC_B	389	47.4	184	38.2	5.57	32	5.54	34	6.65	19.1	2.83	18.1	2.74	30.7	11.4
Site 18D	CC_B	387	47.9	186	38.1	5.47	32.2	5.62	32.9	6.57	19.3	2.76	18.1	2.74	28.6	10.8
Site 13A	BeddedPumice	180	21.9	83.7	16.6	2	14	2.32	13.9	2.66	7.78	1.1	7.21	1.1	12.4	5.79
Site 13C	BeddedPumice	304	37.1	146	29.4	4.55	25.5	4.38	26.4	5.24	15.1	2.25	14.8	2.21	23.8	8.75
Site 13I	BeddedPumice	358	41.8	164	33	4.89	28.6	4.91	29.9	5.86	16.8	2.45	16	2.39	30.3	10.5
Site 13J	BeddedPumice	375	45.2	179	36.8	5.31	31.4	5.22	31.6	6.36	18.4	2.6	17.1	2.62	32.5	11.9
Site 15J	BeddedPumice	332	40.2	159	32.1	4.72	27.5	4.73	28.7	5.65	15.9	2.41	15	2.33	25.3	9.26
Site 15L	BeddedPumice	422	51	199	40.2	5.95	35.1	6.06	36.3	7.31	20.9	3.12	19.7	2.97	35.1	12.6
Site 18C	BeddedPumice	352	42.5	166	33.5	4.98	29.5	4.92	30.2	6	16.8	2.54	16.3	2.48	28.6	10.2
Site 20B	BeddedPumice	351	41.4	164	33.5	5	28.8	4.72	29.2	5.74	16.7	2.37	15.7	2.39	29.3	11
Site 29A1	BeddedPumice	368	44.5	177	36	5.31	30.6	5.23	32.9	6.3	17.8	2.71	17.3	2.59	31.2	10.7
Site 35B3	BeddedPumice	374	45.7	179	36.8	5.37	31.3	5.29	31.7	6.37	17.9	2.68	17.4	2.66	31.5	11.2
Site 40B	BeddedPumice	92.9	11.6	48.7	10.3	2.67	9.23	1.49	8.74	1.66	4.57	0.639	4.08	0.642	7.3	2.83

Continued on next page

Table A.3 – continued from previous page

Sample Name	Correlation	Ce	Pr	Nd	Sm	Eu	Gd	Tb	Dy	Ho	Er	Tm	Yb	Lu	Hf	Ta
Site 40C1	BeddedPumice	348	42.2	165	34.4	4.87	29.4	5.08	30.6	6	17.4	2.62	16.5	2.52	30.9	10.7
Site 35 ULP	US_C	353	42.3	166	35.7	5.44	30.7	5.47	32.1	6.19	17.7	2.66	16.9	2.58	31.2	11.7
Site 35AB2	US_C	355	41.8	163	33.2	4.93	28.5	4.89	29.4	5.92	17	2.41	15.9	2.39	30.9	11
Site 40A	CG_A	352	42	167	33.9	5.02	29.4	4.91	30	5.84	17	2.44	16.2	2.52	30.1	11.4
Site 42A	CG_A	356	42.4	168	33.9	4.97	29.7	4.91	30.6	5.9	16.9	2.43	16.5	2.51	30.9	11.4
Site 38A	US_B	329	39.3	154	32.2	4.69	27.8	4.63	28.4	5.46	15.7	2.23	15.2	2.47	28.8	10.6
Site 38B	US_B	365	43.7	171	35.5	5.14	30.1	5.19	31.1	6.04	17.5	2.56	16.8	2.65	32	11.8
Site 38C	US_B	246	29.9	117	24.8	4.1	21	3.65	21.8	4.29	12.7	1.76	11.5	1.76	21.6	7.85
Site 38D1	US_B	266	31.5	125	26.2	4.32	24.6	4.23	25	4.81	13.9	2.05	13.1	2.01	24.9	9.13
Site 38E	US_B	289	34.5	136	28.3	4.34	24.6	4.13	24.9	4.97	14.3	2.09	13.7	2.13	26.5	9.9
Site 66B	US_A	361	42.7	167	33.9	4.98	29.2	4.96	30.2	5.94	17.1	2.41	15.7	2.39	32.1	11.1
Site 4A1	NCW_H	362	43.2	170	33.9	5.07	30	5.02	30.6	6.04	17.2	2.43	15.9	2.41	32.6	11.2
Site 3B	NCW_F	275	32.8	130	26.4	4.16	23.2	4.01	24.1	4.72	13.6	1.94	13.3	2.03	25.4	9.38
Site 2B	NCW_E	289	34.9	138	28.7	4.53	25.5	4.24	26	5.05	14.7	2.06	13.8	2.14	26.1	9.9
Site 8H	Site8	275	33	131	28.2	4.53	24.8	4.31	26.3	5.11	14.4	2.13	14	2.13	24.5	9.52
Site 8G	Site8	341	30.5	116	23.6	3.36	19.6	3.27	19.9	3.99	11.8	1.77	12.4	1.96	30.7	12.7
Site 6I2	SCW_K	222	26	97.9	19.7	2.48	16.2	2.82	17.1	3.5	10.3	1.55	10.2	1.5	13.9	6.45
Site 6G	SCW_J	268	31.9	124	25.4	3.55	21.5	3.8	23.3	4.69	13.1	2.01	12.7	1.91	13.9	7.17
Site 6C4	SCW_D	222	26.8	104	21.2	3.2	19	3.22	19.6	3.85	11.4	1.63	10.6	1.68	17.9	7.57
Site 6C4_2	SCW_D	209	23.5	88.1	17.8	2.84	14.9	2.71	16.4	3.24	9.42	1.42	9.66	1.47	20.3	7.85
Site 6C5	SCW_D	216	23.6	90	18.5	2.69	15.6	2.67	16.7	3.22	9.34	1.41	9.25	1.48	17.3	7.12
Site 6B	SCW_C	214	24.3	95.4	19.7	2.92	17.2	2.86	17.5	3.43	10	1.44	9.55	1.5	19.6	7.43
Site 6A1	SCW_B	247	28.6	109	22.3	2.55	19.1	3.49	20.6	4.16	12	1.79	11.9	1.87	20.8	7.87
Site 6A2	SCW_B	405	48.6	190	38.4	5.81	34.1	5.68	34.1	6.7	19.3	2.78	18.3	2.85	32.4	12.5
Site 7A	SCW_A2	266	31.8	122	25	3.38	21.5	3.68	22.8	4.6	13.3	1.93	12.8	1.98	21.7	8.98
Site 7B	SCW_A2	250	29.4	113	23.3	3.22	20.6	3.42	21.5	4.28	12.4	1.81	11.9	1.91	20.9	8.43
Site 27A	SCW_A1	267	31.5	123	25.2	3.67	22	3.78	23.4	4.72	13.9	2.02	12.8	2	17	7.21

Continued on next page

Table A.3 – continued from previous page

Sample Name	Correlation	Ce	Pr	Nd	Sm	Eu	Gd	Tb	Dy	Ho	Er	Tm	Yb	Lu	Hf	Ta
Site 8Z	SCW_A1	254	30.1	118	25.3	3.72	22	3.87	24.3	4.78	13.4	2.02	13.3	2.03	23.2	8.56
Site 25A	NCW_A	296	35	135	30.3	4.31	25.3	4.48	27	5.37	15.4	2.31	15.6	2.39	24.3	9.88
Site 62	OldPumice	349	40.9	156	32.1	4.72	27.4	4.79	29	5.73	16.1	2.46	15.9	2.36	23.2	9.42
Site 62 Dup	OldPumice	358	42.7	166	33.2	4.85	28.1	4.93	29.8	5.78	16.6	2.4	16.1	2.38	23.6	9.77
Site 59	OlderObsidian	355	42.3	167	33.2	4.7	28.4	4.92	29.8	5.68	16.6	2.46	15.6	2.36	22.8	9.68
Site 60	OlderObsidian	331	39.7	154	31.7	4.56	27.5	4.7	29	5.63	16.2	2.43	15.4	2.33	23	9.4
Site 62	OlderObsidian	318	39.3	150	30.6	4.41	26.6	4.62	27.2	5.46	15.5	2.33	14.7	2.24	19.4	8.08
Site 63	OlderObsidian	265	32.8	127	25.9	3.7	22.3	3.89	23.4	4.62	13.3	1.96	12.7	1.95	16.8	7.08
Site 64A	OlderObsidian	301	36.1	143	28.9	4.37	25.3	4.36	26.3	5.15	14.7	2.21	14.2	2.13	20.4	8.23
Site 65	OlderObsidian	288	34.6	138	27.7	4.2	24.6	4.27	25.6	4.95	14.5	2.11	14	2.06	19.7	7.74

Continued on next page

Table A.4: Continued whole rock trace element data from Chapter 2

Sample Name	Correlation	Ta	W	Tl	Pb	Bi	Th	U
Site 25B	uc	11.2	2.5	0.28	19	<0.1	19.3	5.31
Site 49A1	uc	9.88	1.8	<0.05	<5	<0.1	<0.05	<0.0‘
Site 49A2	uc	10.4	9.4	0.24	21	<0.1	19.8	5.25
Site 52A1	uc	9.6	2.4	0.25	20	<0.1	18.7	5.16
Site 53A2	uc	9.03	1.6	0.23	18	<0.1	18.2	4.8
Site 58A	CO6	9.79	1.7	0.26	19	<0.1	18.1	5.04
Site 45A1	CG_E	9.42	1.4	0.24	19	<0.1	17.4	4.69
Site 16A1	CO5	10.1	2	0.23	17	<0.1	18	4.94
Site 16A1 Dup	CO5	9.11	3.1	0.26	18	0.1	16.8	4.42
Site 19B	CO5	9.83	8.9	0.22	19	<0.1	18.6	5.06
Site 54	CO5	9.69	1.9	0.24	18	<0.1	18.5	4.93
Site 55	CO5	9.22	2.5	0.26	19	0.1	17.4	4.65

Continued on next page

Table A.4 – continued from previous page

Sample Name	Correlation	Ta	W	Tl	Pb	Bi	Th	U
Site 56A1	CO5	11.9	1.9	0.26	20	<0.1	18.6	5.36
Site 36A2	UrjiLava	12.2	1.3	0.28	22	0.1	18.9	5.39
Site 36A2 Dup	UrjiLava	6.82	1.8	0.11	12	<0.1	10.1	2.64
Site 37	UrjiLava	6.7	0.7	0.09	13	<0.1	10.1	1.71
Site 15A2	WKYP	13.7	1.3	0.22	24	<0.1	20.7	5.25
Site 1A	WKYP	13.9	4.8	0.21	24	<0.1	23	5.52
Site 29B	WKYP	6.6	<0.5	0.08	10	<0.1	9.36	1.84
Site 29B Dup	WKYP	6.78	<0.5	0.05	13	<0.1	9.59	1.92
Site 2A1	WKYP	6.83	0.5	0.19	13	<0.1	9.84	2.71
Site 34B	WKYP	13.1	1	0.2	24	<0.1	19.5	5.41
Site 41C3	WKYP	13.8	0.8	0.16	24	<0.1	20	5.79
Site 46A	WKYP	10.2	1.7	0.28	20	<0.1	19	5.05
Site 12E2	Site12E	9.92	1.7	0.24	18	<0.1	18.1	4.93
Site12D2	Site12D2	11.3	0.9	0.19	19	<0.1	17.1	4.73
Site12D2 Dup	Site12D2	8.97	1.6	0.22	18	<0.1	17.8	4.71
Site 10A	BiftuPDC	10.1	1.8	0.25	20	<0.1	18.2	4.89
Site 12SL	BiftuPDC	8.92	1.7	0.22	17	<0.1	16.7	4.75
Site 33A2	BiftuPDC	9.81	0.7	0.19	17	<0.1	15.2	4.34
Site 51A	BiftuPDC	10.2	<0.5	0.14	17	<0.1	15.9	2.69
Site 9B	BiftuPDC	10.9	4.3	0.23	20	<0.1	19.5	5.24
Site 9C	BiftuPDC	10.2	2.1	0.25	20	<0.1	18.7	5.07
Site 9D	BiftuPDC	10.2	1.9	0.24	19	<0.1	18.9	5.15
Site 9E	BiftuPDC	9.55	1.7	0.23	19	<0.1	19	5.09
Site 9F	BiftuPDC	6.75	1.2	<0.05	10	<0.1	12.6	1.56
Site 9G	BiftuPDC	10.3	2.1	0.28	18	<0.1	19.5	5.36
Site 17A2L1	CC_C_Lithic	11	0.8	0.19	19	<0.1	16.4	4.67
Site 17A3L1	CC_C_Lithic	11.2	16	0.25	19	<0.1	17.9	5.22

Continued on next page

Table A.4 – continued from previous page

Sample Name	Correlation	Ta	W	Tl	Pb	Bi	Th	U
Site 17A3L2	CC_C_Lithic	11	<0.5	0.2	20	0.1	16.8	4.69
Site 17A3L3	CC_C_Lithic	9.49	1.9	0.24	17	<0.1	16.4	4.47
Site 17A3L4	CC_C_Lithic	12	0.7	0.21	21	<0.1	17.9	5.07
Site 17A4L1	CC_C_Lithic	11.7	0.6	0.23	21	<0.1	17.5	5.03
Site 17A4L2	CC_C_Lithic	14.1	1.2	0.25	26	0.1	21.3	5.93
Site 17A4L3	CC_C_Lithic	11.3	1.9	0.31	22	<0.1	20.8	5.72
Site 17A4L4	CC_C_Lithic	10.3	1.6	0.28	19	<0.1	19.1	4.59
Site 15H	CC_C	12	1	0.22	21	0.1	17.4	4.85
Site 39D	CC_C	11.1	1.9	0.24	20	0.1	19.2	5.43
Site 39F4	CC_C	10.7	0.5	0.22	18	<0.1	15.8	4.26
Site 15I	CC_B	11.4	2.4	0.28	20	<0.1	19.7	5.43
Site 18D	CC_B	10.8	2	0.23	18	0.1	19.5	5.43
Site 13A	BeddedPumice	5.79	0.5	0.1	9	<0.1	10.2	2.76
Site 13C	BeddedPumice	8.75	1.8	0.24	17	<0.1	15	4.34
Site 13I	BeddedPumice	10.5	9.7	0.26	20	0.1	17.9	4.4
Site 13J	BeddedPumice	11.9	1.3	0.21	22	0.1	18.3	5.14
Site 15J	BeddedPumice	9.26	1.8	0.25	18	<0.1	16.8	4.62
Site 15L	BeddedPumice	12.6	2.6	0.26	23	0.1	21.6	5.84
Site 18C	BeddedPumice	10.2	1.9	0.4	18	0.3	17.5	4.72
Site 20B	BeddedPumice	11	3.1	0.22	22	0.1	16.7	4.71
Site 29A1	BeddedPumice	10.7	2.2	0.22	19	<0.1	18.7	5.14
Site 35B3	BeddedPumice	11.2	3.3	0.26	20	<0.1	19.2	5.2
Site 40B	BeddedPumice	2.83	<0.5	0.05	<5	<0.1	3.74	0.97
Site 40C1	BeddedPumice	10.7	1.8	0.26	19	<0.1	18.8	4.89
Site 35 ULP	US_C	11.7	18.5	0.23	21	0.1	18.3	5.13
Site 35AB2	US_C	11	1.8	0.26	20	0.1	17.3	4.72
Site 40A	CG_A	11.4	1.5	0.24	20	<0.1	16.8	4.73

Continued on next page

Table A.4 – continued from previous page

Sample Name	Correlation	Ta	W	Tl	Pb	Bi	Th	U
Site 42A	CG_A	11.4	0.8	0.21	21	0.1	17	4.76
Site 38A	US_B	10.6	<0.5	0.19	19	<0.1	15.9	4.5
Site 38B	US_B	11.8	1.2	0.21	20	<0.1	17.9	4.97
Site 38C	US_B	7.85	0.7	0.09	12	<0.1	11.7	2.97
Site 38D1	US_B	9.13	26.4	0.21	16	<0.1	13.9	4.02
Site 38E	US_B	9.9	0.9	0.18	18	<0.1	14.3	3.94
Site 66B	US_A	11.1	1.5	0.27	20	<0.1	17.7	4.95
Site 4A1	NCW_H	11.2	1.5	0.27	20	<0.1	17.8	5.03
Site 3B	NCW_F	9.38	<0.5	0.18	17	<0.1	13.4	3.85
Site 2B	NCW_E	9.9	0.7	0.17	16	<0.1	14.4	4.07
Site 8H	Site8	9.52	27	0.22	16	<0.1	14.7	4.31
Site 8G	Site8	12.7	3.1	0.19	23	0.1	17.5	3.51
Site 6I2	SCW_K	6.45	0.9	0.16	14	<0.1	13.6	3.16
Site 6G	SCW_J	7.17	1.4	0.15	15	<0.1	14.2	3.8
Site 6C4	SCW_D	7.57	0.5	0.17	13	<0.1	11.3	3.13
Site 6C4_2	SCW_D	7.85	<0.5	0.26	13	<0.1	13.3	3.38
Site 6C5	SCW_D	7.12	<0.5	0.16	13	<0.1	12.5	1.97
Site 6B	SCW_C	7.43	<0.5	0.14	12	<0.1	11.1	2.69
Site 6A1	SCW_B	7.87	1.6	0.2	15	<0.1	13.3	3.68
Site 6A2	SCW_B	12.5	1.1	0.24	22	0.1	19.3	5.35
Site 7A	SCW_A2	8.98	<0.5	0.16	14	<0.1	14.5	3.36
Site 7B	SCW_A2	8.43	2.3	0.19	14	<0.1	13.8	3.83
Site 27A	SCW_A1	7.21	1.7	0.25	14	0.1	14.4	4.32
Site 8Z	SCW_A1	8.56	1.4	0.17	17	<0.1	14	4.14
Site 25A	NCW_A	9.88	<0.5	0.17	17	<0.1	17.6	2.3
Site 62	OldPumice	9.42	2	0.27	19	0.1	17.5	4.49
Site 62 Dup	OldPumice	9.77	1.8	0.26	19	0.1	18	4.78

Continued on next page

Table A.4 – continued from previous page

Sample Name	Correlation	Ta	W	Tl	Pb	Bi	Th	U
Site 59	OlderObsidian	9.68	2.1	0.32	19	0.2	17.9	4.83
Site 60	OlderObsidian	9.4	1.6	0.26	18	0.1	16.7	4.5
Site 62	OlderObsidian	8.08	1.9	0.25	14	<0.1	16	4.11
Site 63	OlderObsidian	7.08	2.1	0.21	14	<0.1	13.4	3.6
Site 64A	OlderObsidian	8.23	1.9	0.21	16	<0.1	15.2	4.11
Site 65	OlderObsidian	7.74	1.5	0.2	16	<0.1	14.7	3.95

Continued on next page

Appendix B

Appendices for Chapter 3

This appendix contains information on the magma storage depths at Corbetti and the geochemcial data used for the thermometry and hygrometry presented in Chapter 3.

Table B.1: Estimated magma storage depths using a range of geophysical and petrological methods. Depths were calculated using a crustal dnsity of 2800 gm^{-3} (Wilks et al., 2017). Depsite the large uncertainty, data collected in this study agree well with independent estimates from geophysical observations.

Method	Pressure (MPa)	Depth (km)	Notes	Reference
CPX-only Barometry	50-190	1.8-6.9	Error of 320 MPa	This study
RhyoliteMELTS	100–250	3.6-9.1	Rhyolite MELTS not calibrated for peralkaline compositions	This study
Melt Inclusions	100-150	3.6-5.4		Iddon and Edmonds (2020)
Elastic Point Source Model	–	7		Gottsmann et al. (2020)
Mogi Source	–	~6-7		Lloyd et al. (2018a)
Magnetotelluric Survey	–	~5	Depth of the top of the convective hot zone	Gíslason et al. (2015)
Seismic Survey	–	~5 km	Low Vp/Vs ratio suggestive of geothermal fluids < 5 km depth	Lavayssière et al. (2019)

Glass compositions for the basaltic tuff (NCW_H) normalised to 100 wt.%. These glass compositions were used for the thermometry.

Glass#	SiO_2	Al_2O_3	CaO	MnO	FeOt	K_2O	TiO_2	Na_2O	MgO	P_2O_5
NCW_H_G1_1	48.55	14.01	10.46	0.23	13.13	0.80	3.48	2.97	5.74	0.57
NCW_H_G1_2	49.17	14.03	10.29	0.21	12.73	0.82	3.47	3.05	5.63	0.58
NCW_H_G2_1	52.24	14.04	8.56	0.26	11.83	1.39	3.12	3.30	4.34	0.84
NCW_H_G2_2	52.45	14.06	8.50	0.21	11.95	1.38	3.15	3.06	4.34	0.81
NCW_H_G3_1	51.41	14.17	8.99	0.18	11.99	1.23	3.20	3.18	4.81	0.74
NCW_H_G3_2	51.67	14.23	8.91	0.22	11.74	1.28	3.07	3.28	4.76	0.75
NCW_H_G4_1	48.51	14.03	10.68	0.21	12.96	0.74	3.57	2.94	5.81	0.50
NCW_H_G4_2	48.47	13.93	10.74	0.25	13.00	0.69	3.53	3.04	5.87	0.41
NCW_H_G5_1	48.73	13.89	10.46	0.24	13.04	0.78	3.49	3.11	5.70	0.51
NCW_H_G5_2	48.61	13.94	10.62	0.25	13.14	0.74	3.51	2.96	5.74	0.48
NCW_H_G6_1	53.99	14.23	7.70	0.25	11.12	1.66	2.87	3.34	3.90	0.89
NCW_H_G6_2	53.62	14.36	7.72	0.24	11.21	1.61	2.93	3.23	3.95	0.94
NCW_H_G7_1	48.38	14.15	10.69	0.22	12.99	0.70	3.53	3.06	5.82	0.47
NCW_H_G7_2	48.94	14.04	10.29	0.24	12.95	0.76	3.45	3.05	5.69	0.54
NCW_H_G8_1	50.44	14.67	9.96	0.16	11.67	0.91	3.08	3.16	5.51	0.42
NCW_H_G8_2	50.15	14.53	9.91	0.21	11.95	0.95	3.02	3.27	5.59	0.36
NCW_H_G9_1	52.42	14.09	8.43	0.22	11.59	1.41	3.20	3.52	4.31	0.81
NCW_H_G9_2	51.69	14.00	8.74	0.26	11.85	1.41	3.27	3.77	4.15	0.83
NCW_H_G10_1	48.07	14.19	10.79	0.17	13.09	0.68	3.54	3.06	5.92	0.44
NCW_H_G10_2	48.50	15.11	10.72	0.21	12.56	0.65	3.30	3.15	5.36	0.43
NCW_H_G11_1	48.40	14.04	10.69	0.20	12.99	0.68	3.48	3.05	5.94	0.52
NCW_H_G11_2	48.61	14.03	10.63	0.23	12.95	0.71	3.46	2.97	5.96	0.45
NCW_H_G12_1	52.57	14.08	8.59	0.25	12.02	1.30	3.22	2.88	4.24	0.82
NCW_H_G12_2	52.09	14.21	8.57	0.25	11.97	1.37	3.20	3.21	4.30	0.80
NCW_H_G13_1	48.46	14.10	10.68	0.21	12.86	0.75	3.44	3.12	5.85	0.50

Continued on next page

Table B.3 – continued from previous page

Glass#	SiO_2	Al_2O_3	CaO	MnO	FeOt	K_2O	TiO_2	Na_2O	MgO	P_2O_5
NCW_H_G13_2	48.17	13.99	10.74	0.25	13.06	0.72	3.44	3.15	5.95	0.48
NCW_H_G14_1	48.49	14.06	10.50	0.22	13.12	0.75	3.57	3.10	5.67	0.52
NCW_H_G14_2	49.52	14.07	10.15	0.20	12.68	0.95	3.32	3.21	5.25	0.60
NCW_H_G15_1	48.71	13.93	10.74	0.21	12.90	0.71	3.54	3.12	5.64	0.49
NCW_H_G15_2	48.45	13.89	10.82	0.18	13.39	0.72	3.64	2.99	5.51	0.41
NCW_H_G16_1	47.91	13.91	10.95	0.23	13.11	0.65	3.51	3.08	6.00	0.48
NCW_H_G16_2	48.16	13.98	10.92	0.22	13.10	0.64	3.45	2.93	6.06	0.51
NCW_H_G17_1	48.27	13.99	10.82	0.19	12.99	0.67	3.50	3.02	6.08	0.47
NCW_H_G17_2	48.60	13.63	10.72	0.24	12.92	0.78	3.55	2.88	6.13	0.51
NCW_H_G18_1	48.33	14.05	10.70	0.18	13.11	0.68	3.45	2.92	6.02	0.53
NCW_H_G18_2	48.26	14.05	10.80	0.25	12.99	0.67	3.54	3.01	5.94	0.50
NCW_H_G19_1	48.78	13.86	10.55	0.17	12.97	0.74	3.52	3.12	5.75	0.49
NCW_H_G19_2	48.07	13.90	10.85	0.23	13.27	0.69	3.55	2.97	5.91	0.51
NCW_H_G20_1	48.52	13.96	10.86	0.24	12.83	0.72	3.45	2.94	5.98	0.50
NCW_H_G20_2	48.35	13.95	10.80	0.20	13.03	0.67	3.49	2.96	5.99	0.49
NCW_H_G49_1	47.95	14.19	10.90	0.26	12.98	0.71	3.47	3.01	5.98	0.50
NCW_H_G49_2	47.96	14.10	10.82	0.25	13.24	0.64	3.59	2.89	6.05	0.46
NCW_H_G21_1	48.10	14.10	10.73	0.18	13.06	0.71	3.53	3.04	5.98	0.56
NCW_H_G21_2	48.35	13.88	10.84	0.24	13.16	0.65	3.46	2.92	5.98	0.52
NCW_H_G22_1	51.14	13.51	8.97	0.28	12.79	1.27	3.34	2.97	4.80	0.81
NCW_H_G22_2	51.15	13.56	8.91	0.22	12.90	1.30	3.31	3.10	4.72	0.82
NCW_H_G23_1	48.90	13.94	10.44	0.22	12.87	0.83	3.50	3.07	5.57	0.58
NCW_H_G23_2	48.75	13.83	10.45	0.22	13.21	0.86	3.57	3.06	5.43	0.61
NCW_H_G24_1	52.08	14.11	8.65	0.20	11.81	1.38	3.16	3.29	4.31	0.92
NCW_H_G24_2	51.44	14.13	8.04	0.27	12.30	1.31	2.86	2.98	5.79	0.86
NCW_H_G25_1	52.23	14.16	8.52	0.27	11.77	1.42	3.24	3.21	4.38	0.81
NCW_H_G25_2	52.23	14.32	8.53	0.21	11.80	1.41	3.12	3.10	4.33	0.87

Continued on next page

Table B.3 – continued from previous page

Glass#	SiO_2	Al_2O_3	CaO	MnO	FeOt	K_2O	TiO_2	Na_2O	MgO	P_2O_5
NCW_H_G26_1	51.05	14.47	9.38	0.19	11.54	1.10	3.00	3.42	5.24	0.59
NCW_H_G26_2	50.82	14.32	9.43	0.20	11.69	1.05	3.05	3.40	5.24	0.71
NCW_H_G27_1	53.76	14.22	7.59	0.26	10.96	1.72	2.88	3.39	3.96	1.16
NCW_H_G27_2	53.61	14.43	7.75	0.22	10.95	1.62	2.83	3.36	4.00	1.21
NCW_H_G28_1	51.26	13.57	8.80	0.26	12.56	1.29	3.39	3.17	4.69	0.85
NCW_H_G28_2	51.87	14.17	8.72	0.22	11.77	1.34	3.09	3.35	4.57	0.88
NCW_H_G29_1	53.37	14.22	7.94	0.25	11.24	1.52	2.92	3.20	4.23	1.02
NCW_H_G29_2	53.10	14.35	7.91	0.27	11.28	1.52	2.91	3.46	4.22	0.98
NCW_H_G30	47.98	10.97	6.51	0.05	21.97	1.35	5.97	0.37	3.80	1.03
NCW_H_G31_1	53.23	14.30	7.75	0.25	11.20	1.55	2.87	3.59	4.08	1.14
NCW_H_G31_2	53.13	14.29	7.65	0.25	11.26	1.59	2.85	3.63	4.11	1.19
NCW_H_G32_1	48.49	14.07	10.73	0.20	12.94	0.75	3.49	2.94	5.89	0.49
NCW_H_G32_2	48.15	14.15	10.89	0.20	12.96	0.67	3.52	2.90	6.05	0.49
NCW_H_G33_1	51.95	14.26	8.50	0.26	11.63	1.37	2.99	3.58	4.48	0.92
NCW_H_G33_2	51.95	14.22	8.54	0.25	11.55	1.43	3.01	3.55	4.49	0.90
NCW_H_G34_1	52.48	14.33	8.37	0.23	11.44	1.41	3.01	3.34	4.42	0.96
NCW_H_G34_2	52.39	14.40	8.40	0.23	11.49	1.38	2.96	3.25	4.55	0.90
NCW_H_G35_1	50.24	14.55	9.74	0.22	11.87	1.04	3.00	3.33	5.42	0.56
NCW_H_G35_2	50.07	14.61	9.84	0.20	11.94	0.96	3.09	3.24	5.46	0.47
NCW_H_G36	48.05	14.00	10.90	0.19	13.13	0.66	3.52	3.01	6.05	0.45
NCW_H_G37_1	52.77	14.74	8.78	0.22	10.73	1.35	2.71	3.53	4.69	0.49
NCW_H_G37_2	52.63	14.91	8.82	0.22	10.68	1.36	2.65	3.53	4.72	0.40
NCW_H_G38_1	51.75	14.90	9.19	0.19	11.00	1.29	2.76	3.37	5.11	0.44
NCW_H_G38_2	52.12	14.89	9.09	0.16	10.90	1.29	2.76	3.28	5.05	0.44
NCW_H_G39_1	52.56	14.23	8.11	0.23	11.41	1.56	2.84	3.49	4.30	1.28
NCW_H_G39_2	52.40	14.38	8.12	0.22	11.38	1.50	2.83	3.55	4.42	1.19
NCW_H_G39_3	52.45	14.23	8.06	0.25	11.17	1.57	2.90	3.70	4.37	1.27

Continued on next page

Table B.3 – continued from previous page

Glass#	SiO_2	Al_2O_3	CaO	MnO	FeOt	K_2O	TiO_2	Na_2O	MgO	P_2O_5
NCW_H_G39_4	52.26	14.20	8.18	0.24	11.44	1.47	2.91	3.62	4.42	1.22
NCW_H_G39_5	52.47	14.26	7.97	0.24	11.39	1.56	2.92	3.51	4.30	1.32
NCW_H_G40_1	52.44	14.08	8.14	0.25	11.46	1.56	2.86	3.61	4.38	1.23
NCW_H_G40_2	51.41	14.31	8.74	0.27	11.69	1.30	2.94	3.47	4.79	1.09
NCW_H_G40_3	51.40	14.22	8.77	0.22	11.77	1.34	2.91	3.63	4.68	1.06
NCW_H_G40_4	51.41	14.28	8.69	0.25	11.80	1.30	3.01	3.45	4.72	1.03
NCW_H_G40_5	51.14	14.22	8.71	0.25	11.89	1.37	3.02	3.57	4.73	1.09
NCW_H_G40_6	51.58	14.15	8.82	0.19	11.72	1.32	3.03	3.29	4.72	1.10
NCW_H_G41_1	47.74	14.97	10.68	0.20	12.40	0.64	3.01	2.97	6.79	0.60
NCW_H_G41_2	47.32	15.03	10.79	0.18	12.50	0.59	3.07	3.05	6.85	0.61
NCW_H_G42_1	47.41	14.90	10.76	0.19	12.41	0.62	3.14	3.06	6.84	0.64
NCW_H_G42_2	47.38	15.20	10.67	0.20	12.50	0.57	3.02	2.88	6.96	0.60
NCW_H_G42_3	47.51	14.96	10.71	0.22	12.28	0.60	3.10	2.97	7.02	0.63
NCW_H_G43_1	52.37	14.47	8.72	0.21	11.07	1.38	2.73	3.47	4.77	0.80
NCW_H_G43_2	52.34	14.63	8.65	0.20	10.97	1.38	2.73	3.53	4.78	0.78
NCW_H_G43_3	52.39	14.57	8.72	0.24	10.99	1.35	2.79	3.34	4.75	0.83
NCW_H_G44_1	52.78	14.25	8.03	0.25	11.37	1.51	2.82	3.25	4.35	1.29
NCW_H_G44_2	52.39	14.25	8.17	0.27	11.33	1.51	2.93	3.31	4.49	1.30
NCW_H_G44_3	52.46	14.11	8.24	0.24	11.62	1.57	2.90	3.22	4.42	1.23
NCW_H_G45_1	47.69	14.82	10.74	0.19	12.58	0.63	3.21	2.95	6.54	0.64
NCW_H_G45_2	47.61	14.83	10.80	0.21	12.68	0.64	3.29	2.86	6.51	0.58
NCW_H_G45_3	47.26	14.63	10.84	0.22	12.75	0.58	3.23	2.99	6.74	0.64
NCW_H_G46_1	49.79	25.08	12.84	0.06	4.82	0.27	1.30	3.51	2.05	0.28
NCW_H_G46_2	48.24	14.01	10.81	0.20	13.00	0.74	3.46	2.97	5.86	0.70
NCW_H_G46_3	47.78	13.88	10.80	0.21	13.31	0.65	3.55	2.98	6.13	0.67
NCW_H_G45_1	51.46	14.01	8.94	0.22	12.14	1.31	2.97	3.07	4.75	1.09
NCW_H_G45_2	51.06	14.01	9.05	0.22	12.22	1.24	3.13	2.98	4.92	1.11

Continued on next page

Table B.3 – continued from previous page

Glass#	SiO_2	Al_2O_3	CaO	MnO	FeOt	K_2O	TiO_2	Na_2O	MgO	P_2O_5
NCW_H_G46_1	51.75	14.95	9.16	0.17	10.99	1.23	2.73	3.45	5.11	0.45
NCW_H_G46_2	51.62	14.89	9.14	0.21	11.00	1.18	2.70	3.45	5.21	0.55
NCW_H_G47_1	47.52	14.97	10.62	0.20	12.50	0.55	2.99	3.00	6.99	0.66
NCW_H_G47_2	47.37	14.95	10.74	0.22	12.44	0.56	3.09	3.07	6.98	0.58
NCW_H_G47_3	47.36	14.96	10.70	0.18	12.45	0.63	3.03	2.91	7.06	0.64
NCW_H_G48_1	52.09	14.68	9.18	0.15	11.06	1.18	2.73	3.26	5.10	0.52

Table B.4: Analysis of olivine phenocrysts found within NCW_H normalised to 100 wt.%. Where these phenocrysts were hosted in a glass shard, the name of this is given and it's composition can be found in Table B.3

Olivine Name	Host Glass	Core/rim	SiO_2	Al_2O_3	CaO	MnO	FeO	K_2O	TiO_2	Na_2O	MgO	P_2O_5
Ol1	NCW_H_G1	Rim	39.09	0.03	0.31	0.26	19.90	0.00	0.05	0.00	40.75	0.08
Ol1	NCW_H_G1	Core	39.05	0.07	0.27	0.28	18.13	0.00	0.04	0.00	41.97	0.21
Ol2	NCW_H_G3	Rim	39.11	0.05	0.27	0.29	19.37	0.02	0.03	0.00	41.10	0.04
Ol2	NCW_H_G3	Core	39.33	0.04	0.28	0.25	18.72	0.01	0.04	0.00	41.66	0.03
Ol3	NCW_H_G7	Rim	38.91	0.03	0.32	0.29	19.81	0.01	0.04	0.01	40.63	0.08
Ol3	NCW_H_G7	Core	39.05	0.08	0.28	0.29	18.55	0.00	0.05	0.00	41.77	0.24
Ol4	NCW_H_G8	Rim	38.98	0.05	0.30	0.33	19.93	0.00	0.03	0.04	40.32	-0.02
Ol4	NCW_H_G8	Core	38.66	0.04	0.27	0.33	20.72	0.01	0.06	0.03	39.56	0.03
Ol5	NCW_H_G9	Rim	38.86	0.01	0.32	0.30	20.04	0.00	0.01	0.00	40.56	0.04
Ol5	NCW_H_G9	Core	38.91	0.05	0.29	0.32	19.92	0.00	0.06	0.00	40.22	0.10
Ol6	NCW_H_G10	Rim	38.92	0.07	0.28	0.29	20.45	0.01	0.03	0.00	40.03	0.01
Ol6	NCW_H_G10	Core	38.82	0.04	0.24	0.30	19.84	0.01	0.01	0.00	40.32	0.14
Ol7	NCW_H_G12	Rim	38.65	0.05	0.32	0.34	22.01	0.02	0.08	0.00	38.99	0.00
Ol7	NCW_H_G12	Core	39.36	0.05	0.26	0.27	18.25	0.01	0.03	0.04	41.80	0.00
Ol8	NCW_H_G13	Rim	38.89	0.05	0.30	0.27	19.51	0.00	0.03	0.01	41.18	-0.02
Ol8	NCW_H_G13	Core	38.88	0.02	0.29	0.28	19.52	0.01	0.02	0.00	40.83	0.07

Continued on next page

Table B.4 – continued from previous page

Olivine Name	Host Glass	Core/rim	SiO_2	Al_2O_3	CaO	MnO	FeO	K_2O	TiO_2	Na_2O	MgO	P_2O_5
Ol9	NCW_H_G14	Rim	39.04	0.05	0.29	0.26	19.05	0.01	0.02	0.01	41.07	0.06
Ol9	NCW_H_G14	Core	39.06	0.08	0.25	0.28	18.84	0.00	0.05	0.03	41.54	0.28
Ol10	NCW_H_G16	Rim	38.89	0.03	0.31	0.28	20.80	0.00	0.03	0.03	39.41	0.04
Ol10	NCW_H_G16	Core	38.63	0.05	0.24	0.31	21.09	0.01	0.03	-0.01	39.41	0.03
Ol11	NCW_H_G16	Rim	37.73	0.04	0.25	0.40	23.81	0.00	0.02	0.02	36.91	0.04
Ol11	NCW_H_G16	Core	38.46	0.06	0.26	0.34	20.61	0.00	0.03	0.02	39.92	0.11
Ol12	NCW_H_G18	Rim	38.80	0.04	0.31	0.28	19.20	0.00	0.04	0.03	40.90	-0.02
Ol12	NCW_H_G18	Core	38.53	0.06	0.29	0.30	19.64	0.00	0.05	0.04	40.27	0.18
Ol13	NCW_H_G19	Rim	38.53	0.03	0.32	0.31	20.76	0.00	0.05	0.02	39.91	0.08
Ol13	NCW_H_G19	Core	38.81	0.04	0.31	0.33	20.46	0.00	0.05	0.05	40.05	0.06
Ol14	NCW_H_G20	Rim	38.85	0.04	0.31	0.27	18.60	0.00	0.02	0.00	41.14	0.06
Ol14	NCW_H_G20	Core	39.03	0.06	0.27	0.26	18.22	0.00	0.04	0.00	41.73	0.06
Ol15	NCW_H_G49	Rim	38.84	0.02	0.31	0.32	20.04	0.02	0.03	0.01	40.12	0.01
Ol15	NCW_H_G49	Core	39.16	0.05	0.29	0.29	19.16	0.01	0.04	0.01	41.26	0.05
Ol16	NCW_H_G21	Rim	38.59	0.03	0.32	0.33	20.53	0.00	0.03	0.02	39.98	0.09
Ol16	NCW_H_G21	Core	38.78	0.04	0.28	0.28	19.16	0.00	0.02	0.01	41.30	0.08
Ol17	NCW_H_G25	Rim	37.91	0.04	0.28	0.43	24.34	0.00	0.04	0.03	36.92	0.10
Ol17	NCW_H_G25	Core	38.41	0.03	0.31	0.32	20.62	0.00	0.01	0.00	39.70	0.06
Ol18	NCW_H_G32	Rim	38.49	0.03	0.33	0.32	21.65	0.01	0.03	0.02	39.04	0.03
Ol18	NCW_H_G32	Core	38.53	0.04	0.28	0.33	20.30	0.00	0.03	0.00	40.23	0.18

Table B.5: Compositions of plagioclase phenocrysts found within the basaltic tuff (NCW_H). The glass composition within whihc these phenocrysts were hosted is also given. These glass compositions were used for the plagioclase-liquid thermometry and hygrometry and can be found in Table B.3

Plag#	Rim/Core	Host Glass #	SiO_2	Al_2O_3	CaO	MnO	FeO	K_2O	TiO_2	Na_2O	MgO	P_2O_5
Plag_1	Rim	NCW_H_G2	51.53	30.25	13.22	0.02	0.61	0.12	0.10	3.97	0.16	0.01

Continued on next page

Table B.5 – continued from previous page

Plag#	Rim/Core	Host Glass #	SiO_2	Al_2O_3	CaO	MnO	FeO	K_2O	TiO_2	Na_2O	MgO	P_2O_5
Plag_1	Core	NCW_H_G2	51.82	30.01	13.04	-0.01	0.64	0.16	0.07	4.06	0.18	0.03
Plag_2	Rim	NCW_H_G4	50.47	30.96	14.11	0.01	0.71	0.11	0.09	3.37	0.15	0.02
Plag_2	Core	NCW_H_G4	51.61	30.19	13.22	-0.01	0.70	0.11	0.12	3.87	0.19	0.00
Plag_3	Rim	NCW_H_G5	51.81	29.76	13.21	0.01	0.79	0.17	0.13	3.93	0.20	0.00
Plag_3	Core	NCW_H_G5	51.00	30.70	13.78	0.02	0.59	0.13	0.08	3.53	0.19	0.00
Plag_4	Rim	NCW_H_G10	51.38	30.11	13.56	0.02	0.84	0.16	0.12	3.62	0.18	0.02
Plag_4	Core	NCW_H_G10	51.12	30.55	13.82	-0.01	0.65	0.10	0.09	3.51	0.16	0.01
Plag_5	Rim	NCW_H_G11	50.89	28.95	13.08	0.02	2.04	0.18	0.47	3.59	0.72	0.05
Plag_5	Core	NCW_H_G11	52.26	29.38	13.01	0.01	0.83	0.21	0.10	3.97	0.18	0.04
Plag_6	Rim	NCW_H_G12	51.16	30.33	13.69	-0.02	0.72	0.11	0.10	3.70	0.19	0.03
Plag_6	Core	NCW_H_G12	51.82	29.97	13.27	0.01	0.67	0.15	0.11	3.81	0.19	0.01
Plag_7	Rim	NCW_H_G12	52.18	29.42	12.90	0.00	0.86	0.17	0.15	4.09	0.19	0.04
Plag_7	Core	NCW_H_G12	51.08	30.40	13.74	0.01	0.72	0.12	0.15	3.57	0.19	0.03
Plag_8	Rim	NCW_H_G15	50.89	30.53	13.87	0.03	0.83	0.12	0.10	3.43	0.18	0.02
Plag_8	Core	NCW_H_G15	51.78	29.79	13.17	-0.01	0.74	0.17	0.11	3.98	0.19	0.08
Plag_9	Rim	NCW_H_G15	51.33	30.25	13.50	0.00	0.85	0.14	0.11	3.55	0.19	0.08
Plag_9	Core	NCW_H_G15	51.82	29.94	13.22	-0.01	0.74	0.12	0.11	3.89	0.19	0.00
Plag_10	Rim	NCW_H_G16	52.55	29.37	12.52	0.03	0.75	0.21	0.13	4.31	0.15	0.00
Plag_10	Core	NCW_H_G16	51.87	29.84	13.32	0.01	0.70	0.17	0.06	3.85	0.18	0.01
Plag_11	Rim	NCW_H_G17	51.26	30.28	13.62	0.02	0.78	0.13	0.12	3.60	0.16	0.01
Plag_11	Core	NCW_H_G17	50.93	30.34	13.94	0.00	0.78	0.12	0.11	3.56	0.17	0.03
Plag_12	Rim	NCW_H_G22	51.40	30.16	13.49	0.01	0.80	0.13	0.12	3.73	0.16	0.00
Plag_12	Core	NCW_H_G22	50.78	30.74	14.03	-0.02	0.73	0.12	0.09	3.32	0.20	0.01
Plag_13	Rim	NCW_H_G23	51.72	29.85	13.26	0.01	0.85	0.13	0.12	3.85	0.20	0.01
Plag_13	Core	NCW_H_G23	51.40	30.12	13.38	-0.02	0.83	0.12	0.12	3.81	0.21	0.02
Plag_14	Rim	NCW_H_G24	52.79	29.14	12.35	-0.01	0.80	0.24	0.11	4.41	0.14	0.03
Plag_14	Core	NCW_H_G24	51.76	30.04	13.12	0.04	0.71	0.16	0.10	3.89	0.15	0.02

Continued on next page

Table B.5 – continued from previous page

Plag#	Rim/Core	Host Glass #	SiO_2	Al_2O_3	CaO	MnO	FeO	K_2O	TiO_2	Na_2O	MgO	P_2O_5
Plag_15	Rim	NCW_H_G25	51.92	30.00	13.17	-0.02	0.71	0.15	0.09	3.78	0.14	0.04
Plag_15	Core	NCW_H_G25	51.45	30.19	13.57	-0.01	0.61	0.15	0.14	3.71	0.15	0.03

Table B.6: Composition of the rare clinopyroxenes found within the basaltic tuff (NCW_H) normalised to 100 wt.%

CPX#	SiO_2	Al_2O_3	CaO	MnO	FeOt	K_2O	TiO_2	Na_2O	MgO	P_2O_5
NCW_H_CPX_1_Rim	48.40	0.16	17.02	2.21	30.06	0.00	0.34	1.27	0.48	0.01
NCW_H_CPX_1_Core	48.48	0.13	17.05	2.16	30.09	-0.02	0.31	1.35	0.44	0.00
NCW_H_CPX_2	48.29	0.15	17.89	2.14	29.35	0.00	0.33	1.19	0.54	0.03

Table B.7: Compositions of the rare alkali-feldspar phenocrysts found within the basaltic tuff (NCW_H). These are likely scavenged from an older melt. Data are normalised to 100 wt.%

Kspar#	Rim/Core	SiO_2	Al_2O_3	CaO	MnO	FeO	K_2O	TiO_2	Na_2O	MgO	P_2O_5
NCW_H_Kspar_1	Rim	66.76	18.51	0.02	0.02	0.66	7.07	0.02	6.91	0.02	0.01
NCW_H_Kspar_1	Core	66.94	18.47	0.03	0.02	0.70	7.14	0.02	6.66	0.01	0.01
NCW_H_Kspar_2	Core	66.97	18.59	0.03	-0.01	0.51	7.23	0.02	6.66	0.00	-0.01
NCW_H_Kspar_2	Rim	66.79	18.79	0.02	0.01	0.53	7.27	0.02	6.56	0.00	0.02
NCW_H_Kspar_3	Rim	51.81	29.98	13.06	-0.01	0.71	0.16	0.11	4.02	0.15	0.00
NCW_H_Kspar_3	Core	51.85	30.05	13.31	-0.01	0.59	0.15	0.10	3.76	0.18	0.02
NCW_H_Kspar_4	Rim	66.81	18.92	0.12	0.03	0.46	6.40	0.02	7.21	0.00	0.03
NCW_H_Kspar_4	Core	67.23	18.92	0.08	0.01	0.37	6.32	0.03	7.10	-0.01	-0.03
NCW_H_Kspar_5	Rim	66.87	18.14	0.01	0.00	0.93	7.36	-0.01	6.69	0.02	-0.01
NCW_H_Kspar_5	Core	67.03	18.13	0.02	0.01	0.91	7.38	0.02	6.49	0.00	0.00

Table B.8: Composition of Obsidian lithics found within NCW_H normalised to 100 wt.%

Glass Name	SiO_2	Al_2O_3	CaO	MnO	FeO	K_2O	TiO_2	Na_2O	MgO	P_2O_5
NCW_H_RG_1	76.42	11.30	0.23	0.11	2.63	4.64	0.18	4.34	0.01	0.00
NCW_H_RG_2_1	76.51	11.27	0.22	0.13	2.59	4.74	0.15	4.31	0.00	0.01
NCW_H_RG_2_2	76.26	11.19	0.21	0.11	2.58	4.83	0.15	4.52	0.01	0.00
NCW_H_RG_2_3	76.42	11.15	0.22	0.11	2.56	4.78	0.19	4.48	0.01	0.00
NCW_H_RG_3_1	75.92	11.12	0.24	0.09	2.76	5.15	0.18	4.37	0.00	0.00
NCW_H_RG_3_2	76.75	11.06	0.15	0.06	2.41	5.22	0.19	4.03	0.00	0.00
NCW_H_RG_4_1	76.08	11.72	0.31	0.09	2.46	4.61	0.25	4.32	0.04	0.00
NCW_H_RG_4_2	74.96	11.67	0.31	0.09	3.70	4.36	0.44	4.35	0.01	0.04
NCW_H_RG_5_1	76.00	10.78	0.20	0.13	3.62	4.68	0.26	4.15	0.02	0.00
NCW_H_RG_5_2	76.01	10.82	0.20	0.15	3.61	4.59	0.27	4.22	0.00	0.00
NCW_H_RG_6_1	76.22	11.14	0.22	0.08	2.80	4.62	0.18	4.51	0.00	0.05
NCW_H_RG_6_2	75.97	11.29	0.23	0.11	2.73	4.68	0.17	4.54	0.00	0.00
NCW_H_RG_7_1	76.24	11.24	0.21	0.12	2.74	4.64	0.19	4.40	0.00	0.00
NCW_H_RG_7_2	76.28	11.26	0.22	0.11	2.70	4.65	0.17	4.43	0.00	0.00

Table B.9: Glass analysis for NCW_F normalised to an anhydrous composition of 100 wt.%. All data in wt.%. For the KSpar-Liquid thermometry and hygrometry, each glass compositions was matched with every KSpar composition. Only those which passed the equilibirum test of Mollo et al. 2015 (when $^{Ksp-melt}Kd_{Or-Ab}$ 'measured' versus' 'Predicted' plot on a 1:1 line ± 0.05) are presented in Chapter 3

Glass#	SiO_2	Al_2O_3	CaO	MnO	FeOt	K_2O	TiO_2	Na_2O	MgO	P_2O_5
NCW_F_G1	75.06	9.61	0.26	0.27	5.13	4.86	0.32	4.35	0.00	0.05
NCW_F_G2	74.68	9.50	0.21	0.25	5.41	4.70	0.35	4.72	0.02	0.00
NCW_F_G3	75.14	9.56	0.09	0.20	5.59	5.24	0.35	3.60	0.00	0.05
NCW_F_G4	74.93	9.64	0.31	0.28	5.28	4.53	0.34	4.55	0.02	0.02

Continued on next page

Table B.9 – continued from previous page

Glass#	SiO_2	Al_2O_3	CaO	MnO	FeOt	K_2O	TiO_2	Na_2O	MgO	P_2O_5
NCW_F_G5	74.92	9.56	0.10	0.26	5.27	4.82	0.31	4.56	0.02	0.00
NCW_F_G6	74.84	9.76	0.19	0.27	4.99	5.05	0.31	4.50	0.00	0.00
NCW_F_G7	74.79	9.21	0.10	0.30	6.01	5.26	0.34	3.75	0.02	0.00
NCW_F_G8	73.82	11.65	0.14	0.19	4.27	2.94	0.21	6.69	0.02	0.00
NCW_F_G9	75.45	9.45	0.18	0.26	5.60	4.64	0.36	3.83	0.00	0.02
NCW_F_G10	75.86	9.69	0.29	0.24	5.30	4.23	0.35	3.92	0.02	0.00
NCW_F_G11	74.96	9.72	0.14	0.24	5.15	5.02	0.31	4.26	0.00	0.01
NCW_F_G12	74.48	9.54	0.17	0.25	5.48	5.01	0.34	4.58	0.01	0.04
NCW_F_G13	74.69	9.96	0.09	0.24	4.92	5.17	0.34	4.45	0.01	0.00
NCW_F_G14	74.80	9.65	0.29	0.27	5.22	4.81	0.32	4.46	0.00	0.03
NCW_F_G15	74.84	9.48	0.08	0.27	5.52	5.19	0.34	4.09	0.00	0.02
NCW_F_G16	74.49	9.66	0.27	0.26	5.37	5.22	0.36	4.16	0.03	0.01
NCW_F_G17	74.80	9.70	0.29	0.25	5.25	4.97	0.35	4.07	0.00	0.02
NCW_F_G18	74.74	10.01	0.13	0.25	4.89	5.40	0.35	4.05	0.00	0.00
NCW_F_G19	76.37	9.66	0.11	0.29	5.56	4.81	0.34	2.62	0.03	0.03
NCW_F_G20	75.39	9.61	0.13	0.25	5.44	5.29	0.33	3.42	0.00	0.01
NCW_F_G21	74.88	9.68	0.27	0.26	5.39	4.59	0.34	4.46	0.01	0.01
NCW_F_G22	74.98	9.90	0.17	0.21	4.89	5.15	0.32	4.25	0.01	0.01
NCW_F_G23	75.65	9.87	0.32	0.28	5.22	4.67	0.34	3.41	0.02	0.00
NCW_F_G24	74.88	9.65	0.17	0.24	5.49	5.78	0.32	3.35	0.00	0.02
NCW_F_G25	74.56	9.59	0.24	0.25	5.23	5.25	0.28	4.49	0.00	0.01
NCW_F_G26	74.74	9.94	0.16	0.21	4.95	5.00	0.33	4.54	0.02	0.00
NCW_F_G27	74.96	10.02	0.10	0.22	4.94	5.28	0.33	4.04	0.03	0.00
NCW_F_G28	76.14	9.59	0.18	0.28	5.40	4.03	0.36	3.79	0.03	0.00
NCW_F_G29	74.75	9.69	0.30	0.26	5.61	4.82	0.38	4.02	0.00	0.01

Table B.10: Compositions of alkali-feldspars found within NCW_F. Data are in wt.% and normalised to 100 wt.%. Were transects have been conducted the rim and the core position have been noted.

Kspar#	Rim/Core	SiO_2	Al_2O_3	CaO	MnO	FeOt	K_2O	TiO_2	Na_2O	MgO	P_2O_5
Kspar1_1	*Rim*	66.92	18.49	0.03	0.00	0.65	6.60	0.00	7.31	0.00	0.01
Kspar1_2		67.17	18.26	0.01	0.02	0.63	6.78	0.00	7.07	0.00	0.00
Kspar1_3		66.78	18.53	0.02	0.00	0.61	7.00	0.00	7.05	0.02	-0.02
Kspar1_4		67.14	18.41	0.01	0.01	0.62	6.81	0.01	6.99	0.01	-0.01
Kspar1_5		67.05	18.51	0.01	-0.01	0.61	6.83	0.00	6.93	-0.02	-0.01
Kspar1_6		67.10	18.40	0.01	0.04	0.83	6.76	0.00	6.84	-0.01	0.00
Kspar1_7		66.93	18.32	0.02	0.02	0.91	6.82	-0.01	6.89	0.00	-0.03
Kspar1_8	*Core*	67.24	18.38	0.01	0.00	0.65	6.75	0.01	6.92	0.01	-0.01
Kspar2_1	*Rim*	66.96	18.32	0.01	-0.02	0.56	6.61	0.02	7.51	0.01	0.00
Kspar2_2		66.98	18.67	0.01	-0.01	0.56	6.51	0.02	7.22	-0.01	0.02
Kspar2_3		67.16	18.45	0.01	-0.01	0.55	6.52	0.04	7.23	0.00	0.05
Kspar2_4		67.13	18.47	0.01	0.00	0.56	6.56	0.02	7.25	-0.01	-0.02
Kspar2_5	*Core*	67.29	18.55	0.02	0.00	0.50	6.55	0.02	7.06	-0.01	0.01
Kspar3_1	*Rim*	66.91	18.25	0.02	0.00	0.95	6.98	0.00	6.87	-0.01	-0.03
Kspar3_2	*Core*	66.96	18.17	0.02	-0.01	0.94	6.89	0.01	6.88	0.01	0.05
Kspar4_1	*Rim*	67.23	18.31	0.07	-0.02	0.68	7.12	0.02	6.49	0.01	-0.02
Kspar4_2	*Core*	67.15	18.34	0.02	-0.02	0.85	7.03	-0.01	6.59	0.00	0.02
Kspar5_1	*Rim*	67.06	18.16	0.00	0.00	0.92	7.34	0.02	6.48	0.02	0.01
Kspar5_2	*Core*	67.02	18.26	0.03	-0.01	0.89	7.21	0.00	6.55	0.00	0.02
Kspar6_1	*Rim*	66.83	18.34	0.01	-0.01	0.81	6.86	0.02	7.04	0.00	0.03
Kspar6_2		66.79	18.32	0.02	0.03	0.89	6.95	0.02	6.91	0.01	0.06
Kspar6_3		67.01	18.40	0.01	0.01	0.87	6.92	0.04	6.72	-0.01	-0.04
Kspar6_4		66.89	18.19	-0.01	0.01	0.83	7.05	0.02	6.98	0.01	0.01
Kspar6_5		67.00	18.34	0.01	0.03	0.82	7.01	0.01	6.79	-0.01	0.00
Kspar6_6		66.84	18.32	0.01	0.00	0.81	7.07	0.02	6.92	0.00	0.01

Continued on next page

Table B.10 – continued from previous page

Kspar#	Rim/Core	SiO_2	Al_2O_3	CaO	MnO	FeOt	K_2O	TiO_2	Na_2O	MgO	P_2O_5
Kspar6_7		67.13	18.29	0.00	-0.01	0.82	6.97	0.01	6.76	0.00	0.01
Kspar6_8		66.97	18.33	0.01	-0.01	0.84	6.97	0.04	6.75	0.00	-0.01
Kspar6_9		66.88	18.22	0.01	-0.02	0.85	7.12	0.01	6.89	-0.01	0.00
Kspar6_10		67.07	18.30	0.00	0.00	0.81	7.01	0.02	6.78	-0.01	0.01
Kspar6_11		67.08	18.31	0.01	-0.01	0.82	6.98	0.01	6.78	0.00	-0.01
Kspar6_12		66.77	18.38	0.00	0.00	0.78	7.13	0.04	6.90	-0.02	0.01
Kspar6_13		66.96	18.30	0.01	0.01	0.78	7.19	0.03	6.70	0.00	-0.01
Kspar6_14		66.76	18.33	0.00	-0.02	0.79	7.29	0.00	6.81	-0.01	0.01
Kspar6_15		66.99	18.20	0.01	0.01	0.88	7.11	0.01	6.73	0.00	0.00
Kspar6_16		67.03	18.21	0.00	0.01	0.87	7.06	0.00	6.79	0.01	0.00
Kspar6_17		67.07	18.41	0.01	0.03	0.75	7.14	0.00	6.58	0.01	0.00
Kspar6_18		66.94	18.28	-0.01	0.02	0.86	7.08	0.00	6.78	-0.01	0.02
Kspar6_19		67.19	18.29	0.01	0.00	0.80	7.02	0.01	6.67	0.01	-0.01
Kspar6_20	*Core*	66.86	18.24	0.00	-0.01	0.84	7.19	-0.01	6.75	0.02	0.01
Kspar7_1	*Rim*	67.16	18.33	0.02	0.00	0.82	6.59	0.01	7.08	-0.01	-0.01
Kspar7_2	*Core*	67.25	18.46	0.00	0.01	0.59	6.70	0.02	6.93	0.00	-0.01
Kspar8_1	*Rim*	67.06	18.53	0.03	0.04	0.62	6.64	-0.01	7.08	-0.01	0.00
Kspar8_2	*Core*	67.01	18.48	0.01	0.02	0.62	6.88	0.00	6.96	0.01	0.02
Kspar9_1	*Rim*	66.74	18.29	0.12	0.00	0.69	7.09	0.02	7.05	0.01	0.00
Kspar9_2	*Core*	66.88	18.45	0.01	0.00	0.68	7.05	0.01	6.92	-0.02	-0.01
Kspar10_1	*Rim*	67.02	18.43	0.02	0.00	0.71	7.11	0.03	6.69	0.00	0.00
Kspar10_2	*Core*	67.05	18.41	0.03	0.00	0.70	7.00	0.00	6.79	0.01	0.00
Kspar11_1	*Rim*	67.32	18.35	0.02	0.01	0.78	6.99	0.01	6.52	0.00	-0.05
Kspar11_2	*Core*	66.97	18.44	0.01	0.02	0.79	7.08	0.03	6.66	0.00	-0.03
Kspar12_1	*Rim*	67.25	18.55	0.09	-0.02	0.55	6.35	0.01	7.17	-0.01	0.01
Kspar12_2		67.27	18.57	0.02	0.01	0.52	6.40	0.00	7.17	-0.01	-0.01
Kspar12_3		67.19	18.61	0.04	0.02	0.51	6.36	0.00	7.13	0.00	0.01

Continued on next page

Table B.10 – continued from previous page

Kspar#	Rim/Core	SiO_2	Al_2O_3	CaO	MnO	FeOt	K_2O	TiO_2	Na_2O	MgO	P_2O_5
Kspar12_4		67.34	18.50	0.05	0.00	0.54	6.38	0.00	7.12	0.01	0.04
Kspar12_5		67.13	18.57	0.03	-0.01	0.58	6.44	0.03	7.22	-0.01	-0.01
Kspar12_6		67.34	18.49	0.02	-0.01	0.55	6.45	0.00	7.10	0.00	0.03
Kspar12_7		67.20	18.57	0.02	0.02	0.58	6.38	0.00	7.22	-0.01	0.01
Kspar12_8		67.10	18.62	0.03	-0.01	0.59	6.43	0.03	7.21	0.00	-0.01
Kspar12_9		67.28	18.56	0.03	0.01	0.54	6.28	0.01	7.29	-0.01	0.01
Kspar12_10		67.21	18.55	0.01	0.01	0.49	6.41	0.01	7.25	0.02	0.02
Kspar12_11		67.29	18.55	0.02	-0.01	0.51	6.36	0.03	7.22	-0.01	-0.01
Kspar12_12		67.10	18.59	0.03	0.01	0.54	6.41	0.02	7.27	0.01	-0.02
Kspar12_13		67.13	18.61	0.03	-0.02	0.52	6.42	0.01	7.25	0.01	0.02
Kspar12_14		67.18	18.58	0.05	-0.01	0.53	6.43	0.03	7.18	0.00	0.02
Kspar12_15		67.08	18.63	0.04	0.02	0.66	6.35	0.02	7.15	0.00	0.00
Kspar12_16		67.19	18.56	0.03	-0.03	0.66	6.44	0.02	7.08	0.01	-0.01
Kspar12_17		67.23	18.39	0.03	0.02	0.72	6.45	0.00	7.12	0.01	0.01
Kspar12_18		67.10	18.50	0.02	-0.02	0.69	6.45	0.01	7.16	0.00	0.02
Kspar12_19		67.23	18.38	0.03	0.00	0.71	6.41	0.02	7.15	0.02	0.04
Kspar12_20	*Core*	67.07	18.40	0.02	0.02	0.71	6.29	0.00	7.40	-0.01	-0.01
Kspar13_1	*Rim*	67.12	18.34	0.00	0.01	0.75	6.73	0.01	7.03	-0.01	0.01
Kspar13_2		67.44	18.27	0.01	0.00	0.72	6.59	0.01	6.94	0.00	0.01
Kspar13_3		67.07	18.45	0.02	0.00	0.69	6.68	0.01	7.03	0.00	-0.03
Kspar13_4		67.15	18.51	0.02	0.00	0.51	6.78	0.00	7.03	0.01	-0.01
Kspar13_5	*Core*	67.18	18.55	0.03	0.02	0.49	6.75	0.00	6.87	0.02	0.04
Kspar14_1	*Rim*	67.10	18.28	0.03	-0.01	0.70	6.84	0.00	7.05	-0.01	0.01
Kspar14_2	*Core*	66.93	18.45	0.00	-0.01	0.82	6.90	-0.01	6.85	-0.02	-0.02
Kspar15_1	*Rim*	67.29	18.51	0.02	0.01	0.47	6.58	0.04	7.06	0.00	0.01
Kspar15_2	*Core*	67.18	18.52	0.03	0.01	0.60	6.58	0.02	7.05	0.00	0.00
Kspar16_1	*Rim*	67.01	18.65	0.01	-0.01	0.75	6.80	-0.02	6.77	-0.01	0.01

Continued on next page

Table B.10 – continued from previous page

Kspar#	Rim/Core	SiO_2	Al_2O_3	CaO	MnO	FeOt	K_2O	TiO_2	Na_2O	MgO	P_2O_5
Kspar16_2	*Core*	66.99	18.25	0.00	0.00	0.97	7.05	0.03	6.70	0.01	-0.05
Kspar17_1	*Rim*	67.34	18.65	0.05	-0.02	0.50	6.36	0.00	7.06	0.00	0.01
Kspar17_2	*Core*	67.25	18.42	0.02	0.00	0.81	6.34	-0.01	7.05	0.00	0.01
Kspar18_1	*Rim*	66.70	18.32	0.00	-0.01	0.75	7.44	0.01	6.75	0.01	0.02
Kspar18_2		67.19	18.41	0.02	-0.02	0.70	7.14	0.00	6.54	0.00	-0.02
Kspar18_3	*Core*	67.09	18.25	0.01	0.01	0.82	7.20	0.01	6.60	0.00	-0.02
Kspar20_1	*Rim*	66.73	18.12	0.01	-0.01	0.95	7.48	0.00	6.66	-0.02	-0.06
Kspar20_2	*Core*	66.83	18.23	0.00	-0.02	0.91	7.36	0.00	6.56	-0.01	0.00
Kspar21_1	*Rim*	67.52	18.64	0.01	0.00	0.59	6.17	0.00	7.04	-0.03	0.01
Kspar21_2	*Core*	67.00	18.61	0.03	0.01	0.56	6.68	0.02	7.08	-0.01	0.01
Kspar22_1	*Rim*	66.43	18.11	0.00	0.02	1.03	7.70	0.05	6.67	-0.01	-0.04
Kspar22_2	*Core*	66.77	18.10	0.00	0.01	1.00	7.52	0.03	6.54	0.00	0.04
Kspar23_1	*Rim*	66.50	18.15	0.00	0.01	0.96	7.92	-0.01	6.45	0.00	-0.02
Kspar23_2	*Core*	66.42	18.24	-0.01	0.03	0.97	7.82	0.01	6.46	0.01	0.03
Kspar24_1	*Rim*	66.92	18.34	0.01	0.01	0.79	6.61	0.03	7.26	0.01	-0.02
Kspar24_2	*Core*	66.91	18.35	0.02	-0.02	0.69	6.97	0.02	7.03	0.01	-0.02
Kspar25_1	*Rim*	66.80	18.36	0.01	-0.02	0.79	7.00	0.01	6.96	0.01	0.01
Kspar25_2	*Core*	66.87	18.20	0.01	0.00	0.86	7.28	0.00	6.76	0.00	-0.04
Kspar26_1	*Rim*	67.05	18.49	0.02	0.00	0.66	6.85	0.01	6.84	0.02	0.05
Kspar26_2	*Core*	66.95	18.28	0.02	0.00	0.86	6.88	0.02	7.00	-0.01	-0.02
Kspar27_1	*Rim*	66.95	18.61	0.00	0.00	0.55	6.85	-0.01	7.03	0.00	-0.03
Kspar27_2	*Core*	66.89	18.41	0.02	0.00	0.70	6.92	0.01	6.95	0.00	-0.03
Kspar28_1	*Rim*	67.07	18.24	0.02	-0.03	0.77	6.75	0.01	7.14	0.00	0.00
Kspar28_2	*Core*	66.88	18.36	0.01	-0.01	0.80	6.83	0.01	7.11	-0.02	-0.02
Kspar29_1	*Rim*	67.07	18.49	0.02	0.00	0.74	6.47	0.02	7.13	0.00	0.01
Kspar29_2	*Core*	66.96	18.60	0.02	0.00	0.67	6.48	-0.01	7.25	0.01	0.00
Kspar30_1	*Rim*	66.91	18.04	0.00	0.00	0.94	7.44	-0.01	6.64	-0.01	0.02

Continued on next page

Table B.10 – continued from previous page

Kspar#	Rim/Core	SiO_2	Al_2O_3	CaO	MnO	FeOt	K_2O	TiO_2	Na_2O	MgO	P_2O_5
Kspar30_2	*Core*	66.81	18.12	0.00	-0.01	0.97	7.45	0.04	6.59	0.00	0.00
Kspar31_1	*Rim*	67.14	18.52	0.02	-0.03	0.74	6.71	0.03	6.79	0.01	0.00
Kspar31_2	*Core*	66.90	18.27	0.03	-0.01	0.89	6.99	0.00	6.86	0.02	0.04
Kspar32_1	*Rim*	67.12	18.42	0.02	-0.01	0.56	6.68	0.02	7.11	-0.01	0.00
Kspar32_2	*Core*	67.16	18.66	0.04	0.01	0.54	6.64	0.01	6.92	0.01	0.02
Kspar33_1	*Rim*	66.96	18.34	-0.01	-0.01	0.68	7.02	0.01	6.98	0.00	0.00
Kspar33_2	*Core*	66.80	18.17	0.01	0.00	0.93	7.39	0.00	6.68	0.01	-0.02
Kspar34_1	*Rim*	66.79	18.29	0.01	-0.02	0.93	7.67	0.01	6.24	0.00	-0.01
Kspar34_2		66.79	18.18	0.00	0.02	0.91	7.80	0.01	6.26	0.01	0.00
Kspar34_3	*Core*	66.66	18.37	-0.01	-0.03	0.89	7.89	0.03	6.06	0.00	-0.01
Kspar35_1	*Rim*	66.96	18.42	0.03	0.01	0.84	6.44	0.02	7.26	0.02	0.01

Table B.11: Clinopyroxene compositions recorded in NCW_F. All elements reported in wt.% and normalised to 100 wt.%. Core and Rim compositions noted.

Core/Rim	CPX#	SiO_2	Al_2O_3	CaO	MnO	FeOt	K_2O	TiO_2	Na_2O	MgO	P_2O_5
Rim	CPX1_1	47.89	0.16	17.52	2.32	29.58	-0.01	0.30	1.55	0.68	0.00
Core	CPX1_2.	48.05	0.14	17.45	2.31	29.39	-0.01	0.32	1.59	0.63	0.04
Rim	CPX2_1	47.90	0.17	17.05	2.14	29.78	0.00	0.35	2.02	0.46	0.00
Rim	CPX3_1	48.13	0.16	17.41	2.11	29.29	0.01	0.38	1.78	0.64	0.04
	CPX3_2	48.03	0.16	17.45	2.25	29.42	0.01	0.31	1.69	0.63	0.03
	CPX3_3	48.10	0.12	17.46	2.13	29.55	0.01	0.32	1.63	0.61	0.02
	CPX3_4	47.97	0.15	17.59	2.10	29.50	0.01	0.34	1.64	0.60	0.04
	CPX3_5	47.87	0.14	17.45	2.14	29.65	0.00	0.32	1.75	0.63	0.00
	CPX3_6	48.08	0.14	17.52	2.20	29.51	-0.02	0.35	1.58	0.59	0.01
	CPX3_7	48.16	0.14	17.61	2.15	29.44	0.01	0.33	1.52	0.62	0.02
	CPX3_8	47.96	0.13	17.51	2.20	29.61	0.00	0.34	1.62	0.62	0.00

Continued on next page

Table B.11 – continued from previous page

Core/Rim	CPX#	SiO_2	Al_2O_3	CaO	MnO	FeOt	K_2O	TiO_2	Na_2O	MgO	P_2O_5
	CPX3_9	48.02	0.16	17.43	2.18	29.53	0.01	0.32	1.61	0.63	0.04
	CPX3_10	47.94	0.12	17.29	2.22	29.58	0.00	0.37	1.76	0.64	0.03
	CPX3_11	48.05	0.15	17.28	2.20	29.67	0.00	0.38	1.66	0.59	0.01
	CPX3_12	47.90	0.16	17.24	2.21	29.80	0.02	0.41	1.66	0.58	0.02
	CPX3_13	48.47	0.29	16.42	2.24	29.61	0.11	0.39	1.88	0.54	0.03
	CPX3_15	47.85	0.26	16.80	2.39	30.00	0.04	0.33	1.73	0.59	0.01
	CPX3_16	48.14	0.13	16.91	2.21	29.79	0.01	0.36	1.74	0.63	0.02
	CPX3_17	47.99	0.15	17.07	2.21	29.76	0.02	0.40	1.73	0.59	0.05
	CPX3_18	47.95	0.11	17.05	2.19	29.88	0.00	0.44	1.74	0.60	0.02
	CPX3_19	48.15	0.11	16.88	2.27	29.80	-0.01	0.38	1.71	0.59	0.00
Core	CPX3_20	47.77	0.16	16.98	2.22	29.95	0.00	0.45	1.86	0.58	0.00
Rim	CPX4_1	48.04	0.10	17.23	2.24	29.61	-0.01	0.35	1.72	0.63	0.02
Core	CPX4_2	47.88	0.12	17.81	2.23	29.56	-0.02	0.32	1.39	0.64	0.01
Rim	CPX5_1	47.94	0.14	17.56	2.23	29.65	0.03	0.34	1.44	0.65	0.01
Core	CPX5_2	48.12	0.13	17.37	2.16	29.48	0.00	0.34	1.67	0.64	0.01
Rim	CPX6_1	48.35	0.15	17.32	2.16	29.35	0.02	0.33	1.68	0.64	0.01
	CPX6_2	48.18	0.12	17.54	2.15	29.40	0.02	0.31	1.62	0.62	0.02
	CPX6_3	47.84	0.08	17.68	2.16	29.50	0.02	0.30	1.67	0.65	0.05
	CPX6_4	48.09	0.15	17.46	2.25	29.41	0.00	0.36	1.62	0.58	0.05
	CPX6_5	48.13	0.15	17.51	2.17	29.34	0.02	0.36	1.61	0.68	0.02
	CPX6_6	48.20	0.12	17.37	2.20	29.56	0.02	0.33	1.58	0.60	0.00
	CPX6_7	47.95	0.15	17.20	2.15	29.69	-0.02	0.34	1.76	0.64	0.02
	CPX6_8	47.97	0.15	17.26	2.20	29.68	0.00	0.34	1.71	0.62	0.02
	CPX6_9	48.13	0.15	17.38	2.20	29.50	-0.01	0.31	1.69	0.60	0.04
	CPX6_10	47.98	0.15	17.37	2.15	29.67	0.02	0.36	1.65	0.60	0.02
	CPX6_11	48.12	0.14	17.28	2.24	29.58	0.00	0.32	1.69	0.57	0.01
	CPX6_12	48.11	0.14	17.28	2.17	29.55	-0.01	0.36	1.72	0.61	0.03

Continued on next page

Table B.11 – continued from previous page

Core/Rim	CPX#	SiO_2	Al_2O_3	CaO	MnO	FeOt	K_2O	TiO_2	Na_2O	MgO	P_2O_5
	CPX6_13	47.91	0.14	17.37	2.16	29.70	0.01	0.33	1.66	0.65	0.05
	CPX6_14	48.17	0.14	17.23	2.24	29.61	-0.01	0.35	1.67	0.60	0.00
Core	CPX6_15	48.00	0.15	17.36	2.19	29.47	0.01	0.33	1.69	0.64	0.05
Rim	CPX7_1	47.82	0.14	18.20	2.50	29.09	0.00	0.35	1.02	0.84	0.00
Rim	CPX8_1	48.09	0.15	17.48	2.20	29.41	0.02	0.35	1.61	0.62	0.05
Core	CPX8_2	48.07	0.16	17.51	2.27	29.39	-0.01	0.32	1.57	0.61	0.00
Core	CPX9_2	48.00	0.13	17.28	2.26	29.68	0.00	0.34	1.62	0.64	0.04

Table B.12: Composition of single fayalite phenocrysts found within NCW_F. Oxides reported in wt.% and normalised to 100 wt.%

Core/Rim	Fayalite#	SiO_2	Al_2O_3	CaO	MnO	FeOt	K_2O	TiO_2	Na_2O	MgO	P_2O_5
Rim	1/1.	29.76	0.00	0.26	5.94	63.66	0.01	0.03	0.03	0.33	0.00
Core	1/2.	29.87	0.02	0.23	5.96	63.59	0.00	0.01	0.00	0.33	0.00

Table B.13: Clinopyroxene compositions within the enclave found within NCW_F. Compositions reported in wt.% and normalized to 100 wt.%

Sample	SiO_2	Al_2O_3	CaO	MnO	FeO	K_2O	TiO_2	Na_2O	MgO	P_2O_5
NCW_F_En_CPX_1	51.27	1.63	20.45	0.34	10.63	0.02	1.21	0.30	14.09	0.06
NCW_F_En_CPX_2	50.77	2.26	20.24	0.34	11.08	0.12	1.43	0.41	13.30	0.04
NCW_F_En_CPX_3	50.50	2.54	20.84	0.28	9.48	0.03	1.58	0.47	14.22	0.05
NCW_F_En_CPX_4	50.64	2.72	20.67	0.22	9.50	0.08	1.58	0.35	14.20	0.05
NCW_F_En_CPX_5	50.83	2.24	20.84	0.25	9.71	0.01	1.55	0.33	14.23	0.01
NCW_F_En_CPX_6	50.42	2.42	21.14	0.23	9.30	0.01	1.60	0.37	14.49	0.02
NCW_F_En_CPX_7	50.57	2.72	21.12	0.23	9.09	0.02	1.61	0.40	14.25	0.00
NCW_F_En_CPX_8	51.47	1.56	20.50	0.33	10.46	0.03	1.13	0.37	14.09	0.05

Continued on next page

Table B.13 – continued from previous page

Sample	SiO_2	Al_2O_3	CaO	MnO	FeO	K_2O	TiO_2	Na_2O	MgO	P_2O_5
NCW_F_En_CPX_9	51.26	1.96	20.64	0.29	9.88	0.01	1.36	0.36	14.22	0.02
NCW_F_En_CPX_10	51.27	1.95	20.58	0.29	10.22	0.03	1.33	0.37	13.94	0.02
NCW_F_En_CPX_11	50.54	2.70	20.78	0.25	9.68	0.02	1.72	0.40	13.91	0.01

Table B.14: Feldspar compositions found within the crystalline enclave in NCW_F. All data reported in wt.% and normalized to 100 wt.%. For the two feldspar thermometry presented in Chapter 3 each alkali feldspar composition was matched with each plagioclase composition.

Sample	SiO_2	Al_2O_3	CaO	MnO	FeO	K_2O	TiO_2	Na_2O	MgO	P_2O_5
NCW_F_En_Feldspar_1	52.24	29.73	12.77	0.00	0.68	0.24	0.11	4.09	0.11	0.03
NCW_F_En_Feldspar_2	52.63	28.97	12.11	0.01	1.11	0.33	0.16	4.54	0.13	0.02
NCW_F_En_Feldspar_3	54.15	28.34	10.99	0.00	0.80	0.39	0.16	5.08	0.06	0.02
NCW_F_En_Feldspar_4	53.74	27.90	11.23	0.01	1.56	0.46	0.16	4.78	0.17	0.00
NCW_F_En_Feldspar_5	61.09	19.12	6.05	0.07	2.52	1.98	0.32	7.11	1.74	0.01
NCW_F_En_Feldspar_6	57.04	26.40	8.67	0.02	0.59	0.75	0.14	6.31	0.05	0.02
NCW_F_En_Feldspar_7	63.75	22.00	3.00	0.00	0.42	2.71	0.11	8.04	0.00	0.00
NCW_F_En_Feldspar_8	63.22	22.07	3.39	0.00	0.84	2.20	0.16	8.04	0.06	0.02
NCW_F_En_Feldspar_9	54.58	28.15	10.62	0.00	0.68	0.42	0.13	5.33	0.06	0.02
NCW_F_En_Feldspar_10	53.60	28.77	11.55	0.02	0.74	0.29	0.15	4.74	0.09	0.04
NCW_F_En_Feldspar_11	54.21	28.26	11.11	0.01	0.80	0.37	0.17	5.04	0.05	-0.02
NCW_F_En_Feldspar_12	56.35	26.55	8.92	0.03	1.26	0.67	0.11	5.86	0.19	0.06
NCW_F_En_Feldspar_13	59.51	24.82	6.63	0.01	0.64	0.96	0.12	7.21	0.09	0.01
NCW_F_En_Feldspar_14	55.96	27.02	9.35	0.01	0.85	0.48	0.17	6.02	0.09	0.05
NCW_F_En_Feldspar_15	53.76	28.62	11.54	-0.01	0.69	0.31	0.12	4.89	0.07	0.00
NCW_F_En_Feldspar_16	64.50	20.74	2.36	-0.01	0.47	3.75	0.18	7.77	0.04	0.19
NCW_F_En_Feldspar_17	64.09	21.25	2.72	-0.01	0.62	3.13	0.13	7.95	0.07	0.05
NCW_F_En_Feldspar_18	58.87	24.80	7.21	0.00	0.78	0.85	0.12	7.05	0.08	0.23

Continued on next page

Table B.14 – continued from previous page

Sample	SiO_2	Al_2O_3	CaO	MnO	FeO	K_2O	TiO_2	Na_2O	MgO	P_2O_5
NCW_F_En_Feldspar_19	53.79	28.49	11.40	-0.01	0.78	0.32	0.18	4.93	0.10	0.02
NCW_F_En_Feldspar_20	59.78	24.07	6.17	0.00	1.24	1.60	0.14	6.79	0.22	0.00
NCW_F_En_Feldspar_21	53.73	28.44	11.22	0.01	0.90	0.34	0.21	5.07	0.07	0.02
NCW_F_En_Feldspar_22	54.30	28.05	10.80	-0.01	0.93	0.44	0.16	5.24	0.12	-0.03
NCW_F_En_Feldspar_23	58.22	25.71	7.71	0.00	0.69	0.80	0.13	6.65	0.06	0.04

Appendix C

Appendices for Chapter 4

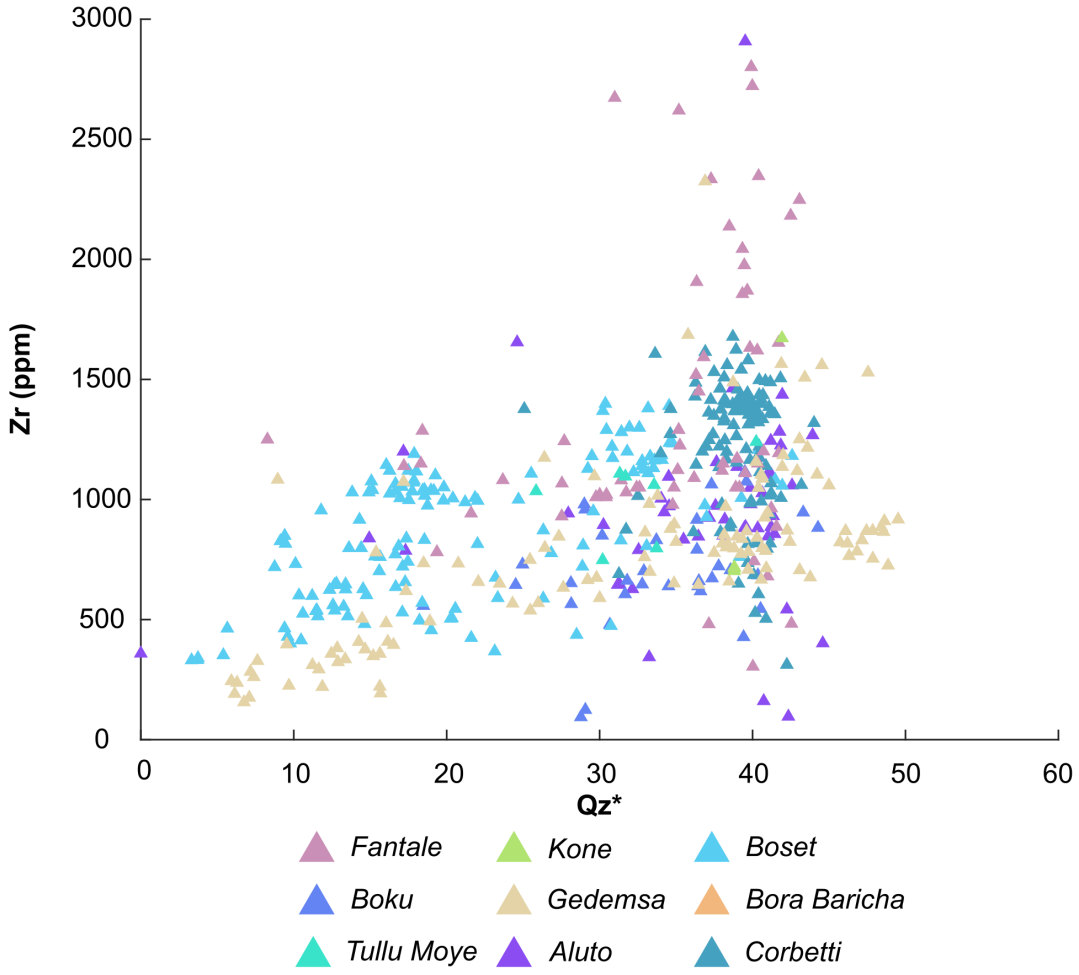

Figure C.1: Variation in Zr content with Qz*. Only data for Zr concentrations for whole rock data are available, therefore there is minimal data beyond the whole-rock minimum composition (Qz* = 40.5; White et al. 2023).

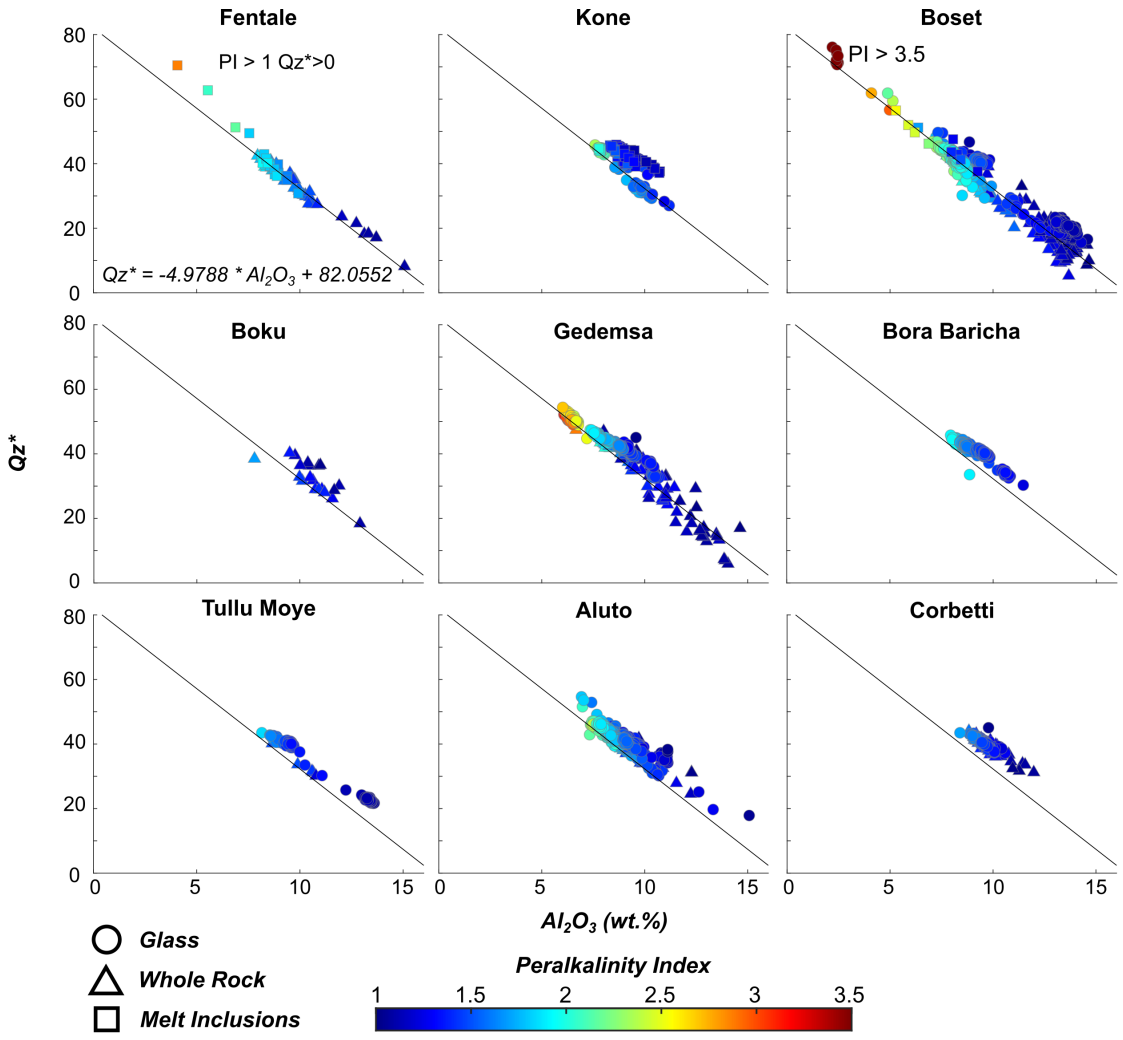

Figure C.2: Change in calculated Qz* value with Al_2O_3 concentration in glass, whole rock and melt inclusions. Samples coloured by their peralkalinity index. Demonstrates a strong negative correlation between Al_2O_3 and Qz* in peralkaline products (Qz*> 0 & PI > 1) across the MER. Trendline is defined by White et al. (2023) for Pantelleria, Italy. Whilst some of the scatter in these figures can be attributed to glass and whole rock compositions, there is generally good agreement whith centres such as Corbetti showing no difference between whole-rock and glass data. Distinctive trends in glass compositions can be observed at Kone and Gedemsa which relate to geochemically distinct stratigraphic units.

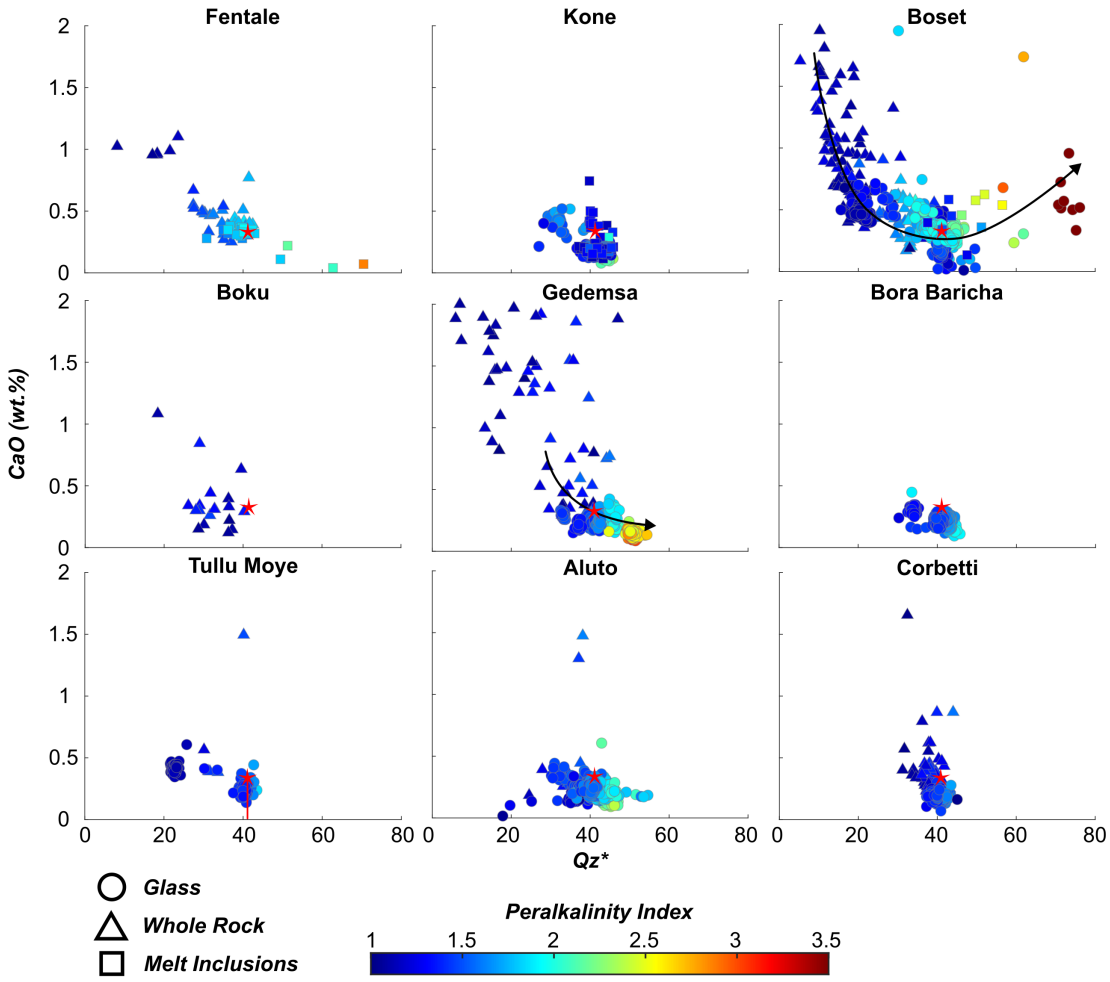

Figure C.3: Variation in CaO across the MER with Qz*. Arrows at Gedemsa and Boset highlight the two main trends observed within the rift. At Boset there is a clear increase in the concentration of CaO at Qz* > 40 however this is not observed at Gedemsa.

Table C.1: Overview of mineral assemblages reported in trachyte and rhyolite magmas across the MER.

Volcano	Rock Chemistry	Material	Mineral assemblage	Notes	Citation
Aluto	Trachytic	Ignimbrite	Fe-Ti Oxides, Aen, Afs, Fa		Iddon et al. (2019)
Aluto	Rhyolite	Lava	Aen, Aeg, Afs, Qz		Iddon et al. (2019)
Aluto	Trachytic	Lava	Afs, Plag	Plagioclase in groundmass	Hutchison et al. (2016c)
Aluto	Trachytic	Scoria	Aeg, Afs	Both Afs and Aeg are xenocryst	Hutchison et al. (2016c)
Aluto	Rhyolite	Ignimbrite	Fe-Ti Oxides, CPX, Aeg, Afs		Hutchison et al. (2016c)
Aluto	Rhyolite	Lava	Fe-Ti Oxides, Aen, Aeg, Afs, Qz, Amph	Qz- feldspar granophyric textures identified	Hutchison et al. (2016c)
Aluto	Rhyolite	Lava	Aen, Aeg, Afs, Qz, Bi		Gleeson et al. (2017)
Aluto	Rhyolite	Lava	Aeg, Afs, Qz, Bi		Gleeson et al. (2017)
Aluto	Rhyolite	Lava	Fe-Ti Oxides, Aen, Aeg, Afs, Qz, Bi		Gleeson et al. (2017)
Aluto	Rhyolite	Lava	Aen, Aeg, Afs, Qz, Bi		Gleeson et al. (2017)
Fantale	Pantellerite	Lava	Afs (anorthoclase), Qz, Fa, Aeg		Gibson (1972)
Fantale	Peralkaline	Eutaxitic Tuff	Afs (anorthoclase), Qz, Il, Aen		Gibson (1970)
Fantale	Trachyte	Lava	Afs (oligoclase), Fa, Ferro-augite		Gibson (1974)
Fantale	Rhyolite	Lava	Afs (anorthoclase), Ferro-hedenbergite, Fa, Aeg, Qz		Gibson (1974)

Continued on next page

Table C.1 – continued from previous page

Volcano	Rock Chemistry	Material	Mineral assemblage	Notes	Citation
Fantale	Pantellerite	Lava	Afs (Sanidine), Aeg, Qz, Ferro-hedenbergite, Alkali Amph		Gibson (1974)
Kone	Rhyolite	Ignimbrite	Afs (anorthoclase), Qz, Aen, Aeg		Iddon et al. (2019)
Kone	Rhyolite	Pumice	Afs (anorthoclase), Aen, Fe-Ti oxides		Iddon et al. (2019)
Kone	Trachyte	Lava	Afs (anorthoclase), Aen, Fe-Ti oxides	Afs, Qz, Aen in groundmass	Iddon et al. (2019)
Kone	Trachyte/Rhyolite	Lava	Afs, Qz, Il, Aen	Sodic-Amph and Cossyrite in groundmass	Cole (1969)
Kone	-	Syenite Inclusion	Augite, aegirine, Fe-Hastingsite, Afs (anorthoclase), Qz, sodic Amph, arfvedsonite		Cole (1969)
Boset	Peralkaline Rhyolite		Afs (anorthoclase), sanidine, Aen, Fa		Brotzu et al. (1980)
Boset	Peralkaline Rhyolite		Afs (anorthoclase), Aen, Ti-magnetite, Amph, Il, apatite		Brotzu et al. (1980)
Boset	Peralkaline Rhyolite		Afs (anorthoclase), augite, olivine, Ti-magnetite, apatite		Brotzu et al. (1980)
Boset	Pantellerite		Afs (anorthoclase), Ferro-hedenbergite, cossyrite, Arfvedsonite, Qz, Fa		Brotzu et al. (1980)
Boset	Peralkaline Rhyolite		Afs (anorthoclase), hedenbergite		Macdonald et al. (2012)
Boset	Peralkaline Rhyolite		Aeg, hedenbergite		Macdonald et al. (2012)

Continued on next page

Table C.1 – continued from previous page

Volcano	Rock Chemistry	Material	Mineral assemblage	Notes	Citation
Boset	Peralkaline Rhyolite		Afs, CPX, olivine, Fe-Ti oxides, apatite	Groundmass same as phenocryst + Qz	Macdonald et al. (2012)
Boset	Peralkaline Rhyolite		Afs, CPX, olivine, Aeg, Fe-Ti oxides	Groundmass: Qz, feldspar, Aen, Aeg and Il in groundmass	Macdonald et al. (2012)
Boset	Trachyte/ Rhyolites		Afs (anorthoclase, Sanidine), Hedenbergite, Fa	Fe-augite (hedenbergite), rare Aen. Groundmass devitrified and Afs present.	Ronga et al. (2009)
Corbetti	Peralkaline Rhyolite	Welded Ignimbrite	Qz, Afs, Aeg	Enclave present containing Pl, Afs, CPX, Fe-Ti oxides	Chapter3
Corbetti	Peralkaline Rhyolite	Ignimbrite	Qz, Afs, rare Aeg and Fa	Qz phenocrysts highly fractured	Chapter 3
Corbetti	Peralkaline Rhyolite	Obsidian	Qz, Afs, Fe-Ti Oxides, rare Aen	Microlites aligned in flow direction	Chapter 3
Gedemsa	Peralkaline Rhyolite		Qz, Afs, CPX, Fa, Fe-Ti Oxides		Barberio et al. (1999)
Gedemsa		Lava	Afs, Fa, Aen, Alkali-pyroxene, Amph		Peccerillo et al. (2003)
Gedemsa		Pumice	Afs, Alkali-pyroxene, Aen, Amph		Peccerillo et al. (2003)
Gedemsa		Ignimbrite	Afs, Fa, Aen, Alkali-pyroxene, Bi, Fe-Ti Oxides		Peccerillo et al. (2003)
BBTM		Lava	Afs, Qz, Aen, Opx		Tadesse et al. (2023)

Continued on next page

Table C.1 – continued from previous page

Volcano	Rock Chemistry	Material	Mineral assemblage	Notes	Citation
BBTM	Peralkaline Rhyolite	Rhyolite Pyroclast	Afs, Qz, Aen, CPX, OPX, Amph	Apatite inclusions in pyroxenes	Tadesse et al. (2023)
BBTM		Glomerocrysts	Afs, Aen, OPX, CPX, Qz, Amph		Tadesse et al. (2023)

Table C.2: Details of the composition of each of the mineral phases used for the mass balance modelling. Where available, mineral data from the volcano of interest was used.

Mineral ab	SiO_2	TiO_2	Al_2O_3	FeOt	CaO	MgO	MnO	K_2O	Na_2O	P_2O_5	Volcano	Citation
Minerals used for Aluto												
Kspar1	67.8774	0	18.5425	0.3003	0.1109	0	0	5.024	8.1602	0	Aluto	Gleeson et al. (2017)
Kspar3	67.915	0	18.0417	0.6233	0	0	0	6.0086	7.3706	0	Aluto	Gleeson et al. (2017)
Kspar4	67.3109	0	17.8417	0.7717	0	0	0	6.6711	7.0991	0	Aluto	Gleeson et al. (2017)
Kspar5	67.735	0	17.5782	0.8285	0	0	0	7.0277	6.7793	0	Aluto	Gleeson et al. (2017)
Kspar6	66.647	0	17.8978	0.999	0	0	0	8.0291	5.9203	0	Aluto	Gleeson et al. (2017)
Kspar9	65.7708	0	17.4209	1.062	0	0	0	9.0252	5.5014	0	Aluto	Gleeson et al. (2017)
Fayalite	29.73	0	0	66.47	0.75	0.81	2.07	0	0	0	Boset	Brotzu et al. (1980)
Magnatite_1	0	22.19	0.28	73.3	0	0.12	2.4	0	0	0	Boset	Ronga et al. (2009)
Ilmenite_1	0	52.02	0.02	46.41	0	0	2.17	0	0	0	Boset	Ronga et al. (2009)
Ilmenite_2	0	46.89	0.2	43.1	0	0	2.83	0	0	0	Boset	Ronga et al. (2009)
Magnatite_2	0.08	24.85	0.05	69.76	0	0.04	1.92	0	0	0	Pantelleria	White et al. (2023)
Ap	0	0	0	2.5	50.32	0	0.08	0.23	0.16	39.99	Pantelleria	White et al. (2023)
Aenigmatite_1	39.33	7.74	1.33	39.69	1.02	0.09	1.15	0.32	5.8	0	Boset	Ronga et al. (2009)
Aenigmatite_2	41.79	8.94	0.29	42.27	0.21	0.12	1.23	0.02	7.48	0	Boset	Ronga et al. (2009)
CPX1	49.55	0.71	1.09	19.49	20.08	6.8	1.64	0	0.56	0	Boset	Ronga et al. (2009)
CPX2	48.16	0.77	0.4	27.3	19.68	1.72	2.01	0	0.74	0	Boset	Ronga et al. (2009)

Continued on next page

Table C.2 – continued from previous page

Mineral ab	SiO_2	TiO_2	Al_2O_3	FeOt	CaO	MgO	MnO	K_2O	Na_2O	P_2O_5	Volcano	Citation
CPX3	50.34	1.49	0.1	28.62	9.02	0.05	0.79	0	7.85	0	Boset	Ronga et al. (2009)
CPX4	49.62	1.19	0.12	28.67	13.69	0.22	1.39	0	4.95	0	Boset	Ronga et al. (2009)
CPX5	47.71	0.42	0.13	30.03	18.27	0.12	1.38	0	1.41	0	Boset	Ronga et al. (2009)
CPX7	52.25	0.75	1.26	12.16	17.84	14.23	0.52	0	0.48	0	Boset	Ronga et al. (2009)
CPX9	49.22	1.05	0.39	28.13	17.17	0.7	2	0	1.05	0	Boset	Ronga et al. (2009)
Q	100	0	0	0	0	0	0	0	0	0		
Amphibole	48.89	2.31	1.18	29.36	5.6	4.27	1.26	1.13	5.15	0	Pantelleria	White et al. (2023)
Biotite	35.92	3.37	6.46	39.75	0	1.17	0.37	8.27	0.54	0	Pantelleria	White et al. (2023)
Minerals used for Boset and Kone												
Fayalite	29.73	0	0	66.47	2.07	0.81	0.75	0	0	0	Boset	Ronga et al. (2009)
Magnatite_1	0	22.19	0.28	73.3	2.4	0.12	0	0	0	0	Boset	Ronga et al. (2009)
Ilmenite_1	0	52.02	0.02	46.41	2.17	0	0	0	0	0	Boset	Ronga et al. (2009)
Ilmenite_2	0	46.89	0.2	43.1	2.83	0	0	0	0	0	Boset	Ronga et al. (2009)
Ilmenite_3	0	51.01	0	45.8	3.14	0.06	0	0	0	0	Boset	Ronga et al. (2009)
Magnatite_2	0.08	24.85	0.05	69.76	1.92	0.04	0	0	0	0	Pantelleria	White et al. (2023)
Apatite	0	0	0	2.5	0.08	0	50.32	0.16	0.23	39.99	Pantelleria	White et al. (2023)
Aenigmattie_1	39.33	7.74	1.33	39.69	1.15	0.09	1.02	5.8	0.32	0	Boset	Ronga et al. (2009)
Aenigmattie_2	41.79	8.94	0.29	42.27	1.23	0.12	0.21	7.48	0.02	0	Boset	Ronga et al. (2009)
Kspar1	63.9	0	22.28	0	0	0	3.47	8.45	1.91	0	Boset	Ronga et al. (2009)
Kspar2	68.22	0	18.88	0.51	0	0	0.05	9.48	3.41	0	Boset	Ronga et al. (2009)
Kspar3	66.82	0	19.43	0.17996941	0	0	0.49	8.19	4.79	0	Boset	Ronga et al. (2009)
Kspar4	67.01	0	18.79	0.82785926	0	0	0.01	7.6	6.02	0	Boset	Ronga et al. (2009)
CPX1	49.55	0.71	1.09	19.49	1.64	6.8	20.08	0.56	0	0	Boset	Ronga et al. (2009)
CPX2	48.16	0.77	0.4	27.3	2.01	1.72	19.68	0.74	0	0	Boset	Ronga et al. (2009)
CPX3	50.34	1.49	0.1	28.62	0.79	0.05	9.02	7.85	0	0	Boset	Ronga et al. (2009)
CPX4	49.62	1.19	0.12	28.67	1.39	0.22	13.69	4.95	0	0	Boset	Ronga et al. (2009)
CPX5	47.71	0.42	0.13	30.03	1.38	0.12	18.27	1.41	0	0	Boset	Ronga et al. (2009)

Continued on next page

Table C.2 – continued from previous page

Mineral ab	SiO_2	TiO_2	Al_2O_3	FeOt	CaO	MgO	MnO	K_2O	Na_2O	P_2O_5	Volcano	Citation
CPX7	52.25	0.75	1.26	12.16	0.52	14.23	17.84	0.48	0	0	Boset	Ronga et al. (2009)
CPX9	49.22	1.05	0.39	28.13	2	0.7	17.17	1.05	0	0	Boset	Ronga et al. (2009)
Q	100	0	0	0	0	0	0	0	0	0		
Amphibole	48.89	2.31	1.18	29.36	1.26	4.27	5.6	5.15	1.13	0	Pantelleria	White et al. (2023)
Minerals used for Corbetti												
Fayalite	29.76	0.03	-0.01	63.66	5.94	0.33	0.26	0.03	0.01	0	Corbetti	Chapter 3
CPX1	48.47	0.39	0.29	29.61	2.24	0.54	16.42	1.88	0.11	0.03	Corbetti	Chapter 3
CPX2	47.9	0.35	0.17	29.78	2.14	0.46	17.05	2.02	0	0	Corbetti	Chapter 3
CPX3	52.50	0.98	0.19	30.49	0.80	0.13	3.72	11.16	0.00	0.06	Corbetti	Chapter 3
CPX4	51.27	1.21	1.63	10.63	0.34	14.09	20.45	0.3	0.02	0.06	Corbetti	Chapter 3
KSPAR1	66.86	0	18.55	0.61	0	0.02	0.02	7.06	7.01	0	Corbetti	Chapter 3
KSPAR2	66.98	0.03	18.42	0.71	0	0	0.02	6.68	7.1	0	Corbetti	Chapter 3
Kspar1_B	63.9	0	22.28	0	0	0	3.47	8.45	1.91	0	Boset	Ronga et al. (2009)
Kspar2_B	68.22	0	18.88	0.51	0	0	0.05	9.48	3.41	0	Boset	Ronga et al. (2009)
Ilmenite	0	52.02	0.02	46.41	2.17	0	0	0	0	0	Boset	Ronga et al. (2009)
Magnatite	0.08	24.85	0.05	69.76	1.92	0.04	0	0	0	0	Boset	Ronga et al. (2009)
Apatite	0	0	0	2.5	0.08	0	50.32	0.16	0.23	39.99	Pantelleria	White et al. (2023)
Aenigmatite_1	39.33	7.74	1.33	39.69	1.15	0.09	1.02	5.8	0.32	0	Boset	Ronga et al. (2009)
Aenigmatite_2	41.79	8.94	0.29	42.27	1.23	0.12	0.21	7.48	0.02	0	Boset	Ronga et al. (2009)
Quartz	100	0	0	0	0	0	0	0	0	0		
Amphibole	48.89	2.31	1.18	29.36	1.26	4.27	5.6	5.15	1.13	0	Pantelleria	White et al. (2023)
Minerals used for Gedemsa												
Fayalite	29.79	0	0	64.799972	6.36	0.08	0.58	0	0	0	Gedemsa	Peccerillo et al. (2003)
CPX1	49.08	1.23	0.56	35.4306602	1.1	0.23	3.11	6.41	1.45	0	Gedemsa	Peccerillo et al. (2003)
CPX2	47.36	1.05	0.55	29.0589518	2.63	0.41	19.19	0.57	0.02	0	Gedemsa	Peccerillo et al. (2003)
CPX3	48.24	4.35	0.53	31.029726	1.72	1.01	3.91	6.63	1.18	0	Gedemsa	Peccerillo et al. (2003)
Kspar1	66.85	0.08	18.58	0.37800378	0	0	0.11	7.16	5.98	0	Gedemsa	Peccerillo et al. (2003)

Continued on next page

Table C.2 – continued from previous page

Mineral ab	SiO_2	TiO_2	Al_2O_3	FeOt	CaO	MgO	MnO	K_2O	Na_2O	P_2O_5	Volcano	Citation
Kspar2	66.85	0.07	18.67	0.27900279	0	0	0.13	7.21	5.7	0	Gedemsa	Peccerillo et al. (2003)
Kspar3	66.95	0.01	17.34	2.03402034	0	0	0.02	6.67	6.74	0	Gedemsa	Peccerillo et al. (2003)
Kspar4	65.64	0.04	22.14	0.2700027	0	0	2.07	8.25	1.71	0	Gedemsa	Peccerillo et al. (2003)
Kspar5	64.92	0.07	21.89	0.26100261	0	0	2.23	8.2	2.14	0	Gedemsa	Peccerillo et al. (2003)
Aenigmatite	40.99	8.76	0.38	38.00918	0.12	0	0.29	7.08	0.01	0	Gedemsa	Peccerillo et al. (2003)
Magnatite_1	0	22.19	0.28	73.3	2.4	0.12	0	0	0	0	Boset	Ronga et al. (2009)
Ilmenite	0	52.02	0.02	46.41	2.17	0	0	0	0	0	Boset	Ronga et al. (2009)
Magnatite_2	0.08	24.85	0.05	69.76	1.92	0.04	0	0	0	0	Boset	Ronga et al. (2009)
Apatite	0	0	0	2.5	0.08	0	50.32	0.16	0.23	39.99	Pantelleria	White et al. (2023)
Quartz	100	0	0	0	0	0	0	0	0	0		
Amphibole	48.89	2.31	1.18	29.36	1.26	4.27	5.6	5.15	1.13	0	Pantelleria	White et al. (2023)
CPX4	50.34	1.49	0.1	28.62	0.79	0.05	9.02	7.85	0	0	Boset	Ronga et al. (2009)

Table C.3: Details of each of the mass balance model results which information on the different mineral phases predicted to crystallise with their composition. Table covers model runs A - W

Corbetti		Colby et al. (2022)						
A	Parent		Daughter	Kspar2	Q	CPX1	CPX	Fa	Il
	Qz*								
wt.%	33.62		41.22						
SiO_2	75.44		76.65	66.98	100.00	48.47	52.50	29.76	0.00
TiO_2	0.25		0.27	0.03	0.00	0.39	0.98	0.03	52.02
Al_2O_3	11.56		9.87	18.42	0.00	0.29	0.19	-0.01	0.02
FeOt	2.92		3.78	0.71	0.00	29.61	30.49	63.66	46.41
MnO	0.13		0.15	0.00	0.00	2.24	0.80	5.94	2.17
MgO	0.02		0.07	0.00	0.00	0.54	0.13	0.33	0.00
CaO	0.36		0.30	0.02	0.00	16.42	3.72	0.26	0.00
Na_2O	4.48		3.87	6.68	0.00	1.88	11.16	0.03	0.00

K_2O	4.73		4.88		7.10	0.00	0.11	0.00	0.01	0.00
P_2O_5	0.02		0.03		0.00	0.00	0.03	0.06	0.00	0.00
		f/c%		r						
		74.09		0.00	0.66	0.29	0.02	0.02	0.01	0.00

Corbetti B		**Colby et al. (2022)**							
		Parent		**Daughter**	**Kspar2**	**Q**	**CPX1**	**Fa**	**Mg2**
		Qz*							
wt.%		33.62		43.19					
SiO_2	75.44		76.11		66.98	100.00	48.47	29.76	0.08
TiO_2	0.25		0.33		0.03	0.00	0.39	0.03	24.85
Al_2O_3	11.56		9.19		18.42	0.00	0.29	-0.01	0.05
FeOt	2.92		5.01		0.71	0.00	29.61	63.66	69.76
MnO	0.13		0.21		0.00	0.00	2.24	5.94	1.92
MgO	0.02		0.07		0.00	0.00	0.54	0.33	0.04
CaO	0.36		0.25		0.02	0.00	16.42	0.26	0.00
Na_2O	4.48		4.22		6.68	0.00	1.88	0.03	0.00
K_2O	4.73		4.45		7.10	0.00	0.11	0.01	0.00
P_2O_5	0.02		0.02		0.00	0.00	0.03	0.00	0.00
		f/c%		r					
		70.14		0.00	0.68	0.03	0.02	0.01	0.28

Corbetti C		**Colby et al. (2022)**						
		Parent		**Daughter**	**Kspar 2**	**Q**	**CPX1**	**CPX3**	**Aeg**
		Qz*							
wt.%		33.99		41.23					
SiO_2	75.39		76.65		66.98	100.00	48.47	52.50	39.33
TiO_2	0.26		0.27		0.03	0.00	0.39	0.98	7.74
Al_2O_3	11.43		9.87		18.42	0.00	0.29	0.19	1.33

FeOt	3.01		3.78		0.71	0.00	29.61	30.49	39.69
MnO	0.13		0.15		0.00	0.00	2.24	0.80	1.15
MgO	0.03		0.07		0.00	0.00	0.54	0.13	0.09
CaO	0.41		0.30		0.02	0.00	16.42	3.72	1.02
Na_2O	4.47		3.87		6.68	0.00	1.88	11.16	5.80
K_2O	4.76		4.88		7.10	0.00	0.11	0.00	0.32
P_2O_5	0.02		0.03		0.00	0.00	0.03	0.06	0.00
		f/c%		r					
		67.33		0.00	0.66	0.28	0.02	0.01	0.28

Corbetti D		**Colby et al. (2022)**							
		Parent		**Daughter**	**Kspar 2**	**Q**	**CPX1**	**CPX3**	**Fa**	**Il**
		Qz*							
wt.%		36.72		41.23						
SiO_2	75.70		76.65		66.98	100.00	48.47	52.50	29.76	0.00
TiO_2	0.27		0.27		0.03	0.00	0.39	0.98	0.03	52.02
Al_2O_3	10.77		9.87		18.42	0.00	0.29	0.19	-0.01	0.02
FeOt	3.57		3.78		0.71	0.00	29.61	30.49	63.66	46.41
MnO	0.16		0.15		0.00	0.00	2.24	0.80	5.94	2.17
MgO	0.02		0.07		0.00	0.00	0.54	0.13	0.33	0.00
CaO	0.30		0.30		0.02	0.00	16.42	3.72	0.26	0.00
Na_2O	4.33		3.87		6.68	0.00	1.88	11.16	0.03	0.00
K_2O	4.77		4.88		7.10	0.00	0.11	0.00	0.01	0.00
P_2O_5	0.01		0.03		0.00	0.00	0.03	0.06	0.00	0.00
		f/c%		r						
		39.44		0.00	0.65	0.28	0.01	0.04	0.02	0.00

Corbetti E		**Colby et al. (2022)**							
		Parent		**Daughter**	**Kspar 2**	**Q**	**CPX1**	**CPX4**	**Mg2**	**Ap**

			Qz*						
wt.%		36.98		42.24					
SiO_2	73.93		75.02		66.98	100.00	48.47	51.27	0.08	0.00
TiO_2	0.35		0.33		0.03	0.00	0.39	1.21	24.85	0.00
Al_2O_3	10.04		9.06		18.42	0.00	0.29	1.63	0.05	0.00
FeOt	4.92		5.34		0.71	0.00	29.61	10.63	69.76	2.50
MnO	0.20		0.27		0.00	0.00	2.24	0.34	1.92	0.08
MgO	0.09		0.03		0.00	0.00	0.54	14.09	0.04	0.00
CaO	0.39		0.22		0.02	0.00	16.42	20.45	0.00	50.32
Na_2O	5.28		5.25		6.68	0.00	1.88	0.30	0.00	0.16
K_2O	4.61		4.32		7.10	0.00	0.11	0.02	0.00	0.23
P_2O_5	0.04		0.01		0.00	0.00	0.03	0.06	0.00	39.99
		f/c%		r						
		15.79		0.00	0.83	0.10	0.02	0.03	0.02	0.01

Corbetti F	**Colby et al. (2022) Parent**		**Fontijn et al. (2018) Daughter**		**Kspar 2**	**Q**	**CPX1**	**CPX4**	**Fa**	**Aeg**
			Qz*							
wt.%		36.98		42.31						
SiO_2	73.93		75.03		66.98	100.00	48.47	51.27	29.76	39.33
TiO_2	0.35		0.28		0.03	0.00	0.39	1.21	0.03	7.74
Al_2O_3	10.04		9.13		18.42	0.00	0.29	1.63	-0.01	1.33
FeOt	4.92		4.59		0.71	0.00	29.61	10.63	63.66	39.69
MnO	0.20		0.31		0.00	0.00	2.24	0.34	5.94	1.15
MgO	0.09		0.02		0.00	0.00	0.54	14.09	0.33	0.09
CaO	0.39		0.24		0.02	0.00	16.42	20.45	0.26	1.02
Na_2O	5.28		5.54		6.68	0.00	1.88	0.30	0.03	5.80
K_2O	4.61		4.53		7.10	0.00	0.11	0.02	0.01	0.32
P_2O_5	0.04		0.04		0.00	0.00	0.03	0.06	0.00	0.00
		f/c%		r						

	30.70	0.01	0.65	0.23	0.02	0.02	0.03	0.07

Corbetti G	**Colby et al. (2022) Parent**	**Fontijn et al. (2018) Daughter**	**Kspar 2**	**Q**	**CPX4**	**Fa**	**Il**	**Ap**
	Qz*							
wt.%	36.98	41.19						
SiO_2	73.93	75.10	66.98	100.00	51.27	29.76	0.00	0.00
TiO_2	0.35	0.31	0.03	0.00	1.21	0.03	52.02	0.00
Al_2O_3	10.04	9.44	18.42	0.00	1.63	-0.01	0.02	0.00
FeOt	4.92	4.61	0.71	0.00	10.63	63.66	46.41	2.50
MnO	0.20	0.13	0.00	0.00	0.34	5.94	2.17	0.08
MgO	0.09	0.02	0.00	0.00	14.09	0.33	0.00	0.00
CaO	0.39	0.18	0.02	0.00	20.45	0.26	0.00	50.32
Na_2O	5.28	5.42	6.68	0.00	0.30	0.03	0.00	0.16
K_2O	4.61	4.45	7.10	0.00	0.02	0.01	0.00	0.23
P_2O_5	0.04	0.00	0.00	0.00	0.06	0.00	0.00	39.99
	f/c%	r						
	16.71	0.01	0.71	0.16	0.04	0.08	0.01	0.01

Corbetti H	**Colby et al. (2022) Parent**	**Daughter**	**Kspar 2**	**Q**	**CPX1**	**Fa**	**Mg**	**Amph**
	Qz*							
wt.%	36.31	42.24						
SiO_2	74.46	75.02	66.98	100.00	48.47	29.76	0.08	48.89
TiO_2	0.28	0.33	0.03	0.00	0.39	0.03	24.85	2.31
Al_2O_3	10.39	9.06	18.42	0.00	0.29	-0.01	0.05	1.18
FeOt	4.87	5.34	0.71	0.00	29.61	63.66	69.76	29.36
MnO	0.21	0.27	0.00	0.00	2.24	5.94	1.92	1.26
MgO	0.05	0.03	0.00	0.00	0.54	0.33	0.04	4.27
CaO	0.33	0.22	0.02	0.00	16.42	0.26	0.00	5.60

Na_2O	4.81		5.25		6.68	0.00	1.88	0.03	0.00	5.15
K_2O	4.46		4.32		7.10	0.00	0.11	0.01	0.00	1.13
P_2O_5	0.00		0.01		0.00	0.00	0.03	0.00	0.00	0.00
		f/c%		r						
		48.76		0.01	0.64	0.28	0.02	0.04	0.01	0.02

Corbetti I	**Colby et al. (2022) Parent**		**Fontijn et al. (2018) Daughter**		**Kspar 2**	**Q**	**CPX1**	**CPX4**	**Fa**	**Mg**
		Qz*								
wt.%		36.31		41.19						
SiO_2	74.46		75.10		66.98	100.00	48.47	51.27	29.76	0.08
TiO_2	0.28		0.31		0.03	0.00	0.39	1.21	0.03	24.85
Al_2O_3	10.39		9.44		18.42	0.00	0.29	1.63	-0.01	0.05
FeOt	4.87		4.61		0.71	0.00	29.61	10.63	63.66	69.76
MnO	0.21		0.13		0.00	0.00	2.24	0.34	5.94	1.92
MgO	0.05		0.02		0.00	0.00	0.54	14.09	0.33	0.04
CaO	0.33		0.18		0.02	0.00	16.42	20.45	0.26	0.00
Na_2O	4.81		5.42		6.68	0.00	1.88	0.30	0.03	0.00
K_2O	4.46		4.45		7.10	0.00	0.11	0.02	0.01	0.00
P_2O_5	0.00		0.00		0.00	0.00	0.03	0.06	0.00	0.00
		f/c%		r						
		47.95		0.00	0.62	0.29	0.02	0.01	0.05	0.01

Boset J	**Brotzu et al. (1980) Parent**		**Fontijn et al. (2018) Daughter**	**Mgt**	**Ap**	**Kspar**	**Kspar**	**CPX**	**Amph**
		Qz*							
wt.%	8.75		23.27						
SiO_2	64.70		71.91	0.00	0.00	63.90	66.82	52.25	48.89
TiO_2	0.91		0.26	22.19	0.00	0.00	0.00	0.75	2.31

Al_2O_3	14.55	13.21	0.28	0.00	22.28	19.43	1.26	1.18
FeOt	6.12	3.10	73.30	2.50	0.00	0.18	12.16	29.36
MnO	0.28	0.14	2.40	0.08	0.00	0.00	0.52	1.26
MgO	0.75	0.10	0.12	0.00	0.00	0.00	14.23	4.27
CaO	2.02	0.45	0.00	50.32	3.47	0.49	17.84	5.60
Na_2O	6.43	5.73	0.00	0.16	8.45	8.19	0.48	5.15
K_2O	3.82	4.86	0.00	0.23	1.91	4.79	0.00	1.13
P_2O_5	0.24	0.01	0.00	39.99	0.00	0.00	0.00	0.00
	f/c%	r						
	55.63	0.00	0.05	0.10	0.27	0.48	0.04	0.15

Boset K	**Brotzu et al. (1980) Parent**	**Fontijn et al. (2018) Daughter**	**Il**	**Ap**	**Kspar**	**Kspar4**	**CPX3**	**Amph**
	Qz*							
wt.%	5.39	22.82						
SiO_2	63.73	71.33	0.00	0.00	67.78	67.01	50.34	48.89
TiO_2	0.65	0.27	46.89	0.00	0.00	0.00	1.49	2.31
Al_2O_3	13.68	13.06	0.20	0.00	18.40	18.77	0.10	1.18
FeOt	7.41	3.53	43.10	2.50	0.43	0.85	28.62	29.36
MnO	0.42	0.19	2.83	0.08	0.00	0.00	0.79	1.26
MgO	0.53	0.07	0.00	0.00	0.05	0.00	0.05	4.27
CaO	1.71	0.45	0.00	50.32	0.16	0.07	9.02	5.60
Na_2O	7.57	5.97	0.00	0.16	7.22	7.66	7.85	5.15
K_2O	4.02	4.86	0.00	0.23	5.81	5.89	0.00	1.13
P_2O_5	0.06	0.02	0.00	39.99	0.00	0.00	0.00	0.00
	f/c%	r						
	82.22	0.05	0.01	0.00	0.30	0.43	0.13	0.14

Boset L	**Brotzu et al. (1980) Parent**	**Fontijn et al. (2018) Daughter**	**Fa**	**Aeg**	**Kspar2**	**Kspar4**	**CPX3**	**Amph**

		Qz*						
wt.%	9.40	23.16						
SiO_2	65.04	71.71	29.73	39.33	68.22	67.01	50.34	48.89
TiO_2	0.58	0.24	0.00	7.74	0.00	0.00	1.49	2.31
Al_2O_3	13.28	13.14	0.00	1.33	18.88	18.79	0.10	1.18
FeOt	7.41	3.15	66.47	39.69	0.51	0.83	28.62	29.36
MnO	0.49	0.18	2.07	1.15	0.00	0.00	0.79	1.26
MgO	0.47	0.07	0.81	0.09	0.00	0.00	0.05	4.27
CaO	1.33	0.44	0.75	1.02	0.05	0.01	9.02	5.60
Na_2O	7.55	5.84	0.00	5.80	9.48	7.60	7.85	5.15
K_2O	3.60	4.99	0.00	0.32	3.41	6.02	0.00	1.13
P_2O_5	0.04	0.02	0.00	0.00	0.00	0.00	0.00	0.00
	f/c%	r						
	67.28	0.06	0.00	0.04	0.59	0.11	0.10	0.15

Boset M	**Brotzu et al. (1980) Parent**	**Fontijn et al. (2018) Daughter**	**Aeg**	**Kspar2**	**Kspar4**	**CPX**	**Amph**
		Qz*					
wt.%	9.60	22.83					
SiO_2	64.85	71.33	0.00	68.22	67.01	50.34	48.89
TiO_2	0.60	0.27	0.00	0.00	0.00	1.49	2.31
Al_2O_3	13.09	13.06	0.00	18.88	18.79	0.10	1.18
FeOt	7.48	3.53	2.50	0.51	0.83	28.62	29.36
MnO	0.37	0.19	0.08	0.00	0.00	0.79	1.26
MgO	0.38	0.07	0.00	0.00	0.00	0.05	4.27
CaO	1.49	0.45	50.32	0.05	0.01	9.02	5.60
Na_2O	7.98	5.97	0.16	9.48	7.60	7.85	5.15
K_2O	3.49	4.86	0.23	3.41	6.02	0.00	1.13
P_2O_5	0.05	0.02	39.99	0.00	0.00	0.00	0.00
	f/c%	r					

	68.45	0.13	0.04	0.65	0.05	0.17	0.09

Boset N	**Fontijn et al. (2018)**						
	Parent	**Daughter**	**Fa**	**Aeg**	**Kspar4**	**CPX**	
	Qz*						
wt.%	36.21	42.70					
SiO_2	69.14	72.53	29.73	0.00	67.01	50.34	
TiO_2	0.43	0.15	0.00	0.00	0.00	1.49	
Al_2O_3	8.50	8.22	0.00	0.00	18.79	0.10	
FeOt	8.91	6.68	66.47	2.50	0.83	28.62	
MnO	0.49	0.29	2.07	0.08	0.00	0.79	
MgO	0.01	0.02	0.81	0.00	0.00	0.05	
CaO	0.52	0.29	0.75	50.32	0.01	9.02	
Na_2O	7.26	6.97	0.00	0.16	7.60	7.85	
K_2O	4.27	4.33	0.00	0.23	6.02	0.00	
P_2O_5	0.03	0.03	0.00	39.99	0.00	0.00	
	f/c%	r					
	19.55	0.12	0.04	0.22	0.52	0.20	

Boset O	**Macdonald et al. (2012)**						
	Parent	**Daughter**	**Kspar4**	**Quartz**	**CPxs**	**Fa**	**Mgt1**
	Qz*						
wt.%	38.86	56.48					
SiO_2	71.31	71.19	67.01	100.00	48.16	29.73	0.00
TiO_2	0.52	0.83	0.00	0.00	0.77	0.00	22.19
Al_2O_3	8.78	5.28	18.79	0.00	0.40	0.00	0.28
FeOt	8.40	11.19	0.83	0.00	27.30	66.47	73.30
MnO	0.33	0.49	0.00	0.00	2.01	2.07	2.40
MgO	0.01	0.00	0.00	0.00	1.72	0.81	0.12
CaO	0.44	0.54	0.01	0.00	19.68	0.75	0.00

Na_2O	5.17		5.11		7.60	0.00	0.74	0.00	0.00
K_2O	4.50		4.65		6.02	0.00	0.00	0.00	0.00
P_2O_5	0.01		0.07		0.00	0.00	0.00		0.00
		f/c%		r					
		44.33		0.01	0.70	0.22	0.01	0.05	0.01

Boset P		**Macdonald et al. (2012) Parent Qz***		**Daughter**	**Kspar4**	**Quartz**	**CPX2**	**Fa**
wt.%		38.86		59.42				
SiO_2	71.31		72.77		67.01	100.00	48.16	29.73
TiO_2	0.52		0.80		0.00	0.00	0.77	0.00
Al_2O_3	8.78		5.13		18.79	0.00	0.40	0.00
FeOt	8.40		11.10		0.83	0.00	27.30	66.47
MnO	0.33		0.45		0.00	0.00	2.01	2.07
MgO	0.01		0.00		0.00	0.00	1.72	0.81
CaO	0.44		0.23		0.01	0.00	19.68	0.75
Na_2O	5.17		4.81		7.60	0.00	0.74	0.00
K_2O	4.50		3.92		6.02	0.00	0.00	0.00
P_2O_5	0.01		0.06		0.00	0.00	0.00	
		f/c%		r				
		34.84		0.07	0.83	0.10	0.04	0.02

Boset Q		**Macdonald et al. (2012) Parent Qz***		**Daughter**	**Kspar2**	**Kspar4**	**Quartz**
wt.%		37.78		56.66			
SiO_2	70.68		70.47		68.22	67.01	100.00
TiO_2	0.49		0.86		0.00	0.00	0.00
Al_2O_3	8.72		4.98		18.88	18.79	0.00

FeOt	8.21		11.85	0.51	0.83	0.00
MnO	0.18		0.23	0.00	0.00	0.00
MgO	0.01		0.17	0.00	0.00	0.00
CaO	0.39		0.68	0.05	0.01	0.00
Na_2O	6.59		6.16	9.48	7.60	0.00
K_2O	4.32		4.25	3.41	6.02	0.00
P_2O_5	0.03		0.00	0.00	0.00	0.00
		f/c%	r			
		32.17	0.03	0.35	0.53	0.12

Boset		**Macdonald et al. (2012)**				
R		**Parent**	**Daughter**	**Il**	**Kspar**	**Q**
		Qz*				
wt.%		59.42	75.17			
SiO_2	72.77		69.28	0.00	67.01	100.00
TiO_2	0.80		0.26	52.02	0.00	0.00
Al_2O_3	5.13		2.38	0.02	18.79	0.00
FeOt	11.10		17.81	46.41	0.83	0.00
MnO	0.45		1.36	2.17	0.00	0.00
MgO	0.00		0.00	0.00	0.00	0.00
CaO	0.23		0.33	0.00	0.01	0.00
Na_2O	4.81		3.51	0.00	7.60	0.00
K_2O	3.92		3.61	0.00	6.02	0.00
P_2O_5	0.06		0.33	0.00	0.00	0.00
		f/c%	r			
		39.74	0.69	0.02	0.55	0.42

Kone		**Iddon and Edmonds (2020)**			
S		**Parent**	**Daughter**	**Kspar4**	**Q**

		Qz*						
wt.%	27.02	33.37						
SiO_2	70.22	69.87	67.01	100.00				
TiO_2	0.31	0.35	0.00	0.00				
Al_2O_3	11.18	9.74	18.79	0.00				
FeOt	6.22	7.41	0.83	0.00				
MnO	0.29	0.35	0.00	0.00				
MgO	0.02	0.03	0.00	0.00				
CaO	0.21	0.33	0.01	0.00				
Na_2O	6.19	6.04	7.60	0.00				
K_2O	5.11	4.61	6.02	0.00				
P_2O_5	0.06	0.06	0.00	0.00				
	f/c%	r						
	17.48	0.09	0.98	0.07				

Kone	**Iddon and Edmonds (2020)**							
T	**Parent**	**Daughter**	**Kspar4**	**Q**	**CPX2**	**Fa**	**Mgt1**	**Ap**
		Qz*						
wt.%	22.79	34.04						
SiO_2	70.27	70.50	67.01	100.00	48.16	29.73	0.00	0.00
TiO_2	0.48	0.55	0.00	0.00	0.77	0.00	22.19	0.00
Al_2O_3	10.95	9.56	18.79	0.00	0.40	0.00	0.28	0.00
FeOt	7.25	8.01	0.83	0.00	27.30	66.47	73.30	2.50
MnO	0.33	0.42	0.00	0.00	2.01	2.07	2.40	0.08
MgO	0.04	0.02	0.00	0.00	1.72	0.81	0.12	0.00
CaO	0.40	0.28	0.01	0.00	19.68	0.75	0.00	50.32
Na_2O	5.30	5.70	7.60	0.00	0.74	0.00	0.00	0.16
K_2O	4.64	4.59	6.02	0.00	0.00	0.00	0.00	0.23
P_2O_5	0.12	0.13	0.00	0.00	0.00	0.00	0.00	39.99
	f/c%	r						

	41.48	0.10	0.69	0.21	0.02	0.06	0.02	0.00

Kone U	**Iddon and Edmonds (2020) Parent**	**Fontijn et al. (2018) Daughter**	**Kspar2**	**Q**	**Kspar3**	**Fa**	**Aeg**
	Qz*						
wt.%	37.12	41.75					
SiO_2	75.42	76.28	68.22	100.00	66.82	29.73	39.33
TiO_2	0.26	0.16	0.00	0.00	0.00	0.00	7.74
Al_2O_3	10.71	9.60	18.88	0.00	19.43	0.00	1.33
FeOt	3.59	3.61	0.51	0.00	0.18	66.47	39.69
MnO	0.16	0.21	0.00	0.00	0.00	2.07	1.15
MgO	0.00	0.03	0.00	0.00	0.00	0.81	0.09
CaO	0.21	0.17	0.05	0.00	0.49	0.75	1.02
Na_2O	4.54	3.51	9.48	0.00	8.19	0.00	5.80
K_2O	4.62	6.28	3.41	0.00	4.79	0.00	0.32
P_2O_5	0.00	0.04	0.00	0.00		0.00	0.00
	f/c%	r					
	45.29	0.00	0.29	0.30	0.34	0.02	0.00

Kone V	**Iddon and Edmonds (2020) Parent**	**Fontijn et al. (2018) Daughter**	**Kspar4**	**Q**	**CPX3**	**Fa**	**Mgt**
	Qz*						
wt.%	37.61	41.75					
SiO_2	75.87	76.28	67.01	100.00	50.34	29.73	0.00
TiO_2	0.25	0.16	0.00	0.00	1.49	0.00	22.19
Al_2O_3	10.74	9.60	18.79	0.00	0.10	0.00	0.28
FeOt	3.40	3.61	0.83	0.00	28.62	66.47	73.30
MnO	0.14	0.21	0.00	0.00	0.79	2.07	2.40
MgO	0.00	0.03	0.00	0.00	0.05	0.81	0.12
CaO	0.20	0.17	0.01	0.00	9.02	0.75	0.00

Na_2O	4.32	3.51	7.60	0.00	7.85	0.00	0.00
K_2O	4.56	6.28	6.02	0.00	0.00	0.00	0.00
P_2O_5	0.00	0.04	0.00	0.00	0.00	0.00	0.00
	f/c%	r					
	64.95	0.00	0.60	0.34	0.02	0.02	0.01

Kone W	**Iddon and Edmonds (2020) Parent Qz***	**Fontijn et al. (2018) Daughter**	**Kspar2**	**Q**	**CPX3**	**Mgt**
wt.%	37.61	41.44				
SiO_2	75.87	76.43	68.22	100.00	50.34	0.00
TiO_2	0.25	0.22	0.00	0.00	1.49	22.19
Al_2O_3	10.74	9.74	18.88	0.00	0.10	0.28
FeOt	3.40	4.20	0.51	0.00	28.62	73.30
MnO	0.14	0.20	0.00	0.00	0.79	2.40
MgO	0.00	0.01	0.00	0.00	0.05	0.12
CaO	0.20	0.16	0.05	0.00	9.02	0.00
Na_2O	4.32	3.12	9.48	0.00	7.85	0.00
K_2O	4.56	5.80	3.41	0.00	0.00	0.00
P_2O_5	0.00	0.00	0.00	0.00	0.00	0.00
	f/c%	r				
	35.14	0.00	0.67	0.28	0.03	0.01

Table C.4: Details of mass balance model runs AA-NN exploring the controls on the trends observed in the Qz-Or-Ab-Ac-Ns residua system.

	Glass data from Fontijn et al. (2018) Boset					
AA	**Parent**	**Daughter**	**Kspar**	**Quartz**	**CPX**	**Aeg**

wt.%	MER120	MER120	34.40			
SiO_2	74.86	74.52	67.78	100.00	50.34	41.79
TiO_2	0.19	0.22	0.00	0.00	1.49	8.94
Al_2O_3	9.73	9.13	18.40	0.00	0.10	0.29
FeOt	4.41	5.28	0.43	0.00	28.62	42.27
MnO	0.26	0.20	0.00	0.00	0.79	1.23
MgO	0.00	0.00	0.05	0.00	0.05	0.12
CaO	0.17	0.19	0.16	0.00	9.02	0.21
Na_2O	4.56	3.05	7.22	0.00	7.85	7.48
K_2O	5.42	7.02	5.81	0.00	0.00	0.02
P_2O_5	0.00	0.01	0.00	0.00	0.00	0.00
	f/c %	**r**		**Mass fraction**		
	35.19	0.22	0.60	0.31	0.05	0.03
BB	**Parent**	**Daughter**	**Kspar**	**Quartz**	**CPX**	**Aeg**
wt.%	MER120	MER120	34.40			
SiO_2	74.86	75.19	67.78	100.00	50.34	41.79
TiO_2	0.19	0.26	0.00	0.00	1.49	8.94
Al_2O_3	9.73	9.30	18.40	0.00	0.10	0.29
FeOt	4.41	5.10	0.43	0.00	28.62	42.27
MnO	0.26	0.12	0.00	0.00	0.79	1.23
MgO	0.00	0.00	0.05	0.00	0.05	0.12
CaO	0.17	0.22	0.16	0.00	9.02	0.21
Na_2O	4.56	2.87	7.22	0.00	7.85	7.48
K_2O	5.42	6.54	5.81	0.00	0.00	0.02
P_2O_5	0.00	0.00	0.00	0.00	0.00	0.00
	f/c %	**r**		**Mass Fraction**		
	31.50	0.53	0.62	0.28	0.07	0.02

Aluto

CC	Parent	Daughter	Kspar	Quartz	CPX	Aeg
wt.%	Aluto 24_01_21	Aluto 24_01_21	28.66			
SiO_2	73.90	73.16	67.88	100.00	50.34	41.79
TiO_2	0.20	0.24	0.00	0.00	1.49	8.94
Al_2O_3	8.77	8.68	18.54	0.00	0.10	0.29
FeOt	5.70	6.07	0.30	0.00	28.62	42.27
MnO	0.27	0.20	0.00	0.00	0.79	1.23
MgO	0.01	0.01	0.00	0.00	0.05	0.12
CaO	0.21	0.21	0.11	0.00	9.02	0.21
Na_2O	4.45	4.20	8.16	0.00	7.85	7.48
K_2O	6.09	6.83	5.02	0.00	0.00	0.02
P_2O_5	0.02	0.00	0.00	0.00	0.00	0.00
	f/c %	**r**		**Mass Fraction**		
	17.30	0.04	0.51	0.38	0.07	0.05
DD	**Parent**	**Daughter**	**Kspar**	**Quartz**	**Fa**	**Aeg**
wt.%	Aluto 24_01_21	Aluto 24_01_21	28.55			
SiO_2	74.14	73.16	67.88	100.00	29.73	41.79
TiO_2	0.18	0.24	0.00	0.00	0.00	8.94
Al_2O_3	8.89	8.68	18.54	0.00	0.00	0.29
FeOt	6.10	6.07	0.30	0.00	66.47	42.27
MnO	0.28	0.20	0.00	0.00	2.07	1.23
MgO	0.03	0.01	0.00	0.00	0.81	0.12
CaO	0.16	0.21	0.11	0.00	0.75	0.21
Na_2O	4.32	4.20	8.16	0.00	0.00	7.48
K_2O	5.46	6.83	5.02	0.00	0.00	0.02
P_2O_5	0.03	0.00	0.00	0.00	0.00	0.00
	f/c %	**r**		**Mass Fraction**		
	31.94	0.02	0.51	0.38	0.07	0.03

EE	Parent	Daughter	Kspar	Quartz	CPX	OL	Mgt
wt.%	Syn-Cal	Syn-Cal	39.90				
SiO_2	74.23	75.49	66.95	100.00	49.08	29.79	0.00
TiO_2	0.36	0.25	0.01	0.00	1.23	0.00	22.19
Al_2O_3	9.58	9.20	17.34	0.00	0.56	0.00	0.28
FeOt	5.11	5.22	2.03	0.00	35.43	64.80	73.30
MnO	0.10	0.18	0.00	0.00	1.10	6.36	2.40
MgO	0.03	0.00	0.00	0.00	0.23	0.08	0.12
CaO	0.24	0.21	0.02	0.00	3.11	0.58	0.00
Na_2O	5.76	2.94	6.67	0.00	6.41	0.00	0.00
K_2O	4.29	6.12	6.74	0.00	1.45	0.00	0.00
P_2O_5	0.00	0.04	0.00	0.00	0.00	0.00	0.00
	f/c %	**r**			**Mass Fraction**		
	59.66	0.09	0.69	0.27	0.02	0.01	0.01

FF	Parent	Daughter	Kspar	Quartz	CPX	Il	CPX
wt.%	Syn-Cal	Syn-Cal	39.90				
SiO_2	74.23	74.81	66.95	100.00	50.34	0.00	49.08
TiO_2	0.36	0.31	0.01	0.00	1.49	52.02	1.23
Al_2O_3	9.58	9.18	17.34	0.00	0.10	0.02	0.56
FeOt	5.11	5.59	2.03	0.00	28.62	46.41	35.43
MnO	0.10	0.26	0.00	0.00	0.79	2.17	1.10
MgO	0.03	0.02	0.00	0.00	0.05	0.00	0.23
CaO	0.24	0.20	0.02	0.00	9.02	0.00	3.11
Na_2O	5.76	3.31	6.67	0.00	7.85	0.00	6.41
K_2O	4.29	5.98	6.74	0.00	0.00	0.00	1.45
P_2O_5	0.00	0.03	0.00	0.00	0.00	0.00	0.00
	f/c %	**r**			**Mass Fraction**		
	36.87	0.02	0.68	0.28	0.02	0.01	0.01

GG	Parent	Daughter	Kspar	Quartz	CPX
wt.%	MER087A	MER087A	39.90		
SiO_2	73.08	72.61	66.95	100.00	49.08
TiO_2	0.18	0.20	0.01	0.00	1.23
Al_2O_3	7.75	6.77	17.34	0.00	0.56
FeOt	7.42	8.09	2.03	0.00	35.43
MnO	0.22	0.41	0.00	0.00	1.10
MgO	0.01	0.00	0.00	0.00	0.23
CaO	0.26	0.24	0.02	0.00	3.11
Na_2O	6.31	6.95	6.67	0.00	6.41
K_2O	4.21	4.06	6.74	0.00	1.45
P_2O_5	0.00	0.02	0.00	0.00	0.00
	f/c%	**r**	**Mass Fraction**		
	27.75	0.03	0.60	0.28	0.13

HH	Parent	Daughter	Kspar	Quartz	Aeg	CPX
wt.%	MER087A	MER087A	10.70			
SiO_2	73.44	73.18	65.64	100.00	40.99	49.08
TiO_2	0.28	0.17	0.04	0.00	8.76	1.23
Al_2O_3	8.11	7.62	22.14	0.00	0.38	0.56
FeOt	6.92	7.05	0.27	0.00	38.01	35.43
MnO	0.24	0.26	0.00	0.00	0.12	1.10
MgO	0.02	0.00	0.00	0.00	0.00	0.23
CaO	0.23	0.19	2.07	0.00	0.29	3.11
Na_2O	5.31	5.14	8.25	0.00	7.08	6.41
K_2O	4.96	5.79	1.71	0.00	0.01	1.45
P_2O_5	0.00	0.03	0.00	0.00	0.00	0.00
	f/c%	**r**		**Mass Fraction**		
	15.68	0.05	0.50	0.35	0.14	0.03

II	Parent	Daughter	Kspar	Quartz	Kspar
wt.%	MER082A	MER082A	35.27		34.40
SiO_2	72.46	71.89	66.85	100.00	65.64
TiO_2	0.31	0.36	0.07	0.00	0.04
Al_2O_3	10.46	10.37	18.67	0.00	22.14
FeOt	5.14	5.65	0.28	0.00	0.27
MnO	0.20	0.14	0.00	0.00	0.00
MgO	0.04	0.00	0.00	0.00	0.00
CaO	0.30	0.31	0.13	0.00	2.07
Na_2O	6.05	6.03	7.21	0.00	8.25
K_2O	4.64	4.84	5.70	0.00	1.71
P_2O_5	0.01	0.02	0.00	0.00	0.00
	f/c%	**r**	**Mass Fraction**		
	8.49	0.03	0.41	0.38	0.20
KK	**Parent**	**Daughter**	**Kspar**	**Quartz**	**Ap**
wt.%	MER082A	MER082A	35.27		
SiO_2	72.46	72.07	66.85	100.00	0.00
TiO_2	0.31	0.39	0.08	0.00	0.00
Al_2O_3	10.46	10.33	18.58	0.00	0.00
FeOt	5.14	5.63	0.38	0.00	2.50
MnO	0.20	0.19	0.00	0.00	0.08
MgO	0.04	0.03	0.00	0.00	0.00
CaO	0.30	0.28	0.11	0.00	50.32
Na_2O	6.05	6.05	7.16	0.00	0.16
K_2O	4.64	4.64	5.98	0.00	0.23
P_2O_5	0.01	0.01	0.00	0.00	39.99
	f/c%	**r**	**Mass Fraction**		
	8.26	0.02	0.68	0.31	0.01
JJ	**Parent**	**Daughter**	**Kspar**	**Quartz**	**Aeg**

wt.%	MER082A	MER082A	10.70		
SiO_2	72.34	71.89	65.64	100.00	40.99
TiO_2	0.30	0.36	0.04	0.00	8.76
Al_2O_3	10.69	10.37	22.14	0.00	0.38
FeOt	5.29	5.65	0.27	0.00	38.01
MnO	0.14	0.14	0.00	0.00	0.12
MgO	0.01	0.00	0.00	0.00	0.00
CaO	0.29	0.31	2.07	0.00	0.29
Na_2O	6.25	6.03	8.25	0.00	7.08
K_2O	4.27	4.84	1.71	0.00	0.01
P_2O_5	0.03	0.02	0.00	0.00	0.00
	f/c%	**r**	**Mass Fraction**		
	11.92	0.13	0.62	0.32	0.07

WR and Glass data from Macdonald et al, (2012)

LL	**Parent**	**Daughter**	**Kspar**	**CPX**	**Aen**	**Aen**	**Amph**
wt%	B350_WR	B350					
SiO_2	70.11	71.19	68.22	50.34	39.33	41.79	48.89
TiO_2	0.58	0.83	0.00	1.49	7.74	8.94	2.31
Al_2O_3	8.64	5.28	18.88	0.10	1.33	0.29	1.18
FeOt	9.13	11.19	0.51	28.62	39.69	42.27	29.36
MnO	0.30	0.49	0.00	0.79	1.15	1.23	1.26
MgO	0.00	0.00	0.00	0.05	0.09	0.12	4.27
CaO	0.38	0.54	0.05	9.02	1.02	0.21	5.60
Na_2O	6.30	5.11	9.48	7.85	5.80	7.48	5.15
K_2O	4.27	4.65	3.41	0.00	0.32	0.02	1.13
P_2O_5	0.02	0.07	0.00	0.00	0.00	0.00	0.00
	f/c%	r					
	27.01	0.04	0.94	0.01	0.04	0.02	0.01

MM	Parent	Daughter	Kspar	CPX	Aen
wt.%	B350	B350			
SiO_2	70.13	71.19	68.22	50.34	41.79
TiO_2	0.62	0.83	0.00	1.49	8.94
Al_2O_3	8.26	5.28	18.88	0.10	0.29
FeOt	9.08	11.19	0.51	28.62	42.27
MnO	0.29	0.49	0.00	0.79	1.23
MgO	0.00	0.00	0.00	0.05	0.12
CaO	0.28	0.54	0.05	9.02	0.21
Na_2O	6.54	5.11	9.48	7.85	7.48
K_2O	4.23	4.65	3.41	0.00	0.02
P_2O_5	0.08	0.07	0.00	0.00	0.00
	f/c%	**r**			
	25.08	0.20	0.94	0.01	0.05

NN	Parent	Daughter	Kspar	Quartz	CPX	CPX	Fa	Mg2
wt.%	B375	B375						
SiO_2	69.43	69.28	67.01	100.00	49.55	52.25	29.73	0.08
TiO_2	0.60	0.26	0.00	0.00	0.71	0.75	0.00	24.85
Al_2O_3	9.80	2.38	18.79	0.00	1.09	1.26	0.00	0.05
FeOt	9.09	17.81	0.83	0.00	19.49	12.16	66.47	69.76
MnO	0.42	1.36	0.00	0.00	1.64	0.52	2.07	1.92
MgO	0.55	0.00	0.00	0.00	6.80	14.23	0.81	0.04
CaO	0.93	0.33	0.01	0.00	20.08	17.84	0.75	0.00
Na_2O	4.70	3.51	7.60	0.00	0.56	0.48	0.00	0.00
K_2O	4.18	3.61	6.02	0.00	0.00	0.00	0.00	0.00
P_2O_5	0.03	0.33	0.00	0.00	0.00	0.00	0.00	0.00
	f/c%	**r**						
	67.35	0.05	0.71	0.18	0.01	0.05	0.02	0.03